On quantum multi-mode optical imaging
&
Light-atom ensemble interactions

Magnus Tze Loong Hsu

B. Sc. (Hons.), University of Adelaide, 2002

A thesis submitted for the degree of
Doctor of Philosophy at
The Australian National University

THE AUSTRALIAN NATIONAL UNIVERSITY

18 January 2008

Declaration

This thesis is an account of research undertaken between April 2003 and April 2007 at the Department of Physics, Faculty of Science, Australian National University (ANU), Canberra, Australia. The author was a visitor at the California Institute of Technology (Caltech), California, U.S.A., from April 2007 to August 2007, and the work performed at Caltech is reported in Chapter 10.

The majority of the research was supervised by Prof. Ping Koy Lam (ANU), Prof. Hans-Albert Bachor (ANU), Dr. Warwick Bowen (ANU) and Dr. Ben Buchler (ANU). Part of the work reported in Chapter 10 was supervised by Prof. Hideo Mabuchi (Caltech). Unless otherwise indicated, the work present herein is my own.

None of the work presented here has ever been submitted for any degree at this or any other institution of learning.

Magnus Tze Loong Hsu
18 January 2008

Acknowledgements

I would like to begin by thanking my principal supervisor, Prof. Ping Koy Lam. I would not have made the decision to pursue my PhD research at the ANU, had Ping Koy not invited me over for a visit. It was Ping Koy who 'snowballed' my research career and for that I cannot thank him enough. I admire Ping Koy's intuition and his sophistication when it came to problem solving. His team management skills were superb and I thoroughly enjoyed the many Sun Tzu quotes he recited. I would also like to thank my supervisor Prof. Hans Bachor for making sure I was always on track with my research and for constantly reminding me to look at the 'bigger picture'. Hans helped me tremendously to develop my public speaking skills and I thank him for giving me countless opportunities to give talks at international conferences. Dr. Warwick Bowen has been a great friend, a fantastic collaborator and an effective supervisor during the first half of my PhD. It was Warwick who sparked many of the great ideas for the quantum imaging work in this thesis and for motivating a sense of creativity in me, over a *yum-cha*. Dr. Ben Buchler supervised the second half of my PhD research and I will always remember Ben for his great jokes and superb technical abilities. From him, I learnt about 'taming' lasers, quantum optics and single molecules.

Over the course of my PhD, I have had the privilege to work with very talented physicists. Gabriel Hétet and Dr. Oliver Glöckl have been great team-mates on the atomic projects. It was with them that I spent countless hours bouncing ideas, arguing about physics and learnt a great deal from. Dr. Charles Harb has been a great friend and taught me about locking and electronics, over an ice-cream. Together we spent time building up the new ACQAO lab. Dr. Jevon Longdell has a been a great sailing partner and an excellent physicist to work with. I learnt about EIT from him and together, we made the light slow! Thanks also go to Dr. Nick Robins and Daniel Oblak (NBI Denmark) for working together on the MOT experiment. Thank you Nick for teaching me about atoms and diode lasers. In 2006, I had the opportunity to guide Kerry Burke through his Honours research project. I thank Kerry for teaching me physics too and for being a good lab partner.

I have had the opportunity to collaborate with Dr. Vincent Delaubert (ANU, LKB Paris) and Dr. Nicolas Treps (LKB Paris) for the quantum imaging work in this thesis. Together with them, we debated about physics and shared many great jokes over a roast duck. I would also like to thank my other collaborators at the Laboratoire Kastler Brossel (LKB) in Paris - Prof. Claude Fabre, Dr. Aurélien Dantan, Jean Cviklinski, Dr. Alberto Bramati, Dr. Michel Pinard and Dr. Agnès Maître.

The work in Chapter 10 was mainly performed in the laboratory of Prof. Hideo Mabuchi at the California Institute of Technology. I would like to thank Hideo for giving me the opportunity to work in his lab and for the hospitality of his group. During my time there, I have made great friends with the Mabuchi-lab crew - Sheri Stoll, Tony Miller, Mike Armen, Kevin McHale, Dr. Luc Bouten, Yeong Dae Kwon, Gopal Sarma, Orion Crisafulli, Joe Kerckhoff, Nathan Hodas, Dr. Andrew Silberfarb, Dr. Ramon van Handel and Asa Hopkins. Thank you all for providing me with the American experience! Special thanks

also go to my housemates at Chester (Benjamin, Daniel, Christian and Audrey) and to Dr. Keisuke Goda.

I have shared a fantastic journey with the people I shared an office with - Nicolai Grosse, Vikram Sharma, Dr. Mikael Lassen, Jiri Janousek, Christian Weedbrook, Dr. Andrew Lance, Dr. Thomas Symul, Katherine Wagner, Syed Assad, Dr. Hongxin Zhou, Roger Senior, Daniel Alton, Amy Peng, Mike Stefszky and Guy Micklethwait. Thank you all for answering my questions about physics, cryptography and anything else under the sun. I would also like to thank Nicolai for being a great friend, housemate and for the coffee sessions. Thanks also goes to the guys and gals of the Gravitational Wave Physics and Atom Optics groups - Dr. Mal Gray, Dr. Ian Littler, David Rabeling, Kirk McKenzie, Glenn DeVine, Jong Chow, Dr. Ben Sheard, Dr. Dan Shaddock, Dr. Simon Haine, Paul Summers, Dr. Beata Dabrowska, Dr. Sebastian Wuster, Dr. Joe Hope, Dr. Susan Scott, Prof. David McClelland, Dr. Craig Savage, Dr. John Close, Rachel Poldy, John Debs, Matt Jeppesen, Julien Dugue, Graham Dennis, Dr. Mattias Johnsson, Dr. Andre Carvalho and Dr. Christina Figl. Particular thanks to Mal for teaching me about electronics and opening my mind to Buddhism, to John for teaching me about atoms and politics; and to Simon for the dodgy jokes. Special thanks go to Ben and Gab for proof-reading my thesis.

It would not have been possible to navigate the bureaucratic rainforest without the administrative help from Damien Hughes, Sharon Lopez, Huma Cheema, Ruth Wilson and Andrew Papworth. Thank you Damien for making sure I was getting paid and for helping me sort out purchase orders! I would also like to thank Dr. Max Colla for being a great friend and for helping out with computer problems. The guys in the electronics and mechanical workshop have been largely responsible in building the equipment used in the lab. Without their assistance, my PhD would have taken twice as long to complete. I would like to thank Neil Devlin, Paul MacNamara, Paul Tant, Shane Grieves, James Dickson and Neil Hinchey.

Life in Canberra would have been all work and no play had I not made fantastic friends. For that I would like to thank Adelina, Angeline, Joon Meng, Ivory, Clancie, Russel, Lisa, Jason F, Roy, Lee Yuen, Justin, Mi'er, Eleanor, Jason K, Carina, Maxime, Tika, Elvie, Shivani, Yulia, Shellaine, Dansan, Deisigan and Raveen. I am sorry if I have not included your name in this list as I have limited space. Thank you all for the great times, great food, great jokes and for the encouragement throughout. We were almost like family, being away from home, and it has been a pleasure knowing you! Thanks also go to friends in Adelaide for helping my family and myself settle in as new migrants in 1997, in a new country, we now call home - the Atwells, the Moores, the Giordanos, the Kitts, the Tans, the Teohs and the Chans. Thank you for being there and sharing our aspirations.

As they say, we always save the best for last. I would like to take this opportunity to thank my Pa, for dragging me from under the table, to teach me to solve algebra. My Pa took me to see the world and gave me the most valuable gift of all - education. My Mie for looking after me, bringing me up and showering me with love. My Ah Dy for chasing me around the house and for being a great sister. My grandparents for taking me out for breakfast and for teaching me the importance of being a good person. My cousins, aunts and uncles for their love, encouragement and support. Particularly to Uncle Kim for taking care of me in the States, to Makee for encouraging me to pursue her footsteps in science, and to my late aunt, Ah San, for being great the way she has always been...

Abstract

This thesis covers the work of two research topics - *quantum multi-mode optical imaging* and *light-atom ensemble quantum interactions*. In *quantum multi-mode optical imaging*, we study optimal beam displacement and tilt measurements, spatial entanglement and spatial encoding. In *light-atom ensemble quantum interactions*, the generation of squeezed light via the polarisation self-rotation effect in atoms is examined. We then discuss quantum efficacy measurements of delayed light via electromagnetically induced transparency. Finally, we examine atomic spin state squeezing for applications in enhancing the sensitivity of magnetometers and atomic clocks.

For displacement and tilt measurements, we discover that the conventional split detection scheme is non-optimal with ~ 80 % efficiency. Consequently we propose a new detection scheme, based on a homodyne detection setup that has a specifically-tailored local oscillator mode-shape, optimal for small beam displacement and tilt. We show that although the quantum noise limit to displacement and tilt measurements can be surpassed using squeezed light in appropriate spatial modes for both schemes, the spatial homodyning scheme out-performs split detection for all values of squeezing. Thereafter, we show that a position squeezed beam (i.e. the beam position can be determined to an accuracy beyond the standard quantum limit) can be generated. We show that position and momentum entanglement can be generated by interfering two position, or momentum, squeezed beams on a beam-splitter. The position and momentum measurements of these beams can be performed using the optimal spatial homodyne detection scheme. We then compare this form of spatial entanglement with split detection-based spatial entanglement. The possibility of expressing beam position, momentum and orbital angular momentum in one common basis is also examined. The relevant modes responsible for beam position, momentum and orbital angular momentum span the Poincaré sphere. Consequently, spatial entanglement between these modes is proposed as well as the relevant detection schemes. A possible application of multi-mode quantum imaging for increasing the capacities of optical storage devices is then considered. A scheme which encodes information in both the longitudinal and spatial transverse phases of a continuous-wave optical beam is devised. Correspondingly, a split detector-based interferometric scheme is introduced to optimally detect both encoded phase signals. In contrast to present-day optical storage devices, our phase coding scheme has an information storage capacity which scales with the power of the read-out optical beam. We analyse the maximum number of encoding possibilities at the shot noise limit. In addition, we show that using squeezed light, the shot noise limit can be overcome and the number of encoding possibilities increased.

The traversal of an elliptically polarised optical field through a thermal vapour cell can give rise to a rotation of its polarisation axis. This process, known as polarisation self-rotation (PSR), has been suggested as a mechanism for producing squeezed light at atomic transition wavelengths. We show results of the characterisation of PSR in isotopically enhanced Rubidium-87 cells. We observe that, contrary to earlier work, the presence of atomic noise in the thermal vapour overwhelms the observation of squeezing. We present a theory that contains atomic noise terms and show that a null result in squeezing is consistent with this theory. Using electromagnetically induced transparency (EIT), it is possible to delay and store light in atomic ensembles. Published theoretical modelling and recent experiments have suggested that the EIT storage mechanism can be used as a memory for quantum information. We present experiments that quantify the noise performance of an EIT system for conjugate amplitude and phase quadratures. It is shown that our EIT system adds excess noise to the delayed light that has not been predicted by published conventional theoretical modelling. In analogy with other continuous-variable quantum information systems, the performance of our EIT system is characterised in terms of conditional variance and signal transfer. The sensitivity of atomic magnetometers and atomic clocks are ultimately limited by the atomic spin projection noise (i.e. due to the atom number variance), but could be overcome by the use of spin squeezed atoms. We explore the interaction of optical polarisation and atomic spin states via the Faraday effect. Quantum-non demolition measurements of the atomic spin state can therefore be performed to generate atoms in a spin squeezed state. We present theoretical and experimental results towards this goal.

Contents

List of Figures

List of Tables

Chapter 1

Introduction

As far as we can discern, the sole purpose of human existence is to kindle a light in the darkness of mere being.

- Carl Jung, "Memories, Dreams, Reflections" (1962)

1.1 Overview

The field of quantum optics deals with the manipulation and measurement of the properties of light at the quantum level. The discovery of the laser [9] has allowed the field of quantum optics to blossom. Traditionally, quantum optics has considered properties of the light field, generated via resonant and non-resonant atom-light interactions. The properties of the atomic system are often not considered as the atomic system primarily serves as a tool for the manipulation of the light state. Initial interests in quantum optics experiments concerned with examining the Einstein-Podolsky-Rosen paradox [10], via the experiment performed by Wu and Shaknov [11] and measurements of optical coherence, via the Hanbury Brown and Twiss experiment [12]. Following this, other important experiments in quantum optics have also been performed, for example, measuring photon anti-bunching [13], demonstrating the violation of Bell's inequalities [14, 15, 16] and continuous variable quantum entanglement [14, 17, 18], as well as Wheeler's delayed choice measurement [19]. There have also been several work strengthening the validity of quantum mechanics such as the measurement of the Wigner function of a single photon Fock state [20], the production of Schödinger kittens [21, 22] and the generation of larger kitten states [23]. Aside from tests on quantum mechanics, the application of quantum optical techniques to practical applications have been explored, and these include improving the sensitivity of gravitational wave detection, quantum information science and quantum imaging. In *interferometric gravitational wave detection*, squeezed light could be used to enhance the detector sensitivity better than the shot noise limit [24, 25]. For *quantum information*, quantum computing [26] was proposed to be the next generation computing scheme. Quantum computing has made significant progress, in particular, in photonic systems [27, 28, 29, 30, 31, 32], single ion systems [33, 34, 35, 36], single atom systems [37] and nuclear-magnetic resonance systems [38, 39, 40]. Complementing quantum computing is a plethora of quantum information protocols, such as quantum teleportation [41, 42], quantum dense-coding [43, 44, 45], quantum non-demolition measurements [46, 47, 48, 49] and quantum cryptography [50, 51]. In *multi-mode quantum imaging*, physicists have been exploring the generation of spatial entanglement [52, 53, 54, 55, 56], the possibility of resolving images with enhanced sensitivities [57, 58] and increasing data storage capacities

[59, 60]. **Part I** of this thesis examines the spatial multi-mode aspects of quantum optics, for the generation of spatial entanglement and applications to quantum imaging.

Whilst quantum optics has progressed, parallel accomplishments have been demonstrated in atom optics. Atom optics concerns with examining the state of the atomic system, via resonant and non-resonant atom-light interaction processes. Often, the optical state of the light field is not considered, whereby the optical field primarily serves as a means to manipulate the properties of the atomic system. Traditionally, atom optics experiments used thermal atomic sources, with many successful experiments for applications in atomic clocks [61], atomic magnetometry [62, 63, 64, 65] and atomic interferometry [66]. The discovery of laser cooling and trapping techniques then led to the production of cold, trapped atoms [67, 68, 69, 70, 71, 72, 73, 74, 75, 76, 77, 78, 79, 80, 81]. Cold, trapped atoms have been used in gradiometry [82], atomic clocks [83, 84, 85], magnetometry [86], atomic interferometry [87, 88, 89] and as a non-linear medium for the generation of squeezed light [90, 91]. The development of evaporative cooling subsequently led to the production of Bose-Einstein condensates (BECs) [92, 93]. This was a highly significant achievement as the production of a BEC was a demonstration of macroscopic quantum coherence. BECs were out-coupled to produce atom lasers with properties very similar to that of optical lasers [94, 95, 96, 97]. In terms of Fermionic atoms, the production of a degenerate Fermi gas [98] and Cooper pairing [99] have also been demonstrated. This has led to important studies of BEC-BCS (Bardeen-Cooper-Schrieffer) crossovers, which will aid in understanding the physics of high temperature superconductivity [100, 101, 102]. More recently, proposals for creating analogues of gravitational effects in BECs [103, 104] have also been considered.

The next generation of experiments attempted to combine the ideas and successes of both quantum and atom optics to yield quantum-atom optics [105]. In quantum-atom optics, the properties of both atomic and light fields are considered. From a fundamental perspective, it is interesting to explore quantum field effects via atom-light quantum interactions and examine exotic forms of entanglement such as inter-species entanglement between light and atoms [106, 107, 108, 109]. Also, the combination of squeezed light with atoms can lead to the generation of squeezed and entangled atoms lasers [110]. Such proposals are highly interesting as macroscopic entanglement between atomic ensembles with well defined modes can be produced. From an application perspective, the sensitivity of precision measurements could be enhanced. This could lead to more sensitive magnetometers [111, 112, 113, 114] and more precise atomic clocks [115, 116, 117]. An understanding of atom-light interaction will pave the way towards the development of a quantum network for quantum information exchange between quantum computing nodes [118]. A quantum network will consist of quantum memories and quantum computers linked via quantum channels. Such quantum networks could be tomorrow's "quantum world-wide web". Quantum information transfer can be performed effectively using photons since photons travel at the speed of light and do not interact much with its environment. Atoms, however, can be cooled and trapped. Therefore, one could envisage using atoms as a quantum memory for photons, the information carrier. **Part II** of this thesis examines this subject matter.

An overview of the author's view on the amalgamation of quantum and atom optics is shown in Fig. 1.1.

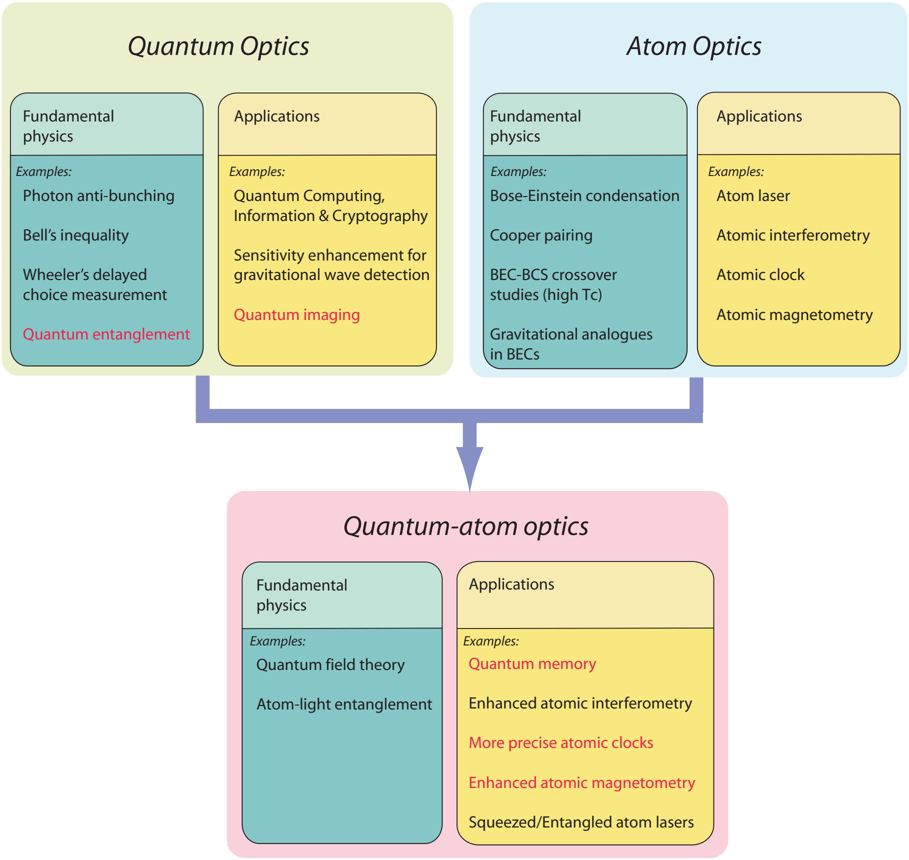

Figure 1.1: A flowchart summarising some of the fundamental physics and practical applications arising from the fields of quantum and atom optics. The combination of both quantum and atom optics yields new physics with the possibility of more practical applications. The text highlighted in red indicates the field of research that the author was involved in, that is described in this thesis.

1.2 Part I: Multi-mode quantum imaging

Early experiments on continuous-variable quantum optics focussed on the generation of non-classical states of light in the quadrature basis [17, 119, 120, 121, 122, 123]. Following successful experiments, manifestations of the light quadratures in terms of the polarisation Stokes variables were explored [124, 125, 91, 126]. The basis change was interesting as polarisation variables couple directly to the spin variables of atomic systems [127, 128]. Experiments demonstrating the interaction of polarisation states of light with the atomic spin states were shown [129, 130, 131, 132, 133, 134, 135, 136, 107, 137]. The spatial basis of light was also being concurrently explored. For example, in the review paper by Kolobov [56] which studied extensively the quantum aspects of imaging [138, 139, 140, 141, 142, 58, 143] and the properties of spatial multi-mode squeezed light. Spatial squeezed and entangled light have applications in sub-shot noise microscopy [57], quantum holographic teleportation [144], ghost imaging [145, 146] and the generation of entangled images [53, 55, 54, 147]. Recent experiments by Langford *et al.* [148] demonstrated the entanglement of spatially encoded quantum states, offering the prospect of quantum information processing in the spatial basis.

We are motivated by the prospect of producing continuous-variable quantum entanglement in the position and momentum variables, as envisaged by Einstein, Podolsky and Rosen [10]. In order to examine this idea, we first had to define beam position and momentum, together with discovering the corresponding optimal detection schemes. During this process, we discovered that split detectors were non-optimal for the detection of optical beam position and momentum [149]. We therefore proposed an optimal detection scheme for beam position and momentum, based on homodyne detection with specially-tailored local oscillator beams (see **Chapter 3**). Based on these discoveries, we were able to generate position-momentum entanglement for continuous-wave optical beams [52] (see **Chapter 4**). Thereafter, the possibility of expressing beam position, momentum and orbital angular momentum in one common basis was examined. The relevant modes responsible for beam position, momentum and orbital angular momentum were discovered to span the Poincaré sphere [150]. Consequently, spatial entanglement between these modes was proposed as well as the relevant detection schemes (see **Chapter 4**).

Spanning the spatial basis for light states has several applications such as in optical tweezers [151, 152, 153, 154], beam positioning measurement [155, 156], tilt locking [157] and optical data storage [59, 60, 158]. Using the techniques of spatial and phase encoding, we proposed a scheme [59] for increasing the capacities of optical data storage disks using interferometric techniques. Our scheme utilises two classes of phase coding - the *longitudinal* and *spatial transverse* phases of an optical beam and are described in detail in **Chapter 5**.

1.3 Part II: Light-atom ensemble interactions

Our primary motivation is to study the interaction between light states and atomic coherences, at the quantum level. We utilise systems consisting of optical beams and atomic ensembles as opposed to single atom (or ion) systems (e.g. cavity quantum electrodynamics systems, that have strong fields interacting with single atoms [159, 160]). Ensemble systems yield information on mean and variance values, whereas single particle systems yield information on a single quantum trajectory. The advantage of an ensemble system is measurement speed, whereby statistical information is obtained within a single measurement. However, in single particle systems, multiple measurements are required in order to procure the statistics corresponding to many identical single particle systems. The disadvantage of ensemble systems over single particle systems is the loss of individual trajectory information. We therefore have to decide which measurement path to take and due to the history of our group (i.e. in continuous-variable quantum optics), we decided to work with ensemble systems.

We first approach this study by exploring the non-linearity of atomic systems. We developed an understanding of the non-linear interaction between light and atoms and its effect on the noise properties of light propagated through atoms, in the context of optical squeezing generation using atoms. Thereafter we studied the possibility of information mapping between light and atoms, both in terms of mean and noise variances. Such a study has practical applications, in particular for the development of a quantum memory [118, 161] (i.e. a memory device which stores quantum information from an optical field) and for enhancing precision measurements (e.g. magnetometry and atomic clocks). We approached the quantum memory problem by studying the electromagnetically induced transparency (EIT) [162] effect which has been used for light slowing [163] and storage [164]. To study the enhancement of precision measurements, quantum non-demolition (QND) measurements of the spin state of atomic ensembles, via the Faraday interaction with the polarisation state of an optical field, is examined.

Early experiments on the generation of squeezed light were performed in atomic systems, by Slusher *et al.* [165, 166]. Other groups [167, 168, 169] have also explored squeezing via atomic systems, but these experiments did not yield squeezing comparable to those of current-day optical parametric oscillation/amplification (OPO/A) systems, since the experiments tended to be technically challenging and parameter spaces were large. Today, the most reliable and widely used method for squeezed light generation is that due to OPO/A [170, 171, 172, 173, 120, 121, 174, 25, 175, 8, 176]. Squeezing via cold atoms in a cavity [90, 91] have been relatively successful but more recent experiments by Ries *et al.* [177] and McCormick *et al.* [178] demonstrated that squeezing could be generated in atomic vapour cells, relatively easily. The experiment of Ries *et al.* [177] was based on the polarisation self-rotation effect whilst the experiment of McCormick *et al.* [178] was based on a four-wave mixing process. Their experimental setups were scalable and offered promise for large squeezing. We are therefore interested in studying the Kerr non-linearity in atomic systems, manifested in the polarisation self-rotation effect [179, 180]. We study the quantum properties of polarisation self-rotation both theoretically and experimentally [181], the details of which are discussed in **Chapter 7**.

The EIT effect is created by the interaction of probe and pump fields, in a 3-level atomic system [162]. A narrow transparency window is created for the probe beam which, in the absence of the pump, would be fully absorbed. Corresponding to the sharp transmission window is a steep dispersion which allows for the reduction in the group velocity of the probe field [163]. A theoretical proposal by Fleischhauer and Lukin [161] showed that by dynamic control of the pump field, the transparency window and group velocity of the probe field can be altered. Turning off the pump field allows the state of the probe field to be transferred to the atomic coherences of the EIT medium. Experimental demonstration of light storage has been performed, for classical signals [164]. There has been much interest in extending the dynamic-EIT scheme to storing quantum information. We approach this problem by studying the quantum state preservation of the probe field after propagation through an EIT medium [182, 183]. Our theoretical and experimental works are discussed in detail in **Chapter 8**.

Improvements in the sensitivity of precision measurements is an important and interesting subject of research. The ‘second’ is defined by a number of oscillations of the radiation corresponding to the transition between the two ground state hyperfine levels of Cesium-133 [83, 84, 85]. Atomic clocks are constructed based on this frequency standard, by locking a microwave oscillator to the Cesium-133 ground state hyperfine transitions [83, 84, 85]. In atomic magnetometry [62, 63, 64, 65], the Larmor precession signals induced in the presence of a magnetic field is measured, since the frequency of the Larmor precession signal is a function of the magnetic field strength. The ultimate sensitivity of these measurements is restricted by the quantum noise limit of the atoms (i.e. the atomic variance as a function of atom number), commonly termed the *atomic projection-noise limit* [184]. The projection noise limit has been observed in atomic clocks [185], atomic magnetometers [112] and atomic spectroscopy [186]. Therefore, there have been proposals to enhance the measurement of the Cs clock transition pseudo-spin [115, 116, 117] and perform sub-shot noise atomic magnetometry [111, 112, 113, 114]. In such applications, squeezing of the collective atomic spin state is required. We are motivated by such goals and discuss our work in this area in **Chapters 9** and **10**.

1.4 List of publications

The majority of the work reported in this thesis have been published in peer-reviewed journals and in conference proceedings, listed below:

Journal articles

1. M. T. L. Hsu, G. Hétet, O. Glöckl, J. J. Longdell, B. C. Buchler, H.-A. Bachor, and P. K. Lam, *Quantum study of information delay via electromagnetically induced transparency*, Physical Review Letters **97**, 183601 (2006).

2. G. Hétet, A. Peng, M. T. Johnsson, M. T. L. Hsu, O. Glöckl, H.-A. Bachor, P. K. Lam and J. J. Hope, *Erratum : Squeezing and entanglement delay using slow light*, Physical Review A **74**, 059902 (2006).

3. M. T. L. Hsu, V. Delaubert, W. P. Bowen, C. Fabre, H.-A. Bachor and P. K. Lam, *A quantum study of multi-bit phase coding for optical storage*, IEEE Journal of Quantum Electronics **10**, 1001 (2006).

4. H.-A. Bachor, V. Delaubert, C. C. Harb, M. T. L. Hsu, P. K. Lam, C. Fabre, and N. Treps, *Spatial quantum effects with continuous-wave laser beams*, Journal of Modern Optics **53**, 597 (2006).

5. M. T. L. Hsu, G. Hétet, A. Peng, C. C. Harb, H.-A. Bachor, M. T. Johnsson, J. J. Hope, P. K. Lam, A. Dantan, J. Cviklinski, A. Bramati and M. Pinard, *Effect of atomic noise on optical squeezing via polarization self-rotation in a thermal vapor cell*, Physical Review A **73**, 023806 (2006).

6. M. T. L. Hsu, W. P. Bowen, N. Treps and P. K. Lam, *Continuous-variable spatial entanglement for bright optical beams*, Physical Review A **72**, 013802 (2005).

7. M. T. L. Hsu, V. Delaubert, P. K. Lam and W. P. Bowen, *Optimal optical measurement of small displacements*, Journal of Optics B: Quantum and Semiclassical Optics **6**, 495 (2004).

8. N. Treps, N. Grosse, W. P. Bowen, M. T. L. Hsu, A. Maître, C. Fabre, H.-A. Bachor and P. K. Lam, *Nano-displacement measurements using spatially multi-mode squeezed light*, Journal of Optics B: Quantum and Semiclassical Optics **6**, S664-S674 (2004).

Conference proceedings

1. G. Hétet, M. T. L. Hsu, O. Glöckl, B. C. Buchler, J. J. Longdell, A. Peng, M. T. Johnsson, J. J. Hope, H.-A. Bachor and P. K. Lam, *Slowing and storing quantum information with EIT*, Proceedings of the 8th International Conference on Quantum Communication, Measurement and Computing, 497-500 (2007).

2. V. Delaubert, M. T. L. Hsu, W. P. Bowen, H.-A. Bachor and P. K. Lam, *TEM_{10} homodyne as an optical small displacement measurement scheme*, 16th Australian Institute of Physics Congress Proceedings, 76 (2005).

3. W. P. Bowen, M. T. L. Hsu, T. Symul, A. M. Lance, B. C. Buchler, R. S. Schnabel, N. Treps, H.-A. Bachor, T. C. Ralph and P. K. Lam, *Photon Number Diagram for Characterizing Continuous Variable Entanglement*, Proceedings of the XVI International Conference on Laser Spectroscopy, 315-323 (2003).

Part I

Quantum multi-mode optical imaging

Chapter 2

Quantum optics theory

Experience without theory is blind, but theory
without experience is mere intellectual play.

- Immanuel Kant

2.1 Formalism

In this chapter, we introduce the basic mathematical formalism used widely in continuous-variable quantum optics. We discuss the differences between single-mode and multi-mode quantum optics. Our formalism covers the multi-modal transverse description of optical fields in detail, as this formalism forms the 'cornerstone' of much work in the proceeding chapters.

2.1.1 Maxwell's equations

In 1865, James Clerk Maxwell wrote down the four important equations which describe the electomagnetic fields completely [187]. The equations laid the foundation for all of electrical and electronics engineering and have been a very powerful tool in understanding electromagnetic phenomena. Maxwell's equations are given by

$$\begin{aligned}
\nabla \times \boldsymbol{E}(\boldsymbol{r},t) &= -\frac{\partial \boldsymbol{B}(\boldsymbol{r},t)}{\partial t} \\
\nabla \times \boldsymbol{B}(\boldsymbol{r},t) &= \epsilon_0\mu_0\frac{\partial \boldsymbol{E}(\boldsymbol{r},t)}{\partial t} + \mu_0\boldsymbol{J}(\boldsymbol{r},t) \\
\epsilon_0\nabla \cdot \boldsymbol{E}(\boldsymbol{r},t) &= \rho \\
\nabla \cdot \boldsymbol{B}(\boldsymbol{r},t) &= 0 \qquad (2.1)
\end{aligned}$$

where $\boldsymbol{E}(\boldsymbol{r},t)$ and $\boldsymbol{B}(\boldsymbol{r},t)$ are the electric field vectors, respectively. ϵ_0 and μ_0 are the respective free-space permittivity and permeability constants; the electric charge density is given by ρ and the current density is given by $\boldsymbol{J}(\boldsymbol{r},t)$.

2.1.2 Quantisation of the electric field

The equations that Maxwell wrote down were however only sufficient to describe the classical mean field properties of electromagnetic fields. In order to describe phenomena such as the blackbody radiation using Plank's law, and the noise fluctuations of electromagnetic fields, Maxwell's classical equations had to be extended to fully describe the quantum mechanical properties of electromagnetic fields [188]. The fundamental particles of the electromagnetic field are photons. In quantisation, the field vectors $\boldsymbol{E}(\boldsymbol{r},t)$ and $\boldsymbol{B}(\boldsymbol{r},t)$ had to be defined as operators. In this section we describe briefly how the quantisation of electromagnetic fields is achieved, which is the basis for all the work of this thesis.

We quantise the fields by re-expressing Maxwell's equations in terms of scalar and vector potentials, ϕ and $\boldsymbol{A}(\boldsymbol{r},t)$.

$$\boldsymbol{E}(\boldsymbol{r},t) = -(\nabla\phi)(\boldsymbol{r},t) - \frac{\partial \boldsymbol{A}(\boldsymbol{r},t)}{\partial t} \tag{2.2}$$

By choosing the Coulomb gauge where the vector potential is $\nabla \cdot \boldsymbol{A} = 0$, the vector potential satisfies the expression given by

$$-\nabla^2 \boldsymbol{A}(\boldsymbol{r},t) + \frac{1}{c^2}\frac{\partial^2 \boldsymbol{A}(\boldsymbol{r},t)}{\partial t^2} = 0 \tag{2.3}$$

We now consider an infinite region of space for the propagation of the electromagnetic field. The solution to the equation above is the sum of all the wave-vector $\boldsymbol{k}$, given by[1]

$$\boldsymbol{A}(\boldsymbol{r},t) = \sum_k \left(\boldsymbol{A}_{\boldsymbol{k}}(t)\exp(-i\omega_{\boldsymbol{k}}t + i\boldsymbol{k}\cdot\boldsymbol{r}) + \boldsymbol{A}^*_{\boldsymbol{k}}(t)\exp(i\omega_{\boldsymbol{k}}t - i\boldsymbol{k}\cdot\boldsymbol{r})\right) \tag{2.4}$$

In order to quantise the electromagnetic field, one has to consider a quantum mechanical harmonic oscillator. Every mode $\boldsymbol{k}$ of the electromagnetic field is associated with a quantum mechanical harmonic oscillator. We now quantise the vector potentials by making the following substitutions [188]

$$\boldsymbol{A}_{\boldsymbol{k}}(t) \rightarrow \sqrt{\frac{\hbar}{2\epsilon_0 V\omega_{\boldsymbol{k}}}}\hat{a}_{\boldsymbol{k}}(t) \qquad \boldsymbol{A}^*_{\boldsymbol{k}}(t) \rightarrow \sqrt{\frac{\hbar}{2\epsilon_0 V\omega_{\boldsymbol{k}}}}\hat{a}^\dagger_{\boldsymbol{k}}(t) \tag{2.5}$$

where we have introduced the dimensionless photon annihilation and creation operators, for the quantum mechanical harmonic oscillator, denoted by $\hat{a}_{\boldsymbol{k}}(t)$ and $\hat{a}^\dagger_{\boldsymbol{k}}(t)$, respectively. The commutation relations for these operators are given by

$$[\hat{a}_{\boldsymbol{k}}(t), \hat{a}^\dagger_{\boldsymbol{k'}}(t)] = \delta_{kk'} \tag{2.6}$$

Note that these operators are not observables[2]. However by acting $\hat{a}^\dagger_{\boldsymbol{k}}(t)$ with $\hat{a}_{\boldsymbol{k}}(t)$, the observable photon number operator is obtained

$$\hat{n}_{\boldsymbol{k}}(t) = \hat{a}^\dagger_{\boldsymbol{k}}(t)\hat{a}_{\boldsymbol{k}}(t) \tag{2.7}$$

where the mean amplitude of this quantity gives the mean number of photons in the mode k, within the quantisation volume V.

We can now write the electric field operator in terms of its positive and negative frequency field components, given by

$$\hat{\boldsymbol{E}}_{\boldsymbol{k}}(\boldsymbol{r},t) = i\sqrt{\frac{\hbar\omega_{\boldsymbol{k}}}{2\epsilon_0 V}}\left(\hat{a}_{\boldsymbol{k}}(t)\exp(-i\omega_{\boldsymbol{k}}t + i\boldsymbol{k}\cdot\boldsymbol{r}) - \hat{a}^\dagger_{\boldsymbol{k}}(t)\exp(i\omega_{\boldsymbol{k}}t - i\boldsymbol{k}\cdot\boldsymbol{r})\right) \tag{2.8}$$

---

[1] We take the infinite sum over $\boldsymbol{k}$ to maintain simplicity in our equations. In actuality, the integral over all modes $\boldsymbol{k}$ should be considered for the free-space electromagnetic field.

[2] An observable has real eigenvalues and is a Hermitian operator.

2.1.3 Amplitude and phase quadratures

We now introduce more convenient observable operators, which are readily measurable in the laboratory. For continuous-variable systems, we are interested in the quadrature operator, given by

$$\hat{X}_k^{\theta}(t) = e^{-i\theta}\hat{a}_{\boldsymbol{k}}(t) + e^{i\theta}\hat{a}_{\boldsymbol{k}}^{\dagger}(t) \tag{2.9}$$

where θ is the quadrature angle. For angles of 0 and $\pi/2$, the amplitude and phase quadratures are obtained, respectively. The amplitude and phase quadratures, written explicitly, are respectively given by

$$\begin{aligned} \hat{X}_k^{+}(t) &= \hat{a}_{\boldsymbol{k}}(t) + \hat{a}_{\boldsymbol{k}}^{\dagger}(t) & (2.10) \\ \hat{X}_k^{-}(t) &= i(\hat{a}_{\boldsymbol{k}}^{\dagger}(t) - \hat{a}_{\boldsymbol{k}}(t)) & (2.11) \end{aligned}$$

Commutation relation

> *One who knows does not speak; one who speaks does not know.*
>
> **- Lao Tzu**

Using the commutation relation of Eq. (2.6), the commutation relation for $\hat{X}_k^{+}(t)$ and $\hat{X}_k^{-}(t)$ is given by

$$[\hat{X}_k^{+}(t), \hat{X}_{k'}^{-}(t)] = 2i\delta_{kk'} \tag{2.12}$$

where the quadrature variances (i.e. $\Delta^2\hat{X}_k^{\theta}(t) = \langle(\hat{X}_k^{\theta}(t) - \langle\hat{X}_k^{\theta}(t)\rangle)^2\rangle$) are related by the Heisenberg uncertainty relation

$$\Delta^2\hat{X}_k^{+}(t)\Delta^2\hat{X}_k^{-}(t) \geq 1 \tag{2.13}$$

This is a very important equation with deep physical insight. It describes the relation between the variances of the amplitude and phase quadratures, within the condition of the Heisenberg uncertainty relation. One could reduce the fluctuations of the amplitude at the expense of having greater fluctuations in the phase and vice versa. For a coherent state light source, $\Delta^2\hat{X}_k^{+}(t) = \Delta^2\hat{X}_k^{-}(t) = 1$, and this defines the *shot noise limit* or *quantum noise limit* (QNL).

2.1.4 Multi-mode and single-mode analyses

Multi-mode analysis

For an electric field operator which takes into account multi-modal behaviour, a sum over all the possible longitudinal and spatial modes have to be considered, given by

$$\hat{\boldsymbol{E}}(\boldsymbol{r},t) = \sum_{k=0}^{\infty} i\sqrt{\frac{\hbar\omega_{\boldsymbol{k}}}{2\epsilon_0 V}}\left(\hat{a}_{\boldsymbol{k}}(t)e^{-i(\omega_{\boldsymbol{k}}t-\boldsymbol{k}\cdot\boldsymbol{r})} - \hat{a}_{\boldsymbol{k}}^{\dagger}(t)e^{i(\omega_{\boldsymbol{k}}t-\boldsymbol{k}\cdot\boldsymbol{r})}\right) \tag{2.14}$$

For the purpose of this thesis, we will only consider the situation where the electromagnetic field consists of a single frequency, or a single longitudinal mode component, ω_0. We are however interested in the spatial multi-mode behaviour of the electromagnetic field. Therefore the electric field operator is written as the sum over an infinite number of modes $u_n(\boldsymbol{r})$, given by

$$\hat{\boldsymbol{E}}(\boldsymbol{r},t) = \sum_{n=0}^{\infty} i\sqrt{\frac{\hbar\omega_0}{2\epsilon_0 V}} \left(\hat{a}_n(t)e^{-i\omega_0 t}u_n(\boldsymbol{r}) - \hat{a}_n^\dagger(t)e^{i\omega_0 t}u_n^*(\boldsymbol{r})\right) \tag{2.15}$$

For brevity we only take the positive frequency part of the electric field operator, given by

$$\hat{\boldsymbol{E}}^+(\boldsymbol{r},t) = \sum_{n=0}^{\infty} i\sqrt{\frac{\hbar\omega_0}{2\epsilon_0 V}}\hat{a}_n(t)e^{-i\omega_0 t}u_n(\boldsymbol{r}) \tag{2.16}$$

where ω_0 is the carrier frequency of the field and $u_n(\boldsymbol{r})$ are the spatial mode functions, which form an orthonormal basis given by

$$\int u_n(\boldsymbol{r})u_{n'}^*(\boldsymbol{r})d^3\boldsymbol{r} = \delta_{nn'} \tag{2.17}$$

We can further simplify our representation of the electric field operator by only considering the slowly varying field envelope operator given by

$$\hat{\mathcal{E}}^+(\boldsymbol{r},\boldsymbol{t}) = \sum_{n=0}^{\infty} i\sqrt{\frac{\hbar\omega_0}{2\epsilon_0 V}}\hat{a}_n(t)u_n(\boldsymbol{r}) \tag{2.18}$$

Single-mode analysis

For most quantum information experiments, a single spatial and longitudinal mode analysis of the electromagnetic field is sufficient to describe the physics. The spatial mode function is simply expressed using plane waves, where $u_k(\boldsymbol{r}) = e^{ik_0 z}$. The slowly varying positive frequency part of the electric field operator is then given by

$$\hat{\mathcal{E}}^+(z,t) = i\sqrt{\frac{\hbar\omega_0}{2\epsilon_0 V}}\hat{a}(t)e^{ik_0 z} \tag{2.19}$$

where ω_0 is the carrier frequency of the single-mode field.

2.2 States of light

2.2.1 Fock state

One of the most natural states to arise from the quantisation of the electromagnetic field is the photon number or Fock state. The Fock state is the eigenstate of the quantum harmonic oscillator for the electromagnetic field. By acting the photon annihilation and creation operators on the photon state $|n\rangle$, a state with an additional or one less photon can be obtained, respectively, given by

$$\hat{a}(t)|n\rangle = \sqrt{n}|n-1\rangle \qquad \hat{a}^\dagger(t)|n\rangle = \sqrt{n+1}|n+1\rangle \tag{2.20}$$

where the ground state of the system is defined by

$$\hat{a}(t)|0\rangle = |0\rangle \tag{2.21}$$

and this is termed the *vacuum state*. Any arbitrary photon state $|n\rangle$ (containing n number of photons) can be obtained from the vacuum state by successive applications of the creation operator, given by

$$|n\rangle = \frac{(\hat{a}^\dagger(t))^n}{\sqrt{n!}}|0\rangle \tag{2.22}$$

The Fock state basis has the completeness relation given by

$$\sum_{n=0}^{\infty} |n\rangle\langle n| = 1 \tag{2.23}$$

The Fock state basis is a convenient basis to work with, for experiments where the photon number is small. This is termed the *discrete-variable* (DV) regime where photon counts detected via avalanche photo-detectors is the main detection technique. The other regime to work in is the regime where the number of photons is large, the *continuous-variable* (CV) regime. In this a regime, an amplified photo-detector is the main means of detection. We are interested in the CV regime and we now adopt the coherent state basis.

2.2.2 Coherent state

The coherent state was first introduced by Glauber. A field in the coherent state has equal fluctuations in both amplitude and phase quadratures; and is in the minimal uncertainty state. In the photon number states basis, the coherent state is given by

$$|\alpha\rangle = e^{-\frac{|\alpha|^2}{2}} \sum_{n=0}^{\infty} \frac{\alpha^n}{\sqrt{n!}}|n\rangle \tag{2.24}$$

where $|n\rangle$ is the state containing exactly n photons, but have undefined phase. In the Schrödinger picture the coherent states can be written as the eigenstates of the photon annihilation operator, given by

$$\hat{a}(t)|\alpha\rangle = \alpha|\alpha\rangle \tag{2.25}$$

where α is the eigenvalue of the coherent state. The coherent state can also be obtained by acting a displacement operator on the vacuum state, given by

$$\begin{aligned} \hat{D}[\alpha]|0\rangle &= e^{\frac{-|\alpha|^2}{2}} e^{\alpha\hat{a}^\dagger - \alpha^*\hat{a}}|0\rangle \\ &= |\alpha\rangle \end{aligned} \tag{2.26}$$

Using these equations, a few quantities of the coherent state can be obtained, given by

$$P(n) = \frac{|\alpha|^{2n} e^{-|\alpha|^2}}{n!} \tag{2.27}$$

$$\langle\hat{n}\rangle = |\alpha|^2 \tag{2.28}$$

$$\Delta\hat{n} = |\alpha| \tag{2.29}$$

where $P(n)$ is the probability to obtain n photons, $\langle\hat{n}\rangle$ is the mean number of photons and $\Delta\hat{n}$ is the standard deviation of the photon number for the coherent state. Based on these, we can write the annihilation operator as

$$\hat{a} = \langle\hat{a}(t)\rangle + \delta\hat{a}(t) \tag{2.30}$$

$$= \alpha(t) + \delta\hat{a}(t) \tag{2.31}$$

where $\langle\hat{a}(t)\rangle$ is a c-number and $\delta\hat{a}(t)$ is the fluctuation part with zero expectation value. Coherent states are readily generated in the laboratory. A laser beam without any classical noise is inherently in a coherent state [189].

2.2.3 Squeezed state

From the uncertainty relation of Eq. (2.13), it is possible to reduce the variance in one quadrature at the expense of increased variance in the orthogonal quadrature. This process is called squeezing. The squeeze operator is given by

$$\hat{S}[r,\theta,t] = \exp\left(\frac{r(e^{-2i\theta}\hat{a}(t)^2 - e^{2i\theta}(\hat{a}^\dagger(t))^2)}{2}\right) \tag{2.32}$$

where r is the squeezing parameter and θ is the squeezing quadrature angle. The squeezing operation is performed by acting the squeeze operator on a vacuum state. The squeezed vacuum and displaced squeezed states are given respectively by

$$|0,r,\theta\rangle = \hat{S}[r,\theta,t]|0\rangle \tag{2.33}$$

$$|\alpha,r,\theta\rangle = \hat{D}[\alpha]\hat{S}[r,\theta,t]|0\rangle \tag{2.34}$$

Squeezed states can be generated via a variety of non-linear processes. Amongst the most popular and reliable sources of squeezed light generation is via the optical parametric oscillation (OPO) process through the $\chi^{(2)}$ non-linearity. The $\chi^{(3)}$ Kerr squeezing process is also used extensively and will be described in Chapter 7.

The OPO process involves the parametric down-conversion of photons. A photon of frequency $2\omega_0$ is down-converted into two photons, one at frequency $\omega_0+\omega$ and the other at frequency $\omega_0-\omega$. In this pair-wise photon creation process, the total energy and momentum are conserved. Therefore, the paired photons are quantum correlated, which gives squeezed and entangled light.

The photon number distributions for the coherent and squeezed states are shown in Fig. 2.1. The coherent state has a Gaussian distribution[3] of photon numbers. The amplitude and phase squeezed states have different photon number distribution for the same squeezing parameter. The vacuum squeezed state only contains even number of photons, indicating pair-wise 'clumping' of photons, as described in the parametric down-conversion process.

2.2.4 Density matrix and Wigner function

Density matrix

The density matrix completely describes the states of a system. In order to calculate the probability, P_ψ, of being in a particular state $|\psi\rangle$, the average over an infinite number of ensembles has to be obtained. The average is given by [105]

$$\langle\hat{\mathcal{O}}\rangle = \sum_i P_{\psi_i}\langle\psi_i|\hat{\mathcal{O}}|\psi_i\rangle \tag{2.35}$$

---

[3] Strictly speaking, a coherent state has a Poissonian distribution of photon numbers. In the limit of large photon numbers, the photon distribution is Gaussian.

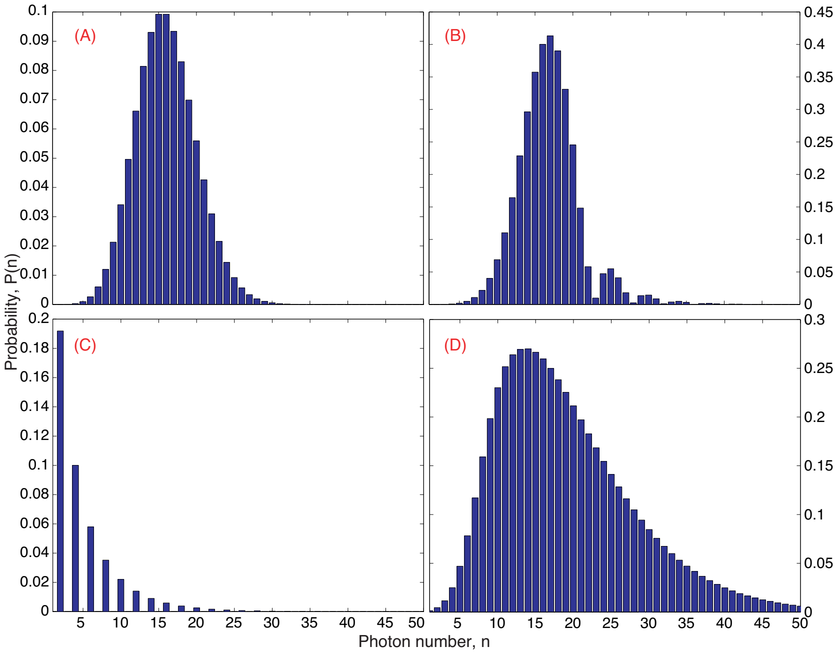

Figure 2.1: (A) Coherent state with $\alpha = 4$. (B) Amplitude squeezing with $r = 0.7$. (C) Vacuum squeezing with $r = 1.2$. (D) Phase squeezing with $r = 0.7$.

where P_{ψ_i} is the probability to be in state $|\psi_i\rangle$ and $\hat{\mathcal{O}}$ is the observable operator. The equation above can be rewritten using the completeness relation in the Fock basis, $\sum_n |n\rangle\langle n|$, giving

$$\begin{aligned}\langle\hat{\mathcal{O}}\rangle &= \sum_n \sum_{\psi_i} P_\psi \langle\psi_i|\hat{\mathcal{O}}|n\rangle\langle n|\psi_i\rangle \\ &= \sum_n \sum_{\psi_i} P_{\psi_i} \langle n|\psi_i\rangle\langle\psi_i|\hat{\mathcal{O}}|n\rangle \\ &= \sum_n \langle n|\hat{\rho}\hat{\mathcal{O}}|n\rangle \qquad (2.36)\end{aligned}$$

where the density operator is defined as

$$\hat{\rho} = \sum_{\psi_i} P_\psi |\psi_i\rangle\langle\psi_i| \qquad (2.37)$$

Since the density matrix is normally expressed in the Fock state basis, the density operator is thus given by[4]

$$\begin{aligned}\hat{\rho} &= \sum_n \sum_m |n\rangle\langle n|\hat{\rho}|m\rangle\langle m| \\ &= \sum_n \sum_m \rho_{nm}|n\rangle\langle m| \qquad (2.38)\end{aligned}$$

---

[4] The density matrix can also be expressed in other bases such as the coherent state basis $|\alpha\rangle$.

Wigner function

In general, it is not very convenient or trivial to characterise the density matrix of a system. Therefore, alternative representations corresponding directly to the density matrix have been invented. These different representations describe the probability distribution of the system. The P-representation introduced by Glauber and Sudarshan is one such representation. It is based on normal ordering of $\hat{a}$ and $\hat{a}^\dagger$ and thus only provides a classical probability distribution for the system[5].

Wigner introduced a quasi-probability function based on symmetric ordering. This function can take negative values and always exists. In the Schrödinger picture, the Wigner function is given by [190]

$$W(\langle\hat{X}^+(t)\rangle, \langle\hat{X}^-(t)\rangle) = \int_{-\infty}^{\infty} \frac{e^{ix\langle\hat{X}^-(t)\rangle}}{\pi} \left\langle \langle\hat{X}^+(t)\rangle - \frac{x}{4} \middle| \hat{\rho} \middle| \langle\hat{X}^+(t)\rangle + \frac{x}{4} \right\rangle dx \tag{2.39}$$

where $\langle\hat{X}^+(t)\rangle$ and $\langle\hat{X}^-(t)\rangle$ are the mean field components of the amplitude and phase quadratures, respectively. The Wigner function representation is useful in experiments since the only measurement required is that of the quadrature amplitudes[6].

The Wigner functions of a coherent state $|\alpha\rangle$, squeezed state $|0, r\rangle$ and number state $|n\rangle$ are given respectively by [192, 190, 193]

$$\begin{aligned}
W_{|\alpha\rangle}(\langle\hat{X}^+(t)\rangle, \langle\hat{X}^-(t)\rangle) &= \frac{2}{\pi}\exp\left(-\frac{(\langle\hat{X}^+(t)\rangle - \alpha^+(t))^2 + (\langle\hat{X}^-(t)\rangle - \alpha^-(t))^2}{2}\right) \\
W_{|0,r\rangle}(\langle\hat{X}^+(t)\rangle, \langle\hat{X}^-(t)\rangle) &= \frac{2}{\pi}\exp\left(-\frac{\langle\hat{X}^+(t)\rangle^2 e^{-2r} + \langle\hat{X}^-(t)\rangle^2 e^{2r}}{2}\right) \\
W_{|n\rangle}(\langle\hat{X}^+(t)\rangle, \langle\hat{X}^-(t)\rangle) &= \frac{2}{\pi}(-1)^n L_n\left(4(\langle\hat{X}^+(t)\rangle^2 + \langle\hat{X}^-(t)\rangle^2)\right) \\
&\quad \times \exp\left(-2(\langle\hat{X}^+(t)\rangle^2 + \langle\hat{X}^-(t)\rangle^2)\right)
\end{aligned} \tag{2.40}$$

where $\alpha^+(t)$ and $\alpha^-(t)$ are the real and imaginary parts of the mean field amplitude, r is the squeezing parameter and $L_n(x)$ is the Laguerre polynomial of order-n.

The Wigner functions of coherent, squeezed and one-photon Fock states are given in Fig. 2.2. The coherent state of Fig. 2.2 (1A) shows a positive Gaussian Wigner function with equal variances in all quadratures. The squeezed state of Fig. 2.2 (2A) shows a positive gaussian Wigner function with asymmetric variances in the amplitude and phase quadratures. In this instance, the phase quadrature is squeezed due to the reduced variance with respect to the variance of the coherent state. The amplitude quadrature is anti-squeezed with an increased variance. The one-photon Fock state of Fig. 2.2 (3A) shows a negative-valued non-Gaussian Wigner function.

Ball-on-stick picture

Typically for Gaussian states, we can represent the state by using the standard deviation contour. This shows the noise in the relevant quadrature, when plotted on an phasor

---

[5] The representation based on anti-normal ordering is the Q-distribution.

[6] To measure the Wigner function, quadrature amplitudes $\langle\hat{X}^\theta(t)\rangle$ are measured from $\theta \in [0, \pi)$. Then the inverse Radon transform is used to reconstruct the total Wigner function from its projected slices [191].

diagram, as shown in Fig. 2.2. For a coherent state with coherent amplitude α, the noise contour is displaced with respect to the origin, as in Fig. 2.2 (1B). The standard deviation of the noise circle is 1, for a coherent or vacuum state. The squeezed state has reduced variance in one quadrature relative to the vacuum state, as shown in Fig. 2.2 (2B). The one-photon Fock state has a standard deviation contour shown in Fig. 2.2 (3B).

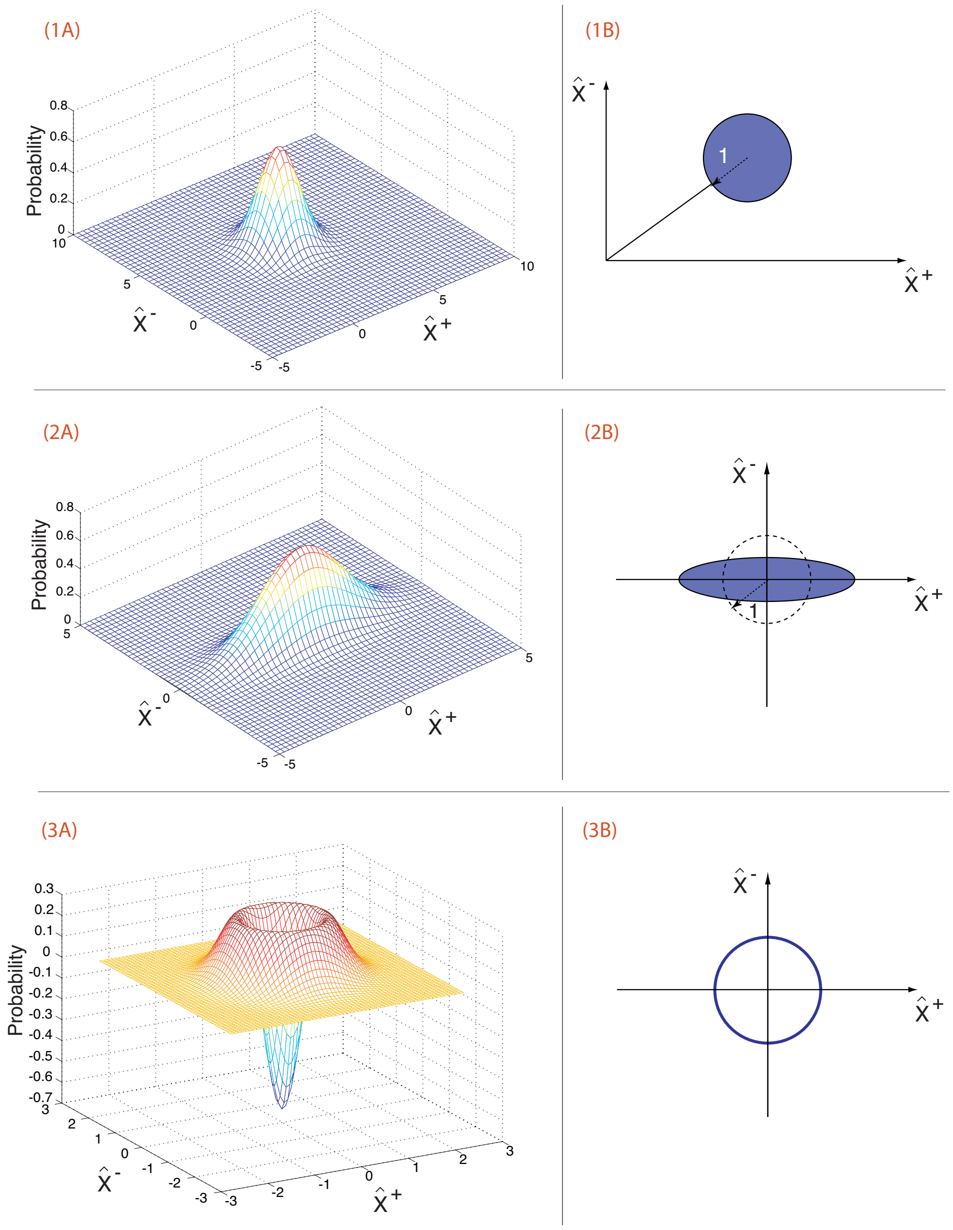

Figure 2.2: (1A) Coherent state with $\alpha^+ = 2$ and $\alpha^- = 3$. (2A) Amplitude squeezing with $r = 0.5$. (3A) Single photon Fock state.

2.2.5 Fourier domain and sideband frequency picture

Since all our measurements were performed at the sideband frequency domain, we now re-define all the relevant field operators in the Fourier domain. The Fourier transform of the time domain annihilation and creation operators are given by

$$\begin{aligned}\tilde{a}(\omega) &\equiv \frac{1}{\sqrt{2\pi}}\int_{-\infty}^{\infty}\hat{a}(t)e^{i\omega t}dt \qquad (2.41)\\ \tilde{a}^\dagger(w) &\equiv \frac{1}{\sqrt{2\pi}}\int_{-\infty}^{\infty}\hat{a}^\dagger(t)e^{i\omega t}dt\end{aligned}$$

where by definition $\hat{a}^\dagger(t) = [\hat{a}(t)]^\dagger$. Also,

$$\begin{aligned}[\tilde{a}(\omega)]^\dagger &= \left[\frac{1}{\sqrt{2\pi}}\int_{-\infty}^{\infty}\hat{a}(t)e^{i\omega t}dt\right]^\dagger \qquad (2.42)\\ &= \frac{1}{\sqrt{2\pi}}\int_{-\infty}^{\infty}\hat{a}^\dagger(t)e^{-i\omega t}dt \qquad (2.43)\\ \Rightarrow [\tilde{a}(-\omega)]^\dagger &= \frac{1}{\sqrt{2\pi}}\int_{-\infty}^{\infty}\hat{a}^\dagger(t)e^{i\omega t}dt \qquad (2.44)\\ &= \tilde{a}^\dagger(w) \qquad (2.45)\end{aligned}$$

Following this, the frequency domain quadrature operators can be defined by taking the Fourier transform of $\hat{X}^\theta(t)$, given by

$$\begin{aligned}\tilde{X}^\theta(\omega) &= \mathcal{F}\{e^{-i\theta}\hat{a}(t) + e^{i\theta}\hat{a}^\dagger(t)\} \qquad (2.46)\\ &= (\cos\theta - i\sin\theta)\tilde{a}(\omega) + (\cos\theta + i\sin\theta)[\tilde{a}(-\omega)]^\dagger \qquad (2.47)\\ &= \cos\theta\left(\tilde{a}(\omega) + [\tilde{a}(-\omega)]^\dagger\right) + i\sin\theta\left(-\tilde{a}(\omega) + [\tilde{a}(-\omega)]^\dagger\right) \qquad (2.48)\\ &= (\cos\theta)\tilde{X}^+(\omega) + (\sin\theta)\tilde{X}^-(\omega)) \qquad (2.49)\\ & \qquad (2.50)\end{aligned}$$

where the amplitude and phase quadratures in the sideband frequency picture are given respectively by

$$\tilde{X}^+(\omega) = \tilde{a}(\omega) + [\tilde{a}(-\omega)]^\dagger \qquad \tilde{X}^-(\omega) = -i\left(\tilde{a}(\omega) + [\tilde{a}(-\omega)]^\dagger\right) \qquad (2.51)$$

The expressions show that there are two frequency components - the positive and negative components. These can be interpreted as sidebands centred around a carrier frequency ω_0. The positive and negative sidebands are rotating at frequencies $\omega_0 + \omega$ and $\omega_0 - \omega$, respectively.

Fig. 2.3 shows models of the sideband picture for coherent and squeezed light. In Fig. 2.3 (A), the sidebands are rotating at frequencies $+\omega$ and $-\omega$ around the carrier frequency ω_0. In Fig. 2.3 (B), a sideband picture of a coherent state is shown, where there exists un-correlated sidebands at all frequencies. For squeezed light the sidebands are correlated across a band of frequencies, as shown in Fig. 2.3 (C).

The corresponding commutation relations in the frequency domain are given by

$$\begin{aligned}\left[\tilde{a}(\omega), \tilde{a}^\dagger(\omega)\right] &= 1 \qquad (2.52)\\ \left[\tilde{X}^+(\omega), \tilde{X}^-(\omega)\right] &= 2i \qquad (2.53)\end{aligned}$$

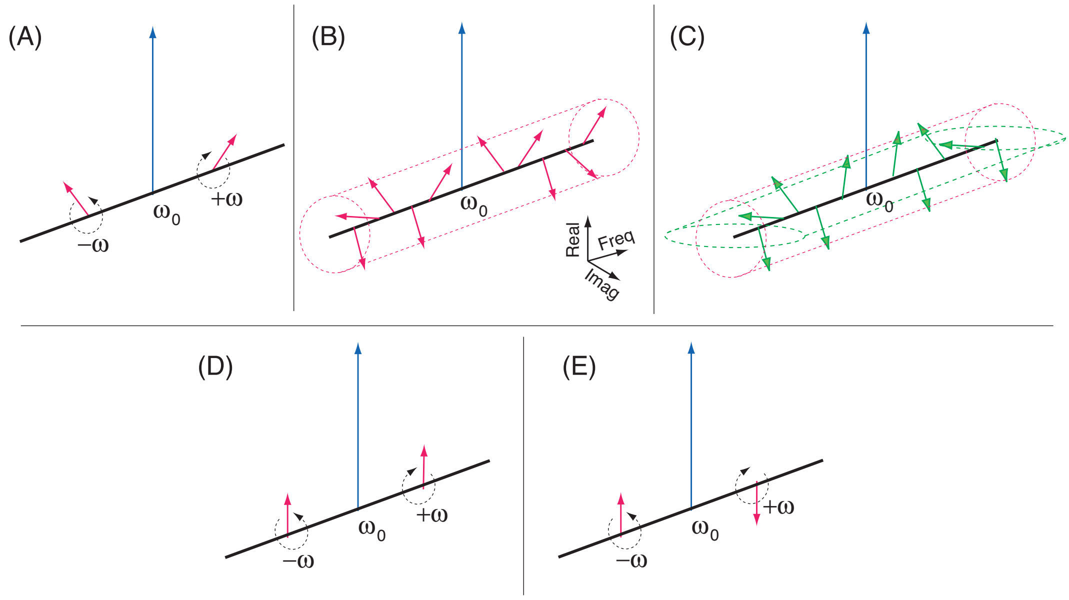

Figure 2.3: (A) Sideband frequency picture with sidebands rotating at frequencies $+\omega$ and $-\omega$ around the carrier frequency ω_0. Sideband picture of (B) quantum noise, (C) squeezing, (D) amplitude modulation and (E) phase modulation.

2.2.6 Phase and amplitude modulation

A signal can be applied at the sideband frequencies. When the sidebands give a non-zero component along the real axis, an amplitude modulation signal on the optical field is obtained. For sidebands which give a non-zero component along the imaginary axis, a phase modulation signal is generated.

We now model the application of a phase modulation onto a field by introducing the imaginary modulation term, given by

$$\begin{aligned}
\hat{a}_{\mathrm{PM}}(t) &= \hat{a}(t)e^{iA_{\mathrm{PM}}\cos(\omega_{\mathrm{PM}}t)} && (2.54)\\
&\simeq \hat{a}(t)\left(1 + iA_{\mathrm{PM}}\cos(\omega_{\mathrm{PM}}t)\right) && (2.55)\\
&= \hat{a}(t)\left(1 + \frac{iA_{\mathrm{PM}}}{2}(e^{i\omega_{\mathrm{PM}}t} + e^{-i\omega_{\mathrm{PM}}t})\right) && (2.56)\\
& && (2.57)
\end{aligned}$$

where A_{PM} is the amplitude of the phase modulation signal at frequency ω_{PM}. We have also assumed $A_{\mathrm{PM}} \ll 1$ to simplify the expressions. Taking the Fourier transform of the expression gives

$$\begin{aligned}
\tilde{a}_{\mathrm{PM}}(\omega) &= \tilde{a}(\omega) + \frac{iA_{\mathrm{PM}}}{2}\int_{-\infty}^{\infty}\left[\hat{a}(t)e^{i(\omega+\omega_{\mathrm{PM}})t} + \hat{a}(t)e^{i(\omega-\omega_{\mathrm{PM}})t}\right]dt && (2.58)\\
&= \tilde{a}(\omega) + \frac{iA_{\mathrm{PM}}}{2}\tilde{a}(\omega+\omega_{\mathrm{PM}}) + \frac{iA_{\mathrm{PM}}}{2}\tilde{a}(\omega-\omega_{\mathrm{PM}}) && (2.59)
\end{aligned}$$

where the phase modulation is composed of sidebands at $\omega + \omega_{\mathrm{PM}}$ and $\omega - \omega_{\mathrm{PM}}$, with imaginary amplitudes, as shown in Fig. 2.3 (E).

To generate amplitude modulation on the field, a real modulation term is introduced,

given by

$$\begin{aligned}\hat{a}_{\mathrm{AM}}(t) &= \hat{a}(t)(1+A_{\mathrm{AM}}\cos(\omega_{\mathrm{AM}}t)) &(2.60)\\ &= \hat{a}(t)\left(1+\frac{A_{\mathrm{AM}}}{2}(e^{i\omega_{\mathrm{AM}}t}+e^{-i\omega_{\mathrm{AM}}t})\right) &(2.61)\\ & &(2.62)\end{aligned}$$

where A_{AM} is the amplitude of the amplitude modulation signal at frequency ω_{AM}. Taking the Fourier transform gives

$$\begin{aligned}\tilde{a}_{\mathrm{AM}}(\omega) &= \tilde{a}(\omega)+\frac{A_{\mathrm{AM}}}{2}\int_{-\infty}^{\infty}\left[\hat{a}(t)e^{i(\omega+\omega_{\mathrm{AM}})t}+\hat{a}(t)e^{i(\omega-\omega_{\mathrm{AM}})t}\right]dt &(2.63)\\ &= \tilde{a}(\omega)+\frac{A_{\mathrm{AM}}}{2}\tilde{a}(\omega+\omega_{\mathrm{AM}})+\frac{A_{\mathrm{AM}}}{2}\tilde{a}(\omega-\omega_{\mathrm{AM}}) &(2.64)\end{aligned}$$

where the amplitude modulation is composed of sidebands at $\omega+\omega_{\mathrm{AM}}$ and $\omega-\omega_{\mathrm{AM}}$, with real amplitudes, as shown in Fig. 2.3 (D).

2.3 Spatial mode basis

The equations of (2.2), (2.3) and (2.8) can be simplified under the paraxial approximation to give the paraxial wave equation describing the mean electric field envelope, given by

$$\left(\frac{\partial^2}{\partial x^2}+\frac{\partial^2}{\partial y^2}-2ik\frac{\partial}{\partial z}\right)\langle\hat{\mathcal{E}}^{+}(\boldsymbol{r},t)\rangle=0 \tag{2.65}$$

Since the dependence on $\boldsymbol{r}$ is explicitly written in Eq. (2.18), and is only contained in the modal functions $u_n(\boldsymbol{r})$, the paraxial wave equation can be re-expressed as [194]

$$\left(\frac{\partial^2}{\partial x^2}+\frac{\partial^2}{\partial y^2}-2ik\frac{\partial}{\partial z}\right)u_n(\boldsymbol{r})=0 \tag{2.66}$$

A general solution of the equation above is the Hermite-Gauss modes. The normalised spatial mode function for the Hermite-Gauss basis is given by

$$\begin{aligned}\mathrm{TEM}_{mn}(x,y,z) &= \left(\frac{2}{\pi w(z)^2}\right)^{1/2}\frac{1}{\sqrt{m!n!2^{m+n}}}H_m\left(\frac{\sqrt{2}x}{w(z)}\right)H_n\left(\frac{\sqrt{2}y}{w(z)}\right)\exp\left[-\frac{x^2+y^2}{w(z)^2}\right]\\ &\quad\times\exp\left[-ik\frac{x^2+y^2}{2R(z)}\right]\exp\left(-i[n+m+1]\phi_G(z)\right)\exp(ikz) \qquad (2.67)\end{aligned}$$

where the transverse beam radius, the radius of curvature of the beam wave-front, the

Rayleigh range and the Gouy phase shift are given respectively by

$$w(z) = w_0\sqrt{1+\left(\frac{z}{z_R}\right)^2} \tag{2.68}$$

$$R(z) = z+\frac{z^2}{z_R} \tag{2.69}$$

$$z_R = \frac{\pi w_o^2}{\lambda} \tag{2.70}$$

$$\phi_G(z) = \arctan\left(\frac{z}{z_R}\right) \tag{2.71}$$

where w_0 is the waist of the beam and the Hermite polynomials are given by

$$H_n(x) = (-1)^n e^{x^2}\frac{d^n}{dx^n}e^{-x^2} \tag{2.72}$$

Other spatial mode bases also exist, such as the Laguerre-Gauss and Ince-Gauss. The solution for the paraxial wave equation in elliptical coordinates is given by the Ince-Gauss modes. The solution for the paraxial wave equation in the circular cylindrical coordinates is given by the Laguerre-Gauss modes.

The Laguerre-Gauss modes are given by

$$\begin{aligned}\mathrm{LG}_{n,l}(r,\phi,z) &= \sqrt{\frac{4n!}{(1+\frac{z^2}{z_R^2})\pi(n+l)!}}\frac{1}{w(z)}\exp(il\phi)\left(\frac{\sqrt{2}r}{w(z)}\right)^l L_n^l\left(\frac{2r^2}{w(z)^2}\right)\exp\left[-\frac{r^2}{w(z)^2}\right]\\ &\times\exp\left[-ik\frac{r^2}{2R(z)}\right]\exp\left(-i[2n+l+1]\phi_G(z)\right)\exp(ikz)\end{aligned} \tag{2.73}$$

where n is the radial number and l is the azimuthal number. The generalised Laguerre polynomials are given by

$$L_n^l(x) = \sum_{m=0}^{n}\binom{n+l}{n-l}\frac{(-x)^m}{m!} \tag{2.74}$$

Fig. 2.4 shows the (A) intensity and (B) amplitude of Hermite-Gauss and Laguerre-Gauss modes as a function of transverse directions x and y. The Hermite-Gauss intensity distribution are given by Fig. 2.4 (1A)-(3A), whilst the electric field amplitude distribution are given by Fig. 2.4 (1B)-(3B). The Laguerre-Gauss intensity distribution are given by Fig. 2.4 (4A)-(6A), whilst the electric field amplitude distribution are given by Fig. 2.4 (4B)-(6B).

2.3.1 Changing spatial mode basis

At times, it is convenient to work in a different basis. Let us consider a change of basis for the $u_n(\boldsymbol{r}) \to v_m(\boldsymbol{r})$ modes. The positive frequency part of the field envelope operator is then given by

$$\hat{\mathcal{E}}^+(\boldsymbol{r},t) = \sum_{n=0}^{\infty} i\sqrt{\frac{\hbar\omega_0}{2\epsilon_0 V}}\hat{a}_n(t)u_n(\boldsymbol{r}) \Rightarrow \sum_{m=0}^{\infty} i\sqrt{\frac{\hbar\omega_0}{2\epsilon_0 V}}\hat{b}_m(t)v_m(\boldsymbol{r}) \tag{2.75}$$

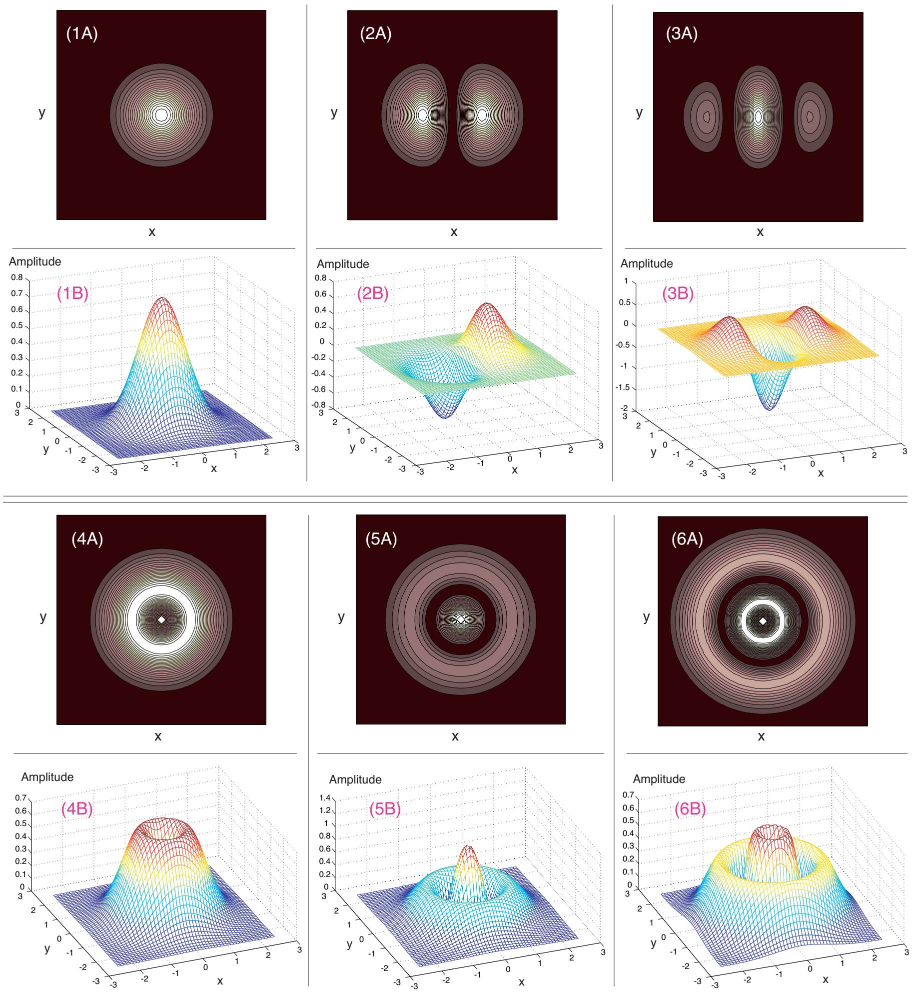

Figure 2.4: Intensity distribution for (1A) TEM$_{00}$, (2A) TEM$_{10}$, (3A) TEM$_{20}$, (4A) LG$^{e}_{10}$, (5A) LG$^{e}_{01}$ and (6A) LG$^{e}_{11}$. Electric field amplitude distribution for (1B) TEM$_{00}$, (2B) TEM$_{10}$, (3B) TEM$_{20}$, (4B) LG$_{01}$, (5B) LG$_{10}$ and (6B) LG$_{11}$. All three axes have arbitrary units.

where the photon annihilation operator for mode basis $u_n(\boldsymbol{r})$ and $v_n(\boldsymbol{r})$ are given by $\hat{a}_n(t)$ and $\hat{b}_n(t)$, respectively.

In order to perform the basis change, the mode-overlap integral is calculated, given by

$$\begin{aligned}
\sum_{n=0}^{\infty}\hat{a}_n(t)\int_{-\infty}^{\infty}u_n(\boldsymbol{r})u_k(\boldsymbol{r})d\boldsymbol{r} &= \sum_{m=0}^{\infty}\hat{b}_m(t)\int_{-\infty}^{\infty}v_m(\boldsymbol{r})u_k(\boldsymbol{r})d\boldsymbol{r} &\quad (2.76)\\
\hat{a}_n(t) &= \sum_{m=0}^{\infty}\hat{b}_m(t)\int_{-\infty}^{\infty}v_m(\boldsymbol{r})u_n(\boldsymbol{r})d\boldsymbol{r} &\quad (2.77)\\
&= \sum_{m=0}^{\infty}\hat{b}_m(t)C_{\mathrm{nm}}(\boldsymbol{r}) &\quad (2.78)
\end{aligned}$$

where $C_{\mathrm{nm}}(\boldsymbol{r})$ are the coefficients of the overlap integral between modes $u_n(\boldsymbol{r})$ and $v_m(\boldsymbol{r})$.

2.4 Detection

In continuous-variable quantum optics, many types of detection techniques are used. A selection of the most commonly used detection schemes are shown in Fig. 2.5. To measure an intensity or amplitude signal, a single direct detector as in Fig. 2.5 (B) can be used. In order to perform a phase sensitive measurement, an interferometric scheme as in Fig. 2.5 (C) is used. These detectors provide amplitude and phase information as a function of time or frequency. However, the detectors provide very limited information on the spatial properties of the optical beam. In order to measure the transverse spatial modes of a field, an array detector as shown in Fig. 2.5 (D) is used. Other simplified array detectors such as the one-dimensional split detector (Fig. 2.5 (E)) or the two-dimensional quadrant detector are commonly used to detect beam displacements and tilt.

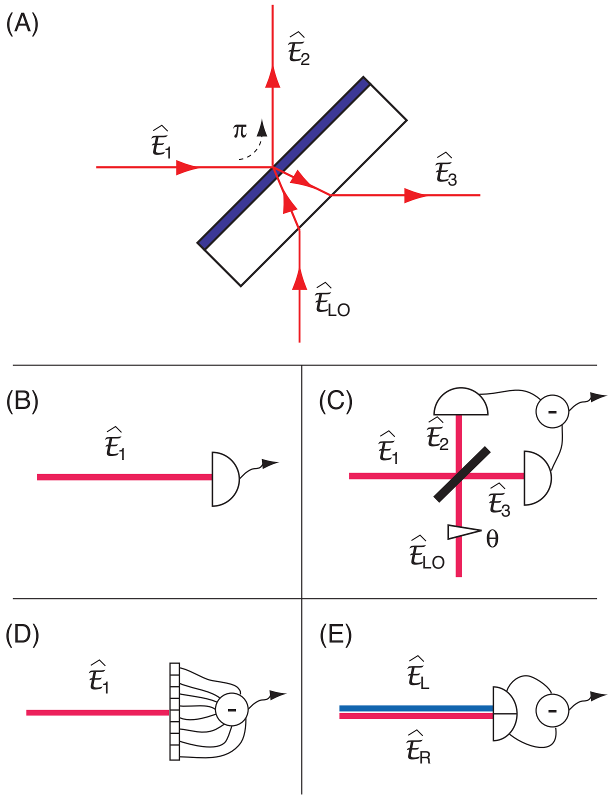

Figure 2.5: (A) A beam-splitter, with input fields $\hat{E}_1$ and $\hat{E}_{\mathrm{LO}}$. The output fields are labelled by $\hat{E}_2$ and $\hat{E}_2$. Field $\hat{E}_1$ undergoes a hard-reflection at the beam-splitter resulting in a π phase shift imposed on the field. (B) Direct detection. (C) Mach-Zehnder based homodyne detection. (D) Array detection. (E) Split detection.

2.4.1 Direct detection

We now consider the direct detection of a laser beam on a single photo-detector, as shown in Fig. 2.5 (B). This process is phase insensitive as it can only measure amplitude signals of the beam. We model the detected signal by calculating the photo-current[7], given by

$$\begin{aligned}
i_1(\omega) &= \frac{2\epsilon_0 V}{\hbar\omega_0}\int_{-\infty}^{\infty}\left(\tilde{\mathcal{E}}^+(\boldsymbol{r},\omega)\right)^\dagger \tilde{\mathcal{E}}^+(\boldsymbol{r},\omega)d\boldsymbol{r} &(2.79)\\
&= \int_{-\infty}^{\infty}\sum_{j,k=0}^{\infty}\left(\alpha_j(\omega)u_j(\boldsymbol{r})+\delta\tilde{a}_j^\dagger(\omega)u_j(\boldsymbol{r})\right)\left(\alpha_k(\omega)u_k(\boldsymbol{r})+\delta\tilde{a}_k(\omega)u_k(\boldsymbol{r})\right)d\boldsymbol{r}\\
&= \sum_{j=0}^{\infty}\left(\alpha_j(\omega)^2+\alpha_j(\delta\tilde{a}_j(\omega)+\delta\tilde{a}_j^\dagger(\omega))+\delta\tilde{a}_j^\dagger\delta\tilde{a}_j(\omega)\right)\\
&= \sum_{j=0}^{\infty}\left(\alpha_j(\omega)^2+\alpha_j(\omega)\delta\tilde{X}_j^+(\omega)\right) &(2.80)
\end{aligned}$$

where we have utilised the linearisation approximation where terms $\delta\tilde{a}_j^\dagger\delta\tilde{a}_j(\omega) \ll \alpha_j^2(\omega)$ are neglected. We also work in the frame where $\alpha_j^* = \alpha_j$. In the above expression the overlap integral between orthogonal modes is zero as shown in Eq. (2.17). Therefore direct detection only gives the amplitude quadrature of the field. The detected signals correspond to $\sum_j \alpha_j(\omega)^2$ whilst the noise terms are given by $\sum_j \alpha_j(\omega)\delta\tilde{X}_j^+(\omega)$, with the scaling of $\alpha_j(\omega)$.

Now we take the usual case where only one mode has a coherent amplitude $\alpha_0(\omega)$, that corresponds to the $u_0(\boldsymbol{r})$ mode. Thus the photo-current reduces to

$$i_1(\omega) = \alpha_0(\omega)^2 + \alpha_0(\omega)\delta\tilde{X}_0^+(\omega) \tag{2.81}$$

where only the amplitude quadrature signal and noise corresponding to mode $u_0(\boldsymbol{r})$ are detected. This result is expected as the signal is only contained in the $u_0(\boldsymbol{r})$ mode and thus the only contributing noise mode is that corresponding to the $u_0(\boldsymbol{r})$ mode as well.

2.4.2 Homodyne detection

In order to perform a phase-sensitive measurement, a reference phase (or 'clock') has to be used. Such a measurement scheme involves an interferometric scheme and there exist many variations of interferometers. The most commonly used interferometer in quantum optics is the Mach-Zehnder interferometer. Before we proceed to model the Mach-Zehnder-based homodyne detector, the quantum effects of a beam-splitter on an input field has to be considered.

The beam-splitter

A schematic of the beam-splitter with input beams is shown in Fig. 2.5 (A). Input beam $\tilde{\mathcal{E}}_1^+(\omega)$ is the beam to be measured, whilst $\tilde{\mathcal{E}}_{\mathrm{LO}}^+(\omega)$ serves as the local oscillator (phase reference) beam. The two output beams of the beam-splitter are denoted by $\tilde{\mathcal{E}}_2^+(\omega)$ and $\tilde{\mathcal{E}}_3^+(\omega)$. Since beam $\tilde{\mathcal{E}}_1^+(\omega)$ undergoes a hard-reflection at the beam-splitter, a π phase

---

[7] This is assuming that every photon is converted into an electron in the detector photo-current.

shift is obtained due to Fresnel reflection. The output electric field operators are given by

$$\begin{aligned}
\tilde{\mathcal{E}}_2^+(\omega) &= \frac{1}{\sqrt{2}}\left(\tilde{\mathcal{E}}_{\mathrm{LO}}^+(\omega) - e^{i\theta}\tilde{\mathcal{E}}_1^+(\omega)\right) && (2.82)\\
&= \frac{1}{\sqrt{2}}\left(\beta_0(\omega)u_0(\boldsymbol{r}) + \sum_{j=0}^{\infty}\delta\tilde{b}_j(\omega)u_j(\boldsymbol{r}) - e^{i\theta}\alpha_0(\omega)u_0(\boldsymbol{r}) - e^{i\theta}\sum_{j=0}^{\infty}\delta\tilde{a}_j(\omega)u_j(\boldsymbol{r})\right)\\
\tilde{\mathcal{E}}_3^+(\omega) &= \frac{1}{\sqrt{2}}\left(\tilde{\mathcal{E}}_{\mathrm{LO}}^+(\omega) + e^{i\theta}\tilde{\mathcal{E}}_1^+(\omega)\right) && (2.83)\\
&= \frac{1}{\sqrt{2}}\left(\beta_0(\omega)u_0(\boldsymbol{r}) + \sum_{j=0}^{\infty}\delta\tilde{b}_j(\omega)u_j(\boldsymbol{r}) + e^{i\theta}\alpha_0(\omega)u_0(\boldsymbol{r}) + e^{i\theta}\sum_{j=0}^{\infty}\delta\tilde{a}_j(\omega)u_j(\boldsymbol{r})\right)
\end{aligned}$$

where a phase factor $e^{i\theta}$ is explicitly introduced and θ is the phase between beam 1 and the local oscillator. We also assume the local oscillator and the input beams only have coherent excitation in the mode-shape $u_0(\boldsymbol{r})$. β_0 and α_0 are the coherent amplitudes of the local oscillator and input beams, respectively.

Mach-Zehnder-based homodyne detection

The output beams 2 and 3 are detected on their respective detectors, as shown in Fig. 2.5 (C). The corresponding photo-currents for beams 2 and 3 are given respectively, by

$$\begin{aligned}
i_2(\omega) &= \frac{2\epsilon_0 V}{\hbar\omega_0}\int_{-\infty}^{\infty}\left(\tilde{\mathcal{E}}_2^+(\omega)\right)^{\dagger}\tilde{\mathcal{E}}_2^+(\omega)d\boldsymbol{r} && (2.84)\\
&= \frac{1}{2}\left(\beta_0(\omega)^2 + \alpha_0(\omega)^2 - 2\beta_0(\omega)\alpha_0(\omega)\cos\theta\right)\\
&\quad+\frac{1}{2}\left(\beta_0(\omega)\delta\tilde{X}_{b_0}^+(\omega) - \beta_0(\omega)\delta\tilde{X}_{a_0}^{-\theta}(\omega) - \alpha_0(\omega)\delta\tilde{X}_{b_0}^{\theta}(\omega) + \alpha_0(\omega)\delta\tilde{X}_{a_0}^+(\omega)\right)\\
i_3(\omega) &= \frac{2\epsilon_0 V}{\hbar\omega_0}\int_{-\infty}^{\infty}\left(\tilde{\mathcal{E}}_3^+(\omega)\right)^{\dagger}\tilde{\mathcal{E}}_3^+(\omega)d\boldsymbol{r} && (2.85)\\
&= \frac{1}{2}\left(\beta_0(\omega)^2 + \alpha_0(\omega)^2 + 2\beta_0(\omega)\alpha_0(\omega)\cos\theta\right)\\
&\quad+\frac{1}{2}\left(\beta_0(\omega)\delta\tilde{X}_{b_0}^+(\omega) + \beta_0(\omega)\delta\tilde{X}_{a_0}^{-\theta}(\omega) + \alpha_0(\omega)\delta\tilde{X}_{b_0}^{\theta}(\omega) + \alpha_0(\omega)\delta\tilde{X}_{a_0}^+(\omega)\right)
\end{aligned}$$

We now take the subtraction of the photo-currents 2 and 3, given by

$$i_-(\omega) = i_3(\omega) - i_2(\omega) = 2\beta_0(\omega)\alpha_0(\omega)\cos\theta + \beta_0(\omega)\delta\tilde{X}_{a_0}^{-\theta}(\omega) \qquad (2.86)$$

where we have used the assumption that the local oscillator is more intense than input beam 1, $\beta_0 \gg \alpha_0$. We can also see that the local oscillator signal and noise terms are cancelled out in this process - a process called *common-mode subtraction.* The equation above is dependent on the phase θ. By setting the phase $\theta = 0$ and $\theta = \pi/2$, respectively, the amplitude and phase quadratures of the input beam 1 are obtained.

When the sum of the photo-currents 2 and 3 are taken, we obtain

$$i_+(\omega) = i_3(\omega) + i_2(\omega) = \beta_0(\omega)^2 + \beta_0(\omega)\delta\tilde{X}_{b_0}^+(\omega) \qquad (2.87)$$

which has the same form as Eq. (2.80), as expected. However, in this case, it is the local oscillator amplitude quadrature that is detected because $\beta_0 \gg \alpha_0$.

2.4.3 Array detection

In order for a detector to measure the beam mode and intensity distribution, an array detector is required. The array detector consists of an array of pixels, each with a transverse area D_j. The photo-current of the light beam at each pixel is then given by

$$i_{D_j}(\omega) = \frac{2\epsilon_0 V}{\hbar\omega_0} \int_{D_j} \left(\hat{\mathcal{E}}^+(\boldsymbol{r},\omega)\right)^\dagger \hat{\mathcal{E}}^+(\boldsymbol{r},\omega) d\boldsymbol{r} \tag{2.88}$$

We can obtain information from the image by computing a function dependent on the intensities of every pixel in the detector.

$$M(D_j(\omega)) = \sum_{j=0}^{N} g_j i_{D_j}(\omega) \tag{2.89}$$

where N is the total number of pixels and g_j is the gain for each pixel[8]. In the limit that the pixel size is infinitessimally small, we obtain

$$M(\omega) = \int_{-\infty}^{\infty} g(\boldsymbol{r}) i_D(\omega) dD \tag{2.90}$$

where D is an infinitessimal pixel area on the idealised array detector.

2.4.4 Split detection

The split detector is the most basic form of the array detector. It is commonly used to detect beam displacements and tilt along one transverse axis. The photo-currents on the left and right hand side of the split detector are given respectively by

$$\begin{aligned} i_L(\omega) &= \frac{2\epsilon_0 V}{\hbar\omega_0} \int_{-\infty}^{0} \left(\hat{\mathcal{E}}^+(\boldsymbol{r},\omega)\right)^\dagger \hat{\mathcal{E}}^+(\boldsymbol{r},\omega) d\boldsymbol{r} & (2.91) \\ &= \sum_{n,m=0}^{\infty} \left(\alpha_n(\omega) + \delta\tilde{a}_n^\dagger(\omega)\right) \left(\alpha_m(\omega) + \delta\tilde{a}_m(\omega)\right) \int_{-\infty}^{0} u_n(\boldsymbol{r}) u_m(\boldsymbol{r}) d\boldsymbol{r} \\ i_R(\omega) &= \frac{2\epsilon_0 V}{\hbar\omega_0} \int_{0}^{\infty} \left(\hat{\mathcal{E}}^+(\boldsymbol{r},\omega)\right)^\dagger \hat{\mathcal{E}}^+(\boldsymbol{r},\omega) d\boldsymbol{r} & (2.92) \\ &= \sum_{n,m=0}^{\infty} \left(\alpha_n(\omega) + \delta\tilde{a}_n^\dagger(\omega)\right) \left(\alpha_m(\omega) + \delta\tilde{a}_m(\omega)\right) \int_{0}^{\infty} u_n(\boldsymbol{r}) u_m(\boldsymbol{r}) d\boldsymbol{r} \\ & & (2.93) \end{aligned}$$

The sum of the photo-currents gives

$$\begin{aligned} i_L(\omega) + i_R(\omega) &= \sum_{n,m=0}^{\infty} \left(\alpha_n(\omega) + \delta\tilde{a}_n^\dagger(\omega)\right) \left(\alpha_m(\omega) + \delta\tilde{a}_m(\omega)\right) \int_{-\infty}^{\infty} u_n(\boldsymbol{r}) u_m(\boldsymbol{r}) d\boldsymbol{r} \\ &= \alpha_n(\omega)^2 + \alpha_n(\omega)\delta\tilde{X}_n(\omega) & (2.94) \end{aligned}$$

---

[8] We have assumed here that the function is linear but this could in principle have non-linear dependence on the pixel intensities.

which is exactly of the same form as Eq. (2.80), since the split detector in sum mode is effectively a direct detector.

The difference photo-current is given by

$$i_L(\omega) - i_R(\omega) = \sum_{n,m=0}^{\infty} \left(\alpha_n(\omega) + \delta\tilde{a}_n^\dagger(\omega)\right) \left(\alpha_m(\omega) + \delta\tilde{a}_m(\omega)\right) \left[\int_{-\infty}^{0} - \int_{0}^{\infty}\right] u_n(\boldsymbol{r}) u_m(\boldsymbol{r}) d\boldsymbol{r} \tag{2.95}$$

2.4.5 Power spectral variance

The power spectral variance is a measure of the amount of power in the fluctuations of a field, within some bandwidth[9], centred around a sideband frequency ω. In continuous-variable quantum optics experiments, the spectrum analyser is often used to measure the power spectral variance of the photo-current, given by [195]

$$V_{\mathrm{D}}(\omega) = \langle (\delta i(\omega))^2 \rangle \tag{2.96}$$

where $\delta i(\omega)$ is the photo-current fluctuation term. Substituting Eq. (2.86), we obtain

$$\begin{aligned} V_{\mathrm{D}}^{\theta}(\omega) &= \beta_0(\omega)^2 \langle (\delta \tilde{X}_{a_0}^{\theta}(\omega))^2 \rangle & (2.97)\\ &= \beta_0(\omega)^2 V_{a_0}^{\theta}(\omega) & (2.98) \end{aligned}$$

We can see in this expression that the power spectral variance of the field scales with the optical power of the beam (in this case of homodyne detection, the scaling follows the local oscillator power), $\beta_0(\omega)^2$. It is common to normalise the power spectral variance with respect to the optical power of the beam, giving

$$V^{\theta}(\omega) = \frac{V_{\mathrm{D}}(\omega)}{\beta_0(\omega)^2} = V_{a_0}^{\theta}(\omega) \tag{2.99}$$

For coherent or vacuum beams, the normalised power spectral variance is given by $V^{\theta}(\omega) = 1$, whilst for squeezed states, $V^{\theta}(\omega) < 1$.

2.5 Einstein-Podolsky-Rosen (EPR) Entanglement

Continuous-variable EPR entanglement in the amplitude and phase quadratures can be generated by combining two squeezed beams with an appropriate phase shift θ_1, on a 50:50 beam-splitter, as shown in Fig. 2.6. The two input squeezed beams are labelled by 1 and 2, whilst the output entangled beams are labelled by 3 and 4. The two entangled beams are measured in the amplitude and phase quadratures.

---

[9] This defines the resolution bandwidth of the measurement device.

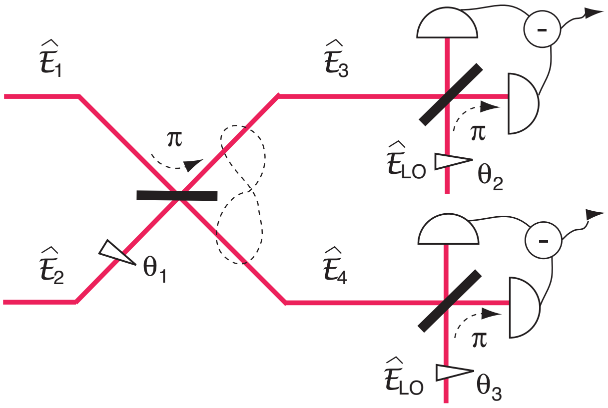

Figure 2.6: The input and output beams are labelled by $\hat{\mathcal{E}}_{1,2}$ and $\hat{\mathcal{E}}_{3,4}$, respectively. The phase between the two input beams is given by θ_1. The local oscillator beams are labelled by $\hat{\mathcal{E}}_{\rm LO}$, with phases θ_2 and θ_3. All beam-splitters in the figure are 50:50 beam-splitters.

The electric field operators for beams 3 and 4 are given respectively by

$$\tilde{\mathcal{E}}_3(\omega) = \frac{1}{\sqrt{2}}\left(e^{i\theta_1}\tilde{\mathcal{E}}_2(\omega) - \tilde{\mathcal{E}}_1(\omega)\right) \tag{2.100}$$

$$= \sum_{j=0}^{\infty} i\sqrt{\frac{\hbar\omega_0}{2\epsilon_0 V}}\sqrt{\frac{1}{2}}\left(e^{i\theta_1}\delta\tilde{b}_j(\omega)u_j(\boldsymbol{r}) - \delta\tilde{a}_j(\omega)u_j(\boldsymbol{r})\right) \tag{2.101}$$

$$\tilde{\mathcal{E}}_4(\omega) = \frac{1}{\sqrt{2}}\left(e^{i\theta_1}\tilde{\mathcal{E}}_2(\omega) + \tilde{\mathcal{E}}_1(\omega)\right) \tag{2.102}$$

$$= \sum_{j=0}^{\infty} i\sqrt{\frac{\hbar\omega_0}{2\epsilon_0 V}}\sqrt{\frac{1}{2}}\left(e^{i\theta_1}\delta\tilde{b}_j(\omega)u_j(\boldsymbol{r}) + \delta\tilde{a}_j(\omega)u_j(\boldsymbol{r})\right) \tag{2.103}$$

where the squeezed beams are assumed to not have any coherent amplitude. The photon annihilation operators corresponding to beams 2 and 1 are given by $\delta\tilde{b}_j(\omega)$ and $\delta\tilde{a}_j(\omega)$, respectively.

The detection system used to measure the amplitude and phase quadratures of beams 3 and 4 is homodyne detection. The homodyne detection system was described in detail in Section 2.4. We now assume beams 1 and 2 to be $\theta_1 = \pi/2$ out of phase. The detected photo-current corresponding to beams 3 and 4 are thus respectively given by

$$\begin{aligned}
i_{3-}^{\theta_2}(\omega) &= \frac{1}{2}\int_{-\infty}^{\infty}\sum_{j,k=0}^{\infty}\Big[\left(\sqrt{\frac{1}{2}}\left(i\delta\tilde{b}_j(\omega)u_j(\boldsymbol{r})-\delta\tilde{a}_j(\omega)u_j(\boldsymbol{r})\right)+e^{i\theta_2}\gamma_0u_0(\boldsymbol{r})+e^{i\theta_2}\delta\tilde{g}_j(\omega)u_j(\boldsymbol{r})\right)^\dagger\\
&\quad\times\left(\sqrt{\frac{1}{2}}\left(i\delta\tilde{b}_k(\omega)u_k(\boldsymbol{r})-\delta\tilde{a}_k(\omega)u_k(\boldsymbol{r})\right)+e^{i\theta_2}\gamma_0u_0(\boldsymbol{r})+e^{i\theta_2}\delta\tilde{g}_k(\omega)u_k(\boldsymbol{r})\right)\\
&\quad-\left(\sqrt{\frac{1}{2}}\left(i\delta\tilde{b}_j(\omega)u_j(\boldsymbol{r})-\delta\tilde{a}_j(\omega)u_j(\boldsymbol{r})\right)-e^{i\theta_2}\gamma_0u_0(\boldsymbol{r})-e^{i\theta_2}\delta\tilde{g}_j(\omega)u_j(\boldsymbol{r})\right)^\dagger\\
&\quad\times\left(\sqrt{\frac{1}{2}}\left(i\delta\tilde{b}_k(\omega)u_k(\boldsymbol{r})-\delta\tilde{a}_k(\omega)u_k(\boldsymbol{r})\right)-e^{i\theta_2}\gamma_0u_0(\boldsymbol{r})-e^{i\theta_2}\delta\tilde{g}_k(\omega)u_k(\boldsymbol{r})\right)\Big]d\boldsymbol{r}\\
&= \frac{\gamma_0}{2}\left(\delta\tilde{X}_{a_0}^{\theta_2}(\omega)-\delta\tilde{X}_{b_0}^{\theta_2-\frac{\pi}{2}}(\omega)\right)
\end{aligned}\tag{2.104}$$

$$\begin{aligned}
i_{4-}^{\theta_3}(\omega) &= \frac{1}{2}\int_{-\infty}^{\infty}\sum_{j,k=0}^{\infty}\Big[\left(\sqrt{\frac{1}{2}}\left(i\delta\tilde{b}_j(\omega)u_j(\boldsymbol{r})+\delta\tilde{a}_j(\omega)u_j(\boldsymbol{r})\right)+e^{i\theta_3}\gamma_0u_0(\boldsymbol{r})+e^{i\theta_3}\delta\tilde{g}_j(\omega)u_j(\boldsymbol{r})\right)^\dagger\\
&\quad\times\left(\sqrt{\frac{1}{2}}\left(i\delta\tilde{b}_k(\omega)u_k(\boldsymbol{r})+\delta\tilde{a}_k(\omega)u_k(\boldsymbol{r})\right)+e^{i\theta_3}\gamma_0u_0(\boldsymbol{r})+e^{i\theta_3}\delta\tilde{g}_k(\omega)u_k(\boldsymbol{r})\right)\\
&\quad-\left(\sqrt{\frac{1}{2}}\left(i\delta\tilde{b}_j(\omega)u_j(\boldsymbol{r})+\delta\tilde{a}_j(\omega)u_j(\boldsymbol{r})\right)-e^{i\theta_3}\gamma_0u_0(\boldsymbol{r})-e^{i\theta_3}\delta\tilde{g}_j(\omega)u_j(\boldsymbol{r})\right)^\dagger\\
&\quad\times\left(\sqrt{\frac{1}{2}}\left(i\delta\tilde{b}_k(\omega)u_k(\boldsymbol{r})+\delta\tilde{a}_k(\omega)u_k(\boldsymbol{r})\right)-e^{i\theta_3}\gamma_0u_0(\boldsymbol{r})-e^{i\theta_3}\delta\tilde{g}_k(\omega)u_k(\boldsymbol{r})\right)\Big]d\boldsymbol{r}\\
&= \frac{\gamma_0}{2}\left(\delta\tilde{X}_{a_0}^{\theta_3}(\omega)+\delta\tilde{X}_{b_0}^{\theta_3-\frac{\pi}{2}}(\omega)\right)
\end{aligned}\tag{2.105}$$

where the local oscillator has coherent amplitude γ_0 in the mode $u_0(\boldsymbol{r})$. The noise terms corresponding to the local oscillator beam are given by $\delta\tilde{g}_j(\omega)$.

A signature of entanglement is the presence of quantum correlation and anti-correlation in the conjugate observables. By computing the sum and difference between the photo-current signals for the amplitude and phase quadratures, respectively, the following are obtained

$$\left\langle\left(i_{\mathrm{N4}-}^{+}(\omega)+i_{\mathrm{N3}-}^{+}(\omega)\right)^2\right\rangle = \gamma_0\left\langle(\delta\tilde{X}_{b_0}^{+}(\omega))^2\right\rangle\rightarrow 0 \tag{2.106}$$

$$\left\langle\left(i_{\mathrm{N4}-}^{-}(\omega)-i_{\mathrm{N3}-}^{-}(\omega)\right)^2\right\rangle = \gamma_0\left\langle(\delta\tilde{X}_{a_0}^{+}(\omega))^2\right\rangle\rightarrow 0 \tag{2.107}$$

where we have assumed beams 1 and 2 to be amplitude squeezed, $\left\langle(\delta\tilde{X}_{b_0}^{+}(\omega))^2\right\rangle\rightarrow 0$ and $\left\langle(\delta\tilde{X}_{a_0}^{+}(\omega))^2\right\rangle\rightarrow 0$. The simultaneous reduction in noise on the correlation and anti-correlation signals in the amplitude and phase quadratures, respectively, is the signature of entanglement.

2.6 Classical control

2.6.1 Classical control theory

Experimental parameters often drift with time. There are many causes for these experimental drifts, such as the contraction and expansion of components due to temperature changes as well as the presence of external mechanical and acoustic noise sources. Therefore, in order to impose stability to the experiment, control is necessary. We will consider the most basic first-order feedback control system [196], shown in Fig. 2.7.

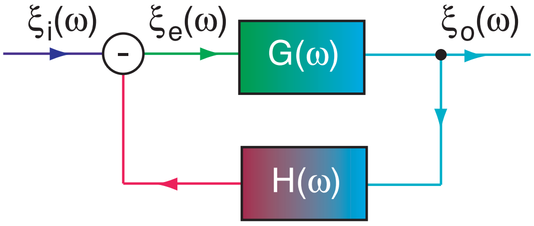

Figure 2.7: The input, error and output signals are given by $\xi_i(\omega)$, $\xi_e(\omega)$ and $\xi_o(\omega)$, respectively. The transfer functions for the system and the feedback controller are given by $G(\omega)$ and $H(\omega)$, respectively.

We will model the feedback loop by first considering the perturbation on an input signal $\xi_i(\omega)$ by a system with transfer function $G(\omega)$. The corresponding output signal is given by $\xi_o(\omega)$. In order to counter-act the perturbation introduced in $G(\omega)$, the output signal has to be fed-back through a 'feedback controller', with transfer function $H(\omega)$. The signal from $H(\omega)$ is then recombined with the input signal to yield an error signal $\xi_e(\omega)$, which now forms the total effective input signal into system $G(\omega)$. We now derive the transfer function of the feedback scheme, by considering the coupled equations given by

$$\xi_e(\omega) = \xi_i(\omega) - H(\omega)\xi_o(\omega) \tag{2.108}$$

$$\xi_o(\omega) = G(\omega)\xi_e(\omega) \tag{2.109}$$

Solving these two equations gives the transfer function of the total system

$$\frac{\xi_o(\omega)}{\xi_i(\omega)} = \frac{G(\omega)}{1 + G(\omega)H(\omega)} \tag{2.110}$$

For $G(\omega)H(\omega) = -1$, the denominator of Eq. (2.110) is 0, giving an unstable feedback system. Eq. (2.110) is a very important equation and forms the main consideration for the design of all the feedback loops used in the experiments of this thesis[10].

Now that the fundamentals of a feedback system are established, we proceed to describe the various methods of deriving error signals.

---

[10] Our feedback controllers (servo systems) are designed to have a $1/f$ roll-off as a function of frequency ω. This is to provide enough gain for lower frequencies and reducing the gain at higher frequencies to avoid the unstable point of -1 in the Nyquist plot of the transfer function for the feedback system. Additional gain can be provided at lower frequencies by the use of an integration stage in the feedback controller. More sophisticated designs of servo controls include a sharp elliptic filter to remove resonances in the system.

2.6.2 Power difference error signal

Suppose that phase quadrature detection is required in an interferometer. Therefore the interferometer is to be stabilised at the half fringe of the interference signal, where the powers at the two outputs of the interferometer are equal. An error signal can therefore be obtained by taking the power difference of the signals from the two outputs of the interferometer. The error signal is given by the signal term of Eq. (2.86), giving

$$\langle i_E(t)\rangle = 2\beta_0(t)\alpha_0(t)\cos\theta(t) \tag{2.111}$$

where $\beta_0(t)$ and $\alpha_0(t)$ are the coherent amplitudes of the two input beams of the interferometer. $\theta(t)$ is the phase difference between the two input fields of the interferometer.

The zero point of the error signal occurs when the input beams are $\pi/2$ out-of-phase. In order to stabilise the system, any deviation from the zero-point error signal will require a counter-action on the phase $\theta(t)$, which is provided by the error signal (with an appropriate phase).

2.6.3 Pound-Drever-Hall (PDH) error signal

The Pound-Drever-Hall (PDH) technique of stabilisation is a very popular technique used in performance applications. The PDH technique is based on the application of a phase modulation to the laser beam [197]. It relies on the dispersion of a system to provide phase shifts on the modulation signal, converting it into an error signal dependent on the phase shift. We consider the signal terms of Eq. (2.85) with an input signal containing phase modulation, given by $e^{i\theta(t)}(\alpha_0(1+iA_{\rm PM}\sin(\omega_{\rm PM}t))$. Thus the signal terms of Eq. (2.85), becomes

$$\begin{aligned}\langle i_3(t)\rangle &= \frac{1}{2}\Big(\beta_0^2+\alpha_0^2+2\beta_0\alpha_0\cos\theta(t)\\ &\quad +\alpha_0^2A_{\rm PM}^2\sin^2(\omega_{\rm PM}t)-2\beta_0\alpha_0A_{\rm PM}\sin\theta(t)\sin(\omega_{\rm PM}t)\Big)\end{aligned} \tag{2.112}$$

where $\beta_0(t)$ and $\alpha_0(t)$ are the coherent amplitudes of the two input beams of the interferometer. $\theta(t)$ is the phase difference between the two input fields of the interferometer. $A_{\rm PM}$ and $\omega_{\rm PM}$ are the amplitude and frequency of the phase modulation signal, respectively.

We assume that one input beam is more intense than the other input beam of the interferometer. The modulation amplitude is also assumed to be small where, $\beta_0 \gg \alpha_0, A_{\rm PM}$. Therefore Eq. (2.112) reduces to

$$\langle i_3(t)\rangle = \frac{1}{2}\Big(\beta_0^2+2\beta_0\alpha_0\cos\theta(t)-2\beta_0\alpha_0A_{\rm PM}\sin\theta(t)\sin(\omega_{\rm PM}t)\Big) \tag{2.113}$$

The detected photo-current is demodulated at frequency $\omega_{\rm PM}$, via a multiplication of the photo-current with the modulation signal, giving

$$\begin{aligned}\langle i_3(t)\rangle\sin(\omega_{\rm PM}t) &= \frac{1}{2}\Big(\beta_0^2\sin(\omega_{\rm PM}t)+2\beta_0\alpha_0\cos\theta(t)\sin(\omega_{\rm PM}t)\\ &\quad -2\beta_0\alpha_0A_{\rm PM}\sin\theta(t)\left[\frac{1}{2}-\frac{\cos(2\omega_{\rm PM}t)}{2}\right]\Big)\end{aligned} \tag{2.114}$$

We now apply a low-pass filter which filters all signals with frequency $\geq \omega_{\mathrm{PM}}$, giving

$$\langle i_E(t)\rangle = -\frac{1}{2}\beta_0\alpha_0 A_{\mathrm{PM}} \sin\theta(t) \tag{2.115}$$

The zero point of the error signal occurs when the input beams are in-phase. The stabilisation at the zero/full-fringe of the interferometer gives a detected amplitude signal.

Note that these techniques can be extended to multiple-beam interferometers, optical cavities, atomic samples and another systems which are dispersive.

2.7 Summary

We have presented the basic quantum optics formalism necessary for understanding the other work described in this thesis.

Chapter 3

Optimal spatial variable measurement

Reductio ad absurdum.

- Zeno

In the 3rd century B.C., there lived King Hiero in Syracuse, Sicily and King Hiero wore a golden crown to celebrate his royalty. One day, King Hiero heard rumours that his royal goldsmith was stealing royal gold and using a silver-gold alloy instead to make jewellery for the king. The king was faced with a dilemma as he did not know how to prove if this was indeed the case. Thereafter, the task of determining precisely the gold content of the royal crown was given to Archimedes. Archimedes was familiar with the concept of densities and that silver was less dense than gold. However, Archimedes was puzzled and could not think of a way to measure the density of the royal crown precisely, without having to reshape it into the shape of a gold bullion, for a weight comparison. One day, while Archimedes was entering the bath tub, he observed that the water level rose correspondingly to how much he was submerged in the water. With this, he realised immediately that he had the solution for measuring the density of the royal crown precisely and ran around town shouting 'Eureka! Eureka!'.

Like Archimedes in ancient times, humans today, are interested in measuring physical quantities precisely and optimally. In continuous-wave optics, measurements of the three mechanical degrees of freedom of a beam are very important. Often it is required to stabilise the positioning of a laser beam for interferometric measurements and for communication between satellites separated by large distances [198, 199]. On the microscopic level, highly precise control of the rotation and displacement of a biological cell is required, thus demanding highly precise properties of an 'optical tweezer' beam [200]. Traditionally, beam displacement and tilt were measured using a simplified array detector - the split detector [155, 156, 198, 199, 151, 152, 153, 154]. For orbital angular momentum measurements, a holographic filter is normally used to filter out the mode component corresponding to orbital angular momentum and the power in that mode is detected [201, 202].

In this chapter, we ask the question that King Hiero asked more than 2 millennia ago - "How do we know if the royal goldsmith is lying to us and stealing our gold?" or rather, "How do we know if our spatial variable measurements are optimal and that we are detecting the maximum signal possible?". We approach this problem by investigating the "noise modes" associated with these various mechanical degrees of freedom. The "noise modes" are the vacuum noise components which are in the same spatial and frequency mode as the signal component. In order for a measurement scheme to detect the signal and its relevant noise component only, the measurement scheme has to be 'tailored' to be optimal in its detection efficiency. Our analysis shows that the "noise modes" corresponding to beam displacement and tilt do not correspond to the "detection mode" of a split detector. The "detection mode" of a detector is the mode which is specifically detected by the detector and depends on the detector geometry. Therefore split detection is not the optimal detection scheme for beam displacement and tilt.

This chapter considers the specific example of beam displacement of a TEM_{00} mode and we show that split detection only measures beam displacement with $\sim 80\%$ efficiency. Our analysis also applies to beam tilt and this is discussed in more detail in the following chapter. We propose an optimal scheme to perform beam displacement and tilt measurements, based on homodyne detection, with specifically tailored local oscillator mode-shapes. Our scheme can be adapted relatively easily to measure beam orbital angular momentum as well. We show that although the quantum noise limit to displacement measurements can be surpassed using squeezed light in appropriate spatial modes for both split and homodyne detection, the homodyning scheme out-performs split detection for all values of squeezing.

The work in this chapter has been published in the journal articles:

- M. T. L. Hsu, V. Delaubert, P. K. Lam, and W. P. Bowen, "Optimal optical measurements of small displacements", Journal of Optics B: Quantum and Semiclassical Optics **6**, 495 (2004).
- N. Treps, N. Grosse, W. P. Bowen, M. T. L. Hsu, A. Maître, C. Fabre, H.-A. Bachor, and P. K. Lam, "Nano-displacement measurements using spatially multimode squeezed light", Journal of Optics B: Quantum and Semiclassical Optics **6**, S664 (2004).
- H.-A. Bachor, V. Delaubert, C. C. Harb, M. T. L. Hsu, P. K. Lam, C. Fabre, and N. Treps, "Spatial quantum effects with continuous-wave laser beams", Journal of Modern Optics **53**, 597 (2006).

3.1 Introduction

Efficient techniques for performing optical beam displacement measurements are crucial for many applications. When an optical beam is reflected from, or transmitted through, an object that is moving, the mechanical movement can be translated to a movement of the optical beam. Characterisation of the transverse position of this beam then yields an extremely accurate measurement of the object movement. Some example applications that use these techniques are: *Atomic force microscopy*, where a beam displacement measurement is used to characterise the vibration of a cantilever, and the force the cantilever experiences [155, 156]; *inter-satellite position stabilisation*, where a displacement measurement allows a receiving satellite to orient itself to an optical beam sent by another satellite, thus allowing a reduction of non-common mode positional vibrations between satellites [198, 199]; and *optical tweezer*, where the position of particles held in an optical tweezer can be detected and controlled by measuring the position of the beam [151, 152, 153, 154]. An understanding of the fundamental limits imposed on these opto-mechanical positional measurements is therefore important.

Recently there has been increasing interest, both theoretical [203] and experimental [204, 1, 205], in using quantum resources to enhance optical displacement measurements.

Much of the interest has been on how multi-mode squeezed light can be used to enhance the outcome of split detector and array detector measurements. This is an important question since split detectors and arrays are the primary instruments presently used in displacement measurements and imaging systems.

In spite of the successes in using multi-mode squeezed light to achieve displacement measurements beyond the quantum noise limit (QNL), we will show in this chapter that split detection is not an optimum displacement measurement. Assuming that the beam under interrogation is a TEM_{00} beam, we perform a multi-modal analysis to derive the QNL for optical displacement measurements. We then analyse split detection, the conventional technique used to characterise beam displacement, and compare it to the QNL. We find that displacement measurement using split detection is not quantum noise limited, and is at best only ~ 80 % efficient. As an alternative, we consider a new homodyne detection scheme, utilising a TEM_{10} mode local oscillator beam. We show that this scheme performs at the QNL in the limit of small displacement. This technique, which we term TEM_{10} homodyne detection, has the potential to enhance many applications presently using split detectors to measure displacement. Furthermore, the QNL for optical displacement measurement can be surpassed by introducing a squeezed TEM_{10} mode into the measurement process.

3.2 Displacement Measurement

3.2.1 Quantum Noise Limit

The position of a light beam can be defined as the mean position of all photons in the beam. Beam displacement is then quantified by the amount of deviation of this mean photon position from some fixed reference axis. In this chapter, we assume that the displaced beam has a transverse TEM_{00} mode-shape. To simplify our analysis, we assume, without loss of generality, a one-dimensional transverse displacement d from the reference axis. The normalised transverse beam amplitude function for a displaced TEM_{00} beam, assuming a waist size of w_0, is given by

$$u_0(x-d) = \left(\frac{2}{\pi w_0^2}\right)^{1/4} \exp\left[-\left(\frac{x-d}{w_0}\right)^2\right] \tag{3.1}$$

The transverse intensity distribution for a beam with a total of N photons is then given by $\langle I \rangle = N u_0^2(x-d)$. This equation essentially describes the normalised Gaussian spatial distribution of photons along one transverse axis of the optical beam.

To provide a simple and concise derivation of the QNL of optical displacement measurement we first make two observations - the $\mathrm{TEM}_{\mathrm{mn}}$ modes are equivalent in quantum and classical treatments and the displacement QNL is the optimum sensitivity achievable when no spatial quantum correlations are present (i.e. when a spatial basis can be chosen in which only one spatial mode is occupied [206]). It follows that if the beam is in a coherent state, each photon in the beam is spatially uncorrelated to that of all other photons. Thus for a TEM_{00} beam, the spatial wavefunction of each photon is defined by the TEM_{00} mode-shape in Eq. (3.1). Therefore, the QNL of optical displacement measurement on a coherent TEM_{00} beam can be calculated directly from the arrival statistics of an ensemble of uncorrelated photons with spatial distribution governed by the TEM_{00} mode-shape. Consequently a detector which discriminates the transverse position of each photon will provide the maximum possible information about the displacement of the beam. Such discrimination could, for example, be achieved using an infinite single photon resolving array with infinitesimally small pixels. Although in reality such a detection device is unfeasible, it nevertheless sets a bound to the information obtainable for beam displacement without resorting to quantum resources. This bound therefore constitutes a quantum noise limited displacement measurement. More practical detection schemes can therefore be benchmarked against this limit.

Let us now examine an optimum measurement of beam displacement using our idealised array detector. Using equation (3.1), the probability distribution of locating photons along the x-axis of the detector is given by

$$P(x) = \sqrt{\frac{2}{\pi w_0^2}} \exp\left[-2\left(\frac{x-d}{w_0}\right)^2\right] \tag{3.2}$$

As each photon in the beam impinges on the array, a single pixel is triggered, locating that photon. The beam displacement is given by the mean photon arrival co-ordinate, $\langle x\rangle$, for an infinitely large ensemble of photons. The uncertainty in the measurement of the beam displacement is given by the standard deviation Δd of the spatial distribution of photon arrivals. The respective mean and standard deviation are then expressed as

$$\begin{aligned} \langle x\rangle &= \int_{-\infty}^{\infty} xP(x)dx = d, && (3.3) \\ \Delta d &= \sqrt{\int_{-\infty}^{\infty} x^2 P(x)dx - d^2} = \frac{w_0}{2}. && (3.4) \end{aligned}$$

Since we possess *a priori* knowledge of the mode-shape of the beam, the arrival of a single photon can therefore give us an estimate of the displacement of our beam with a standard deviation given by Δd. For N photons, the standard deviation becomes $\Delta d_{\mathrm{QNL}} = \Delta d/\sqrt{N}$. The minimum displacement discernible by a given detection apparatus is directly related to the sensitivity of the apparatus, defined here as the derivative of the mean signal divided by its standard deviation. For infinite array detection, the signal expectation value is equal to the displacement. Thus the QNL for optimal displacement measurement sensitivity is given by

$$\mathcal{S}_{\mathrm{QNL}} = \frac{1}{\Delta d_{\mathrm{QNL}}} = \frac{2\sqrt{N}}{w_0} \tag{3.5}$$

A plot of $\mathcal{S}_{\mathrm{QNL}}$ as a function of displacement is shown in Fig. 3.4. Since all pixels in the array are assumed to be identical, the standard deviation Δd_{QNL} is independent of displacement. We therefore observe that $\mathcal{S}_{\mathrm{QNL}}$ is constant for all displacements. $\mathcal{S}_{\mathrm{QNL}}$ is also proportional to $\sqrt{N}$ due to the quantum noise limited nature of the beam. Finally, the inverse scaling with waist size w_0 suggests that the accuracy of a displacement measurement can be enhanced by focussing the beam to a smaller waist.

3.2.2 Split Detection

In the previous section, we saw how an idealised array detector can be used to perform quantum noise limited displacement measurements. Implementation of such a detector, however, is clearly impractical. The most common technique for displacement measurement is *split detection* [156, 204, 1]. In this scheme, the beam under interrogation is incident centrally on a split detector. The difference between the two photo-currents of the two halves then contains information about the displacement of the beam (see Figure 3.1).

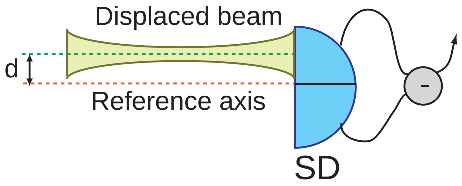

Figure 3.1: Split detection. The difference photo-current of the two halves measures the beam displacement, d.

At this stage we must introduce a more methodical representation of the beam. A beam of frequency ω can be represented by the positive frequency part of the electric field operator $\hat{\mathcal{E}}^+_{\text{in}} e^{i\omega t}$. We are interested in the transverse information of the beam which is fully described by the slowly varying field envelope operator $\hat{\mathcal{E}}^+_{\text{in}}$. We express this operator in terms of the displaced TEM$_{n0}$ basis modes, where n denotes the order of the x-axis Hermite-Gauss mode. Since this chapter considers one-dimensional beam displacement, we henceforth denote the beam amplitude function for the transverse modes with only one index. $\hat{\mathcal{E}}^+_{\text{in}}$ can then be written as

$$\hat{\mathcal{E}}^+_{\text{in}} = i\sqrt{\frac{\hbar\omega}{2\epsilon_0 L}} \sum_{n=0}^{\infty} \hat{a}_n u_n(x-d) \tag{3.6}$$

where $u_n(x-d)$ are the transverse beam amplitude functions for the displaced TEM$_{n0}$ modes, L is a quantisation longitudinal length and $\hat{a}_n$ are the corresponding annihilation operators. $\hat{a}_n$ is normally expressed as $\hat{a}_n = \alpha_n + \delta\hat{a}_n$, where $\alpha_n = \langle \hat{a}_n \rangle$ is the coherent amplitude and $\delta\hat{a}_n$ is a quantum noise operator. Since the beam is assumed to be a TEM$_{00}$ mode, only this mode has coherent excitation and therefore only α_0 is nonzero. The field operator is then given by

$$\hat{\mathcal{E}}^+_{\text{in}} = i\sqrt{\frac{\hbar\omega}{2\epsilon_0 L}} \left(\sqrt{N} u_0(x-d) + \sum_{n=0}^{\infty} \delta\hat{a}_n u_n(x-d) \right) \tag{3.7}$$

where $\alpha_0 = \sqrt{N}$.

The difference photo-current, which provides information on the displacement of the beam relative to the centre of the detector, is given by

$$\begin{aligned} \hat{n}_- &= \hat{n}_{x<0} - \hat{n}_{x>0} \\ &= \frac{2\epsilon_0 L}{\hbar\omega} \left[\int_{-\infty}^{0} dx (\hat{\mathcal{E}}^+_{\text{in}})^\dagger \hat{\mathcal{E}}^+_{\text{in}} - \int_{0}^{\infty} dx (\hat{\mathcal{E}}^+_{\text{in}})^\dagger \hat{\mathcal{E}}^+_{\text{in}} \right] \end{aligned} \tag{3.8}$$

where $\hat{n}_{x<0}$ and $\hat{n}_{x>0}$ are the photon number operators for the left and right halves of the detector, respectively.

Flipped mode basis

Eq. (3.8) can be simplified by changing bases from the TEM$_{n0}$ basis, to a TEM$_{n0}$ basis that has a π-phase flip at the centre of the detector [207, 203]. We denote the flipped mode basis as the TEM$_{\mathrm{f}n0}$ basis. This new basis is termed the *flipped mode basis* and is defined by

$$v_n(x,d) = \begin{cases} u_n(x) & \text{for } x > d \\ -u_n(x) & \text{for } x < d \end{cases} \tag{3.9}$$

where we denote annihilation operators for this basis as $\hat{b}_n$. The first three intensity and amplitude distribution for the flipped modes are shown in Fig. 3.2.

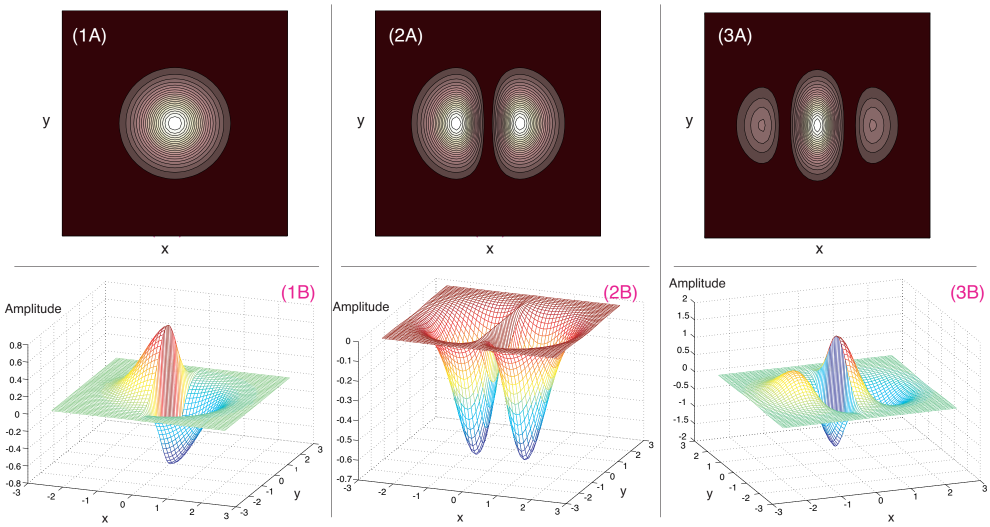

Figure 3.2: Transverse intensity profiles of the (1A) TEM$_{f00}$, (2A) TEM$_{f10}$ and (3A) TEM$_{f20}$ modes. The amplitude distribution function for the (1B) TEM$_{f00}$, (2B) TEM$_{f10}$ and (3B) TEM$_{f20}$ modes.

If the incident TEM$_{00}$ field is bright, such that $N \gg |\langle \delta \hat{a}_n^2 \rangle|$ for all n, the difference photo-current $\hat{n}_-$ can be written compactly as

$$\hat{n}_- = \sqrt{N}\left(\sqrt{N}\zeta_0 + \delta\hat{Y}_0^+\right) \tag{3.10}$$

where $\hat{Y}_0^+$ is the amplitude quadrature operator associated with our new flipped basis, given by $\hat{Y}_0^+ = \langle \hat{Y}_0^+ \rangle + \delta\hat{Y}_0^+ = \hat{b}_0 + \hat{b}_0^\dagger$; and $\zeta_0(d) = \int_{-\infty}^{\infty} v_0(x,d) u_0(x-d) dx$ is the overlap coefficient between the first flipped mode and the displaced TEM$_{00}$ mode. The beam displacement can be inferred from the mean photo-current

$$\langle \hat{n}_- \rangle = N\zeta_0, \tag{3.11}$$

where the standard deviation of the photo-current noise is given by $\Delta\hat{n}_- = \sqrt{\langle \hat{n}_-^2 \rangle - \langle \hat{n}_- \rangle^2} = \sqrt{N}\Delta\hat{Y}_0^+$. For a coherent field, $\Delta\hat{Y}_0^+ = 1$, making $\Delta\hat{n}_- = \sqrt{N}$.

Figure 3.3 (i) shows the normalised difference photo-current $\langle \hat{n}_- \rangle / N$ as a function of beam displacement, d, for split detection. We see that for small displacements where $d \ll w_0$, the normalised difference photo-current is linearly proportional to the displacement

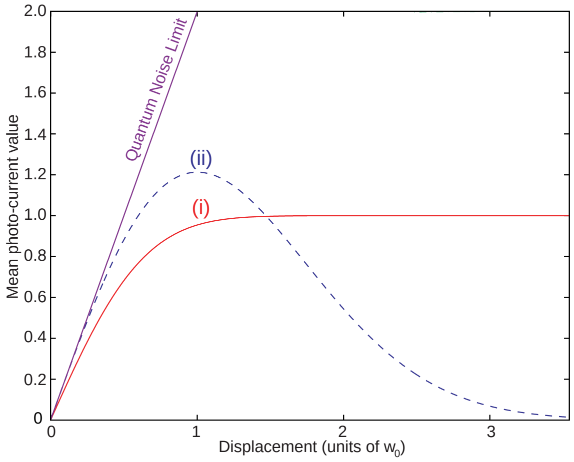

Figure 3.3: Mean value of the normalised difference photo-current, $\langle \hat{n}_-(d)\rangle/N$, as a function of beam displacement, d, for (i) split and (ii) TEM$_{10}$ homodyne detection.

and can be approximated by

$$\langle \hat{n}_- \rangle_{d\ll w_0} = N\zeta_{0,d\ll w_0} \approx \sqrt{\frac{2}{\pi}}\frac{2Nd}{w_0} \tag{3.12}$$

As d approaches the waist size of the beam, w_0, the normalised difference photo-current begins to roll off and asymptotes to a constant for larger d. This can be easily understood, since for $d \gg w_0$ the beam is incident almost entirely on one side of the detector. In this regime, large beam displacements only cause small variations in $\langle \hat{n}_- \rangle$, making is difficult to determine the beam displacement precisely.

The noise of our displacement measurement, Δd_{SD}, is then related to the noise of the difference photo-current, $\Delta \hat{n}_-$, via

$$\Delta d_{\mathrm{SD}} = \frac{\partial d}{\partial \langle \hat{n}_- \rangle}\Delta \hat{n}_- \tag{3.13}$$

giving a sensitivity of

$$\mathcal{S}_{\mathrm{SD}} = \frac{1}{\Delta d_{\mathrm{SD}}} = \frac{\partial \langle \hat{n}_- \rangle}{\partial d}\frac{1}{\sqrt{N}} = \frac{\partial \zeta_0}{\partial d}\sqrt{N} \tag{3.14}$$

for a coherent state. This sensitivity is plotted as a function of displacement in Figure 3.4 (i). In the region of small displacement, we have

$$\mathcal{S}_{\mathrm{SD},d\ll w_0} \approx \sqrt{\frac{2}{\pi}}\frac{2\sqrt{N}}{w_0} \tag{3.15}$$

The efficiency of split detection for small displacement measurement is therefore given by the ratio

$$\epsilon_{\mathrm{SD}} = \frac{\mathcal{S}_{\mathrm{SD},d\ll w_0}}{\mathcal{S}_{\mathrm{QNL}}} = \sqrt{\frac{2}{\pi}} \sim 80\% \tag{3.16}$$

This $\sqrt{2/\pi}$ factor arises from the coefficient of the mode overlap integral, ζ_0, between

$v_0(x,d)$ and $u_0(x-d)$, as shown in Eq. (3.12). Fig. 3.4 (i) shows that the sensitivity of split detection decreases and asymptotes to zero for large displacement. The QNL in the figure confirms that split detection is not optimal for all displacement.

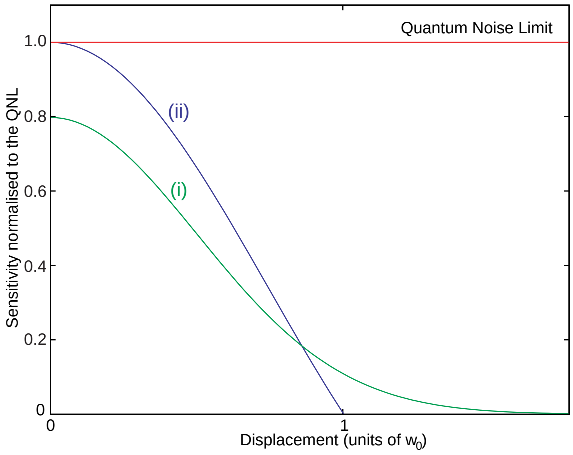

Figure 3.4: Sensitivity response of displacement measurement for (i) split and (ii) TEM$_{10}$ homodyne detection.

3.2.3 TEM$_{10}$ Homodyne Detection

Before proceeding with our proposal for an optimal small beam displacement measurement, let us express the displaced TEM$_{00}$ beam in terms of the centred Hermite-Gauss basis modes

$$u_n(x) = \left(\frac{2}{\pi w_0^2}\right)^{1/4} \frac{1}{\sqrt{n!2^n}} H_n\left(\frac{\sqrt{2}x}{w_0}\right) \exp\left[-\left(\frac{x}{w_0}\right)^2\right] \tag{3.17}$$

where $H_n\left(\frac{\sqrt{2}x}{w_0}\right)$ are the Hermite polynomials. The coefficients of the decomposed basis modes are given by

$$\frac{\alpha_n}{\sqrt{N}} = \int_{-\infty}^{\infty} u_0(x-d)u_n(x)dx = \frac{d^n}{w_0^n\sqrt{n!}} \exp\left[-\frac{d^2}{2w_0^2}\right] \tag{3.18}$$

Plots of these coefficients as a function of beam displacement are shown in Fig. 3.5. We notice that for small displacement only the TEM$_{00}$ and TEM$_{10}$ modes have significant non-zero coefficients [208]. This means that the TEM$_{10}$ mode initially contributes most to the displacement signal. For larger displacement, other higher order modes become significant as their coefficients increase. This suggests that an interferometric measurement of the displaced beam with a centred TEM$_{10}$ mode may be optimal in the small displacement regime.

Figure 3.6 shows the TEM$_{10}$ detection scheme considered in this chapter, the displaced beam is homodyned with a TEM$_{10}$ mode local oscillator. A reference axis for the displacement of the TEM$_{00}$ beam is defined by fixing the axis of the local oscillator. As can be seen from Fig. 3.5, when the input beam is centred, no power is contained in the TEM$_{10}$ mode. Due to the orthonomality of Hermite-Gauss modes, the TEM$_{10}$ local oscillator beam only detects the TEM$_{10}$ vacuum noise of the input beam. However we see from Fig. 3.5 that

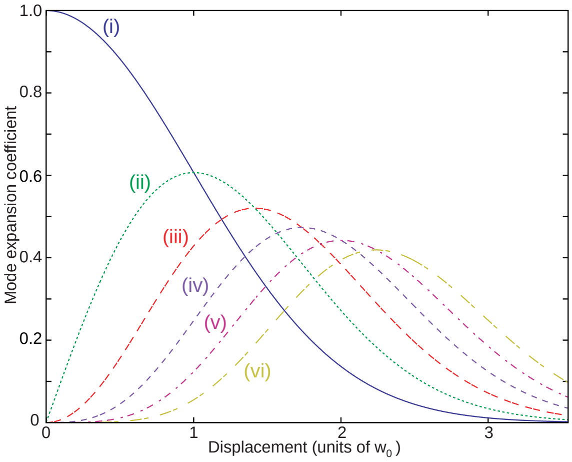

Figure 3.5: Coefficients of the decomposition of the displaced mode in terms of the TEM$_{n0}$ modes for the (i) TEM$_{00}$, (ii) TEM$_{10}$, (iii) TEM$_{20}$, (iv) TEM$_{30}$, (v) TEM$_{40}$ and (vi) TEM$_{50}$ mode components.

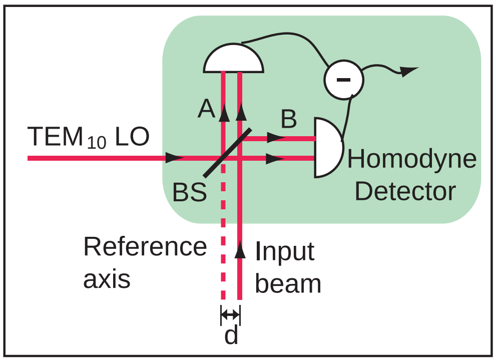

Figure 3.6: TEM$_{10}$ homodyne detection beam displacement measurement. BS: 50/50 beam-splitter, LO: local oscillator.

displacement of the TEM$_{00}$ input beam couples power into the (centred) TEM$_{10}$ mode. This coupled power interferes with the TEM$_{10}$ local oscillator, causing a change in the photo-current observed by the homodyne detector. Therefore, the homodyne detects a signal proportional to the displacement of the input beam.

The electric field operator describing the TEM$_{10}$ local oscillator beam is

$$\hat{\mathcal{E}}^{+}_{\rm LO} = \sqrt{\frac{\hbar\omega}{2\epsilon_0 L}}\left(\sqrt{N_{\rm LO}}\,u_1(x) + \sum_{n=0}^{\infty}\delta\hat{a}_n^{\rm LO}u_n(x)\right) \tag{3.19}$$

where the first bracketed term is the coherent amplitude, the second bracketed term denotes the quantum fluctuations of the beam, and $N_{\rm LO}$ is the number of photons in the local oscillator. Using this expression and that of the input displaced beam, the photon number operators corresponding to the two output beams of the beam-splitter are obtained, given by

$$\hat{n}_{A,B} = \frac{2\epsilon_0 L}{\hbar\omega}\int_{-\infty}^{\infty}(\hat{\mathcal{E}}^+_{A,B})^\dagger \hat{\mathcal{E}}^+_{A,B}dx \tag{3.20}$$

where subscripts $\{A, B\}$ denote the two output beams. From these, the difference photo-current between the two detectors used for homodyning is

$$\begin{aligned}\hat{n}_- &= \sqrt{N_{\mathrm{LO}}}(2\alpha_1 + \delta\hat{X}_1^+)\\ &= \sqrt{N_{\mathrm{LO}}}\left(\frac{2\sqrt{N}}{w_0}d + \delta\hat{X}_1^+\right)\end{aligned} \tag{3.21}$$

where $\delta\hat{X}_1^+ = \delta\hat{a}_1 + \delta\hat{a}_1^\dagger$ is the amplitude quadrature noise operator of the TEM$_{10}$ component of the input beam, and we have assumed that $N_{\mathrm{LO}} \gg N$.

The mean photo-current as a function of beam displacement is shown in Figure 3.3 (ii). For small displacement, the mean photo-current is linearly proportional to the beam displacement. The factor of proportionality, $2\sqrt{N}/w_0$, in this case is the same as that of the array detection scheme. Hence, this shows that the measurement is optimal. For larger displacement, the sensitivity decreases as the displacement increases. This is due to the power of the displaced beam being coupled to higher-ordered TEM$_{n0}$ modes (for $n > 1$) and thus less power is contained in the TEM$_{10}$ mode.

The sensitivity response for the TEM$_{10}$ detection, obtained in the same manner as that for split detection, is shown in Figure 3.4 (ii). In the small displacement regime, we obtain

$$\mathcal{S}_{H,d\ll w_0} = \frac{2\sqrt{N}}{w_0} \tag{3.22}$$

The efficiency of the TEM$_{10}$ detection is then

$$\epsilon_H = \frac{\mathcal{S}_{H,d\ll w_0}}{\mathcal{S}_{\mathrm{QNL}}} = 100\%. \tag{3.23}$$

3.3 Displacement measurement beyond the quantum noise limit

3.3.1 Split Detection with Squeezed Light

It has been shown that the noise measured by split detection is the flipped mode defined in Eq. (3.9) [203]. In order to improve the sensitivity of split detection, squeezing has to be introduced on the flipped mode. This method was demonstrated in the initial work of Treps *et al.* and the resulting spatial correlation between the two halves of the beam was termed *spatial squeezing* [204]. By applying a displacement modulation to the spatially squeezed beam, they demonstrated that sensitivities beyond the QNL could be achieved for beam displacement measurements. Treps *et al.* recently extended their one-dimensional spatial squeezing work to the two orthogonal transverse spatial axes [1, 205]. In this scenario, the photon correlation was measured between the set of top and bottom halves as well as left and right halves of a quadrant detector.

Restricting our analysis to one dimension, Fig. 3.7 (a) shows the detection of an input TEM$_{00}$ beam with a vacuum squeezed symmetric flipped mode $v(x, 0)$ as defined in Eq. (3.9). Loss-less combination of orthogonal spatial modes can be achieved in a number of ways. One example is the use of optical cavities for mixing resonant and non-resonant modes as illustrated in Fig. 3.7. The cavity reflects off the vacuum squeezed symmetric flipped mode whilst transmitting the TEM$_{00}$ beam. The total beam is then displaced and measured using a split-detector. The beam incident on the split detector is described by

$$\begin{aligned}\hat{\mathcal{E}}^+_{\rm in} &= i\sqrt{\frac{\hbar\omega}{2\epsilon_0 L}}\Big(\sqrt{N}u_0(x-d) + \delta\hat{c}_0^{\rm sqz} v_0(x-d,0) \\ &\quad + \sum_{n=1}^{\infty} \delta\hat{c}_n v_n(x-d,0)\Big) \end{aligned} \tag{3.24}$$

where the first term arises from the TEM$_{00}$ mode while the second term describes the vacuum squeezed flipped mode and the last term in Eq. (3.24) represents all other higher order vacuum noise terms. The photo-current difference operator in the limit of small displacement is

$$\hat{n}_- = \sqrt{N}\left(\sqrt{\frac{2}{\pi}}\frac{2\sqrt{N}}{w_0}d + \delta\hat{Z}^+_{0,\rm sqz}\xi_0 + \sum_{n=1}^{\infty}\delta\hat{Z}^+_n\xi_n\right) \tag{3.25}$$

where $\delta\hat{Z}^+_n = \delta\hat{c}_n + \delta\hat{c}^\dagger_n$ are the amplitude quadrature operators. The first bracketed term arises from the mode overlap between the $v_0(x,0)$ and $u_0(x-d)$ modes, which has a value of $\sqrt{2/\pi}$. The second term originates from the mode overlap between the $v_0(x,d)$ and $v_0(x-d,0)$ modes. The last term is a result of the overlap between the $v_0(x,d)$ and $v_n(x-d,0)$ modes. The overlap coefficients are given by $\xi_n = \int_{-\infty}^{\infty} v_0(x,d)v_n(x-d,0)dx$.

Figure 3.8 (i) plots the sensitivity, $\mathcal{S}_{\rm SD}$, as a function of squeezing. Notice that the QNL can only be surpassed with more than 1.9 dB of squeezing. This is a direct consequence of the intrinsic inefficiency of displacement measurement using split detection.

3.3.2 TEM$_{10}$ Homodyne Detection with Squeezed Light

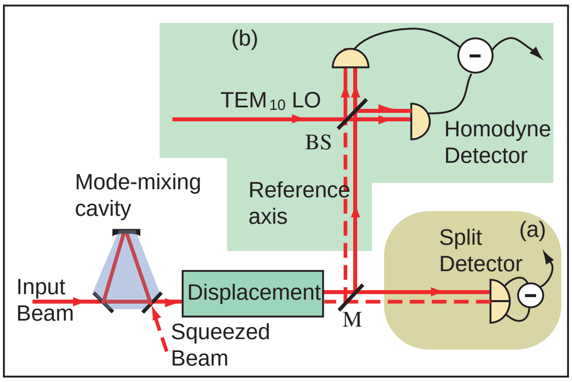

Figure 3.7: Measurement options: (a) Split detection with a vacuum squeezed symmetric flipped mode or (b) TEM$_{10}$ homodyne detection with a vacuum squeezed TEM$_{10}$ mode. Both schemes combine the squeezed beam and the TEM$_{00}$ input beam loss-lessly using an optical cavity. M: mirror, BS: 50/50 beam-splitter, LO: local oscillator.

We have shown that by squeezing the flipped mode and detecting the beam displacement using a split detector, one is able to improve on the displacement sensitivity to beyond the QNL. Correspondingly, we now consider the effect of squeezing the TEM$_{10}$ mode of the detected beam in our homodyne detection. Figure 3.7 shows the combination

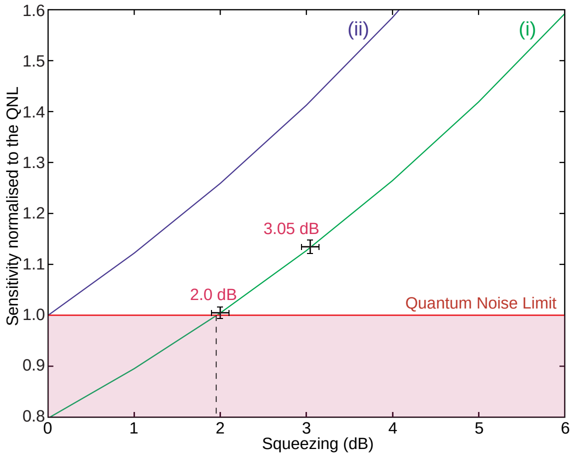

Figure 3.8: Plots of sensitivity, $\mathcal{S}$, for small displacement, as a function of squeezing for (i) split and (ii) TEM_{10} homodyne detection. Shading indicates the region where displacement measurement is below the QNL. The data points were obtained from Ref. [1].

of the TEM_{00} input beam with a vacuum squeezed TEM_{10} beam prior to displacement. The displaced beam is then analysed using homodyne detection with a bright TEM_{10} local oscillator beam as discussed previously (see Fig. 3.7 (b)). The detected beam is given by

$$\begin{aligned}\hat{\mathcal{E}}^{+}_{\mathrm{in}} &= i\sqrt{\frac{\hbar\omega}{2\epsilon_0 L}}\Big(\sqrt{N}u_0(x-d)+\delta\hat{a}_1^{\mathrm{sqz}}u_1(x-d)\\ &\quad +\sum_{n\neq 1}^{\infty}\delta\hat{a}_n u_n(x-d)\Big) \qquad (3.26)\end{aligned}$$

where the first term arises from the TEM_{00} mode, the second term from the squeezed vacuum TEM_{10} mode, and the last term from higher ordered vacuum noise. The difference photo-current between the two detectors used for homodyning is given by

$$\hat{n}_- = \sqrt{N_{LO}}\Big(\frac{2\sqrt{N}}{w_0}d+\delta\hat{X}^{+}_{1,\mathrm{sqz}}\chi_1+\sum_{n\neq 1}^{\infty}\delta\hat{X}^{+}_n\chi_n\Big) \qquad (3.27)$$

where $\chi_n = \int_{-\infty}^{\infty}u_1(x)u_n(x-d)dx$. For small displacement, the overlap between the vacuum squeezed mode and the local oscillator beam is $\sim 100\%$ whilst the last term is negligible.

The sensitivity, $\mathcal{S}_{\mathcal{H}}$, as a function of squeezing on the TEM_{10} mode is shown in Fig. 3.8 (ii). Since the scheme is optimum for small displacement, any amount of squeezing will lead to a sensitivity beyond the QNL. Furthermore, the TEM_{10} detection surpasses the performance of split detection for all values of squeezing.

3.3.3 Discussion

In the paper on quantum displacement measurement by Treps *et al.* [1], displacement measurements of the two transverse axes were performed using split detection with two co-propagating squeezed beams. The squeezing values were 2.0 dB and 3.05 dB for the vertical and horizontal displacement measurement, respectively. Relating this result back to our analysis, we find that the displacement measurements performed were indeed beyond the QNL. These corresponded to sensitivities of 100.5% and 113.0% of the QNL as shown in Fig. 3.8. However, using the same squeezed beams but adopting the TEM_{10} homodyne detection, sensitivities of 126% and 141.5% above the QNL would be achievable.

The TEM_{10} homodyne detection can be extended to perform beam displacement measurements in both transverse dimensions. The TEM_{10} mode component is responsible for beam displacement in one transverse axis. Thus, by symmetry, the TEM_{01} mode component is responsible for beam displacement in the orthogonal transverse axis. Correspondingly, beam displacement measurement in the horizontal or vertical transverse axis can be achieved by adapting the mode-shape of the local oscillator beam to either TEM_{10} or TEM_{01}. To perform optimum larger beam displacement measurements, the local oscillator of the TEM_{10} homodyne detection can be modified by including higher order components of the TEM_{00} displaced beam. Similarly, the homodyning scheme can be extended to measuring displacements of arbitrary mode-shapes assuming *a priori* knowledge of the beam shape.

3.4 Conclusion and future directions

3.4.1 Conclusion

By defining the beam position as the mean photon position of a light beam, optical beam displacement can be measured with reference to a fixed axis. Using an idealised array detection scheme, we derived the QNL associated with optical displacement measurements. A displaced TEM_{00} beam can be decomposed into an infinite series of Hermite-Gauss modes but in the limit of small displacement, only the TEM_{00} and TEM_{10} components are non-negligible. Since the split detector effectively measures the noise of an optical flipped mode [203], it is only $\sim 80\%$ efficient when used to measure the displacement of a TEM_{00} beam. We have proposed an optimum displacement measurement scheme based on homodyne detection. By using a TEM_{10} local oscillator, small displacement signals can be extracted with 100% efficiency. We showed that in this small displacement regime the TEM_{10} homodyne detection performs at the QNL, and is significantly more efficient than split detection.

We have also shown that by mixing the input beam with a squeezed beam in the appropriate mode, we can significantly improve the sensitivity of the TEM_{10} homodyne detection. We compared the sensitivities of both split and TEM_{10} homodyne detection for equal values of squeezing and found that for small displacements the TEM_{10} detection outperforms split detection for all values of squeezing. For split detection, more than 1.9 dB of squeezing is required to achieve a sensitivity beyond the QNL. Whilst for the TEM_{10} detection any amount of squeezing will suffice.

An experimental demonstration of the optimality of the TEM_{10} homodyne detection scheme was published in Refs. [2, 3].

3.4.2 Future directions

The orbital angular momentum, l, of an optical beam is given by the LG_{0l} mode [209]. Therefore, one could improve the sensitivity of rotation measurements by squeezing the light in the LG_{0l} mode. Our spatial homodyne scheme could be used, with a local oscillator in the LG_{0l} mode-shape, for the optimal detection of the rotation signal. An analysis of the orbital angular momentum signal modes for arbitrary mode-shapes should be performed.

Chapter 4

Spatial entanglement

Spukhafte Fernwirkung . . .

- Albert Einstein

Quantum mechanics is strange. The Copenhagen interpretation [210] of quantum mechanics, proposed by Niels Bohr and Werner Heisenberg, ascribes a wave-function to the possible outcomes of a system. Based on this, the actual outcome is purely probabilistic and non-deterministic. A result of the Copenhagen interpretation is the *Complementary Principle* [211], where an object can have simultaneous particle and wave properties. The famous double-slit experiment yielded results which seemed contradictory, depending on the observation process.

The notion that an outcome is non-deterministic disturbed Einstein deeply and he has been quoted stating that, “God does not play dice with the universe” [212]. The issue of non-realism (non-hidden variables) and non-locality (faster than light) for separate component systems disturbed Einstein greatly. Einstein did not believe that separate component systems could ‘communicate’ instantaneously across relativistic separations to be affected by an observation process on one local system. This quantum entanglement effect he termed, “spooky action at a distance” [213]. To counter the strange concepts of the Copenhagen interpretation of quantum mechanics, Einstein, Podolsky and Rosen proposed the *EPR Paradox* [10] to show that quantum theory is incomplete. Einstein argued that quantum theory provides an incomplete characterisation of a system and this has led to the possibility of realism or a “hidden-variables” theory.

In 1964, John Bell proposed a test for locality (not faster than light) and realism (hidden variables). He assumed that a system has definite values which are not influenced by the observation and that information travels at the relativistic limit. This resulted in *Bell’s inequality* [214]. Following Bell’s proposal, many experiments have been conducted and they have all thus far demonstrated a violation of *Bell’s inequality.* The most notable experiments to date are those by Freedman and Clauser [215] and Aspect *et al.* [15, 14, 16]. A result of Bell’s inequality is that a physical theory that satisfies locality and realism cannot be correct. Quantum mechanics is non-local, in the Schrödinger picture, whilst non-realistic, in the Heisenberg picture. However, there also exists a non-local realistic theory by Bohm [216], which can reproduce all the predictions of quantum mechanics [217].

The early experiments that were conducted to demonstrate quantum entanglement were performed with single particles. More recently, the question of whether it is possible to generate entanglement for ensembles of particles has been explored. This has led to some very impressive proposals and experimental demonstrations of continuous-variable quadrature amplitude entanglement [17, 41, 218, 219, 18], polarisation entanglement [124, 220, 221], atomic spin entanglement [129, 130, 222, 132, 133] and atom spin-optical polarisation entanglement [223, 134, 135, 106].

In this chapter, we focus our attention to entanglement of ensembles of photons. Quadrature entanglement and polarisation Stokes entanglement are various manifestations of entanglement in the continuous-variable regime. A natural pertinent question which arises is, "What is the equivalent form of entanglement in the mechanical degree of freedom (i.e. the spatial variable)?". We approach this problem by taking concepts familiar to the single particle regime - position and momentum, and extend it to the continuous-variable regime. Beam displacement (position) and tilt (momentum) have been analysed classically, in terms of modal decompositions of a beam [208]. We extend this analysis by quantising the field operators used to describe the displaced and tilted beam and therefore can identify the "noise modes" relevant to beam position and momentum. We show that these quantities are conjugate observables which satisfy the Heisenberg commutation relations. Therefore, by combining squeezed light in appropriate spatial modes, position-momentum entanglement can be generated for continuous-wave optical beams. Position-momentum entanglement and quadrature entanglement are also shown to be directly equivalent to each other.

Finally a natural question to arise is that relevant to the SU(2) group symmetry properties of polarisation Stokes entanglement - "What is the equivalent of Stokes-operator entanglement for the spatial basis?". In this chapter, we identify the modes which span the Poincaré sphere completely. Therefore, spatial Stokes operators based on the photon annihilation and creation operators in the appropriate modes can be defined. Since the spatial Stokes operators obey the cyclic commutation relation, spatial Stokes entanglement between modes can be generated.

The work in this chapter has been published in

- M. T. L. Hsu, W. P. Bowen, N. Treps, and P. K. Lam, "Continuous-variable spatial entanglement for bright optical beams", Physical Review A **72**, 013802 (2005).

4.1 Introduction

The concept of entanglement was first proposed by Einstein, Podolsky and Rosen in a seminal paper in 1935 [10]. The original Einstein-Podolsky-Rosen (EPR) entanglement, as discussed in the paper, involved the position and momentum of a pair of particles. In this chapter, we draw an analogy between the original EPR entanglement and the position and momentum (x-p) entanglement of bright optical beams.

Entanglement has been reported in various manifestations. For continuous wave (CW) optical beams, these include, quadrature [18, 17] and polarisation [124] entanglement. Spatial forms of entanglement, although well studied in the single photon regime, have not been studied significantly in the continuous wave regime. Such forms of entanglement are interesting as they span a potentially infinite Hilbert space. Spatial EPR entanglement [140] has wide-ranging applications from two-photon quantum imaging [224, 225] to holographic teleportation [226, 144] and interferometric faint phase object quantum imaging [227].

Current studies are focused on x-p entanglement for the few photons regime. Howell *et al.* [147] observed near and far-field quantum correlation, corresponding to the position and momentum observables of photon pairs. Gatti *et al.* [139] have also discussed the spatial EPR aspects in the photons pairs emitted from an optical parametric oscillator below threshold. Other forms of spatial entanglement which are related to image correlation have also been investigated. A scheme to produce spatially entangled images between the signal and idler fields from an optical parametric amplifier has been proposed by Gatti *et al.* [53, 138, 54]. Their work was extended to the macroscopic domain by observing the spatial correlation between the detected signal and idler intensities, generated via the parametric down conversion process [55].

Our proposal considers the possibility of entangling the position and momentum of a free propagating beam of light, as opposed to the entanglement of local areas of images, considered in previous proposals. Our scheme is based on the concept of position squeezed beams where we have shown that we have to squeeze the transverse mode corresponding to the first order derivative of the mean field in order to generate the position squeezed beam [149]. Similarly to the generation of quadrature entangled beams, the position squeezed beams are combined on a beam-splitter to generate x-p entangled beams. We also propose to generate spatial entanglement for split detection, utilising spatial squeezed beams reported by Treps *et al.* [204, 1, 205]. This form of spatial entanglement has applications in quantum imaging systems.

By considering the relevant modal decomposition of displaced and tilted fields, we arrive at general expressions for the position and momentum of an optical beam. We then limit ourselves to the regime of small displacements and tilts. This is the relevant regime for observing quantum optical phenomena, since for large displacements (tilts) the overlap between displaced (tilted) and non-displaced (non-tilted) beams approaches zero and hence they become perfectly distinguishable even in a classical sense. Applying this restriction, we show that as expected the position and momentum of an optical field are Fourier transform related. We then consider the specific case of a beam with TEM_{00} mode-shape. TEM_{00} beams have the unique feature of satisfying the position-momentum uncertainty relation in the equality, and therefore represent an ideal starting point for the generation of spatial entanglement. We explicitly show that the position and momentum observables derived in this chapter for a TEM_{00} beam are conjugate observables which obey the Heisenberg commutation relation. We then propose a scheme to produce x-p entanglement for TEM_{00} optical beams.

4.2 Position-Momentum Entanglement

4.2.1 Definitions - Classical Treatment

Let us consider an optical beam with x- and y- symmetric transverse intensity profile propagating along the z-axis. Since the axes of symmetries remain well defined during propagation, we can relate the beam position relative to these axes. To simplify our analysis we henceforth assume without loss of generality, a one-dimensional beam displacement, d, from the reference x-axis (see Fig. 4.1(a)). We denote the electric field profile of the beam by $E(x)$. For a displaced beam, the electric field profile is given by

$$E_d(x) = E(x) + d\frac{\partial E(x)}{\partial x} + \frac{d^2}{2}\frac{\partial^2 E(x)}{\partial x^2} + \cdots \tag{4.1}$$

In the regime where displacement is much smaller than the beam size, we can utilise the linearised approximation where only the zeroth and first order terms are significant. We

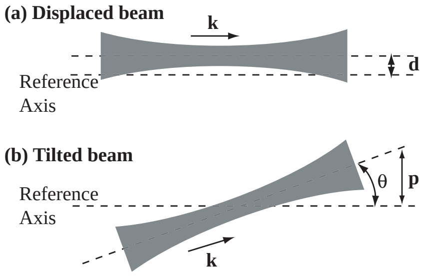

Figure 4.1: (a) Beam displacement d, and (b) beam tilt by angle θ, from a reference axis.

see from this expression that the zeroth order term is not dependent on d, and that the displacement is directly proportional to the derivative of the field amplitude $\partial E(x)/\partial x$ [149].

The transverse beam momentum p on the other hand, can be obtained from the transverse component of the wave-number of the beam, $p = k \sin\theta$, where $k = 2\pi/\lambda$ and the beam tilt is θ. This beam tilt is defined with respect to a pivot point at the beam waist, as shown in Fig. 4.1(b).

The electric field profile for a tilted beam with un-tilted electric field profile $E(x)$ and wavelength λ is given by

$$E_\theta(x) = \exp\left[\frac{i2\pi x \sin\theta}{\lambda}\right] E(x\cos\theta) \tag{4.2}$$

We can again simplify Eq. (4.2) by taking the zeroth and first order Taylor expansion terms to get a transverse beam momentum of $p \simeq k\theta$. In the case of small displacement or tilt, we therefore obtain a pair of equations

$$E_d(x) \approx E(x) + d \; \frac{\partial E(x)}{\partial x} \tag{4.3}$$
$$E_p(x) \approx E(x) + p \; ixE(x) \tag{4.4}$$

Eqs. (4.3) and (4.4) give the field parameters that relate to the displacement and tilt of a beam. For freely propagating optical modes, the Fourier transform of the derivative of the electric field, $\mathcal{F}(\partial E(x)/\partial x)$, is of the form $ixE(x)$. Hence, the Fourier transform of displacement is tilt.

In the case of a single photon, the position and momentum are defined by considering the spatial probability density of the photon, given by $|E(x)|^2/I$, where $I = \int |E(x)|^2 dx$ is the normalisation factor. The mean position obtained from an ensemble of measurements on single photons is then given by $\langle x\rangle = \frac{1}{I}\int x|E(x)|^2 dx$. The momentum of the photon is given from the spatial probability density of the photon in the far-field, or equivalently by taking the Fourier transform of the spatial probability density of the photon. These definitions are consistent with our definitions of position and momentum for bright optical modes.

4.2.2 TEM$_{pq}$ Basis

In theory, spatial entanglement can be generated for fields with any arbitrary transverse mode-shape. However, as with other forms of continuous-variable entanglement, the efficacy of protocols to generate entanglement is highest if the initial states are minimum uncertainty. For position and momentum variables, the minimum uncertainty states are those which satisfy the Heisenberg uncertainty relation $\Delta\hat{x}\Delta\hat{p} \geq \hbar/2$, in the equality. This equality is only satisfied by states with Gaussian transverse distributions [228], therefore we limit our analysis to that of TEM$_{00}$ modes.

A field of frequency ω can be represented by the positive frequency part of the mean electric field $\mathcal{E}^{+}e^{i\omega t}$. We are interested in the transverse information of the beam, described fully by the slowly varying field envelope $\mathcal{E}^{+}$. We express this field in terms of the TEM$_{pq}$ modes. For a measurement performed in an exposure time T, the mean field for a displaced TEM$_{00}$ beam can be written as

$$\mathcal{E}_d^{+}(x) = i\sqrt{\frac{\hbar\omega}{2\epsilon_0 V}}\sqrt{N}\Big(u_0(x) + \frac{d}{w_0}u_1(x)\Big) \tag{4.5}$$

where the first term indicates that the power of the displaced beam is in the TEM$_{00}$ mode while the second term gives the displacement signal contained in the amplitude of the TEM$_{10}$ mode component. The corresponding mean field for a tilted TEM$_{00}$ beam can be written as

$$\mathcal{E}_p^{+}(x) = i\sqrt{\frac{\hbar\omega}{2\epsilon_0 V}}\sqrt{N}\Big(u_0(x) + \frac{iw_0 p}{2}u_1(x)\Big) \tag{4.6}$$

where the second term describes the beam momentum signal, contained in the $\pi/2$ phase-shifted TEM$_{10}$ mode component.

4.2.3 Definitions - Quantum Treatment

We now introduce a quantum mechanical representation of the beam by taking into account the quantum noise of optical modes. We can write the positive frequency part of the electric field operator in terms of photon annihilation operators $\hat{a}$. The field operator is given by

$$\hat{\mathcal{E}}_{\text{in}}^{+} = i\sqrt{\frac{\hbar\omega}{2\epsilon_0 V}}\sum_{n=0}^{\infty}\hat{a}_n u_n(x) \tag{4.7}$$

where $u_n(x)$ are the transverse beam amplitude functions for the TEM$_{pq}$ modes and $\hat{a}_n$ are the corresponding annihilation operators. $\hat{a}_n$ is normally written in the form of $\hat{a}_n = \langle\hat{a}_n\rangle + \delta\hat{a}_n$, where $\langle\hat{a}_n\rangle$ describes the coherent amplitude part and $\delta\hat{a}_n$ is the quantum noise operator.

In the small displacement and tilt regime, the TEM$_{00}$ and TEM$_{10}$ modes are the most significant [149], with the TEM$_{10}$ mode contributing to the displacement and tilt signals. We can rewrite the electric field operator for mean number of photons N as

$$\begin{aligned}\hat{\mathcal{E}}_{in}^{+} &= i\sqrt{\frac{\hbar\omega}{2\epsilon_0 V}}\Big(\sqrt{N}u_0(x) + \frac{\delta\hat{X}_{a0}^{+} + i\delta\hat{X}_{a0}^{-}}{2}u_0(x)\\ &\quad + \sum_{n=1}^{\infty}\Big(\frac{\hat{X}_{a_i}^{+} + i\hat{X}_{a_i}^{-}}{2}\Big)u_i(x)\Big)\end{aligned} \tag{4.8}$$

where the annihilation operator is now written in terms of the amplitude $\hat{X}_a^+$ and phase $\hat{X}_a^-$ quadrature operators.

The displacement and tilt of a TEM$_{00}$ beam is given by the amplitude and phase of the $u_1(x)$ mode in Eqs. (4.5) and (4.6), respectively. We can, therefore, write the beam position and momentum operators, respectively, as

$$\hat{x} = \frac{w_0}{2\sqrt{N}}\hat{X}_{a_1}^+ \tag{4.9}$$

$$\hat{p} = \frac{1}{w_0\sqrt{N}}\hat{X}_{a_1}^- \tag{4.10}$$

4.2.4 Commutation Relation

Two observables corresponding to the position and momentum of a TEM$_{00}$ beam have been defined. We have shown that the position and momentum observables correspond to near- and far-field measurements of the beam, respectively. Hence, we expect from Eqs. (4.9) and (4.10), that the position and momentum observables do not commute. Indeed, the commutation relation between the two quadratures of the TEM$_{10}$ mode is $[\hat{X}_{a_1}^+, \hat{X}_{a_1}^-] = 2i$. This leads to the commutation relation between the position and momentum observables of an optical beam with N photons

$$[\hat{x}, \hat{p}] = \frac{i}{N} \tag{4.11}$$

This commutation relation is similar to the position-momentum commutation relation for a single photon, aside from the $1/N$ factor. The $1/N$ factor is related to the precision with which one can measure beam position and momentum. Rewriting the Heisenberg inequality using the commutation relation, gives

$$\Delta^2\hat{x}\Delta^2\hat{p} \geq \frac{1}{4N}. \tag{4.12}$$

The position measurement of a coherent optical beam gives a signal which scales with N. The associated quantum noise of the position measurement scales with $\sqrt{N}$. Hence the positioning sensitivity of a coherent beam scales as $\sqrt{N}$ [149, 204]. The same consideration applied to the sensitivity of beam momentum measurement shows an equivalent dependence of $\sqrt{N}$. This validates the factor of N in the Heisenberg inequality and the commutation relation for a CW optical beam.

As an aside, it is interesting to consider the implications of the Heisenberg inequality of Eq. (4.12) on recent discussions of ghost imaging in discrete variable quantum optics [142, 146, 145, 141]. In ghost imaging, the spatial resolution of an imaging system is enhanced using a pair of correlated fields. One field passes through the object, and object information is then retrieved through spatially resolved photon coincidences between the two fields. At first glance, the results of Bennink *et al.* [142, 146], and Gatti *et al.* [145] appear contradictory. According to Bennink *et al.* the position-momentum uncertainty relation sets an ultimate resolution limit which can only be surpassed using entangled fields; while Gatti *et al.* show that thermal fields can achieve the same resolution as entangled fields for large N. We see from Eq. (4.12) that these statements are not mutually incompatible. For small N the position and momentum of the beams, and therefore also the imaging resolution, are highly uncertain; however as N becomes large the uncertainty product $\Delta^2\hat{x}\Delta^2\hat{p}$ approaches zero, so that even without quantum resources x and p can be known simultaneously with arbitrary precision.

4.2.5 Entanglement Scheme

We have shown that the position and momentum observables of CW TEM$_{00}$ optical beams satisfy the Heisenberg commutation relation. Consequently, EPR entanglement for the position and momentum of TEM$_{00}$ beams is possible. Experimentally, the usual quadrature entanglement is generated by mixing two amplitude squeezed beams on a 50:50 beamsplitter (see Chapter 2). The same idea can be applied to generate EPR x-p entanglement, by using position squeezed beams [149]. Our scheme to produce x-p entanglement between two CW TEM$_{00}$ optical beams is shown in Figure 4.2. The position squeezed beams in Fig. 4.2 (a) and (b) are generated via the in-phase combination of a vacuum squeezed TEM$_{10}$ beam with a coherent TEM$_{00}$ beam. Such beam combination can be achieved experimentally, for example using an optical cavity or a beam-splitter [205]. The result of the combination is a position squeezed beam. To generate entanglement, we consider beams with zero mean position and momentum, but we are interested in the quantum noise of the position and momentum of the beam. With this assumption, the electric field operators for the two input beams at the beam-splitter are given by

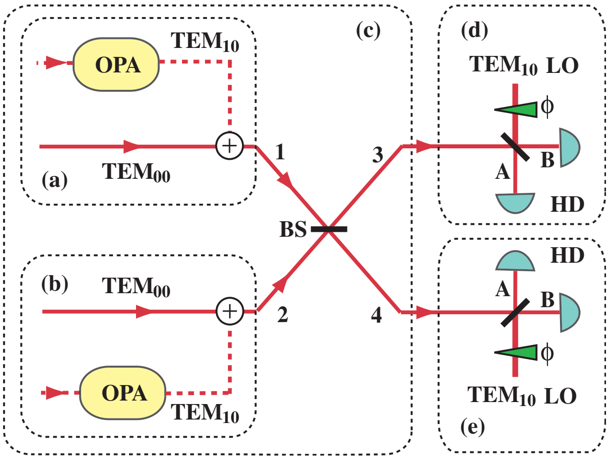

Figure 4.2: Scheme for generating position-momentum entanglement for continuous wave TEM$_{00}$ optical beams. OPA: optical parametric amplifiers for the generation of squeezed light, BS: 50:50 beam-splitter, HD: homodyne detectors, LO: local oscillator beams, ϕ: phase of local oscillator beam.

$$\hat{\mathcal{E}}_1^+ = i\sqrt{\frac{\hbar\omega}{2\epsilon_0 V}}\Big(\sqrt{N}u_0(x) + \sum_{n=0}^{\infty}\delta\hat{a}_n u_n(x)\Big) \tag{4.13}$$

$$\hat{\mathcal{E}}_2^+ = i\sqrt{\frac{\hbar\omega}{2\epsilon_0 V}}\Big(\sqrt{N}u_0(x) + \sum_{n=0}^{\infty}\delta\hat{b}_n u_n(x)\Big) \tag{4.14}$$

where in both equations, the first bracketed term describes the coherent amplitude of the TEM$_{00}$ beam. The second bracketed terms describe the quantum fluctuations present in all modes. For position squeezed states, only the TEM$_{10}$ mode is occupied by a vacuum squeezed mode. All other modes are occupied by vacuum fluctuations. It is also assumed that the number of photons in each of the two beams, during the measurement window, is equal to N. The two position squeezed beams (1,2) are combined, with a $\pi/2$ phase difference, on a 50:50 beam-splitter (BS) in as shown in Fig. 4.2 (c).

The usual input-output relations of a beam-splitter apply. The electric field operators describing the two output fields from the beam-splitter are given by $\hat{\mathcal{E}}_3 = (\hat{\mathcal{E}}_1 + \hat{\mathcal{E}}_2)/\sqrt{2}$ and $\hat{\mathcal{E}}_4 = (\hat{\mathcal{E}}_1 - \hat{\mathcal{E}}_2)/\sqrt{2}$. To demonstrate the existence of entanglement, we seek for quantum correlation and anti-correlation between the position and momentum quantum noise operators. The position operator corresponding to beams 3 and 4 are given respectively by

$$\begin{aligned} \delta\hat{x}_3 &= \frac{w_0}{2\sqrt{2}\sqrt{N}}\Big(\delta\hat{X}^+_{a_1} + \delta\hat{X}^-_{b_1}\Big) \\ &= \frac{1}{\sqrt{2}}\Big(\delta\hat{x}_a + \frac{w_0^2}{2}\delta\hat{p}_b\Big) \qquad (4.15) \\ \delta\hat{x}_4 &= \frac{w_0}{2\sqrt{2}\sqrt{N}}\Big(\delta\hat{X}^+_{a_1} - \delta\hat{X}^-_{b_1}\Big) \\ &= \frac{1}{\sqrt{2}}\Big(\delta\hat{x}_a - \frac{w_0^2}{2}\delta\hat{p}_b\Big) \qquad (4.16) \end{aligned}$$

The momentum operator corresponding to the photo-current difference for beams 3 and 4 are given by

$$\begin{aligned} \delta\hat{p}_3 &= \frac{1}{w_0\sqrt{2\sqrt{N}}}\Big(\delta\hat{X}^-_{a_1} + \delta\hat{X}^+_{b_1}\Big) \\ &= \frac{1}{\sqrt{2}}\Big(\delta\hat{p}_a + \frac{2}{w_0^2}\delta\hat{x}_b\Big) \qquad (4.17) \\ \delta\hat{p}_4 &= \frac{1}{w_0\sqrt{2\sqrt{N}}}\Big(\delta\hat{X}^-_{a_1} - \delta\hat{X}^+_{b_1}\Big) \\ &= \frac{1}{\sqrt{2}}\Big(\delta\hat{p}_a - \frac{2}{w_0^2}\delta\hat{x}_b\Big) \qquad (4.18) \end{aligned}$$

In our case where the two input beams are position squeezed, the sign difference between the position noise operators in Eqs. (4.15) and (4.16) as well as that between the momentum noise operators in Eqs. (4.17) and (4.18) are signatures of correlation and anti-correlation for $\delta\hat{x}$ and $\delta\hat{p}$.

Many criterions exist to characterise entanglement, for example the *inseparability criterion* [229] and the *EPR criterion* [230]. We have adopted the *inseparability criterion* to characterise position-momentum entanglement. For states with Gaussian noise statistics, Duan *et al.* [229] have shown that the *inseparability criterion* is a necessary and sufficient criterion for entanglement.

4.2.6 Covariance matrix and the Inseparability Criterion

We now derive the generalised form of the inseparability criterion (i.e. the product form). Gaussian states can be fully characterised using a covariance matrix. We define a covariance matrix using the photon annihilation and creation operators, given by [190]

$$C(\hat{a}, \hat{a}^\dagger) = \begin{pmatrix} \langle \hat{a}^2\rangle - \langle \hat{a}\rangle^2 & \frac{1}{2}\langle \hat{a}\hat{a}^\dagger + \hat{a}^\dagger\hat{a}\rangle - \langle \hat{a}^\dagger\rangle\langle \hat{a}\rangle \\ \frac{1}{2}\langle \hat{a}\hat{a}^\dagger + \hat{a}^\dagger\hat{a}\rangle - \langle \hat{a}^\dagger\rangle\langle \hat{a}\rangle & \langle (\hat{a}^\dagger)^2\rangle - \langle \hat{a}^\dagger\rangle^2 \end{pmatrix} \qquad (4.19)$$

The covariance matrix can be written in terms of the amplitude and phase quadrature operators, given by

$$C(\hat{X}^+, \hat{X}^-) = \begin{pmatrix} C^{++} & C^{+-} \\ C^{-+} & C^{--} \end{pmatrix} \tag{4.20}$$

where $C^{pq} = \frac{1}{2}\langle \hat{X}^p \hat{X}^q + \hat{X}^q \hat{X}^p \rangle - \langle \hat{X}^p \rangle \langle \hat{X}^q \rangle$ and $p, q \in \{+, -\}$. This equation shows that measurements of the amplitude and phase quadratures are sufficient to completely characterise a Gaussian state.

For a two-mode system, the covariance matrix for the amplitude and phase quadrature operators, is given by [192]

$$C(\hat{X}_a^\pm, \hat{X}_b^\pm) = \begin{pmatrix} C_{aa}^{++} & C_{aa}^{+-} & C_{ab}^{++} & C_{ab}^{+-} \\ C_{aa}^{-+} & C_{aa}^{--} & C_{ab}^{-+} & C_{ab}^{--} \\ C_{ba}^{++} & C_{ba}^{+-} & C_{bb}^{++} & C_{bb}^{+-} \\ C_{ba}^{-+} & C_{ba}^{--} & C_{bb}^{-+} & C_{bb}^{--} \end{pmatrix} \tag{4.21}$$

where the matrix coefficients are given by

$$\begin{aligned} C_{ab}^{pq} &= \frac{1}{2}\langle \hat{X}_a^p \hat{X}_b^q + \hat{X}_b^q \hat{X}_a^p \rangle - \langle \hat{X}_a^p \rangle \langle \hat{X}_b^q \rangle & (4.22) \\ &= \frac{1}{2}\langle \hat{X}_a^p \hat{X}_b^q + \hat{X}_b^q \hat{X}_a^p \rangle & (4.23) \end{aligned}$$

where we have assumed that the two-beam system have no coherent amplitude. We now make the assumption that the two beams labelled by a and b have identical variances and are not cross-quadrature correlated, with the covariance matrix given by

$$C(\hat{X}_a^\pm, \hat{X}_b^\pm) = \begin{pmatrix} C_{aa}^{++} & 0 & C_{ab}^{++} & 0 \\ 0 & C_{aa}^{--} & 0 & C_{ab}^{--} \\ C_{ba}^{++} & 0 & C_{bb}^{++} & 0 \\ 0 & C_{ba}^{--} & 0 & C_{bb}^{--} \end{pmatrix} \tag{4.24}$$

where by symmetry $C_{ab}^{\pm\pm} = C_{ba}^{\pm\pm}$ and $C_{aa}^{\pm\pm} = C_{bb}^{\pm\pm}$. Duan *et al.* [229], have shown that any Gaussian state can be transformed through local unitary Bogoliubov operations into a standard form described by the covariance matrix in Eq. (4.24), with the following conditions

$$\begin{aligned} \frac{C_{aa}^{++} - 1}{C_{bb}^{++} - 1} &= \frac{C_{aa}^{--} - 1}{C_{bb}^{--} - 1} & (4.25) \\ \sqrt{(C_{aa}^{--} - 1)(C_{bb}^{--} - 1)} + |C_{ab}^{++}| &= \sqrt{(C_{aa}^{++} - 1)(C_{bb}^{++} - 1)} + |C_{ab}^{--}| & (4.26) \end{aligned}$$

Duan *et al.* [229] derived the *inseparability criterion*, where any separable quantum state $\rho = \sum_i p_i \rho_{i1} \otimes \rho_{i2}$ satisfies

$$\langle (\hat{X}_I^+)^2 \rangle + \langle (\hat{X}_I^-)^2 \rangle \geq 2\left(g^2 + \frac{1}{g^2}\right) \tag{4.27}$$

where g is a gain factor and

$$\langle (\hat{X}_I^\pm)^2 \rangle = \left\langle \left(g\hat{X}_a^\pm - \frac{1}{g} \frac{C_{ab}^{\pm\pm}}{|C_{ab}^{\pm\pm}|} \hat{X}_b^\pm \right)^2 \right\rangle \tag{4.28}$$

where the factor of 2 in Eq. (4.27), arises due to the use of the amplitude and phase quadrature operators, which satisfy the commutation relation $[\hat{X}^+, \hat{X}^-] = 2i$.

Duan *et al.* [229] showed that any Gaussian state which satisfies the inequality of Eq. (4.27) is a state with a P-function with positive values (i.e. a classical state). Therefore the inseparability criterion is a sufficient and necessary condition for separability for all Gaussian states. A violation of the inequality shows that the state is entangled.

We now proceed to derive the *inseparability criterion* to a more general form, the product form. The expansion of Eq. (4.28) is taken, given by

$$\begin{aligned}
\langle(\hat{X}_I^{\pm})^2\rangle &= g^2\langle(\hat{X}_a^{\pm})^2\rangle + \frac{1}{g^2}\langle(\hat{X}_b^{\pm})^2\rangle - \frac{C_{ab}^{\pm\pm}}{|C_{ab}^{\pm\pm}|}\langle\hat{X}_a^{\pm}\hat{X}_b^{\pm} + \hat{X}_b^{\pm}\hat{X}_a^{\pm}\rangle \\
&= \sqrt{\frac{C_{bb}^{\pm\pm} - 1}{C_{aa}^{\pm\pm} - 1}}C_{aa}^{\pm\pm} + \sqrt{\frac{C_{aa}^{\pm\pm} - 1}{C_{bb}^{\pm\pm} - 1}}C_{bb}^{\pm\pm} - 2|C_{ab}^{\pm\pm}| \\
&= 2\sqrt{(C_{bb}^{\pm\pm} - 1)(C_{aa}^{\pm\pm} - 1)} + \sqrt{\frac{C_{bb}^{\pm\pm} - 1}{C_{aa}^{\pm\pm} - 1}} + \sqrt{\frac{C_{aa}^{\pm\pm} - 1}{C_{bb}^{\pm\pm} - 1}} - 2|C_{ab}^{\pm\pm}| \\
&= \langle(\hat{X}_I^{\mp})^2\rangle
\end{aligned} \tag{4.29}$$

where we have used the conditions given in Eqs. (4.25) and (4.26). Therefore the inseparability criterion can be written as

$$\sqrt{\langle(\hat{X}_I^+)^2\rangle\langle(\hat{X}_I^-)^2\rangle} \geq g^2 + \frac{1}{g^2} \tag{4.30}$$

Since both beams have identical variances (i.e. $C_{bb}^{\pm\pm} = C_{aa}^{\pm\pm}$), thus

$$g = \sqrt{\frac{C_{bb}^{\pm\pm} - 1}{C_{aa}^{\pm\pm} - 1}} = 1 \tag{4.31}$$

and therefore the product form of the inseparability criterion is given by [192]

$$\mathcal{I}(\hat{X}_a^{\pm}, \hat{X}_b^{\pm}) = \sqrt{\langle(\hat{X}_I^+)^2\rangle\langle(\hat{X}_I^-)^2\rangle} \geq 1 \tag{4.32}$$

where a violation of this criterion (i.e. $\mathcal{I} < 1$) shows that the state is inseparable and entangled.

Since the commutation relation for our variables of interest, $\delta\hat{x}$ and $\delta\hat{p}$ is non-equal to $2i$, as shown in Eq. (4.11), we use the normalised product form of the inseparability criterion given by [124, 218, 219, 231, 232]

$$\mathcal{I}(\hat{x}, \hat{p}) = \frac{\langle(\hat{x}_3 + \hat{x}_4)^2\rangle\langle(\hat{p}_3 - \hat{p}_4)^2\rangle}{|[\hat{x}, \hat{p}]|^2} \tag{4.33}$$

for any pair of conjugate observables $\hat{x}$ and $\hat{p}$, and a pair of beams denoted by the subscripts 3 and 4. In this chapter, we consider the two beams to be perfectly interchangeable and have symmetrical fluctuations in the amplitude and phase quadratures. By using observables $\delta\hat{x}$ and $\delta\hat{p}$ from Eqs. (4.15), (4.16), (4.17) and (4.18) as well as the commutation relation of Eq. (4.11) the inseparability criterion for beams 3 and 4 is given by

$$\begin{aligned}\mathcal{I}(\delta\hat{x}, \delta\hat{p}) &= \frac{16N^2}{\omega_0^4}\langle(\delta\hat{x}^+_{a_1})^2\rangle\langle(\delta\hat{x}^+_{b_1})^2\rangle \\ &= \langle(\delta\hat{X}^+_{a_1})^2\rangle\langle(\delta\hat{X}^+_{b_1})^2\rangle \\ &< 1 \end{aligned} \tag{4.34}$$

where we have assumed that the TEM_{10} modes of beams 1 and 2 are amplitude squeezed (i.e. $\langle(\delta\hat{X}^+_{a_1})^2\rangle < 1$ and $\langle(\delta\hat{X}^+_{b_1})^2\rangle < 1$).

Since $\mathcal{I}(\delta\hat{x}, \delta\hat{p}) < 1$, we have demonstrated that CV EPR entanglement between the position and momentum observables of two CW beams can be achieved.

4.2.7 Detection Scheme

Ref. [149] has shown that the optimum small displacement measurement is homodyne detection with a TEM_{10} local oscillator beam (see Fig. 4.2 (d)). When the input beam is centred with respect to the TEM_{10} local oscillator beam, no power is contained in the TEM_{10} mode. Due to the orthogonality of Hermite-Gauss modes, the TEM_{10} local oscillator only detects the TEM_{10} vacuum noise component. As the input beam is displaced, power is coupled into the TEM_{10} mode. This coupled power interferes with the TEM_{10} local oscillator beam, causing a change in photo-current observed at the output of the homodyne detector. Thus the difference photo-current of the TEM_{10} homodyne detector is given by [149]

$$\hat{n}^d_- = \frac{2\sqrt{N}\sqrt{N_{\mathrm{LO}}}}{w_0}\hat{x} \tag{4.35}$$

where N_{LO} and N are the total number of photons in the local oscillator and displaced beams, respectively, with $N_{\mathrm{LO}} \gg N$. The linearised approximation is utilised, where second order terms in $\delta\hat{a}$ are neglected since $N \gg |\langle\delta\hat{a}^2_n\rangle|$ for all n.

In order to measure momentum, one could use a lens to Fourier transform to the far-field plane, where the beam is then measured using the TEM_{10} homodyning scheme. However, we have shown that the the position and momentum of a TEM_{00} beam differs by the phase of the TEM_{10} mode component. Indeed for a tilted TEM_{00} beam, the TEM_{10} mode component is $\pi/2$ phase shifted relative to the TEM_{00} mode component. Consequently the phase quadrature of the TEM_{10} mode has to be interrogated. This can be achieved by utilising a TEM_{10} local oscillator beam with a $\pi/2$ phase difference relative to the TEM_{10} mode component of the TEM_{00} beam. The resulting photo-current difference between the two homodyning detectors, for $N_{\mathrm{LO}} \gg N$, is given by

$$\hat{n}^p_- = w_0\sqrt{N}\sqrt{N_{\mathrm{LO}}}\hat{p} \tag{4.36}$$

4.3 Spatial entanglement for split detection

The entanglement presented in the previous section is analogous to x-p entanglement in the single photon regime. However, the choice of the mean field mode is restricted to the TEM_{00} mode. This limits the richness of a spatial variable and thus excludes the possibility of generating an infinite Hilbert space. To exploit the properties of spatial variables, we now consider more traditional forms of spatial squeezing. Consequently, we study the possibility of generating spatial entanglement for array detection devices, based on spatial squeezed beams.

4.3.1 Spatial Squeezing

Spatial squeezing was first introduced by Kolobov [56]. The generation of spatial squeezed beams for split and array detectors was experimentally demonstrated by Treps *et al.* [1, 205, 204]. A one-dimensional spatial squeezed beam has a spatially ordered distribution, where there exists correlation between the photon numbers in both transverse halves of the beam. A displacement signal applied to this beam can thus be measured to beyond the QNL.

We consider a beam of normalised transverse amplitude function $v_0(x)$ incident on a split detector. The noise of split detection has been shown to be due to the flipped mode [203], given by

$$v_1(x) = \begin{cases} v_0(x) & \text{for } x > 0 \\ -v_0(x) & \text{for } x < 0 \end{cases}$$

When the field is centred at the split-detector, such that the mean value of the measurement is zero, the flipped mode is thus orthogonal to the mean field mode. In this instance, modes $v_i(x)$ (for $i > 1$) can be derived to complete the modal basis. The electric field operator written in this new modal basis is given by

$$\hat{\mathcal{E}}^+ = i\sqrt{\frac{\hbar\omega}{2\epsilon_0 V}}\Big(\sqrt{N}v_0(x) + \sum_{n=0}^{\infty}\delta\hat{c}_n v_n(x)\Big) \tag{4.37}$$

where the first term describes the coherent excitation of the beam in the $v_0(x)$ mode and N is the total number of photons in the beam. It has been shown that the corresponding photon number difference operator for split detection is given by [149]

$$\hat{n}_-^{(+)} = \sqrt{N}\delta\hat{X}_{c0}^+ \tag{4.38}$$

The beam is spatially squeezed if the state of the flipped mode is vacuum squeezed and in phase with the mean field mode (see Fig. 4.3 (a) and (b)).

4.3.2 Spatial Homodyne

Since split detection is commonly used as a detection device for beam position, one would naturally consider taking the Fourier transform of a spatial squeezed beam to obtain the conjugate observable for the beam. However, we have shown that split detection does not correspond exactly to beam position measurement. Thus the Fourier plane of the spatial squeezed beam does not provide the conjugate observable. More practically, the flipped mode is not mode-shape invariant under Fourier transformation. In the far-field, each odd-ordered mode component of the flipped mode obtains a $(2n+1)\pi$ Gouy phase difference, compared to the near-field. Thus the mode-shape in the far-field is no longer a flipped mode. Consequently, far and near-field measurements of a spatial squeezed beam will not give the conjugate observables.

However, we can find the conjugate observables of a spatial squeezed beam by drawing an analogy to standard homodyne detection. In split detection, the equivalent local oscillator mode is the mean field $v_0(x)$ mode. The mode under interrogation by the split detector is the flipped mode $v_1(x)$. In the case of homodyne detection, the phase of the local oscillator beam is varied to measure the conjugate observables (i.e. amplitude and phase quadratures) of the input beam. Adapting this concept to the split detector, the conjugate observables for the spatial squeezed beam are thus the amplitude and phase quadratures of the flipped mode, while the mode-shape of the flipped mode remains unaltered. This is further verified upon inspection of Eq. (4.38).

Our scheme to perform a phase measurement of the flipped mode is shown in Fig. 4.3 (d). In our scheme we assume that the mean field is a TEM_{00} mode. Note that in principle, this analysis could be performed for any mode-shape. The coherent TEM_{00} mode component provides a phase reference for the flipped mode, analogous to that of a local oscillator beam in homodyne detection. Thus the phase quadrature of the flipped mode can be accessed by applying a $\pi/2$ phase shift between the the TEM_{00} mode and the flipped mode noise component. Experimentally, this is achievable using an optical cavity. When the cavity is non-resonant for the $v_0(x)$ and $v_1(x)$ modes it will reflect off the two modes, in phase, onto the split detector. This will give a measurement of the amplitude quadrature of the flipped mode. However, the cavity can be tuned to be partially resonant on the $v_0(x)$ mode while reflecting the flipped mode. A $\pi/2$ phase difference can then be introduced between the reflected $v_0(x)$ and $v_1(x)$ modes, giving a measurement of the phase quadrature of the flipped mode. The corresponding photon number difference operator is

$$\hat{n}_-^{(-)} = \sqrt{N}\delta\hat{X}_{c_0}^- \tag{4.39}$$

which is the orthogonal quadrature of the spatial squeezed beam. The photon number operators corresponding to the two measurements in Eqs. (4.38) and (4.39) are conjugate observables and satisfy the commutation relation $[\hat{n}_-^{(+)}, \hat{n}_-^{(-)}] = 2iN$.

It is important to realise that the number of photons N in Eqs. (4.38) and (4.39) are only approximately equal. This is due to the fact that partial power in the TEM_{00} mode is transmitted by the cavity, when the cavity is partially resonant on the TEM_{00} mode. Although it is possible to implement a scheme that conserves the total number of photons at detection (e.g. loss-lessly separating the mean field and flipped modes and recombining them with a phase difference), we would like to emphasise that our scheme is more simple and intuitive, as well as being valid when N is large.

4.3.3 Entanglement Scheme

In order to generate spatial entanglement for split detection, two spatial squeezed beams labelled 1 and 2 are combined on a 50:50 beam-splitter, as shown in Figure 4.3 (c).

The electric field operators for the two input spatial squeezed beams at the beam-splitter are described in a form identical to that of Eq. (4.37). The annihilation operators of the electric field operators for input beams 1 and 2 are labelled by $\hat{c}_n$ and $\hat{d}_n$, respectively. By following a similar procedure as before, the photon number difference operator for output beams 3 and 4 from the beam-splitter are calculated.

For the amplitude quadrature measurement, the addition of the difference photo-current between beams 3 and 4 yields

$$\hat{n}_{3-}^{(+)} + \hat{n}_{4-}^{(+)} = \sqrt{N}(\delta\hat{X}_{c_0}^+ + \delta\hat{X}_{d_0}^+) \tag{4.40}$$

For the phase quadrature measurement, the subtraction of the difference photo-current

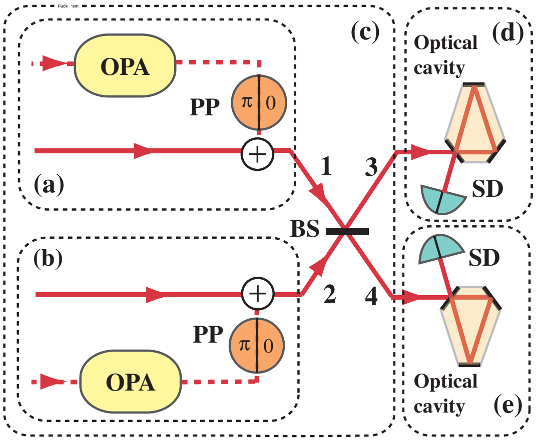

Figure 4.3: Scheme for generating spatial entanglement for TEM_{00} continuous wave light beams. OPA: optical parametric amplifiers for generating squeezed beams, PP: phase plates for producing flipped modes, BS: 50:50 beam-splitter.

between beams 3 and 4 gives

$$\hat{n}_{3-}^{(-)} - \hat{n}_{4-}^{(-)} = \sqrt{N}(\delta\hat{X}_{d_0}^{+} - \delta\hat{X}_{c_0}^{+}) \tag{4.41}$$

To verify spatial entanglement, the *inseparability criterion* is utilised. The substitution of Eqs. (4.40), (4.41) and the commutation relation between the photon number difference operators into the generalised form of the *inseparability criterion* gives

$$\begin{aligned}\mathcal{I}(\delta\hat{n}_{-}^{(+)}, \delta\hat{n}_{-}^{(-)}) &= \frac{N\left(V_{c_0}^2 + 2V_{c_0}V_{d_0} + V_{d_0}^2\right)}{4N} \\ &< 1\end{aligned} \tag{4.42}$$

where $V_{c_0} = \langle(\delta\hat{X}_{c_0}^{+})^2\rangle$ and $V_{d_0} = \langle(\delta\hat{X}_{d_0}^{+})^2\rangle$ are the variances for the flipped mode component of the spatial squeezed beams 1 and 2. The inseparability criterion is satisfied for amplitude squeezed flipped modes $V_{c_0} < 1$ and $V_{d_0} < 1$.

We have proposed a scheme to generate spatial entanglement for split detection, using spatial squeezed beams. Spatial squeezing has been defined for any linear measurement performed with an array detector [206]. Similarly, spatial entanglement corresponding to any linear measurement, can be obtained. For an infinite span array detector with infinitessimally small pixels, it is thus possible to generate multi-mode spatial entanglement.

4.4 Spatial Stokes entanglement

In the preceding sections, we discussed EPR entanglement in the position-momentum observables of optical fields. We also discussed entanglement for split detection, a specific entanglement scheme, generalisable to array detection. We now consider a different form of entanglement, where the Stokes operators (commonly represented on a Poincaré sphere) are the entanglement variables.

In the discrete-variable regime, multi-dimensional entanglement between orbital angular momentum states have been proposed [233, 234] and demonstrated [201]. In Ref. [201], entanglement was generated in the parametric down-conversion process by using pump photons with different orbital angular momentum values. A large body of study has been dedicated to understanding and detecting the orbital angular momentum properties of photons [235, 209, 236, 237, 202, 238, 239, 240, 4]. Applications of light fields with orbital angular momentum have also been proposed, which include the generation of counter-rotating superpositions in Bose-Einstein condensates [241, 242], transfer of orbital angular momentum from an atomic ensemble to a light field [243], and optical angular momentum transfer to trapped particles [244, 245, 246].

Our motivation is to study the generation of spatial entanglement between continuous-variables which obey a commutation relation with cyclic permutations, $[\hat{\mathcal{O}}_x, \hat{\mathcal{O}}_y] = \hat{\mathcal{O}}_z$. These spatial Stokes variables completely span the Poincaré sphere [150], analogous to that of polarisation Stokes operators [247].

Since we are dealing with two-dimensional spatial modes, we denote the normalised transverse beam amplitude functions for the TEM$_{pq}$ mode by $u_{pq}(\boldsymbol{r})$. The positive frequency part of the electric field operator is then written explicitly in terms of a double-subscript sum of the mode $u_{pq}(\boldsymbol{r})$, given by

$$\hat{\mathcal{E}}^{+}(\boldsymbol{r}) = i\sqrt{\frac{\hbar\omega}{2\epsilon_0 V}} \sum_{p,q=0}^{\infty} \hat{a}_{pq} u_{pq}(\boldsymbol{r}) \tag{4.43}$$

where $\hat{a}_{pq}$ is the photon annihilation operator associated with mode $u_{pq}(\boldsymbol{r})$, which can be obtained by projecting the $u_{\mathrm{mn}}(\boldsymbol{r})$ mode onto $\hat{\mathcal{E}}^{+}(\boldsymbol{r})$, given by

$$\hat{a}_{pq} = \iint_{\infty}^{-\infty} dxdy \hat{\mathcal{E}}^{+}(x,y) u_{pq}(x,y) \tag{4.44}$$

Using the two orthogonal TEM$_{p0}$ and TEM$_{0p}$ modes, a variety of modes can be generated. The diagonal modes of the TEM$_{p0}$ and TEM$_{0p}$ modes are given by $u_{p0}^{45^\circ}(\boldsymbol{r}) = u_{0p}(\boldsymbol{r}) - u_{p0}(\boldsymbol{r})$ and $u_{0p}^{45^\circ}(\boldsymbol{r}) = u_{0p}(\boldsymbol{r}) + u_{p0}(\boldsymbol{r})$, respectively. The Laguerre-Gauss modes LG$_{0l}$ with orbital angular momentum $+l$ and $-l$, are given by $u_{0l}^{+l}(\boldsymbol{r}) = u_{0l}(\boldsymbol{r}) + iu_{l0}(\boldsymbol{r})$ and $u_{0l}^{-l}(\boldsymbol{r}) = u_{0l}(\boldsymbol{r}) - iu_{l0}(\boldsymbol{r})$, respectively. An example of the intensity distributions for the diagonal and Laguerre-Gauss modes, generated from the combinations of TEM$_{10}$ and TEM$_{01}$ modes, is shown in Fig. 4.4.

Since the diagonal and rotational modes can be generated purely from two orthogonal TEM$_{p0}$ and TEM$_{0p}$ modes, only by changing the phase between the modes, these set of modes obey the SU(2) group properties. At this point, we restrict our analysis to the TEM$_{10}$ and TEM$_{01}$ modes, for illustrative purposes. In principle, our analysis is valid for all orthogonal TEM$_{p0}$ and TEM$_{0p}$ modes. Using the classical Stokes parameter definition [150], we derive the corresponding quantum mechanical spatial Stokes operators, given by

$$\begin{aligned}
\hat{S}_0 &= \hat{a}_{10}^{\dagger}\hat{a}_{10} + \hat{a}_{01}^{\dagger}\hat{a}_{01} \\
\hat{S}_1 &= \hat{a}_{10}^{\dagger}\hat{a}_{10} - \hat{a}_{01}^{\dagger}\hat{a}_{01} \\
\hat{S}_2 &= \hat{a}_{10}^{\dagger}\hat{a}_{01}e^{i\theta} + \hat{a}_{01}^{\dagger}\hat{a}_{10}e^{-i\theta} \\
\hat{S}_3 &= i\hat{a}_{01}^{\dagger}\hat{a}_{10}e^{-i\theta} - i\hat{a}_{10}^{\dagger}\hat{a}_{01}e^{i\theta}
\end{aligned} \tag{4.45}$$

where θ is the phase difference between the operators $\hat{a}_{10}$ and $\hat{a}_{01}$, corresponding to the TEM$_{10}$ and TEM$_{01}$ modes, respectively. A Poincaré sphere representation of the Stokes

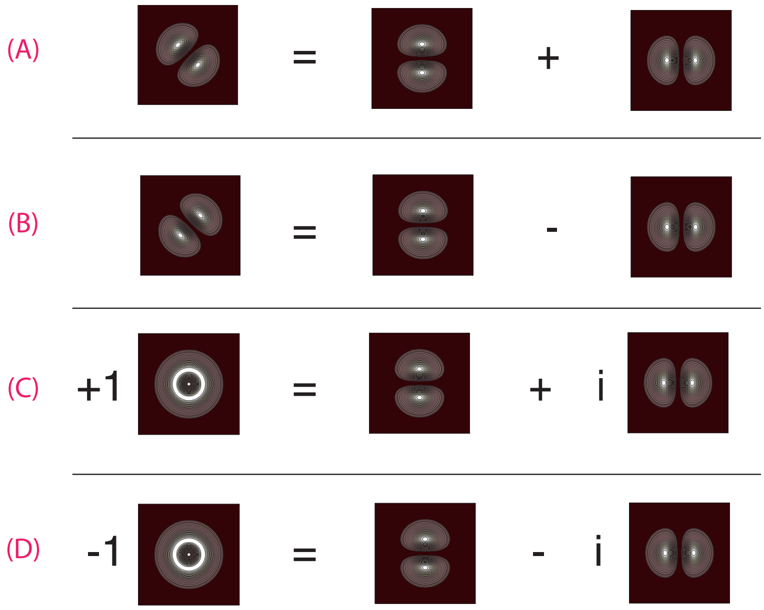

Figure 4.4: Intensity distribution for the modes given by (A) $u_{01}^{45^\circ}(\boldsymbol{r}) = u_{01}(\boldsymbol{r}) + u_{10}(\boldsymbol{r})$, (B) $u_{10}^{45^\circ}(\boldsymbol{r}) = u_{01}(\boldsymbol{r}) - u_{10}(\boldsymbol{r})$, (C) $u_{01}^{+1}(\boldsymbol{r}) = u_{01}(\boldsymbol{r}) + iu_{10}(\boldsymbol{r})$, and (D) $u_{01}^{-1}(\boldsymbol{r}) = u_{01}(\boldsymbol{r}) - iu_{10}(\boldsymbol{r})$.

operators is given in Fig. 4.5 [150].

By using the commutation relations of the photon annihilation and creation operators, $[\hat{a}_{mn}, \hat{a}_{jk}] = \delta_{mj}\delta_{nk}$, the Stokes-operator commutation relations are thus given by

$$\begin{array}{rcl} \left[\hat{S}_1, \hat{S}_2\right] & = & 2i\hat{S}_3 \\ \left[\hat{S}_2, \hat{S}_3\right] & = & 2i\hat{S}_1 \\ \left[\hat{S}_3, \hat{S}_1\right] & = & 2i\hat{S}_2 \end{array} \tag{4.46}$$

which has cyclic permutations.

4.4.1 Spatial Stokes detection

Now that the spatial Stokes operators have been defined, we consider the detection system for the spatial Stokes operators. Analogous to the polarisation Stokes operators, the spatial Stokes detector consists of two detectors, with a mode phase shifter and a mode separator. The spatial Stokes detection system is shown in Fig. 4.6.

Using the linearised formalism as described in the preceding chapters, the mean amplitude of the Stokes operators are given by

$$\begin{array}{rcl} \langle\hat{S}_0\rangle & = & \alpha_{10}^2 + \alpha_{01}^2 = N \\ \langle\hat{S}_1\rangle & = & \alpha_{10}^2 - \alpha_{01}^2 \\ \langle\hat{S}_2\rangle & = & 2\alpha_{10}\alpha_{01}\cos\theta \\ \langle\hat{S}_3\rangle & = & 2\alpha_{10}\alpha_{01}\sin\theta \end{array} \tag{4.47}$$

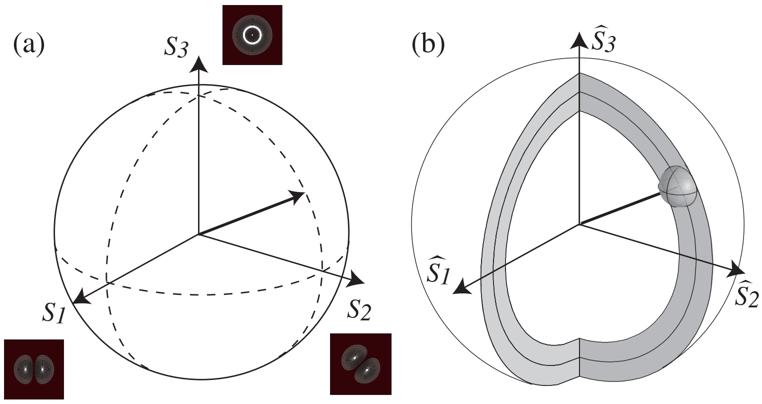

Figure 4.5: (a) Poincare sphere representation based on the spatial modes TEM_{10} and TEM_{01}. S_1 is the Stokes variable for the u_{01} and u_{10} modes, S_2 is the Stokes variable for the $u_{01}^{45^\circ}$ and $u_{10}^{45^\circ}$ modes, and S_3 is the Stokes variable for the u_{01}^{+1} and u_{01}^{-1} modes. (b) Poincare sphere representation for the spatial Stokes operators. The shaded area indicates the quantum noise associated with the mean amplitude of the Stokes operator.

where α_{01} and α_{10} the mean amplitude terms corresponding to modes u_{01} and u_{10}, respectively. $\langle \hat{S}_0 \rangle = N$ is the total mean number of photons. $\langle \hat{S}_1 \rangle$ is the difference in the mean number of photons in the u_{10} and u_{01} modes. $\langle \hat{S}_2 \rangle$ is the difference in the mean number of photons in the $u_{01}^{45^\circ}$ and $u_{10}^{45^\circ}$ modes. $\langle \hat{S}_3 \rangle$ is the difference in the mean number of photons in the u_{01}^{+1} and u_{01}^{-1} modes.

The variance of the Stokes operators are given by

$$\begin{aligned}
\langle (\delta \hat{S}_0)^2 \rangle &= \alpha_{10}^2 \langle (\delta \hat{X}_{a10}^{+})^2 \rangle + \alpha_{01}^2 \langle (\delta \hat{X}_{a01}^{+})^2 \rangle + 2\alpha_{10}\alpha_{01} \langle \delta \hat{X}_{a10}^{+} \delta \hat{X}_{a01}^{+} \rangle \\
\langle (\delta \hat{S}_1)^2 \rangle &= \alpha_{10}^2 \langle (\delta \hat{X}_{a10}^{+})^2 \rangle + \alpha_{01}^2 \langle (\delta \hat{X}_{a01}^{+})^2 \rangle - 2\alpha_{10}\alpha_{01} \langle \delta \hat{X}_{a10}^{+} \delta \hat{X}_{a01}^{+} \rangle \\
\langle (\delta \hat{S}_2)^2 \rangle &= \alpha_{10}^2 \langle (\delta \hat{X}_{a01}^{-\theta})^2 \rangle + \alpha_{01}^2 \langle (\delta \hat{X}_{a10}^{\theta})^2 \rangle + 2\alpha_{10}\alpha_{01} \langle \delta \hat{X}_{a01}^{-\theta} \delta \hat{X}_{a10}^{\theta} \rangle \\
\langle (\delta \hat{S}_3)^2 \rangle &= \alpha_{10}^2 \langle (\delta \hat{X}_{a01}^{-\theta+\frac{\pi}{2}})^2 \rangle + \alpha_{01}^2 \langle (\delta \hat{X}_{a10}^{\theta-\frac{\pi}{2}})^2 \rangle + 2\alpha_{10}\alpha_{01} \langle \delta \hat{X}_{a01}^{-\theta+\frac{\pi}{2}} \delta \hat{X}_{a10}^{\theta-\frac{\pi}{2}} \rangle
\end{aligned} \tag{4.48}$$

Since $\delta \hat{X}_{a10}^{\theta}$ and $\delta \hat{X}_{a01}^{\theta}$ are uncorrelated, therefore the variances of the Stokes operators are simplified to the following expressions

$$\begin{aligned}
\langle (\delta \hat{S}_0)^2 \rangle &= \alpha_{10}^2 \langle (\delta \hat{X}_{a10}^{+})^2 \rangle + \alpha_{01}^2 \langle (\delta \hat{X}_{a01}^{+})^2 \rangle \\
\langle (\delta \hat{S}_1)^2 \rangle &= \alpha_{10}^2 \langle (\delta \hat{X}_{a10}^{+})^2 \rangle + \alpha_{01}^2 \langle (\delta \hat{X}_{a01}^{+})^2 \rangle \\
\langle (\delta \hat{S}_2)^2 \rangle &= \alpha_{10}^2 \langle (\delta \hat{X}_{a01}^{-\theta})^2 \rangle + \alpha_{01}^2 \langle (\delta \hat{X}_{a10}^{\theta})^2 \rangle \\
\langle (\delta \hat{S}_3)^2 \rangle &= \alpha_{10}^2 \langle (\delta \hat{X}_{a01}^{-\theta+\frac{\pi}{2}})^2 \rangle + \alpha_{01}^2 \langle (\delta \hat{X}_{a10}^{\theta-\frac{\pi}{2}})^2 \rangle
\end{aligned} \tag{4.49}$$

4.4.2 Spatial Stokes squeezing

An examination of Eqs. (4.49) show that simultaneous squeezing of at least two Stokes operators is possible, by the use of two squeezed input fields. Examples of these are given by

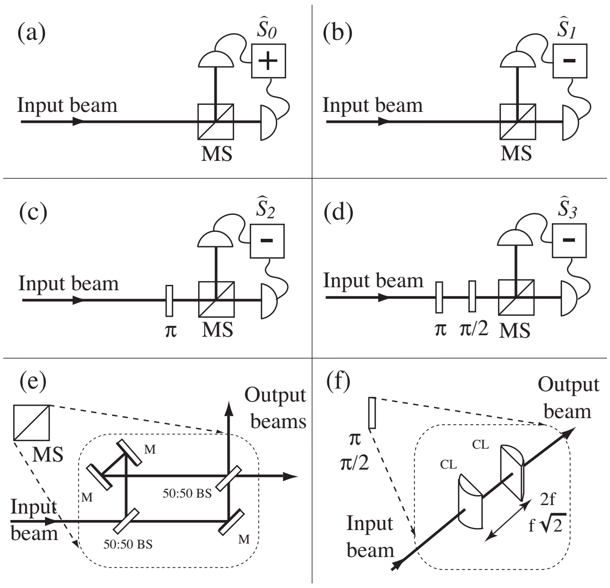

Figure 4.6: Measurements of (a) $\hat{S}_0$ and (b) $\hat{S}_1$, by taking the sum and differences of the photocurrents corresponding to mode components TEM_{10} and TEM_{01}, respectively. Measurements of (c) $\hat{S}_2$ is performed by using a π mode rotator. In order to measure (d) $\hat{S}_3$, π and $\pi/2$ mode rotators are required. (e) An example of a mode separator (MS) is an asymmetric Mach-Zehnder interferometer [2, 3]. The odd and even number of reflections each interferometer arm, together with the relevant phase changes due to Fresnel reflection on the arms, set up appropriate destructive and constructive interference conditions for the odd and even modes on each output arm of the interferometer. The result of this is that the odd and even modes constructively interfere on different arms of the interferometer. (f) The π and $\pi/2$ mode phase shifters could be constructed using a pair of cylindrical lenses with lens separation given by $2f$ and $\sqrt{2}f$, respectively. f is the focal length of the cylindrical lenses, M is a mirror, 50:50 BS is a symmetric non-polarising beam-spliter. Ref. [4] contains a detailed analysis of the π and $\pi/2$ mode-selective phase shifters.

- **Squeezing in $\langle(\delta\hat{S}_0)^2\rangle$, $\langle(\delta\hat{S}_1)^2\rangle$ and $\langle(\delta\hat{S}_2)^2\rangle$.**
  This can be achieved by having amplitude squeezed TEM_{10} and TEM_{01} modes (i.e. $\langle(\delta\hat{X}^{+}_{a10})^2\rangle < 1$ and $\langle(\delta\hat{X}^{+}_{a01})^2\rangle < 1$) and $\theta = 0$.
- **Squeezing in $\langle(\delta\hat{S}_0)^2\rangle$, $\langle(\delta\hat{S}_1)^2\rangle$ and $\langle(\delta\hat{S}_3)^2\rangle$.**
  This can be achieved by having amplitude squeezed TEM_{10} and TEM_{01} modes and $\theta = \pi/2$.
- **Squeezing in $\langle(\delta\hat{S}_2)^2\rangle$ and $\langle(\delta\hat{S}_3)^2\rangle$.**
  Quadrature squeezed TEM_{10} and TEM_{01} modes, at squeezing quadrature angle of $\pi/4$ (i.e. $\langle(\delta\hat{X}^{\frac{\pi}{4}}_{a10})^2\rangle < 1$ and $\langle(\delta\hat{X}^{\frac{\pi}{4}}_{a01})^2\rangle < 1$) and $\theta = \pi/4$.

Phase squeezed TEM_{10} and TEM_{01} modes (i.e. $\langle(\delta\hat{X}^{-}_{a10})^2\rangle < 1$ and $\langle(\delta\hat{X}^{-}_{a01})^2\rangle < 1$) will yield squeezing of $\langle(\delta\hat{S}_2)^2\rangle$ only.

4.4.3 Entanglement scheme

The spatial Stokes entanglement scheme is shown in Fig. 4.7. Two squeezed beams in the TEM_{10} mode, labelled by $\hat{a}_{10,x}$ and $\hat{a}_{10,y}$ are combined on a beam-splitter. The resulting output beams from the beam-splitter are quadrature entangled. The output beams are then each combined with a coherent beam, labelled by $\hat{a}_{01,x}$ and $\hat{a}_{01,y}$, in the TEM$_{01}$ mode on a spatial mode splitter (combiner). The resulting output beams are thus entangled in the spatial Stokes operator basis. Verification of the spatial Stokes entanglement can be performed using the detection scheme described in the preceding sections.

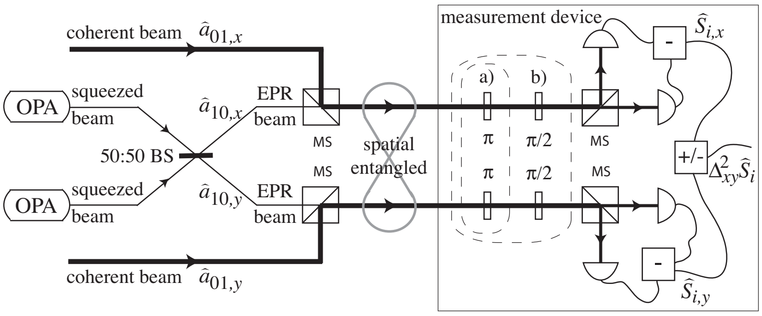

Figure 4.7: Scheme to generate and characterise spatial Stokes entanglement. 50:50 BS is a symmetric non-polarising beam-splitter, π and $\pi/2$ are mode-selective phase shifters.

The sum form of the inseparability criterion is now written in terms of the spatial Stokes operators, using Eqs. (4.46) and (4.47). The degree of inseparability for the three permutations of Stokes operators (assuming $\alpha_{01,x} = \alpha_{01,y} = \alpha_{01}$ and $\alpha_{10,x} = \alpha_{10,y} = \alpha_{10}$) are given by

$$\begin{aligned}
\mathcal{I}(\hat{S}_1, \hat{S}_2) &= \frac{\Delta^2_{x\pm y}\hat{S}_1 + \Delta^2_{x\pm y}\hat{S}_2}{8|\alpha_{10}\alpha_{01}\sin\theta|} \\
\mathcal{I}(\hat{S}_3, \hat{S}_1) &= \frac{\Delta^2_{x\pm y}\hat{S}_1 + \Delta^2_{x\pm y}\hat{S}_3}{8|\alpha_{10}\alpha_{01}\cos\theta|} \\
\mathcal{I}(\hat{S}_2, \hat{S}_3) &= \frac{\Delta^2_{x\pm y}\hat{S}_2 + \Delta^2_{x\pm y}\hat{S}_3}{4|\alpha_{10}^2 - \alpha_{01}^2|}
\end{aligned} \tag{4.50}$$

where the conditional variance is defined as $\Delta^2_{x\pm y}\hat{\mathcal{O}} = \min\langle(\delta\hat{\mathcal{O}}_x \pm \delta\hat{\mathcal{O}}_y)^2\rangle$. Since we assume that $\alpha^2_{10,x,y} \ll \alpha^2_{01,x,y}$, the conditional variances for the spatial Stokes operators are thus given by

$$\begin{aligned}
\Delta^2_{x\pm y}\hat{S}_1 &= \alpha_{01}^2\Delta^2_{x\pm y}\hat{X}^+_{a01} \\
\Delta^2_{x\pm y}\hat{S}_2 &= \alpha_{01}^2\Delta^2_{x\pm y}\hat{X}^\theta_{a10} \\
\Delta^2_{x\pm y}\hat{S}_3 &= \alpha_{01}^2\Delta^2_{x\pm y}\hat{X}^{\theta-\frac{\pi}{2}}_{a10}
\end{aligned} \tag{4.51}$$

Substituting these expressions into Eqs. (4.50), gives

$$\mathcal{I}(\hat{S}_1, \hat{S}_2) = \frac{\alpha_{01}}{8\alpha_{10}|\sin\theta|}\left(\Delta^2_{x\pm y}\hat{X}^{+}_{a_{01}} + \Delta^2_{x\pm y}\hat{X}^{\theta}_{a_{10}}\right) \tag{4.52}$$

$$\mathcal{I}(\hat{S}_3, \hat{S}_1) = \frac{\alpha_{01}}{8\alpha_{10}|\cos\theta|}\left(\Delta^2_{x\pm y}\hat{X}^{+}_{a_{01}} + \Delta^2_{x\pm y}\hat{X}^{\theta-\frac{\pi}{2}}_{a_{10}}\right) \tag{4.53}$$

$$\mathcal{I}(\hat{S}_2, \hat{S}_3) = \frac{\alpha^2_{01}}{4|\alpha^2_{10}-\alpha^2_{01}|}\left(\Delta^2_{x\pm y}\hat{X}^{\theta}_{a_{10}} + \Delta^2_{x\pm y}\hat{X}^{\theta-\frac{\pi}{2}}_{a_{10}}\right) \tag{4.54}$$

It is important to note that the inseparability criteria of Eqs. (4.52) and (4.53) scale with respect to α_{01}/α_{10}. For increasing α_{01}/α_{10}, the correlation in $\hat{X}^{+}_{a_{01}}$ and $\hat{X}^{\theta}_{a_{10}}$ have to be correspondingly increased, in order to maintain inseparability. This could potentially be a technical difficulty for experiments. For $\alpha_{01}/\alpha_{10} \rightarrow 0$, the inseparability values increases to infinity and thus the verification of inseparability is not possible. Therefore, in experiments, a compromise in α_{01}/α_{10} values and sufficient degree of correlation in $\hat{X}^{+}_{a_{01}}$ and $\hat{X}^{\theta}_{a_{10}}$ have to be considered, to demonstrate inseparability.

Eq. (4.54) can be simplified further to

$$\begin{aligned}\mathcal{I}(\hat{S}_2, \hat{S}_3) &= \frac{1}{4}\left(\Delta^2_{x\pm y}\hat{X}^{\theta}_{a_{10}} + \Delta^2_{x\pm y}\hat{X}^{\theta-\frac{\pi}{2}}_{a_{10}}\right) \\ &= \frac{1}{4}\left(\Delta^2_{x\pm y}\hat{X}^{+}_{a_{10}} + \Delta^2_{x\pm y}\hat{X}^{-}_{a_{10}}\right)\end{aligned} \tag{4.55}$$

where we have assumed $\theta = 0$ and $\alpha^2_{01} \gg \alpha^2_{10}$. In this situation, quadrature entanglement of the TEM_{10} input modes (as shown in Fig. 4.7) will yield spatial Stokes entanglement between $\hat{S}_2$ and $\hat{S}_3$.

4.5 Conclusion

We have identified the position and momentum of a TEM_{00} optical beam. By showing that $\hat{x}$ and $\hat{p}$ are conjugate observables that satisfy the Heisenberg commutation relation, a continuous variable *x*-*p* entanglement scheme was proposed.

A form of spatial entanglement which has applications in quantum imaging was also explored. The detection schemes for quantum imaging are typically array detectors. In this chapter, we considered the split detector. We utilised the one-dimensional spatial squeezing work of Treps *et al.* [204] and proposed a spatial homodyning scheme for the spatial squeezed beam. By identifying the conjugate observables for the spatial squeezed beam as the amplitude and phase quadratures of the flipped mode, we showed that split detection-based spatial entanglement can be obtained.

We also studied the generation of spatial Stokes entanglement. The detection scheme for spatial Stokes operators was identified and the generation of spatial Stokes squeezing was analysed. Our spatial Stokes entanglement scheme is analogous to that of polarisation Stokes entanglement [124] and could have potential applications for the transfer of spatial Stokes entanglement from optical fields to atomic ensembles [241, 242, 243, 244, 245, 246].

Chapter 5

Application of spatial quantum optics for phase coding

".-- ...   . -   -.. -.   -.. ...   ..-. .-.
.- -. .   ... -.-. .... ?"

Humans have been obsessed with the possibility of encoding information for millennia. The Chinese produced the *I Ching* ("Book of Changes") in 2852 BC. A symbolic system based on hexagrams with broken and/or solid lines (i.e. binary) is the main coding system of the *I Ching*. Many scholars explain that the 64 codes in the *I Ching* describe the evolution of phenomena and events - that change is a natural progression of nature, whilst others argue that the *I Ching* is purely a form of divination. If one were to accept the former interpretation, the *I Ching* could be one of the first human endeavours at information dense-coding. On the other side of the globe, the Romans invented the *Caesar cipher* where each letter in the text was substituted by another letter, at some fixed number of positions further down the alphabet. This form of information encoding was performed to encrypt information but does not provide any information compression.

Information theory was pioneered by Claude Shannon who developed theories on information compression using entropy arguments. In this chapter, we are interested in 'packing' as much information as possible into a memory device. However, we do not approach this problem from the information theoretic perspective but from the quantum experimentalist perspective. Our motivation is to imagine a new scheme to increase the information storage capacities of optical memories. Instead of taking the traditional path of using lasers with ever smaller wavelengths and improving data compression algorithms, we investigate interferometric techniques to perform phase encoding. Our scheme encodes information in both the longitudinal and spatial transverse phases of a continuous-wave optical beam. One could envisage that using array detection, coupled with interferometers, multi-modal transverse and phase properties of an optical beam can be resolved.

Fig. 5.1 illustrates our idea of information encoding where an input beam in a single-mode is sent into a modal encoder (e.g. a transmissive or reflective phase mask). The encoded beam could suffer power reduction due to a variety of sources such as absorptive loss and having non-propagating evanescent wave components. The output encoded beam could have a multi-modal transverse feature, up to mode order n, when decomposed in terms of the input modal basis. All the possible encoded information would then be described by functions f_m which are dependent on the modal components $E_1, \cdots, E_n$. In order for the phase coding scheme to have successful encoding, the number of functions

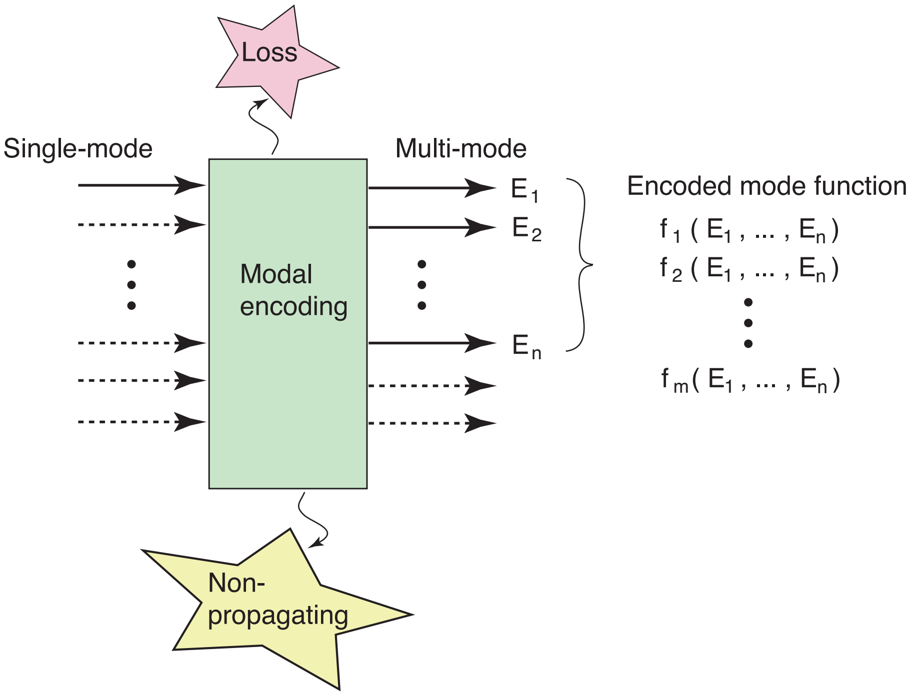

Figure 5.1: The input field consists of a single-mode mean field, represented by the solid-line arrow. The broken-line arrows represent vacuum mode coupling in other orthogonal modes to the single-mode mean field. The output field consists of a multi-mode expansion of means fields E_n, in terms of the input mode basis, represented by the solid-line arrows. The broken-line arrows show the vacuum modes. The possible functions to describe the encoded information is represented by $f_m(E_1, \cdots, E_n)$.

has to be less than or equal to the total number of mode components (i.e. $m \leq n$). To achieve dense-coding capacities, the number m has to be maximised above a certain specified signal-to-noise ratio.

In this chapter, we describe a simplified (specific) form of split detector-based interferometric scheme to optimally detect both encoded longitudinal and transverse phase signals. In contrast to present-day optical storage devices, our phase coding scheme has an information storage capacity which scales with the power of the read-out optical beam. We analyse the maximum number of encoding possibilities at the shot noise limit. In addition, we show that using squeezed light, the shot noise limit can be overcome and the number of encoding possibilities increased. We discuss a possible application of our phase coding scheme for increasing the capacities of optical storage devices, such as compact discs and digital versatile discs.

The work in this chapter has been published in the journal article:

- M. T. L. Hsu, V. Delaubert, W. P. Bowen, C. Fabre, H.-A. Bachor and P. K. Lam, “A quantum study of multibit phase coding for optical storage”, IEEE Journal of Quantum Electronics **42**, 1001 (2006).

5.1 Introduction

The optical compact disc (CD) was developed in 1979 as a collaboration between two corporations - Sony and Philips. Today, the CD has wide-ranging storage applications from the audio-visual to computer industries. The CD system is based on a 780 nm laser (laser spot size of 2.1 μm) with a storage capacity of approximately 670 MB. Since their introduction there has been increasing demand for greater storage capacities in optical discs. The digital versatile disc (DVD), based on a 650 nm laser system (spot size of 1.3 μm), was introduced. Depending on the format, it can have storage capacities ranging from 4.7 GB to 17.1 GB. More recently, the HD DVD and Blu-Ray discs based on a 405 nm laser system were released. The HD DVD system has a spot size of 0.76 μm and storage capacities of 15 GB to 45 GB, whilst Blu-Ray disc systems have a smaller spot size of 0.6 μm, with capacities of 25 GB to 100 GB [158].

Whilst nano-technology allows the fabrication of mechanical surfaces with nanometer size structures, it is the diffraction limit of the read-out optics that prevents data storage densities beyond those of present day systems. The trend of compacting more information into an optical disc therefore primarily relies on the use of shorter wavelength lasers to achieve smaller diffraction limited spot sizes. One could envisage that in the not too distant future, such improvement in the storage density would require the use of very short wavelength light beyond the ultra-violet spectrum that cannot be generated with known laser optics.

To date, there have been a number of suggested alternatives for obtaining higher optical storage densities. For example, currently under development are next generation holographic devices, the holographic versatile disc (HVD), which have capacities exceeding 300 GB through the usage of volume storage. An alternative approach depends on the encoding of spatial details beyond the diffraction limit of the read-out laser beam [158]. This approach requires the use of near-field microscopy techniques to resolve sub-diffraction limited features.

In this chapter, we revisit a well known alternative of using interferometric techniques [57, 227, 224, 225, 142, 146, 145, 55, 56, 140] to extend optical storage density. We propose to perform multi-bit phase-front coding of optical beams in an interferometric setup. Our scheme does not require holographic nor near-field optics, instead it utilises two classes of phase coding - the *longitudinal* and *spatial transverse* phases of an optical beam. We encode information in the longitudinal phase of a beam, which could take discrete values ranging from 0 to π. The total number of encodable phase values scales with the power of the read-out optical beam. We then introduce an extra encoding degree of freedom, the spatial transverse phase-front profile of the beam. Note that the spatial features of a beam are limited by diffraction. In this chapter, dense storage is achieved via small changes in longitudinal phase. We restrict all beam spatial structure to above the diffraction limit, and as a result can describe the beam using the paraxial approximation. In order to resolve the encoded longitudinal phase of the beam, an interferometric scheme is required. To resolve the spatial phase profile of the beam, a multi-segment photo-detector (e.g. a charge-coupled device (CCD)) can be used.

This chapter is sectioned as follows. We first reduce our analysis of spatial phase-front beam encoding to the situation of a two-pixel array detector, the split detector [155, 156, 151, 152, 153, 154]. We identify the possible phase profiles symmetric with a split detector and give a modal analysis for these spatial profiles. We also introduce the longitudinal phase of the beam and show how an interferometric scheme based on split detectors can be used to simultaneously obtain information on the longitudinal and spatial phases. A quantum analysis of the measurement noise is then presented. We identify the maximum number of encodable longitudinal phases at the shot noise limit (SNL). We then show that using squeezed light, one can overcome the shot noise limit and thus the number of encoding possibilities can be further increased. Consequently, we analyse the spectral properties of the signal and noise of the encoded beam. We compare single and consecutive measurement techniques, and show that consecutive measurements provides an improved signal-to-noise ratio (SNR), whilst ensuring compatibility with squeezed light frequency regimes.

5.2 Classical Phase Coding

We consider the detection of a specific set of possible transverse and longitudinal phase transformations of a TEM$_{00}$ field. To detect such transformations requires a spatially selective detection system such as a CCD array, split detector or specifically configured homodyne detector [149]. Split detectors in particular offer fast response (in the GHz regime) and high efficiency. These factors are critical in high bandwidth optical systems. We therefore concentrate our analysis on split detectors.

Restricting our analysis to one dimension, the set of eigenmodes that best describe split detectors is the flipped eigenmode basis [203, 207], as defined in Chapter 3.

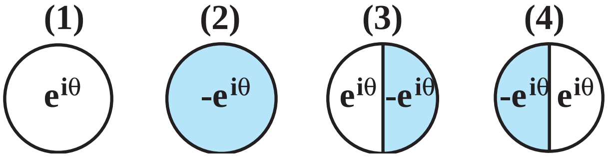

Figure 5.2: The four possible phase-front profiles resulting from the transformation on the input $u_0(x)$ beam.

To encode split detector compatible information on the phase-front of a TEM$_{pq}$ beam, π phase flips of this kind should therefore be applied. This results in four possible bit values, corresponding to the four possible two-pixel π phase shifts on $u_0(x)$, as illustrated in Fig. 5.2. A longitudinal phase factor $e^{i\theta}$ is also introduced to increase the total number of encoding possibilities. The phase coded modes introduced in Fig. 5.2 are described by the following transformation

$$u_0(x) \xrightarrow{(1)} e^{i\theta}u_0(x) \tag{5.1}$$

$$u_0(x) \xrightarrow{(2)} -e^{i\theta}u_0(x) \tag{5.2}$$

$$u_0(x) \xrightarrow{(3)} e^{i\theta}u_{f0}(x) \tag{5.3}$$

$$u_0(x) \xrightarrow{(4)} -e^{i\theta}u_{f0}(x). \tag{5.4}$$

In order to resolve the four possible phase-front profiles of Eqs. (5.1)-(5.4), we propose the phase coding scheme shown in Fig. 5.3. Beam 1 undergoes a phase-front transformation upon traversing a phase object (PO), resulting in transformed beam 3. Subsequently, beams 2 and 3 are combined on a 50:50 beam-splitter and the two output beams are detected using split detectors. Each field can be represented by the positive frequency part of its mean electric field $\mathcal{E}^+e^{-i\omega t}$, where ω is the optical frequency. We are interested in the transverse information described fully by the slowly varying field envelope $\mathcal{E}^+$. For a measurement performed in an exposure time T, the mean field for input beams 1 and 2 are given by

$$\mathcal{E}_1^+(x,t) = i\sqrt{\frac{\hbar\omega}{2\epsilon_0 cT}}\alpha_0(t)u_0(x) \tag{5.5}$$

$$\mathcal{E}_2^+(x,t) = ie^{i\phi}\sqrt{\frac{\hbar\omega}{2\epsilon_0 cT}}\beta_0(t)u_0(x) \tag{5.6}$$

where $\alpha_0(t)$ and $\beta_0(t)$ are the coherent amplitudes of the TEM$_{00}$ input beams 1 and 2, respectively. ϕ represents the longitudinal phase of beam 2.

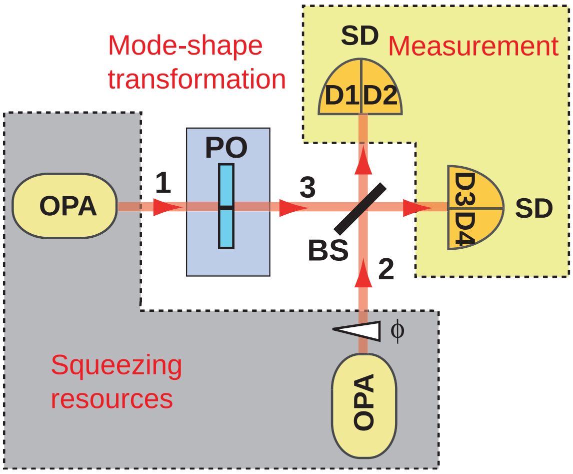

Figure 5.3: Two-pixel phase coding scheme. BS: beam-splitter, SD: split-detector. D1, D2, D3, D4: labels for the split detector segments. OPA: optical parametric amplifier, PO: phase object.

The photo-current signal for all segments of the split detectors are then calculated. The photo-current signal is related directly to the mean photon number, given by $n_{x<0} = \frac{2\epsilon_0 cT}{\hbar\omega}\int_{-\infty}^{0} dx\mathcal{E}^\dagger\mathcal{E}$ and $n_{x>0} = \frac{2\epsilon_0 cT}{\hbar\omega}\int_{0}^{\infty} dx\mathcal{E}^\dagger\mathcal{E}$, for split detector $x<0$ and $x>0$ segments, respectively.

Table 5.1: The photo-current signal terms.

Transformed Mode	Combination **A** $(D_1 - D_2)$ $+(D_3 - D_4)$	Combination **B** $(D_1 + D_2)$ $+(D_3 + D_4)$	Combination **C** $(D_1 - D_2)$ $-(D_3 - D_4)$	Combination **D** $(D_1 + D_2)$ $-(D_3 + D_4)$
$e^{i\theta}u_0(x)$	0	$\alpha_0^2 + \beta_0^2$	0	$2\alpha_0\beta_0\sin(\phi-\theta)$
$-e^{i\theta}u_0(x)$	0	$\alpha_0^2 + \beta_0^2$	0	$-2\alpha_0\beta_0\sin(\phi-\theta)$
$e^{i\theta}u_{\rm f0}(x)$	0	$\alpha_{\rm f0}^2 + \beta_0^2$	$2\alpha_{\rm f0}\beta_0\sin(\phi-\theta)$	0
$-e^{i\theta}u_{\rm f0}(x)$	0	$\alpha_{\rm f0}^2 + \beta_0^2$	$-2\alpha_{\rm f0}\beta_0\sin(\phi-\theta)$	0

We consider four possible combinations for the pair-wise photo-current addition and subtraction, with the photo-current signal terms shown in Table 5.1. The table shows that for both combinations **A** and **B**, all four mode transformations have identical signal values of 0 and $\alpha_0(t)^2 + \beta_0(t)^2$, respectively. Thus the phase-front transformation on the input beam cannot be determined. Combinations **C** and **D**, on the other hand, allow the $u_{\rm f0}(x)$ and $u_0(x)$ modes to be detected respectively with a sign change for the different phase-front transformation. Moreover, the phase coding scheme is sensitive to the differential longitudinal phase $(\theta - \phi)$.

Note that ϕ has to be calibrated in order to determine the encoded phase θ. ϕ is scanned between 0 and π until an extremum value of $\pm 2\alpha_0\beta_0$ is obtained. For example, for combination **D**, a value of $-2\alpha_0\beta_0$ for $\phi = \phi_{\rm opt}$ tells us that the encoded mode-shape is $-u_0(x)$ with longitudinal phase $\theta = \pi/2 - \phi_{\rm opt}$. The maximal signal is obtained for a phase difference of $\phi - \theta = \pi/2$. This interferometric scheme therefore enables a unique distinction of all of the four phase-front transforms given in Eqs. (5.1)-(5.4).

5.3 Quantum Phase Coding

We would like to quantify the maximum number of encoding possibilities, whose limit is ultimately set by the SNL. The SNL is identified and ways to improve the sensitivity of the measurement using squeezed light are shown. Consider the field operators in the sideband frequency domain, Ω. For brevity, we do not explicitly denote the frequency dependence for the field operators hereon, which are given by

$$\begin{aligned} \hat{\mathcal{E}}_1^+ &= i\sqrt{\frac{\hbar\omega}{2\epsilon_0 cT}}\left(\alpha_0 u_0(x) + \sum_{n=0}^{\infty}\delta\hat{a}_n u_n(x)\right) && (5.7)\\ \hat{\mathcal{E}}_2^+ &= ie^{i\phi}\sqrt{\frac{\hbar\omega}{2\epsilon_0 cT}}\left(\beta_0 u_0(x) + \sum_{n=0}^{\infty}\delta\hat{b}_n u_n(x)\right), && (5.8)\end{aligned}$$

where the first terms are the coherent amplitude of the $u_0(x)$ mode. The second terms are the quantum fluctuations $\delta\hat{a} = \hat{a} - \langle\hat{a}\rangle$ and $\delta\hat{b} = \hat{b} - \langle\hat{b}\rangle$, with $\hat{a}$ and $\hat{b}$ being annihilation operators, of beams 3 and 2 in Fig. 5.3, respectively. Depending on the phase-front transformation on beam 1, the field operator describing beam 3 is given by

$$\begin{aligned} \hat{\mathcal{E}}_3^{(1)+} &= ie^{i\theta}\sqrt{\frac{\hbar\omega}{2\epsilon_0 cT}}\left(\alpha_0 u_0(x) + \sum_{n=0}\delta\hat{a}_n u_n(x)\right)\\ \hat{\mathcal{E}}_3^{(2)+} &= -ie^{i\theta}\sqrt{\frac{\hbar\omega}{2\epsilon_0 cT}}\left(\alpha_0 u_0(x) + \sum_{n=0}\delta\hat{a}_n u_n(x)\right)\\ \hat{\mathcal{E}}_3^{(3)+} &= ie^{i\theta}\sqrt{\frac{\hbar\omega}{2\epsilon_0 cT}}\left(\alpha_{\rm f0} u_{\rm f0}(x) + \sum_{n=0}\delta\hat{a}_{\rm fn} u_{\rm fn}(x)\right)\\ \hat{\mathcal{E}}_3^{(4)+} &= -ie^{i\theta}\sqrt{\frac{\hbar\omega}{2\epsilon_0 cT}}\left(\alpha_{\rm f0} u_{\rm f0}(x) + \sum_{n=0}\delta\hat{a}_{\rm fn} u_{\rm fn}(x)\right)\end{aligned} \quad (5.9)$$

where the superscript denotes the transformations corresponding to Eqs. (5.1)-(5.4).

The RF photo-current for all segments of the split detectors are then calculated similarly to the previous section. The overlap integrals in the expressions for the photo-current sum and difference operators are simplified using the respective orthogonality properties of the $u_n(x)$ and $u_{\rm fn}(x)$ modes [204, 1, 205].

The photo-current noise corresponding to combinations **C** and **D** are shown in Table 5.2, where we have defined the quadrature noise operator as $\delta\hat{X}_a^{\psi} = e^{-i\psi}\delta\hat{a} + e^{i\psi}\delta\hat{a}^{\dagger}$. We assume the phase-front transformation is loss-less. Therefore the photon statistics of the transformed field are unchanged relative to the initial field, so that $|\alpha_{\text{f}0}| = |\alpha_0| = |\alpha|$ and $\langle(\delta\hat{X}_{a_{\text{f}0}}^{\psi})^2\rangle = \langle(\delta\hat{X}_{a_0}^{\psi})^2\rangle = \langle(\delta\hat{X}_{a}^{\psi})^2\rangle$. Table 5.2 therefore suggests that squeezing the input beams 1 and 2 will lead to enhanced noise performances.

Table 5.2: Photo-current noise.

Transformed Mode	Combination **C** $(D_1 - D_2) - (D_3 - D_4)$	Combination **D** $(D_1 + D_2) - (D_3 + D_4)$
$e^{i\theta}u_0(x)$	$-\beta_0\delta\hat{X}_{a_{\text{f}0}}^{(\phi-\theta+\pi/2)} + \alpha_0\delta\hat{X}_{b_{\text{f}0}}^{(\theta-\phi+\pi/2)}$	$-\beta_0\delta\hat{X}_{a_0}^{(\phi-\theta+\pi/2)} + \alpha_0\delta\hat{X}_{b_0}^{(\theta-\phi+\pi/2)}$
$-e^{i\theta}u_0(x)$	$\beta_0\delta\hat{X}_{a_{\text{f}0}}^{(\phi-\theta+\pi/2)} - \alpha_0\delta\hat{X}_{b_{\text{f}0}}^{(\theta-\phi+\pi/2)}$	$\beta_0\delta\hat{X}_{a_0}^{(\phi-\theta+\pi/2)} - \alpha_0\delta\hat{X}_{b_0}^{(\theta-\phi+\pi/2)}$
$e^{i\theta}u_{\text{f}0}(x)$	$-\beta_0\delta\hat{X}_{a_{\text{f}0}}^{(\phi-\theta+\pi/2)} + \alpha_{\text{f}0}\delta\hat{X}_{b_0}^{(\theta-\phi+\pi/2)}$	$-\beta_0\delta\hat{X}_{a_0}^{(\phi-\theta+\pi/2)} + \alpha_{\text{f}0}\delta\hat{X}_{b_{\text{f}0}}^{(\theta-\phi+\pi/2)}$
$-e^{i\theta}u_{\text{f}0}(x)$	$\beta_0\delta\hat{X}_{a_{\text{f}0}}^{(\phi-\theta+\pi/2)} - \alpha_{\text{f}0}\delta\hat{X}_{b_0}^{(\theta-\phi+\pi/2)}$	$\beta_0\delta\hat{X}_{a_0}^{(\phi-\theta+\pi/2)} - \alpha_{\text{f}0}\delta\hat{X}_{b_{\text{f}0}}^{(\theta-\phi+\pi/2)}$

We now determine the maximum number of encoding possibilities in our phase coding scheme. The encoding limit is determined by the minimum longitudinal phase difference detectable $\Delta\theta_{\text{min}}$. This corresponds to when the signal and noise variances are equal (i.e. SNR =1).

The SNR is calculated by taking the ratio of the signal and noise variances, given by $\langle n\rangle^2$ and $\langle\delta\hat{n}^2\rangle$, respectively. The corresponding SNR of the measurement for the $\pm u_0$ and $\pm u_{\text{f}0}$ modes are denoted by $\mathcal{R}_{\mathbf{C}}$ and $\mathcal{R}_{\mathbf{D}}$, respectively, and have the same form given by

$$\mathcal{R} = \frac{4\alpha_0^2\beta_0^2\sin^2(\phi-\theta)}{\alpha_0^2\langle(\delta\hat{X}_{b_0}^{\psi})^2\rangle + \beta_0^2\langle(\delta\hat{X}_{a_0}^{\psi})^2\rangle} \tag{5.10}$$

If the input beams are coherent with $\langle(\delta\hat{X}_{a_0}^{\psi})^2\rangle = \langle(\delta\hat{X}_{b_0}^{\psi})^2\rangle = 1$, then $\mathcal{R}^{\text{coh}} = 4\alpha_0^2\beta_0^2\sin^2(\phi-\theta)/(\alpha_0^2+\beta_0^2)$. This coherent state SNR serves as a benchmark, for comparison with the SNR achievable with squeezing. For quadrature squeezed input beams 1 and 2 (i.e. $\langle(\delta\hat{X}_{a_0}^{\psi})^2\rangle, \langle(\delta\hat{X}_{b_0}^{\psi})^2\rangle < 1$), we see directly that $\mathcal{R}^{\text{sqz}} > \mathcal{R}^{\text{coh}}$. Squeezed input beams therefore increase the SNR achievable for all possible mode transformations.

Note that in the limit $\beta_0 \gg \alpha_0$, our phase imaging scheme reduces to that of a homodyne measurement with a SNR given by $\mathcal{R}_{\text{hom}} = 4\alpha_0^2\sin^2(\phi-\theta)/\langle(\delta\hat{X}_{a_0}^{\psi})^2\rangle$. The signal and noise contribution arise from the transverse mode defined by the local oscillator mode-shape.

The minimum longitudinal phase difference detectable (i.e. SNR =1) is given by

$$\Delta\theta_{\text{min}} = \sin^{-1}\sqrt{\frac{\alpha_0^2\langle(\delta\hat{X}_{b_0})^2\rangle + \langle(\delta\hat{X}_{a_0})^2\rangle\beta_0^2}{4\alpha_0^2\beta_0^2}} \tag{5.11}$$

where we have assumed that the phase difference between beams 2 and 3 have been optimised to $\phi - \theta = \pi/2$. Since the longitudinal phase of beam 3 is determined modulo π, the total number of resolvable phase levels is $\pi/\Delta\theta_{\text{min}}$, which scales with the power of the read-out optical beam α. Note that this contrasts with conventional optical storage devices which are restricted to only two encodable values (i.e. '0' and '1'), with a SNR proportional to the power of the read-out beam.

Including the four possible transverse encoding combinations, the total number of encodable levels for our phase coding scheme is therefore given by

$$L_{\max} = \frac{4\pi}{\Delta\theta_{\min}} \tag{5.12}$$

We now consider $L_{\max}$ levels for a fixed optical power and show how this can be improved via squeezing. The mean number of photons per bandwidth-time in an optical field $\bar{n}$ can be related to its coherent amplitude α, amplitude $\langle(\delta\hat{X}^{+})^2\rangle$ and phase $\langle(\delta\hat{X}^{-})^2\rangle$ quadrature noise variances by

$$\bar{n} = \frac{1}{4}(\alpha^2 + \langle(\delta\hat{X}^{+})^2\rangle + \langle(\delta\hat{X}^{-})^2\rangle - 2). \tag{5.13}$$

The first thing to note is that for squeezed states, $\bar{n}$ is non-zero even when $\alpha = 0$. Indeed, as the squeezing increases (for amplitude squeezing $\langle(\delta\hat{X}^{+})^2\rangle \rightarrow 0$ and $\langle(\delta\hat{X}^{-})^2\rangle \rightarrow \infty$) $\bar{n}$ increases monotonically. With regards to our phase-front detection scheme, these photons do not contribute to the signal, α, and therefore for a given optical power, $\bar{n}$, a balance must be obtained between using photons to minimise the noise (maximise the squeezing), and to maximise the signal (maximise α).

In this section, $L_{\max}$ for a fixed optical power was maximised numerically. This was performed over all possible ratios of photons used to minimise the noise, and those used to maximise the signal. The total optical power is the sum of the number of photons in each of the input beams, each individually given by Eq. (5.13). We considered three cases. In the first case, to provide a benchmark, we considered $L_{\max}$ levels when no squeezing was available, and both input beams were coherent. In the second case, squeezing was allowed for beam 1 but beam 2 was coherent. In the third case, both input beams were squeezed. The maximum $L_{\max}$ levels for each of these cases is shown in Fig. 5.4. We see that by far, the best $L_{\max}$ levels is achieved when both beams are allowed to be squeezed, with $\sim 25\%$ capacity improvement over the coherent state case when 100 photons per bandwidth-time are used. In the case of only one squeezed beam, the capacity improvement is $\sim 10\%$.

Of course, due to decoherence and inefficiencies, arbitrary levels of squeezing are not available. Therefore, it is interesting to consider not only the maximum $L_{\max}$ levels that can be achieved, but also whether the amount of squeezing required to achieve it are feasible. The amount of squeezing required to achieve the maximum $L_{\max}$ levels for a given total photon number are shown in Fig. 5.5 for both the one squeezed beam and two squeezed beam cases. In both cases, when less than 10 photons per time are utilised, squeezing levels below 10 dB are required. Although challenging, such levels of squeezing are experimentally achievable [176]. For more than 10 photons per bandwidth-time however, the level of squeezing required to achieve the maximum encodable levels fast becomes unfeasible. Therefore, utilising squeezed light in the phase-front detection scheme presented here will only be beneficial when less than 10 photons are available per measurement interval.

Coherent beams can allow a large number of encodable levels. Assuming similar parameters to CD technology and idealised shot noise limited performance, we can encode up to 5000 levels, for a 1 mW beam (λ = 780 nm, spot size = 2.1μm) in the limit that $\beta_0 \gg \alpha$, during a 10 μs measurement time (where SNR = 60 dB, based on current technology specifications). Therefore up to 12-bit encoding per site is possible. The capacity of CDs can be potentially increased to 8 GB. For lower SNR standards (SNR=50), 19-bit encoding per site can be achieved, giving a capacity increase of up to 13 GB. Squeezing can further improve the maximum encodable levels in the limit of low laser power. Similar

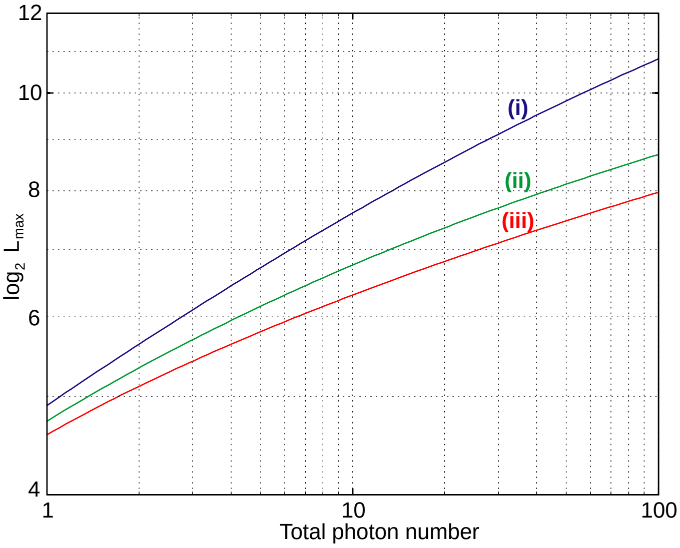

Figure 5.4: Maximum $\log_2 L_{\mathrm{max}}$ levels of the phase-front coding scheme as a function of the total mean number of photons / (Hz.s) utilised in the protocol. (i) Both input beams amplitude squeezed, (ii) beam 1 amplitude squeezed and beam 2 coherent, (iii) both input beams coherent.

to the multi-bit encoding schemes of P. Török's group [158], our scheme is a significant improvement over current technology where only one bit per site is encoded.

5.4 Potential Application to Optical Storage

In this section, we investigate the compatibility of our phase coding scheme with an optical disc read-out scheme.

5.4.1 Optical disc scheme

In conventional CDs, the information is encoded in binary format, by burning physical indentations (commonly termed 'pits') on the disc. Regions where no physical indentations exist are termed 'lands'. A transition between 'pit' and 'land' encodes for '1', whereas no transition encodes for '0' [248]. The reflected beam intensity from a focussed laser beam onto the disc allows bit read-out, as the beam undergoes large diffractive losses when impinging on a 'land'-'pit' transition.

We propose to store more than one level on a single 'pit' site, by encoding levels as shown on Fig. 5.6. The information is contained in the longitudinal and transverse phase domains for each 'pit'. The longitudinal phase is determined by the depth of the 'pit', $\lambda\theta/(2\pi)$, while the transverse phase profile is determined from its shape. By assuming that the phase transformation structure is larger than the diffraction limit, and since the longitudinal phase shift is not constrained by the diffraction limit, we can assume that the reflected field has the same transverse profile as in Fig. 5.2. Note that when the transverse structure is below the diffraction limit, the beam profiles of Fig. 5.2 cannot be generated [60]. In this situation, two approaches can be used to obtain the transverse profile of the read-out beam - (i) by using Maxwell's equations, and/or (ii) by performing an initial

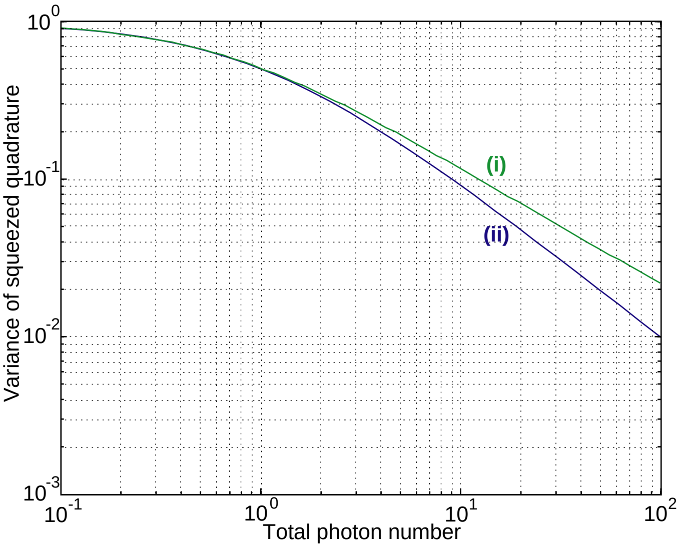

Figure 5.5: Shot noise normalised level of squeezing required to achieve the optimum number of encodable levels as a function of the total mean number of photons per bandwidth-time utilised in the protocol. (i) Beam 1 amplitude squeezed and beam 2 coherent, (ii) both input beams amplitude squeezed.

experimental calibration of all the possible transverse mode profiles, since we posses *a priori* knowledge of the transverse phase structures.

Therefore, the reflection of the read-out beam has one of the four possible transverse mode profiles, ±u$_0$(x) or $\pm u_{f0}(x)$, with an additional global phase shift θ. This reflected beam (i.e. beam 3) can then be combined with beam 2 on a 50:50 beam-splitter, as shown in Fig. 5.3 to perform the phase information decoding.

Thus far, our analysis has not considered the spectral properties of the read-out signal and noise. Since the optical disc is spinning and the laser read-out time is limited, the spectral power density of a realistic optical disc detection differs from that of an idealised static phase sensing scheme. We examine these issues in the following subsections.

5.4.2 Spectral power density for a single measurement

We first consider the information extraction from a time-limited static disc read-out. N photons are detected in a time interval T, as represented on the inset of Fig. 5.7, where the integrated photo-current provides the encoded information.

Using a single top hat function as a time measurement window, the Wiener-Khinchine relation yields the signal power spectral density (PSD), $\mathcal{S}_1(\nu)$ [249]. In the case of a double sided power spectrum, the signal PSD is given by [249]

$$\mathcal{S}_1(\nu) = T\left[\int_{-\infty}^{\infty} s(\nu').\mathrm{sinc}(\pi T(\nu'-\nu))d\nu'\right]^2 \tag{5.14}$$

where ν is the frequency and $s(\nu)$ is the signal linear spectral density in the limit of an infinite time measurement, defined as $s(\nu)=\sqrt{\mathcal{S}(\nu)}$. $\mathcal{S}(\nu)$ is the number of photons per bandwidth-time.

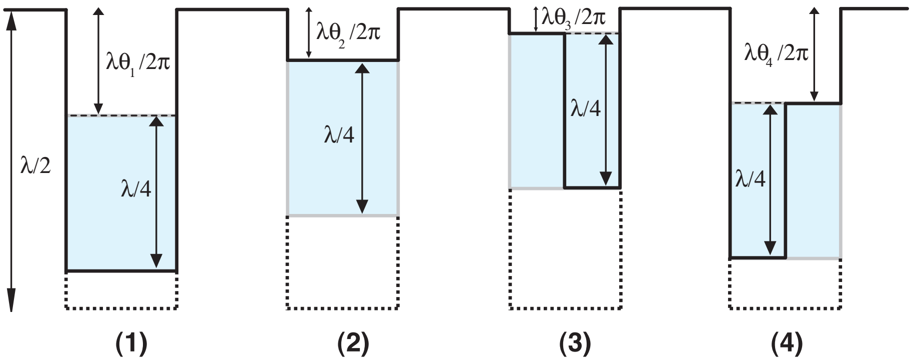

Figure 5.6: Examples of bit encoding allowing denser information storage on optical discs. The binary information is encoded in the transverse and longitudinal phases of the reflected read-out laser beam. The depth of the 'pit' can range from discrete values between 0 and $\lambda/2$. Hence $\theta_1 \in (\lambda/4, \lambda/2]$ and $\theta_2 \in (0, \lambda/4]$, where λ is the laser wavelength and θ is the longitudinal phase shift of the laser beam. Note that the 'pit' depth is half that of the phase shift experienced by the read-out laser beam due to a round-trip propagation from the optical disc.

For a single measurement, $s(\nu)$ is given by $s(\nu) = N\delta(\nu)$, where N is the number of photons per time in the signal and $\delta(\nu)$ is a delta function centred at DC. Thus Eq. (5.14) becomes

$$\mathcal{S}_1(\nu) = N^2 T \mathrm{sinc}^2(\pi T \nu) \tag{5.15}$$

where the signal PSD has a squared cardinal sine distribution with a maximum at DC. Fig. 5.7 shows the normalised signal and noise PSD.

The noise power spectral density, $\mathcal{N}(\nu) = \xi(\nu)^2$ is now obtained. We assume that read-out lasers are shot noise limited. Thus the noise linear spectral density is white and proportional to $\sqrt{N}$, given by $\xi(\nu) = \sqrt{N}$. The integration time in our measurement is T and the noise PSD is given by

$$\mathcal{N}_1(\nu) = NT \left[\int_{-\infty}^{\infty} \mathrm{sinc}(\pi T(\nu' - \nu)) d\nu' \right]^2 = \frac{N}{T} \tag{5.16}$$

where the white noise spectrum has an amplitude of $\sqrt{N/T}$. We have chosen $N = 1/T^2$ for Fig. 5.7 such that the noise power is approximately equal to the maximum signal power.

The typical measurement time of a DVD device is $T = 0.1$ μs, corresponding to $N = 10^{14}$ photons/s for a read-out laser of 20 μW power at a wavelength of $\lambda \simeq 1$ μm. The signal spectrum therefore is in the DC to 10 MHz regime. Improvements on the measurement sensitivity beyond the shot noise limit thus requires broadband squeezing from DC to 10 MHz. Although low frequency squeezing has recently been demonstrated [24, 250], many technical challenges exist.

An alternative solution, compatible with current technology, could be the sampling or modulation of the read-out beam to artificially shift the signal to a higher frequency range. For optical discs rotating at approximately 10 bit/μs (4.32 Mb/s for CDs, and 26.16 Mb/s for DVDs), the sampling or modulation frequencies can be at least 1 GHz, which is compatible with squeezing frequency ranges. However, the disadvantage of such an approach is that the photon number in the signal sidebands is low. The majority of the

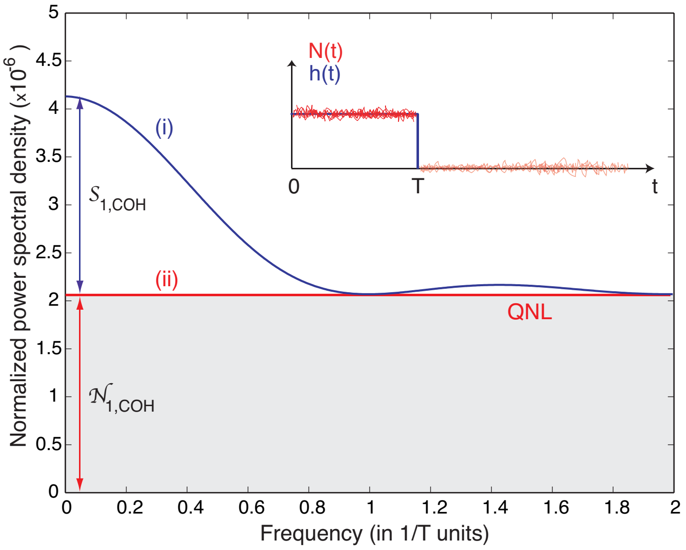

Figure 5.7: The normalised (i) signal $\mathcal{S}_1(\nu)$ and (ii) noise $\mathcal{N}_1(\nu)$ PSD for a single measurement in a time interval T. $\mathcal{S}_1(0)$ and $\mathcal{N}_1(0)$ are the maximum signal and noise powers at DC. The inset shows the sequence corresponding to a single top hat measurement window, $h(t)$, with $N(t)$ photons.

photons are still distributed in the frequency regime around DC. Thus the improvement in the SNR may not be significant.

5.4.3 Spectral power density for consecutive measurements

We now propose to perform consecutive 'pit' measurements where the centre of the signal PSD is shifted to a higher frequency. Two consecutive measurements of the variable $N(t)$ during two time intervals of length T, separated by a delay T', is shown schematically on the inset of Fig. 5.8.

The difference between two consecutive measurements yields a signal PSD given by the contribution of each individual sine-wave at frequency ν, to the total signal, and averaging over all possible initial phases Θ, giving

$$\mathcal{S}_2(\nu) = \mathcal{S}(\nu)\eta_2(\nu) \tag{5.17}$$

where $\eta_2(\nu)$ is given by

$$\eta_2(\nu) = \kappa\Big\langle \left(\int_0^T - \int_{T+T'}^{2T+T'} \sin(2\pi\nu t + \Theta) dt \right)^2 \Big\rangle \tag{5.18}$$

and where κ is a normalisation constant. Note that a similar calculation can be applied to the single measurement case.

The signal and noise PSD for $T' = 0$ are shown in Fig. 5.8. The signal PSD is shifted to the MHz frequency regime (which is more compatible with routinely obtained experimental squeezing frequency regimes). The signal PSD maximum is at $\nu \sim 0.35/T$ for $T' = 0$. This is also the regime where the bandwidth is maximum. Increasing T' shifts the maximum

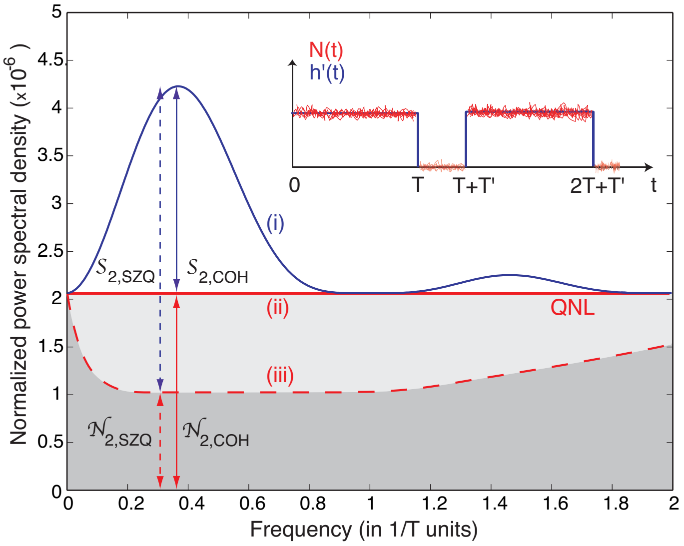

Figure 5.8: (i) Normalised signal $\mathcal{S}_2(\nu)$, (ii) shot noise and (iii) squeezed noise $\mathcal{N}_2(\nu)$ PSD for two consecutive measurements of time intervals T separated by a delay $T' = 0$. The maximum signal and noise powers are respectively, $\mathcal{S}_{2,\mathrm{COH}}$ and $\mathcal{N}_{2,\mathrm{COH}}$, for a coherent state read-out laser at $\nu \sim 0.35/T$. In the case of a squeezed read-out laser, the maximum signal and noise powers are denoted by $\mathcal{S}_{2,\mathrm{SQZ}}$ and $\mathcal{N}_{2,\mathrm{SQZ}}$, respectively. The inset shows the sequence corresponding to two consecutive measurements.

signal power to lower frequencies and sharpens the distribution. Thus the bandwidth reduces with increasing T'. For $T' = T$, the maximum signal power is for example ~ 1.5 times larger than that for the $T' = 0$ case and occurs at $\nu \sim 0.2/T$, whereas the bandwidth reduces by half. T' can thus be tuned to obtain an optimum for signal power, bandwidth and compatibility with squeezing frequencies.

The SNR of interest in our optical memory scheme corresponds to that of a single frequency ν, as defined in Eq. (5.10). Therefore our proposed optical memory scheme will require a frequency mixer or bandpass filter centred at ν, where the measurement SNR is maximum.

Differential consecutive measurements is a technique already employed in current optical disc devices, as it allows the cancellation of common-mode classical noise, provided that the phase of the read-out laser is well calibrated in a ‘pit’-to-‘pit’ measurement. Furthermore, the maximum of the normalised PSD for consecutive measurements is slightly larger than that for the single measurement case, assuming a coherent state read-out laser with the same parameters. If a broadband 3 dB squeezed state is used as the read-out laser, the SNR doubles for consecutive measurements. However the SNR improvement for the case of a single measurement is negligible. This is because low frequency noise sources (e.g. acoustic noise) overwhelm the squeezing.

5.5 Conclusion

We have presented a scheme to perform longitudinal and transverse spatial phase coding of continuous-wave optical beams. We have shown that by performing selective combinations of photo-current addition and subtraction, the phase coded signal can be extracted. In order to optimise the phase signal, the longitudinal phase of beam 2 has to be calibrated and optimised such that $\phi = \pi/2 + \theta$. Whilst current CD technologies are limited by a number of different noise sources, such as thermal-Johnson noise and electronic noise, our analysis assumes shot noise limited performance. The maximum number of encoding possibilities for this regime was calculated, suggesting significant improvement with our phase coding scheme. However, by using squeezed light, the shot noise limit can be overcome and thus the maximum number of encodable levels increased. We then presented a possible application of our phase coding scheme in increasing the capacities of optical storage devices. We analysed the performance of single measurement techniques and showed that the signal and noise PSD are centred around DC sideband frequencies. We then analysed the PSD of differential consecutive measurements and showed that the PSD spectrum is shifted to higher sideband frequencies. In order to extract the phase signal, frequency mixing or narrow bandpass filtering techniques can be used. The differential consecutive measurement technique provides a good SNR whilst ensuring compatibility with squeezing frequencies.

Our phase coding scheme can be extended to implement a multi-pixel array detector. Delaubert *et al.* [60] has performed a quantum study of multi-pixel array detection and shown that it is possible to perform multi-pixel transverse spatial phase encoding. Possible implementation of a multi-pixel scheme would require the incorporation of multiple interferometers and the use of multi-squeezed beams or a multi-mode OPO system [251].

5.6 Future Directions

5.6.1 Quantum noise and diffraction limits

In imaging problems, the resolution of the details of an image and the signal-to-noise ratio (SNR) of the image are two factors which limit the imaging system.

The detail-resolution of an image is restricted by diffraction and involves resolving the overlapping peaks of Airy disks. A fiducial limit was correspondingly introduced, termed the *diffraction limit*, which is based on the Rayleigh criterion. For a circular aperture, the Rayleigh criterion yields the minimum resolvable angle θ, given by

$$\sin\theta = 1.22\frac{\lambda}{d} \tag{5.19}$$

where the factor of 1.22 arises from the first zero of the Airy function, λ is the wavelength and d is the aperture diameter. An imaging system is diffraction limited when the first diffraction minimum of the image overlaps with the maximum of another image. In order to increase the detail-resolution, the wavelength of the imaging light has to be reduced.

The SNR of an image scales with the number of photons in the optical field used in imaging. For a coherent state optical field, the noise in the measurement is due to that of shot noise. In order to increase the SNR, one could increase the number of photons of the imaging beam.

Kolobov and Fabre [58] discussed the limits imposed by quantum noise on the resolution of fine details in optical images. A similar analysis to Ref. [58] could be performed on our phase imaging scheme, assuming a fixed optical power, P. By increasing the number of photons, N, the image SNR increases. However, the wavelength, λ of the imaging field is also increased (since $P = Nhc/\lambda$) and therefore the detail-resolution decreases. However, one could reduce the wavelength of the imaging field to increase the detail-resolution at the expense of reducing the SNR of the image (since N decreases). Since optical power could be limited in an optical imaging system (due to photo-bleaching of image samples, limited laser power, etc.), it may be a worthwhile study to optimise the photon number and wavelength of the optical field.

Part II

Light-atom ensemble quantum interactions

Chapter 6

Experimental techniques

I don't have to have faith, I have experience.

- Joseph Campbell

6.1 Introduction

In this chapter, we introduce the common experimental techniques used in the experiments described in this thesis. The principles and techniques of laser cooling and trapping are described in Chapter 10, as those techniques are specific to the cold atom experiment.

6.2 The laser

Experiments in quantum optics rely greatly on the optical source. Therefore, an understanding of the noise properties, the frequency and intensity stability of the laser source is vital.

The laser beams used in our quantum measurements were derived from a 1 W Ti:Sapphire laser (MBR-110 from Coherent), pumped by a 7 W Verdi laser. The Ti:Sapphire laser had a bow-tie cavity configuration, with a birefringent filter used for coarse frequency tuning. Finer frequency tuning was achieved using an intra-cavity etalon. The laser was frequency locked with respect to the etalon which provided single-mode operation and medium-term frequency stability (measured drifts were approximately 20 MHz over a time window of 10 minutes). The laser was tunable in wavelength across $\sim$ 750 - 850 nm.

In order to measure the amplitude quadrature noise of the Ti:Sapphire laser, we used a self-homodyne detection scheme, shown in Fig. 6.1 (A). The measured amplitude quadrature noise of the laser is shown in Fig. 6.1 (B). The results show that the (i) laser noise is above the (ii) shot noise level, from DC-1 MHz. Therefore the laser had excess noise and was not shot noise limited within the DC-1 MHz sideband frequency range. Modulation peaks were also present on the laser, in particular a strong ($\sim$ 50 dB) etalon locking modulation signal located at 87 kHz, together with its harmonics. The (iii) dark noise of the homodyne detection was approximately 10 dB below the shot noise level.

The laser noise spectrum shows that the Ti:Sapphire laser was non-ideal for quantum measurements. The 87 kHz locking signal could saturate the RF response of detectors. Therefore checks were constantly performed to ensure that detector saturation was not occurring. The broadband 10 dB noise from DC to 1 MHz was common-mode rejected

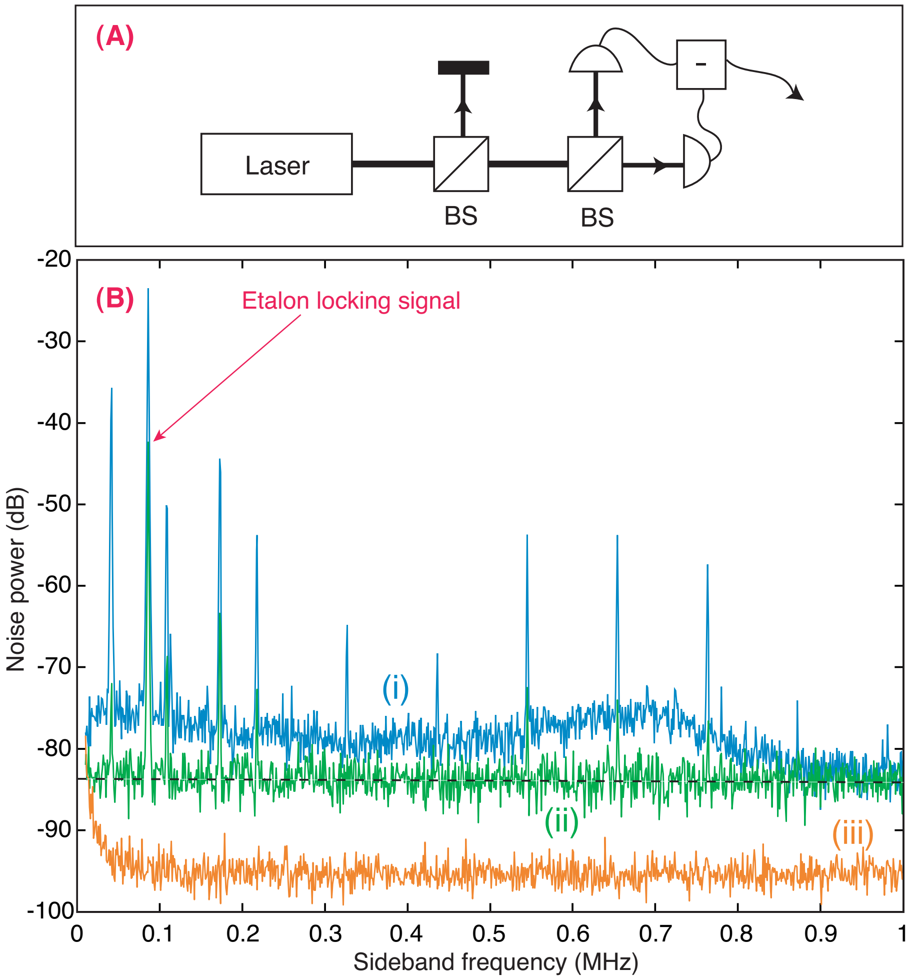

Figure 6.1: (A) Schematic diagram illustrating the self-homodyne measurement scheme. BS: beam-splitter. (B) Measurement of the amplitude quadrature noise power of the Ti:Sapphire laser, as a function of sideband frequency. The curves indicate (i) laser noise, (ii) shot noise level and (iii) detector dark noise. The resolution bandwidth is 1 kHz, video bandwidth is 1 kHz and the results were averaged over 5 measurements.

in a subtracted homodyne scheme as the homodyne detectors typically had 30-40 dB common-mode subtraction across the detection bandwidth.

A feed-forward scheme to cancel out the 87 kHz locking peak was implemented and suppression of the locking signal by up to 30 dB was achieved. However, the feed-forward scheme was not stable over long time scales and therefore the feed-forward scheme was not implemented in our experiments. An attempt was also made in implementing a feedback “noise-eating” scheme and suppression of the 87 kHz locking peak by up to 10 dB was achieved. However the suppression was not significant enough to warrant the use of a feedback noise cancellation scheme. Our feedback scheme was limited by the gain and bandwidth of the actuation stage of the feedback system.

6.3 Atomic source

Often it is not possible to resolve the atomic transitions, in a thermal cloud of atoms, via direct absorption measurement. Although the natural homogeneous linewidth of the atomic transitions may be small, the atomic transitions tend to be broadened in a vapour gas of atoms. The broadening mechanisms can be classified into two classes, *inhomogeneous* and *homogeneous broadening*. *Inhomogeneous broadening* occurs in a non-uniform manner over different atoms (e.g. Doppler broadening), whilst *homogeneous broadening* occurs uniformly across all atoms (e.g. pressure broadening). In an atomic vapour cell, as commonly used in our experiments, the main source of broadening is that due to the Doppler effect.

6.3.1 Doppler broadening

An atomic gas sample typically consists of an ensemble of atoms moving in different directions, with different velocities. The fraction of atoms within the velocity range of v to $v + dv$ is given by the Maxwell-Boltzmann distribution [252]

$$f(v)dv = \sqrt{\frac{m}{2\pi k_B T}} \exp\left(-\frac{mv^2}{2k_B T}\right) dv \tag{6.1}$$

where m is the mass of the atom, k_B is Boltzmann's constant and T is the temperature of the atomic gas.

We now discuss the Doppler effect on the absorption width of an atomic gas, illustrated in Fig. 6.2. Consider an atom moving at velocity v, in the reference frame of the laboratory (see Fig. 6.2 (A)). The atom is illuminated from two opposing directions with laser beams of frequency ω. Changing to the reference frame where the atom is at rest, the frequencies of the two laser beams are no longer ω. The laser beam from the left has a frequency of $\omega_R = \omega - kv$, which is red-shifted. The laser beam from the right is blue-shifted in frequency, to $\omega_B = \omega + kv$. The resonant frequency of the atomic transition is given by ω_0, in the reference frame of the atom, and $k = \omega_0/c$ is the wave-vector. Therefore, the laser beam is resonant with the atoms when the following condition is satisfied

$$\omega_R = \omega_0 \qquad \text{or} \qquad \omega_B = \omega_0 \tag{6.2}$$

Expressing these equations in terms of the velocity gives

$$v = \frac{c|\omega - \omega_0|}{\omega_0} \tag{6.3}$$

Since the atom is resonant with the laser for a range of frequencies ω, the absorption width of the atoms is then directly proportional to the Maxwell-Boltzmann velocity distribution function of the atoms, given by

$$A(v) = C\sqrt{\frac{m}{2\pi k_B T}} \exp\left(-\frac{mc^2|\omega - \omega_0|^2}{2k_B T\omega_0^2}\right) \tag{6.4}$$

where C is a normalisation constant. Therefore, the linewidth of the atomic transitions are broadened according to the thermal distribution of the atomic vapour cloud. A direct measurement of the natural linewidth of an atomic species in a gas sample, simply by scanning the frequency ω of the laser, is thus not possible.

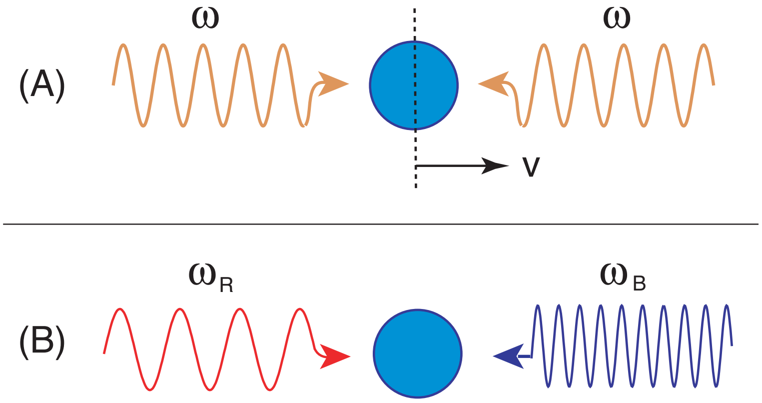

Figure 6.2: Illustration of the Doppler effect in atoms. (A) In the reference frame of the laboratory, the atom is moving in a certain direction with velocity v, and is illuminated by two counter-propagating laser beams, each with frequency ω. (B) In the reference frame of the atom, the two laser beams have different frequencies given by the red-shifted frequency ω_R and the blue-shifted frequency ω_B.

6.3.2 Saturated absorption spectroscopy

There are many techniques to perform Doppler-free spectroscopy, to resolve the atomic transitions of a thermal atom cloud sample. Examples of these techniques include, *crossed beam spectroscopy* [253], *two-photon spectroscopy* [254, 255], *laser polarisation spectroscopy* [256] and *saturated absorption spectroscopy* [257, 258]. Our experiments rely heavily on the technique of *saturated absorption spectroscopy*, which we describe in this section.

When an intense optical beam is on resonance with an atomic transition, a majority of the atoms in the ground state are raised to the excited state. The result is a depopulation of the ground state, a *hole burning* process. The width of the hole-burning is given by [252]

$$\Delta\omega_{\text{hole}} = \gamma\sqrt{1+\frac{I}{I_{\text{sat}}}} \tag{6.5}$$

where γ is the natural linewidth and I_{sat} is the saturation intensity of the atomic transition.

Saturated absorption spectroscopy consists of a strong pump beam and a weak probe beam, propagating in opposite directions, as shown in Fig. 6.3. When the frequency of the lasers are non-resonant with the atomic transition $\omega \neq \omega_0$, the pump laser burns a hole for the class of atoms which move at velocity v_1. Since the probe laser is weak, it gets absorbed by the class of atoms moving at velocity v_2. When the pump and probe lasers are resonant with the atomic transition $\omega = \omega_0$, the pump laser burns a hole for atoms with velocity $v \simeq 0$ and thus the absorption for the probe laser is reduced. For laser beams with total power $I = I_{\text{sat}}$, the width of the observed atomic transition is given by $\Delta\omega_{\text{hole}} = \sqrt{2}\gamma$, which is a factor of $\sqrt{2}$ greater than the actual hyperfine width γ, but significantly less than that of the inhomogeneous Doppler width.

An artefact of saturated absorption spectroscopy is the cross-over resonance. When the pump and probe lasers have a frequency midway between two atomic transitions, ω_1 and ω_2 (where the transitions are separated by a width $\delta_{1\to2}$, less than that of the Doppler width), an additional feature appears at the midway frequency $\omega_{1\to2}$. Since the laser frequency is midway, the pump laser will burn holes at $(\omega_1 + \delta_{1\to2})$ or $(\omega_2 - \delta_{1\to2})$.

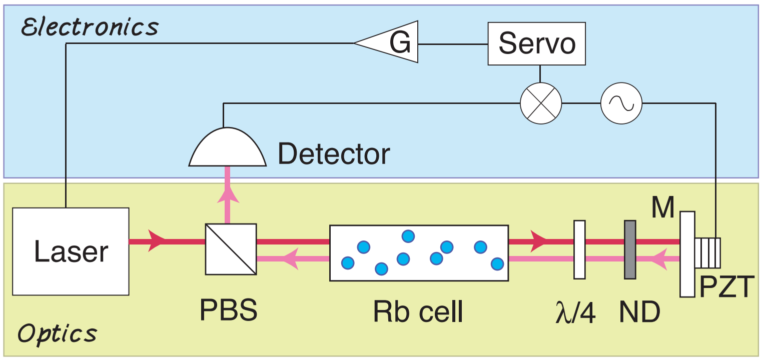

Figure 6.3: Experimental scheme for saturated absorption spectroscopy. PBS: polarising beam-splitter, $\lambda/4$: quarter wave-plate, ND: neutral density filter for attenuation, M: mirror, PZT: piezo-electric actuator.

Therefore the probe beam has reduced absorption at the midway frequency, resulting in a cross-over resonance feature.

In our experiments, the diameter of the saturated absorption spectroscopy beams were enlarged to approximately the diameter of the atomic vapour cell. This ensured more atoms were interacting with the laser beams and therefore a higher signal-to-noise ratio for the saturated absorption signals were obtained. The vapour cells were also heated to increase the atomic density.

In our experiments, we utilised two species of alkali atoms - *Rubidium-87* (^{87}Rb) and *Cesium-133* (^{133}Cs).

Rubidium-87 lines

^{87}Rb has two lines corresponding to two groups of the excited state, the $5^2S_{1/2}$ and $5^2S_{3/2}$ states. The ^{87}Rb D_2 and D_1 hyperfine transitions are shown in Fig. 6.4 (A) and (B), respectively. The ground state for ^{87}Rb is given by the $|5^2S_{1/2}, F = 1, 2\rangle$ hyperfine transitions. The excited states corresponding to wavelengths of 780 and 795 nm are given by the $|5^2P_{3/2}, F = 0, 1, 2, 3\rangle$ and $|5^2P_{1/2}, F = 1, 2\rangle$ hyperfine transitions, respectively.

Our measurements of the hyperfine structure of ^{87}Rb for the D1 and D2 lines are shown respectively in Figs. 6.5 (B) and 6.6 (B).

Cesium-133 lines

^{133}Cs has two lines corresponding to two groups of the excited state, the $6^2S_{1/2}$ and $6^2S_{3/2}$ states. The ^{133}Cs D_2 and D_1 hyperfine transitions are shown in Fig. 6.7 (A) and (B), respectively. The ground state for ^{133}Cs is given by the $|6^2S_{1/2}, F = 3, 4\rangle$ hyperfine transitions. The excited states corresponding to wavelengths of 852 and 895 nm are given by the $|6^2P_{3/2}, F = 2, 3, 4, 5\rangle$ and $|6^2P_{1/2}, F = 3, 4\rangle$ hyperfine transitions, respectively.

6.4 Laser frequency stabilisation

In order to stabilise the frequency of the laser to an atomic resonance line, an error signal is derived. Using saturated absorption spectroscopy, the atomic absorption lines become well

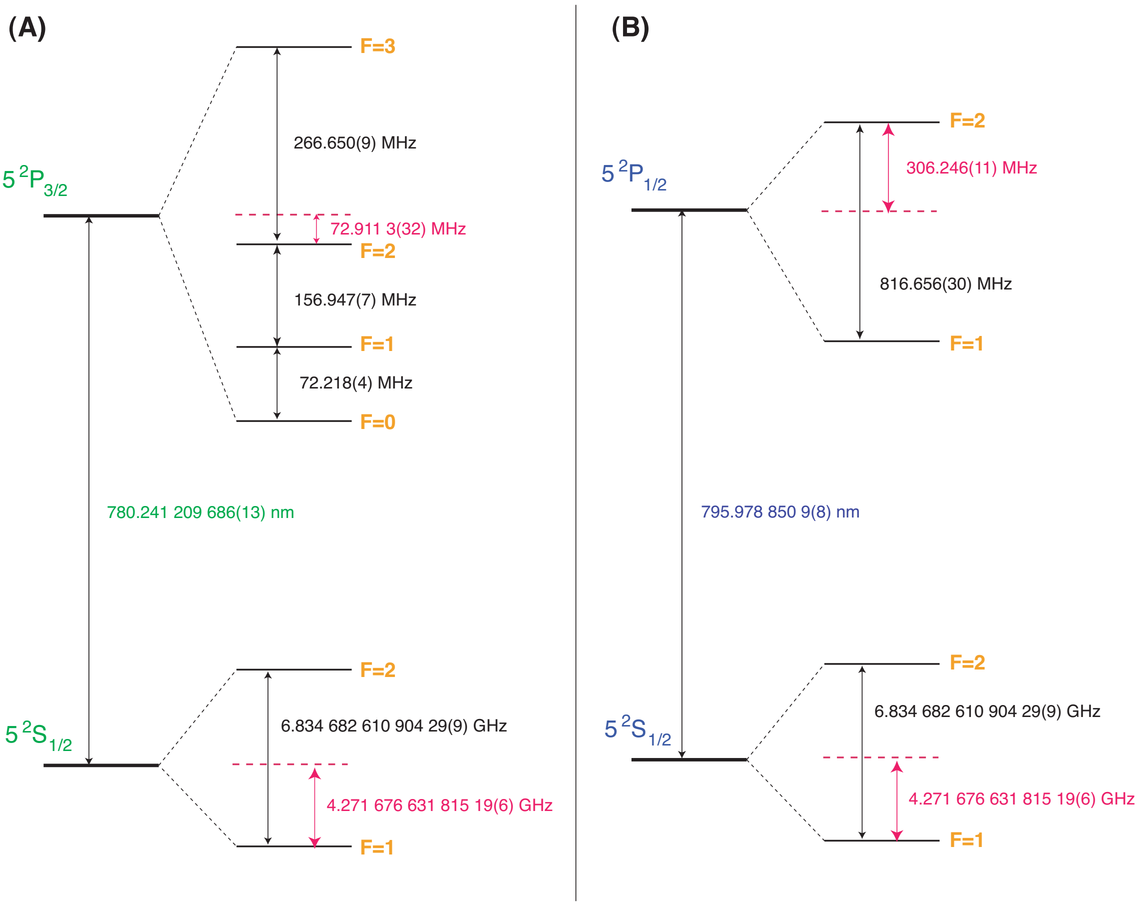

Figure 6.4: The numbers for the (A) D2 and (B) D1 lines of ^{87}Rb were obtained from [5, 6, 7]. A comprehensive line data for ^{87}Rb is given by D. A. Steck and can be obtained from http://steck.us/alkalidata/ .

resolved. Since the atomic lines have a sharp transmission profile, there is a corresponding dispersion, from the Kramers-Kronig relations [259]. Therefore, a phase modulation signal can be applied onto the probe beam to derive an error signal corresponding to the atomic hyperfine levels. The dispersion will result in the sidebands of the modulation signal to experience varying phase shifts. When the probe beam is detected and mixed down at the same frequency, the differential phase shifts are converted into an amplitude modulation signal, which constitutes the error signal [260, 261, 262]. Experimentally, we applied the phase modulation signal either by modulating the current of the diode laser, or in the case of a Ti:Sapphire laser, we used an acousto-optic modulator for modulation. The error signals corresponding to the hyperfine structure of ^{87}Rb are shown in Figs. 6.5 (A) and 6.6 (B).

6.4.1 Ti:Sapphire laser frequency stabilisation

The Ti:Sapphire laser was the main “work horse” for our experiments and stabilisation of the laser frequency was critical in most of our experiments. However the internal frequency stabilisation system for the Ti:Sapphire laser was insufficient for our experimental requirements. Within the Ti:Sapphire laser unit, the output beam was partially reflected

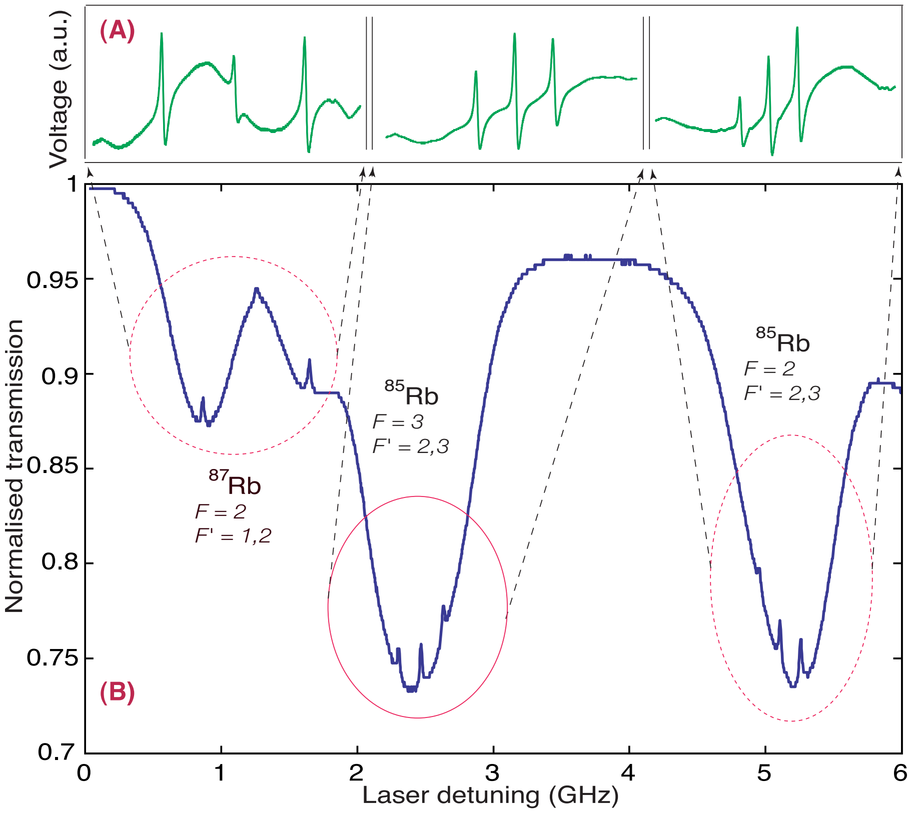

Figure 6.5: (A) Error signals and (B) saturated absorption spectroscopy signals for the D1 line of ^{87}Rb and ^{85}Rb. Note that ^{85}Rb is present in a natural mixture Rb vapour cell.

into a reference cavity to derive an error signal to stabilise the laser to the reference cavity. However, the reference cavity had a slow length drift which induced a slow frequency drift on the Ti:Sapphire laser. Therefore the Ti:Sapphire internal locking system had to be bypassed. The Ti:Sapphire laser was instead stabilised to an atomic transition, which was a significantly more stable reference than the internal reference cavity system. In order to bypass the internal locking system, a beam block was inserted in front of the photodetector that detected the reflected signal from the reference cavity; within the Ti:Sapphire laser unit.

The saturated absorption spectroscopy scheme shown in Fig. 6.3, was implemented for the Ti:Sapphire laser. The saturated absorption signal was sent to an SRS lock-in amplifier. The lock-in amplifier mixed down and filtered the photodetector signal to yield an error signal. The error signal was then fed to a home-built servo system and consequently to the Ti:Sapphire laser.

The procedures for the Ti:Sapphire laser locking involved first scanning the frequency of the laser as this gave an indication of the laser frequency. In order to lock to the desired atomic transition, the scan amplitude (i.e. scan width) was reduced. The scan offset was correspondingly adjusted such that the zero-crossing of the error signal always remained at the centre of the scan. This procedure was performed until the scan amplitude was turned down to zero. At this stage, the gain of the error signal into the laser was increased. The DC level of the absorption signal was observed and should be stabilised to the peak

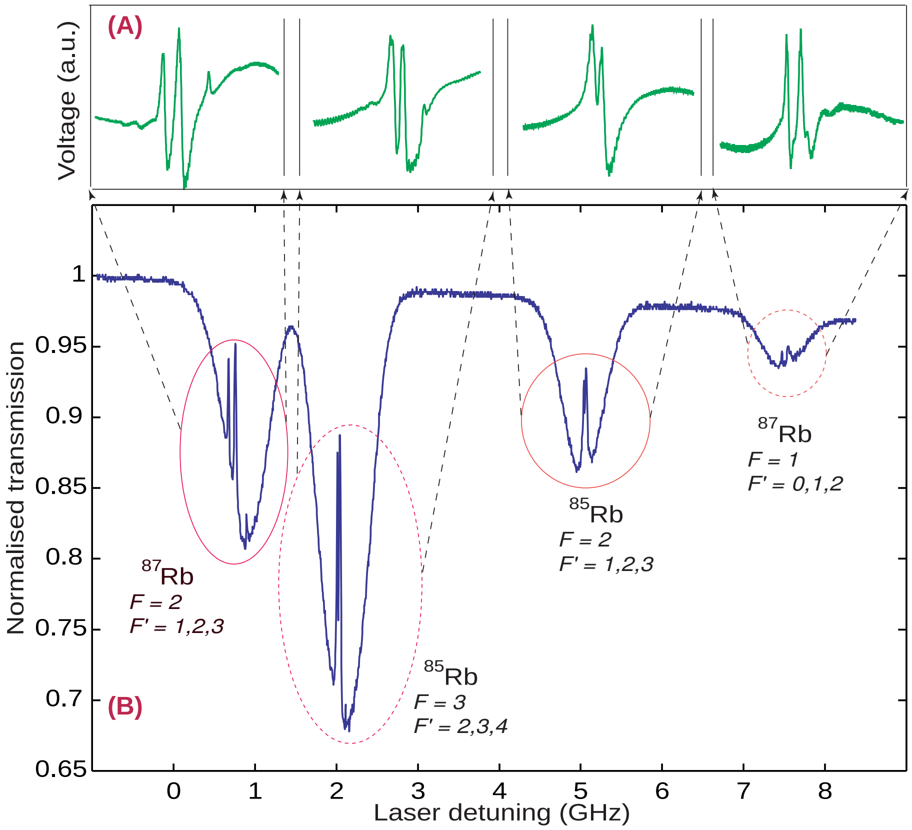

Figure 6.6: (A) Error signals and (B) saturated absorption spectroscopy signals for the D2 line of ^{87}Rb and ^{85}Rb. Note that ^{85}Rb is present in a natural mixture Rb vapour cell.

level of the relevant atomic transition. Thereafter, the integrator circuit was turned on, providing integration of the error signal between DC-100 Hz, to yield higher gain at low frequencies.

6.4.2 Diode laser frequency stabilisation

We also utilised extended cavity diode lasers (ECDLs) in our experiments, particularly for the magneto-optical trap experiments. In order to derive the error signal for frequency stabilisation of ECDLs, the saturated absorption setup shown in Fig. 6.3 was used. The current of the ECDL was modulated to provide phase modulation. Alternatively, a phase modulation signal can be applied on the probe beam, via the use of a piezo-electric actuator mounted on the retro-reflecting mirror, shown in Fig. 6.3. The detected signal from the saturated absorption setup was then detected and mixed down to yield an error signal. The error signal was fed into a servo system, which was then fed back to the PZT controlling the grating angle in the ECDL. Since tuning of the grating angle alters the frequency of the ECDL, the feedback stabilised the ECDL to atomic resonance.

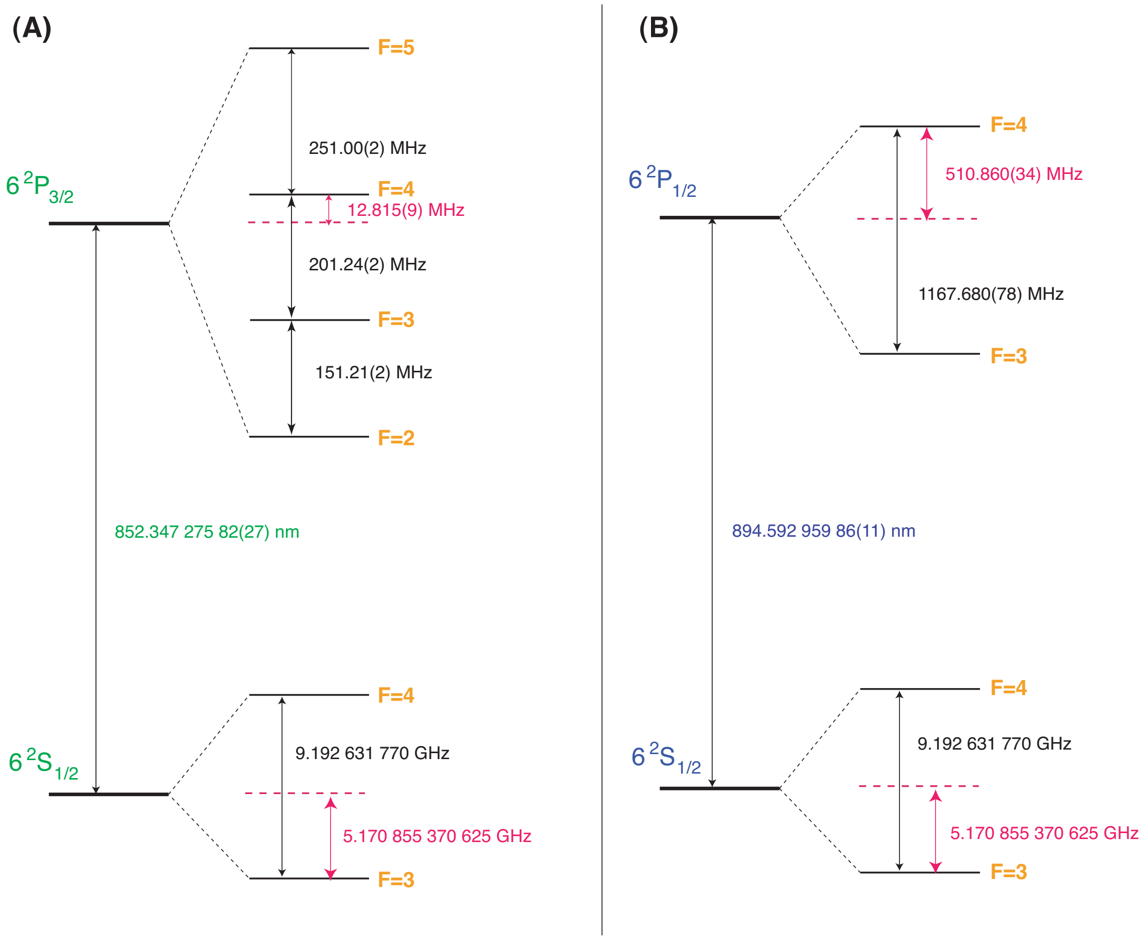

Figure 6.7: The numbers for the (A) D2 and (B) D1 lines of ^{133}Cs were obtained from D. A. Steck (http://steck.us/alkalidata/).

6.5 Atomic vapour cells

The experiments described in Chapters 7 and 8 used atomic vapour cells as the atomic source. The vapour cell consisted of isotopically enhanced ^{87}Rb. The cells typically had a diameter of 25 mm and length of 75 mm, are uncoated and do not contain any buffer gas. The atomic source for the work discussed in Chapter 10 used a cold atom cloud of ^{87}Rb atoms in a magneto-optical trap configuration. Details of this cold atom experiment are discussed in Chapter 10.

The atomic vapour cell had to be mounted and heated. Heating could not be performed using electrical resistors or Peltier heating elements as these could induce stray magnetic fields in the vapour cell. Therefore, we adopted a water heating scheme.

The vapour cell was mounted in a cell holder, made out of Delrin (the mechanical diagrams are shown in Appendix B). An illustration of the cell holder is shown in Fig. 6.8. The cell holder consisted of 2 parts. The main body was located at the far bottom, with its cover located at the far top. Within the main body, rested the black unit which had a water reservoir and a curved surface for the cell to rest on. The water pipes connected to the black unit. Hot water was pumped into the cell holder to heat up the vapour cell, from the bottom. A thermistor was placed at the top of the cell to monitor the cell temperature. The temperature of the cell could be varied between 20° C and 75° C.

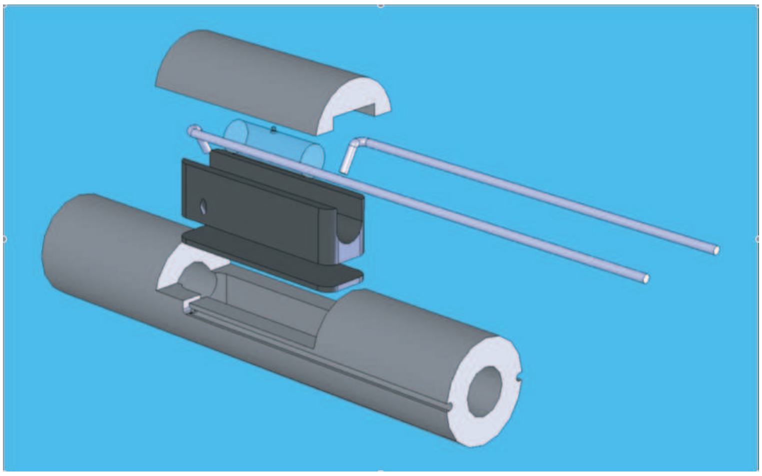

Figure 6.8: Schematic diagram showing the cell holder assembly.

6.6 Magnetic field compensation

In our experiments, it was important to compensate for stray background magnetic fields. Often, we were interested in the coherences between degenerate ground states. The presence of an external magnetic field can induce Zeeman shifts between these ground states, therefore affecting the coherences. For example, in EIT where degenerate ground states are used, the Zeeman shift was particularly problematic as it resulted in a two-photon detuning between the atomic transitions accessed by the pump and probe beams. Therefore, the transmission and dispersion of the EIT system was affected dramatically. For ^{87}Rb, the Zeeman shift is approximately 1 MHz/G. Thus a field with mG strengths will induce Zeeman shifts on the order of kHz.

The background magnetic fields were measured as a function of frequency, in all three orthogonal directions, as shown in Fig. 6.9. The DC field is on the order of mG with decreasing amplitude at higher frequencies. Harmonics of the 50 Hz AC line signal were also observed.

We used two cylindrical layers of μ-metal alloy to enclose the vapour cell. The μ-metal container had a high magnetic permeability and therefore the magnetic fields were drawn to the metal. The result was that the inner central region of the μ-metal cylinder had very small magnetic fields. We performed measurements inside the μ-metal cylinder to study the magnetic field suppression, the results of which are shown in Fig. 6.10.

The double layer μ-metal cylinder suppressed stray background magnetic fields by up to two orders of magnitude across a large range of magnetic field frequencies. This was a significant improvement in magnetic field management and therefore μ-metal cylinders were utilised in the experiments.

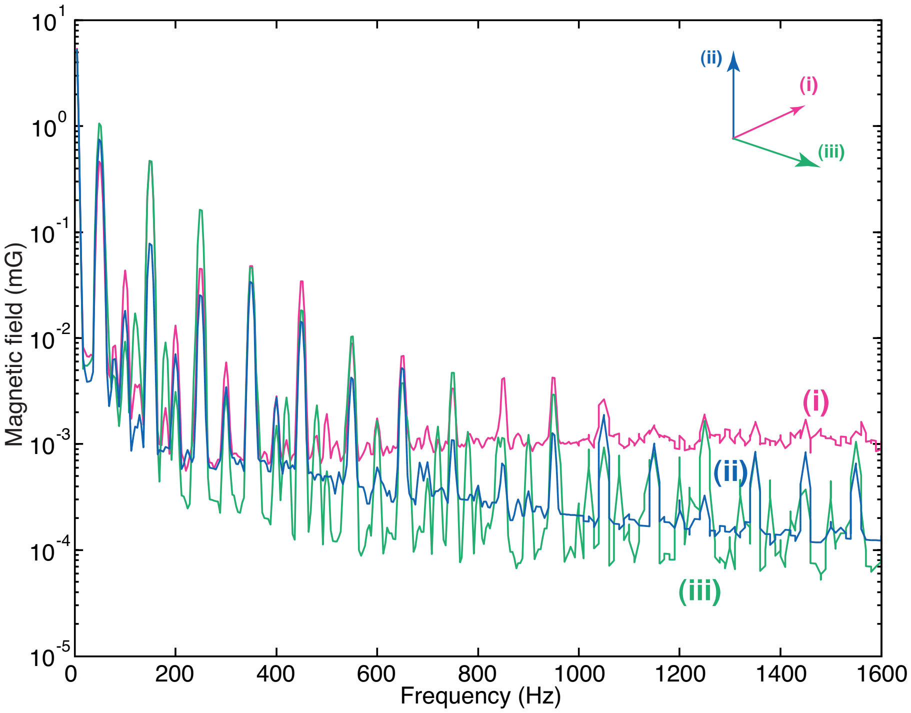

Figure 6.9: Measurements of the magnetic field strength on the optical table, in the region surrounding the MOT and cell experiments. The different curves correspond to the different spatial directions as indicated on the top right direction indicator.

6.7 Detection

Most of the detectors used in our experiments were built in-house. We used Silicon photodiodes (Hamamatsu S3883) that typically had measured quantum efficiencies of 94.5 %. The quantum efficiency of a batch of bare photodiodes was measured by focussing a laser beam onto the photodiode. A sensitive ammeter was then used to measure the output current across the photodiode. The quantum efficiency is given by the ratio of the number of electrons produced to the number of photons illuminating the photodiode. A separate calibrated photo-detector was used to measure the optical power of the laser beam illuminating the photodiode.

The home-built detectors consisted of a trans-impedance stage, followed by two separate amplified outputs (see Appendix A.1 for the electronic circuit diagram). The bandwidth of the detectors varied between 10-15 MHz. In order to AC-couple the output of the detectors, an 1 μF capacitor was inserted at the detector output. Typically, for a 5 mW beam, the detectors offered a 10 dB clearance between the shot noise and detector dark noise power levels.

6.8 Interferometry

The theory of the Mach-Zehnder interferometric technique, used in homodyne detection of amplitude and phase quadrature signals, was discussed in Chapters 2 and 3. In this section, we give a brief intuitive description of how error signals are derived in Mach-

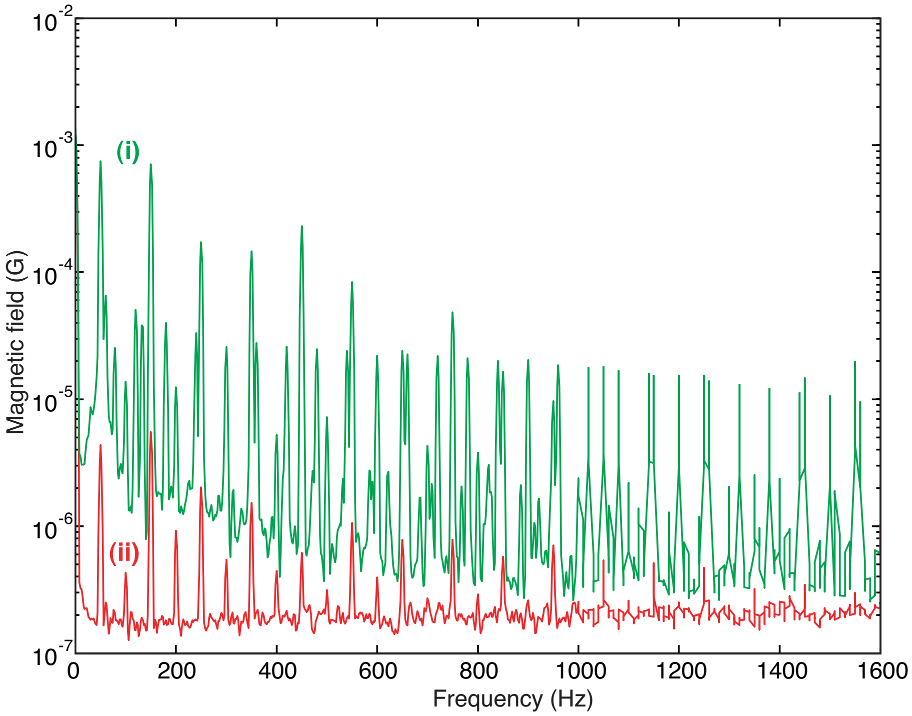

Figure 6.10: Measurements of the magnetic field (i) without and (ii) within the μ-metal cylinder.

Zehnder interferometers, in order to stabilise the length of the interferometer.

The interference signal can be observed by scanning the length of one arm of the interferometer with respect to the other. At the peak of the interference fringe, an error signal can be obtained by applying a phase modulation signal. A phase signal will experience differential phase shifts around this peak region which yields an error signal. This error signal allows locking for amplitude quadrature detection. At the mid-fringe region, an error signal can be obtained by taking the subtraction between the two detected outputs of the interferometer. The error signal allows locking for phase quadrature detection.

6.9 Locking servo

The locking servo system used in our experiments typically consisted of an integration stage, an offset and a gain stage, a $1/f$ filter stage and an optional elliptic filter stage. The integration stage provided higher gain at low frequency and typically integrated signals from DC to 20 Hz. The offset and gain stages gave the error signal the appropriate offset and gain; with the $1/f$ filter stage determining the bandwidth of the servo system. The optional elliptic filter serves to filter out the first resonance of the piezo-electric transducer (PZT) actuation system, so as to extend the frequency response of the servo system. The resonance frequency of the actuation system is dependent on the PZT type and mounting with the mirror and counter-weight.

The amplitude and phase parts of the transfer function for a typical servo system used in our experiments are shown in Fig. 6.11 (A) and (B), respectively. The example shown has an elliptic filter corresponding to an actuation system resonance[1] of $\sim$ 14 kHz.

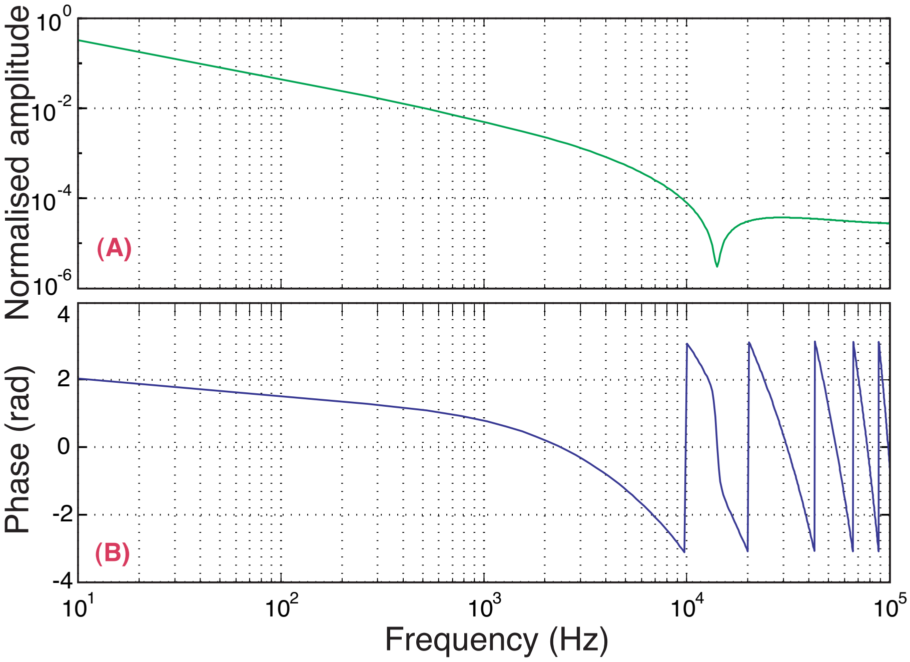

Figure 6.11: The (A) amplitude and (B) phase parts of the transfer function for the servo locking system.

The electronic circuit diagrams for the locking servo and high-voltage amplifier (for driving the PZT) are shown in Appendices A.2 and A.3, respectively.

6.10 Summary

This chapter summarises the various basic experimental techniques utilised in the subsequent work described in this thesis. Details of the magneto-optical trapping apparatus are described in Chapter 10,

---

[1] It is possible to extend the resonance frequency of the actuation system by a factor of two by clamping the mirror with the PZT. This is as opposed to gluing the mirror onto the PZT. Also, the counter-weight should have a large mass.

Chapter 7

Polarisation self-rotation

Look for it, and it can't be seen.
Listen for it, and it can't be heard.
Grasp for it, and it can't be caught.
These three cannot be further described,
so we treat them as The One.

It's highest is not bright.
It's depths are not dark.
Unending, un-nameable, it returns to nothingness.
Form-less forms, and image-less images,
subtle, beyond all understanding.

Approach it and you will not see a beginning;
follow it and there will be no end.
When we grasp the Tao of the ancient ones,
we can use it to direct our life today.
To know the ancient origin of Tao
this is the beginning of wisdom.

- Lao Tzu, from the *Tao Te Ching*
(a public domain translation by J. H. McDonald)

Does vacuum exist? For centuries, many cultures have been obsessed with understanding the concept of the vacuum. Newton argued that the vacuum existed, since there is a large amount of space outside the space occupied by matter. However, Aristotle and Descartes argued that "nothing could not be something".

With the discovery of quantum theory, the vacuum has been interpreted in a different manner. Specifically, in quantum optics, a quanta of vacuum preserves the commutation relations, in the presence of loss on an optical field, and this relates to the concept of coupling to a vacuum reservoir. Vacuum is also interpreted as the source of the ultimate noise floor in any optical measurement - the *quantum noise limit* or *shot noise* [263]. However, quantum opticians have been manipulating the noise properties of light by 'shifting' the noise from one variable to another. The process of such noise manipulation is called *squeezing* [264] (formally defined in Chapter 2). A variety of techniques are available to generate squeezed light, such as the optical parametric oscillation/amplification (OPO/A) process [170, 171, 172, 173, 120, 121, 174, 25, 175, 8], second harmonic generation [265, 266, 267, 119, 268, 269, 270, 271], four-wave mixing [122, 123, 165, 166, 272, 178], Kerr [273, 274, 275, 276, 18, 277, 90, 91, 167, 168, 169, 177] and diode-laser feedback mechanisms [278, 279, 280]. To date, the most widely used and reliable source of squeezed light is generated via the optical parametric oscillation process.

The generation of squeezed light using atomic ensembles has been explored using various mechanisms such as the four-wave mixing [165, 166, 178] and Kerr [90, 91, 167, 168, 169, 177] processes. In particular, two recent experiments have revived interest in squeezed light generation using atomic vapour cells. The 4-wave mixing squeezing experiment of McCormick *et al.* [178] showed that up to 8.1 dB of squeezing is generated (assuming correction for loss). The polarisation self-rotation squeezing experiment of Ries *et al.* [177] measured squeezing of 0.85 dB, with theoretical models by Matsko *et al.* [179] predicting up to 8 dB of squeezing. These experiments showed great promise as they were experimentally simpler, scalable and more cost-effective systems; compared to OPO systems. In this chapter, we investigate the technique of generating squeezed light using the Kerr process in atomic vapour cells, based on the polarisation self-rotation effect.

The traversal of an elliptically polarised optical field through a thermal vapour cell can give rise to a rotation of its polarisation axis. This process, known as polarisation self-rotation (PSR), has been suggested as a mechanism for producing squeezed light at atomic transition wavelengths. In this chapter, we show results of the characterisation of PSR in isotopically enhanced Rubidium-87 cells. We observed that, contrary to earlier work [179, 177], the presence of atomic noise in the thermal vapour overwhelms the observation of squeezing. We present a theory that contains atomic noise terms and show that a null result in squeezing is consistent with this theory.

The work in this chapter has been published in

- M. T. L. Hsu, G. Hétet, A. Peng, C. C. Harb, H.-A. Bachor, M. T. Johnsson, J. J. Hope, P. K. Lam, A. Dantan, J. Cviklinski, A. Bramati and M. Pinard, "Effect of atomic noise on optical squeezing via polarisation self-rotation in a thermal vapour cell", Physical Review A **73**, 023806 (2006).

7.1 Introduction

Squeezing is the reduction of the noise variance of an optical field below the quantum noise limit (QNL). Many applications, ranging from increased sensitivity of interferometric measurements [24] to quantum entanglement based information protocols [17, 41, 42], are reliant on squeezed light. Recently, Duan *et al.* [118] proposed a long-distance quantum communication network that is based on the interaction of atomic ensembles with squeezed and entangled light beams. To achieve such goals, squeezed light at atomic wavelengths is required.

Conventionally, squeezing can be generated via efficient non-linear optical processes, such as $\chi^{(2)}$ parametric down-conversion [17, 174, 184, 281]. The transparency windows of non-linear optical crystals and phase matching conditions, however, may not coincide with some atomic transitions. For example, commonly used Sodium and Rubidium atomic transition wavelengths are difficult to access via $\chi^{(2)}$ crystals. Another method of generating squeezed light is to utilise the $\chi^{(3)}$ atomic Kerr effect at the required atomic wavelength. These experiments, however, require ultra-cold atoms confined in cavities and are therefore technically challenging [90, 91].

Recently, there has been a proposal for generating atomic wavelength squeezing via the single traversal of an optical field through a thermal vapour cell [179]. This proposal promises a simple, scalable and cost-effective means of generating squeezed light for Rb and potentially for other atomic species. Due to the ac Stark shift and optical pumping-induced refractive index changes of the atomic vapour, an elliptically polarised input field will experience an intensity dependent rotation of the optical polarisation axes [180]. This effect, known as polarisation self-rotation (PSR), was suggested as a non-linear mechanism for squeezing [282, 179]. Assuming negligible atomic spontaneous emission noise, Matsko *et al.* [179] developed a phenomenological model that treats PSR as a cross-phase modulation mechanism. In the situation of a linearly polarised input field propagating through the vapour cell, a non-linear cross-phase interaction occurs between the two circularly polarised field components. This results in the squeezing of the output vacuum field mode that is orthogonally polarised to the input field. Analogous to cross-phase modulation squeezing in optical fibres [273, 274, 275, 276, 18, 277], it was suggested that 6 dB of PSR squeezing is possible with thermal Rb vapour cell. Subsequently Ries *et al.* [177] reported an observation of 0.85 dB maximum squeezing from a Rb vapour cell and attributed their squeezing to PSR.

The phenomenological model of PSR squeezing by Matsko *et al.* [179] ignored effects such as atomic spontaneous emission. In contrast, Josse *et al.* [221] pointed out the importance of noise terms arising from the atomic dynamics that could possibly degrade, if not totally destroy, squeezing. The model of Josse *et al.* [221] was based on the interaction of a linearly polarised field with 4-level atoms. They showed that in the above saturation regime, the atomic noise contribution could potentially be larger than the squeezing term. Nevertheless, in the below saturation regime and at sideband frequencies larger than the atomic relaxation rate, squeezing on the vacuum mode can be generated via the cross-Kerr effect induced by the bright field. Such a regime, however, can only be obtained with ultra-cold trapped atoms enclosed in an optical cavity [91].

This chapter is structured as follows - In Section 7.2, we review the theoretical works of Matsko *et al.* [179] and Josse *et al.* [221]. We modified the analysis of Josse *et al.* [221] to the case of a single traversal optical field through a thermal vapour cell. In Section 7.3, we report measurements of both the transmissivity and the PSR of an elliptically polarised field through an isotopically enhanced ^{87}Rb vapour cell on both the D_1 and D_2 lines. We then study the noise properties of the outgoing vacuum field. The parameter regime investigated extends beyond the squeezing regime reported in Ref. [177]. In contradiction to the results in Ref. [177], no optical squeezing was observed. Instead, we observed excess quadrature noise above the QNL for a wide range of parameters. Finally, in Section 7.4 we relate experimental results to the theory and show that under our experimental conditions, where atomic spontaneous emission is significant, squeezing is overwhelmed by atomic noise terms.

7.2 Theory

7.2.1 Cross-phase modulation squeezing

For cross-phase modulation squeezing in fibres, a bright input optical pulse in the x-polarisation is delivered into a weakly birefringent optical fibre. As a result of the $\chi^{(3)}$ non-linearity in the fibre, the annihilation ($\hat{a}_y$) and creation ($\hat{a}_y^\dagger$) operators for the y-polarised vacuum field become coupled [273, 274, 275, 276]. The equation of motion for the y-polarised field, in the rotating frame, is given by

$$\frac{\partial}{\partial z}\hat{a}_y(z,t) = i\frac{\kappa}{3}(2|\langle\hat{a}_x\rangle|^2\hat{a}_y + \langle\hat{a}_x\rangle^2\hat{a}_y^\dagger) \tag{7.1}$$

where $\kappa = n_2\hbar\omega_0^2/(cA)$ is the Kerr coefficient, n_2 is the non-linear index coefficient of the medium, ω_0 is the carrier frequency and A is the effective transverse area of the propagating field. The last term of Eq. (7.1) describes the cross-Kerr coupling between the bright x- and vacuum y-linearly polarised fields, and is responsible for generating squeezing in the y-polarised field.

Matsko *et al.* [179] proposed that the PSR effect in atomic vapour can be used to generate vacuum squeezing. Their proposal was related to the mechanism of cross-phase coupling between two orthogonal polarisation fields. We consider the PSR effect [180], where an elliptically polarised field undergoes a rotation in its polarisation ellipse upon propagation through an atomic medium. For an optically thin medium, the rotation angle is given by

$$\phi = \mathcal{G}\epsilon(0)l \tag{7.2}$$

where $\mathcal{G}$ is the PSR parameter (dependent on the input field intensity and frequency), $\epsilon(0)$ is the input field ellipticity (assumed to be small and constant during propagation and thus $\epsilon(0) = \epsilon(l)$) and l is the length of the medium. One could take the analogy of the PSR effect to the quantum regime by considering a bright linearly x-polarised input field. The PSR effect projects fluctuations of the bright x-polarised field onto the y-polarised vacuum field. The relative phase between the x- and y-polarised fields then provides amplification or attenuation of the y-polarised field. This effect could potentially result in the reduction of the quantum fluctuations of the y-polarised field.

We will now introduce a methodical representation for our optical field. For a measurement performed in an exposure time T, a freely propagating single-mode optical field can be described by the electric field operator given by

$$\hat{E}(z,t) = \mathcal{E}_0\left(\hat{a}(z,t)e^{i(kz-\omega t)} + \hat{a}^\dagger(z,t)e^{-i(kz-\omega t)}\right) \tag{7.3}$$

where $\mathcal{E}_0 = \sqrt{\frac{\hbar\omega}{2\epsilon_0 cT\mathcal{A}}}$, $\hat{a}(z,t)$ and $\hat{a}^\dagger(z,t)$ are the slowly varying field envelope annihilation and creation operators, respectively. z is the field propagation axis, ω is the field carrier frequency and $\mathcal{A}$ is the quantisation cross-section area. We can simplify the expression by introducing $\chi = kz-\omega t$ and phenomenologically extend the classical PSR[1] to the quantum regime. The resulting y-polarised field at the output of the PSR medium is given by

$$\begin{aligned}\hat{E}_y(l) \;=\; & \mathcal{E}_0\Big[\hat{a}_y(0)\left(e^{i\chi} - i\mathcal{G}l\cos\chi\right) \\ & +\hat{a}_y^\dagger(0)\left(e^{-i\chi} + i\mathcal{G}l\cos\chi\right)\Big]\end{aligned} \tag{7.4}$$

The photon number variance for the $\hat{E}_y(l)$ field, taking into account a phenomenological

---

[1] The classical PSR equation is given in Ref. [179]. The positive frequency part of the electric field amplitude for the y-polarised mode, undergoing PSR, is given by $E_y^+ = (\mathcal{E}_y(0) + \mathcal{G}l\epsilon(0)\mathcal{E}_x(0))e^{i\chi}$.

absorption parameter α [179], is given by

$$\begin{aligned}\langle \hat{E}_y^{\dagger}(l)\hat{E}_y(l)\rangle &= \mathcal{E}_0\Big[\Big(1-2\mathcal{G}l\sin\chi\cos\chi \\ &\quad +\mathcal{G}^2l^2\cos^2\chi\Big)e^{-\alpha l}+(1-e^{-\alpha l})\Big] \qquad (7.5)\end{aligned}$$

where the y-polarised field has zero mean amplitude and for appropriate values of the phase χ, squeezing of the y-polarised field can be observed. Such a model predicts squeezing values of 6-8 dB below the QNL. However, crucial details such as spontaneous emission and atomic noise are completely ignored, the effects of which can reduce, if not completely destroy, squeezing.

7.2.2 Squeezing in a 4-level System

Since optical pumping is the main cause of PSR in the above saturation regime [179, 283], which is the relevant regime in our experiment, we can approximate the D_1 and D_2 lines of ^{87}Rb using a 4-level atom model. In such a regime, the influence of atomic coherences are negligible. We thus explore the alternative cross-Kerr squeezing model proposed by Josse *et al.* [221]. In the model, 4-level atoms interact with two orthogonal circularly polarised fields, as shown in Fig. 7.1. In the experiment of Ref. [91], squeezing was obtained in the vacuum field (orthogonally polarised to the bright input field) from ultra-cold trapped atoms, enclosed in a cavity. The 4-level squeezing model approximated the level structure of ultra-cold Cesium atoms ($|6S_{1/2}, F = 4\rangle$ to $|6P_{3/2}, F = 5\rangle$), used in the experiment. In this section, we extend this cavity model to a single-propagation scenario for a single-mode bright x-polarised input field. We derive the equation of motion describing the noise fluctuations of the output y-polarised vacuum field.

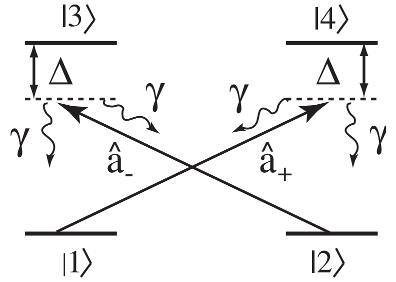

Figure 7.1: Two orthogonal σ_+ and σ_- circularly polarised light fields interacting with a 4-level atomic system.

Hamiltonian

The interaction Hamiltonian for a 4-level atomic system interacting with two optical fields, with left- and right-circular polarisation, is given by

$$\begin{aligned}\hat{\mathcal{H}}_{\text{int}} &= \sum_{j=1}^{N} e\hat{\boldsymbol{r}}_j \cdot \hat{E}(\boldsymbol{r}_j,t) &(7.6)\\ &= -\sum_{j=1}^{N}\left(d_{14}\hat{\sigma}_{14}^{(j)} + d_{14}^{*}\hat{\sigma}_{41}^{(j)} + d_{23}\hat{\sigma}_{23}^{(j)} + d_{23}^{*}\hat{\sigma}_{32}^{(j)}\right)\cdot\left(\hat{E}_{+}(\boldsymbol{r}_j,t) + \hat{E}_{-}(\boldsymbol{r}_j,t)\right) &(7.7)\end{aligned}$$

where $d_{\mu\nu}$ is the dipole moment for the $|\mu\rangle \to |\nu\rangle$ transition. The atomic dipole operator for the j-th atom at location $\boldsymbol{r}_j$ is given by $\hat{\sigma}_{\mu\nu}^{(j)} = |\mu^{(j)}\rangle\langle\nu^{(j)}|$.

We now separate the electric field operator into the positive and negative frequency components. The positive and negative frequency parts of the electric field operator are given by

$$\hat{E}^{\pm}(z,t) = \hat{\mathcal{E}}^{\pm}(z,t)\exp\left(\pm i\omega_0(\frac{z}{c} - t)\right) \qquad (7.8)$$

where ω_0 is the central frequency of the field and z is the distance along the propagation direction of the field. $\hat{\mathcal{E}}^{+}(z,t)$ and $\hat{\mathcal{E}}^{-}(z,t)$ are the positive and negative frequency parts of the slowly varying field envelope operator, respectively. The spatial dependence of the fields are not considered and thus the fields are assumed to be plane waves.

The interaction Hamiltonian written in terms of the electric field envelope operator is then given by

$$\begin{aligned}\hat{\mathcal{H}}_{\text{int}} &= -\sum_{j=1}^{N}\left(g\hat{\sigma}_{14}^{(j)} + g\hat{\sigma}_{41}^{(j)} + g\hat{\sigma}_{23}^{(j)} + g\hat{\sigma}_{32}^{(j)}\right)\\ &\quad\cdot\left(\hat{\mathcal{E}}_{+}^{+}(\boldsymbol{r}_j,t)e^{-i\omega_{+}t} + \hat{\mathcal{E}}_{+}^{-}(\boldsymbol{r}_j,t)e^{i\omega_{+}t} + \hat{\mathcal{E}}_{-}^{+}(\boldsymbol{r}_j,t)e^{-i\omega_{-}t} + \hat{\mathcal{E}}_{-}^{-}(\boldsymbol{r}_j,t)e^{i\omega_{-}t}\right) &(7.9)\end{aligned}$$

where we have assumed that the dipole moment for the transitions are all equal and real, given by $d_{14} = d_{14}^{*} = d_{23} = d_{23}^{*} = g$.

The interaction Hamiltonian for a 4-level atomic system (corresponding to Fig. 7.1) for an optically thick medium (where we replace the sum by an integral over the atomic ensemble length L) and under the rotating wave approximation, is given by

$$\begin{aligned}\hat{\mathcal{H}}_{\text{int}} &= \hbar n A_{\text{eff}}\int_0^l dz\Big[\Delta\hat{\sigma}_{44}(z,t) + \Delta\hat{\sigma}_{33}(z,t) - g\Big(\hat{\mathcal{E}}_{+}(z,t)\hat{\sigma}_{41}(z,t) + \hat{\mathcal{E}}_{+}^{\dagger}(z,t)\hat{\sigma}_{14}(z,t)\\ &\quad + \hat{\mathcal{E}}_{-}(z,t)\hat{\sigma}_{32}(z,t) + \hat{\mathcal{E}}_{-}^{\dagger}(z,t)\hat{\sigma}_{23}(z,t)\Big)\Big] &(7.10)\end{aligned}$$

where n is the atomic density and g is the atom-field coupling constant. The atomic dipole operator at position z in the rotating frame is defined by locally averaging over a transverse slice containing many atoms

$$\hat{\sigma}_{ij}(z,t) = \frac{1}{nA\delta z}\sum_{z_k\in\delta z} e^{\frac{i(\omega_i-\omega_j)z_k}{c}}|i\rangle_k\langle j|_k \qquad (7.11)$$

Equations of motion

The time and longitudinal propagation of the fields through the EIT system is described by the equations of motion for the atomic dipole and field operators. The equation of motion for the atomic dipole operator is obtained from the Heisenberg equation of motion, given by

$$i\hbar\frac{\partial\hat{\sigma}_{\mu\nu}}{\partial t} = [\hat{\sigma}_{\mu\nu}, \hat{\mathcal{H}}_{\rm int}] \tag{7.12}$$

The optical Bloch equations for the atomic variables are then given by

$$\begin{aligned}
\frac{\partial}{\partial t}\hat{\sigma}_{14} &= -(\gamma+i\Delta)\hat{\sigma}_{14} + ig\hat{\mathcal{E}}_+(\hat{\sigma}_{11}-\hat{\sigma}_{44}) + \hat{F}_{14}\\
\frac{\partial}{\partial t}\hat{\sigma}_{23} &= -(\gamma+i\Delta)\hat{\sigma}_{23} + ig\hat{\mathcal{E}}_-(\hat{\sigma}_{22}-\hat{\sigma}_{33}) + \hat{F}_{23}\\
\frac{\partial}{\partial t}\hat{\sigma}_{11} &= \gamma(\hat{\sigma}_{33}+\hat{\sigma}_{44}) - ig\hat{\mathcal{E}}_+\hat{\sigma}_{41} + ig\hat{\mathcal{E}}_+^\dagger\hat{\sigma}_{14} + \hat{F}_{11}\\
\frac{\partial}{\partial t}\hat{\sigma}_{22} &= \gamma(\hat{\sigma}_{33}+\hat{\sigma}_{44}) - ig\hat{\mathcal{E}}_-\hat{\sigma}_{32} + ig\hat{\mathcal{E}}_-^\dagger\hat{\sigma}_{23} + \hat{F}_{22}\\
\frac{\partial}{\partial t}\hat{\sigma}_{33} &= -2\gamma\hat{\sigma}_{33} + ig\hat{\mathcal{E}}_-\hat{\sigma}_{32} - ig\hat{\mathcal{E}}_-^\dagger\hat{\sigma}_{23} + \hat{F}_{33}\\
\frac{\partial}{\partial t}\hat{\sigma}_{44} &= -2\gamma\hat{\sigma}_{44} + ig\hat{\mathcal{E}}_+\hat{\sigma}_{41} - ig\hat{\mathcal{E}}_+^\dagger\hat{\sigma}_{14} + \hat{F}_{44}
\end{aligned} \tag{7.13}$$

where we have introduced the spontaneous decay term γ and Langevin noise operators $\hat{F}_{ij}$ that arise from the coupling of atoms to a vacuum reservoir. The Maxwell-Bloch equations describing the σ_+ and σ_--polarised optical fields are given respectively by

$$\left(\frac{\partial}{\partial t} + c\frac{\partial}{\partial z}\right)\hat{\mathcal{E}}_+(z,t) = igN\hat{\sigma}_{14}(z,t) \tag{7.14}$$

$$\left(\frac{\partial}{\partial t} + c\frac{\partial}{\partial z}\right)\hat{\mathcal{E}}_-(z,t) = igN\hat{\sigma}_{23}(z,t) \tag{7.15}$$

where N is the total number of atoms. To deduce the noise properties of the field, we write the operators in the form $\hat{\mathcal{E}} = \langle\hat{\mathcal{E}}\rangle + \delta\hat{\mathcal{E}}$ and use the linearisation approximation.

Steady state solutions

The steady state mean field solutions for the atomic dipole operators are given by

$$\langle\hat{\sigma}_{14}\rangle = \frac{ig\langle\hat{\mathcal{E}}_+\rangle}{\gamma+i\Delta}\left(\frac{1}{2(1+s)}\right) \tag{7.16}$$

$$\langle\hat{\sigma}_{23}\rangle = \frac{ig\langle\hat{\mathcal{E}}_-\rangle}{\gamma+i\Delta}\left(\frac{1}{2(1+s)}\right) \tag{7.17}$$

$$\langle\hat{\sigma}_{11}\rangle = \langle\hat{\sigma}_{22}\rangle = \frac{2+s}{4(1+s)} \tag{7.18}$$

$$\langle\hat{\sigma}_{33}\rangle = \langle\hat{\sigma}_{44}\rangle = \frac{s}{4(1+s)} \tag{7.19}$$

where the mean field for the left and right-circularly polarised optical fields are related to the x-polarised input field by $\langle\hat{\mathcal{E}}_+\rangle = -\langle\hat{\mathcal{E}}_-\rangle = \langle\hat{\mathcal{E}}_x\rangle/\sqrt{2}$. The saturation parameter is given by $s = I_x/(\gamma^2+\Delta^2)$ where $I_x = |g\langle\hat{\mathcal{E}}_x\rangle|^2$ is the mean field intensity.

Field equations

The fluctuation terms of the field operators in the Fourier domain are obtained by taking the Fourier transform of the Maxwell-Bloch equations of Eqs. (7.14) and (7.15), given by

$$\begin{aligned}\left(-i\omega + c\frac{\partial}{\partial z}\right)\delta\tilde{\mathcal{E}}_+(z,t) &= igN\delta\tilde{\sigma}_{14}(z,t) &\quad (7.20)\\ \left(-i\omega + c\frac{\partial}{\partial z}\right)\delta\tilde{\mathcal{E}}_-(z,t) &= igN\delta\tilde{\sigma}_{23}(z,t) &\quad (7.21)\end{aligned}$$

The fluctuation terms of the atomic dipole operators in the Fourier domain are obtained by taking the Fourier transform of Eqs. (7.13)-(7.15), given by

$$\begin{aligned}-i\omega\delta\tilde{\sigma}_{14} &= -(\gamma+i\Delta)\delta\tilde{\sigma}_{14} + ig\langle\tilde{\mathcal{E}}_+\rangle(\delta\tilde{\sigma}_{11}-\delta\tilde{\sigma}_{44}) + ig\delta\tilde{\mathcal{E}}_+(\langle\tilde{\sigma}_{11}\rangle - \langle\tilde{\sigma}_{44}\rangle) + \tilde{F}_{14}\\ -i\omega\delta\tilde{\sigma}_{23} &= -(\gamma+i\Delta)\delta\tilde{\sigma}_{23} + ig\langle\tilde{\mathcal{E}}_-\rangle(\delta\tilde{\sigma}_{22}-\delta\tilde{\sigma}_{33}) + ig\delta\tilde{\mathcal{E}}_-(\langle\tilde{\sigma}_{22}\rangle - \langle\tilde{\sigma}_{33}\rangle) + \tilde{F}_{23}\\ -i\omega\delta\tilde{\sigma}_{11} &= \gamma(\delta\tilde{\sigma}_{33}+\delta\tilde{\sigma}_{44}) - ig\langle\tilde{\mathcal{E}}_+\rangle\delta\tilde{\sigma}_{41} - ig\delta\tilde{\mathcal{E}}_+\langle\tilde{\sigma}_{41}\rangle + ig\langle\tilde{\mathcal{E}}_+^\dagger\rangle\delta\tilde{\sigma}_{14} + ig\delta\tilde{\mathcal{E}}_+^\dagger\langle\tilde{\sigma}_{14}\rangle + \tilde{F}_{11}\\ -i\omega\delta\tilde{\sigma}_{22} &= \gamma(\delta\tilde{\sigma}_{33}+\delta\tilde{\sigma}_{44}) - ig\langle\tilde{\mathcal{E}}_-\rangle\delta\tilde{\sigma}_{32} - ig\delta\tilde{\mathcal{E}}_-\langle\tilde{\sigma}_{32}\rangle + ig\langle\tilde{\mathcal{E}}_-^\dagger\rangle\delta\tilde{\sigma}_{23} + ig\delta\tilde{\mathcal{E}}_-^\dagger\langle\tilde{\sigma}_{23}\rangle + \tilde{F}_{22}\\ -i\omega\delta\tilde{\sigma}_{33} &= -2\gamma\delta\tilde{\sigma}_{33} + ig\langle\tilde{\mathcal{E}}_-\rangle\delta\tilde{\sigma}_{32} + ig\delta\tilde{\mathcal{E}}_-\langle\tilde{\sigma}_{32}\rangle - ig\langle\tilde{\mathcal{E}}_-^\dagger\rangle\delta\tilde{\sigma}_{23} - ig\delta\tilde{\mathcal{E}}_-^\dagger\langle\tilde{\sigma}_{23}\rangle + \tilde{F}_{33}\\ -i\omega\delta\tilde{\sigma}_{44} &= -2\gamma\delta\tilde{\sigma}_{44} + ig\langle\tilde{\mathcal{E}}_+\rangle\delta\tilde{\sigma}_{41} + ig\delta\tilde{\mathcal{E}}_+\langle\tilde{\sigma}_{41}\rangle - ig\langle\tilde{\mathcal{E}}_+^\dagger\rangle\delta\tilde{\sigma}_{14} - ig\delta\tilde{\mathcal{E}}_+^\dagger\langle\tilde{\sigma}_{14}\rangle + \tilde{F}_{44}\end{aligned} \quad (7.22)$$

Eqs. (7.22) are solved by considering the pairing of dipole operators to yield three coupled equations given by

$$\begin{aligned}(\gamma+i\Delta-i\omega)(\delta\tilde{\sigma}_{14}+\delta\tilde{\sigma}_{23}) &= \frac{ig\langle\tilde{\mathcal{E}}_x\rangle}{\sqrt{2}}(\delta\tilde{\sigma}_{11}-\delta\tilde{\sigma}_{22}+\delta\tilde{\sigma}_{33}+\delta\tilde{\sigma}_{44})\\ &\quad -\sqrt{2}g(\langle\tilde{\sigma}_{11}\rangle-\langle\tilde{\sigma}_{44}\rangle)\delta\tilde{\mathcal{E}}_y + \tilde{F}_{14}+\tilde{F}_{23}\\ (2\gamma-i\omega)(\delta\tilde{\sigma}_{33}-\delta\tilde{\sigma}_{44}) &= -\frac{ig\langle\tilde{\mathcal{E}}_x\rangle}{\sqrt{2}}(\delta\tilde{\sigma}_{32}+\delta\tilde{\sigma}_{41}) + \frac{ig\langle\tilde{\mathcal{E}}_x^\dagger\rangle}{\sqrt{2}}(\delta\tilde{\sigma}_{23}+\delta\tilde{\sigma}_{14})\\ &\quad +\sqrt{2}g(\langle\tilde{\sigma}_{41}\rangle\delta\tilde{\mathcal{E}}_y + \langle\tilde{\sigma}_{14}\rangle\delta\tilde{\mathcal{E}}_y^\dagger) + \tilde{F}_{33}-\tilde{F}_{44}\\ -i\omega(\delta\tilde{\sigma}_{11}-\delta\tilde{\sigma}_{22}) &= -\frac{ig\langle\tilde{\mathcal{E}}_x\rangle}{\sqrt{2}}(\delta\tilde{\sigma}_{41}+\delta\tilde{\sigma}_{32}) + \frac{ig\langle\tilde{\mathcal{E}}_x^\dagger\rangle}{\sqrt{2}}(\delta\tilde{\sigma}_{14}+\delta\tilde{\sigma}_{23})\\ &\quad +\sqrt{2}g(\langle\tilde{\sigma}_{41}\rangle\delta\tilde{\mathcal{E}}_y + \langle\tilde{\sigma}_{14}\rangle\delta\tilde{\mathcal{E}}_y^\dagger) + \tilde{F}_{11}-\tilde{F}_{22} \quad (7.23)\end{aligned}$$

where we have introduced the field operator for the y-polarised vacuum mode given by $\tilde{\mathcal{E}}_y = -i(\tilde{\mathcal{E}}_+ + \tilde{\mathcal{E}}_-)/\sqrt{2}$. We now define new dipole operators to simplify the above expressions, given by

$$\tilde{B} = \frac{\delta\tilde{\sigma}_{14}+\delta\tilde{\sigma}_{23}}{\sqrt{2}} \qquad \tilde{C} = \delta\tilde{\sigma}_{11}-\delta\tilde{\sigma}_{22} \qquad \tilde{D} = \delta\tilde{\sigma}_{33}-\delta\tilde{\sigma}_{44} \quad (7.24)$$

By assuming that the sideband frequencies of interest are less than the atomic detuning

$(\omega \ll \Delta)$ and solving for Eqs. (7.23), the following expressions are obtained

$$\begin{aligned}
\tilde{C} &= \frac{2ig^2\gamma(2\gamma - i\omega)\left(\langle\tilde{\mathcal{E}}_x\rangle\delta\tilde{\mathcal{E}}_y^\dagger - \langle\tilde{\mathcal{E}}_x^\dagger\rangle\delta\tilde{\mathcal{E}}_y\right)}{(\gamma^2+\Delta^2)(2+s)[(\gamma s(\gamma - i\omega) - i\omega(2\gamma - i\omega)]} + \frac{\frac{-\gamma}{2}s\tilde{F}_D + (2\gamma + \frac{\gamma s}{2} - i\omega)\tilde{F}_C}{[(\gamma s(\gamma - i\omega) - i\omega(2\gamma - i\omega)]} \\
\tilde{D} &= \frac{2g^2\gamma\omega\left(\langle\tilde{\mathcal{E}}_x\rangle\delta\tilde{\mathcal{E}}_y^\dagger - \langle\tilde{\mathcal{E}}_x^\dagger\rangle\delta\tilde{\mathcal{E}}_y\right)}{(\gamma^2+\Delta^2)(2+s)[(\gamma s(\gamma - i\omega) - i\omega(2\gamma - i\omega)]} + \frac{\frac{-\gamma}{2}s\tilde{F}_C + (\frac{\gamma s}{2} - i\omega)\tilde{F}_D}{[(\gamma s(\gamma - i\omega) - i\omega(2\gamma - i\omega)]} \\
\tilde{B} &= \frac{2g^3\gamma\langle\tilde{\mathcal{E}}_x\rangle\left(-\langle\tilde{\mathcal{E}}_x\rangle\delta\tilde{\mathcal{E}}_y^\dagger + \langle\tilde{\mathcal{E}}_x^\dagger\rangle\delta\tilde{\mathcal{E}}_y\right)(\gamma - i\omega)}{(\gamma + i\Delta)(\gamma^2+\Delta^2)(2+s)[(\gamma s(\gamma - i\omega) - i\omega(2\gamma - i\omega)]} - \frac{g}{(\gamma + i\Delta)(2+s)}\delta\tilde{\mathcal{E}}_y \\
&\quad + \frac{ig\langle\tilde{\mathcal{E}}_x\rangle[(2\gamma - i\omega)\tilde{F}_C - i\omega\tilde{F}_D]}{2(\gamma + i\Delta)[(\gamma s(\gamma - i\omega) - i\omega(2\gamma - i\omega)]} + \frac{\tilde{F}_{14} + \tilde{F}_{23}}{\sqrt{2}(\gamma + i\Delta} \qquad (7.25)
\end{aligned}$$

where the Langevin operators denoted by $\tilde{F}_C$ and $\tilde{F}_D$ are given by

$$\tilde{F}_C = -\frac{ig\sqrt{2}\langle\tilde{\mathcal{E}}_x\rangle(\tilde{F}_{14}^\dagger + \tilde{F}_{23}^\dagger)}{2(\gamma - i\Delta)} + \frac{ig\sqrt{2}\langle\tilde{\mathcal{E}}_x^\dagger\rangle(\tilde{F}_{14} + \tilde{F}_{23})}{2(\gamma + i\Delta)} + \tilde{F}_{11} - \tilde{F}_{22} \qquad (7.26)$$

$$\tilde{F}_D = -\frac{ig\sqrt{2}\langle\tilde{\mathcal{E}}_x\rangle(\tilde{F}_{14}^\dagger + \tilde{F}_{23}^\dagger)}{2(\gamma - i\Delta)} + \frac{ig\sqrt{2}\langle\tilde{\mathcal{E}}_x^\dagger\rangle(\tilde{F}_{14} + \tilde{F}_{23})}{2(\gamma + i\Delta)} + \tilde{F}_{33} - \tilde{F}_{44} \qquad (7.27)$$

Using these equations, the equation of motion for the quantum fluctuations of the y-polarised vacuum mode is therefore given by

$$\begin{aligned}
\left(-i\omega + c\frac{\partial}{\partial z}\right)\delta\tilde{\mathcal{E}}_y &= = gN\tilde{B} \\
\left(-i\omega + c\frac{\partial}{\partial z}\right)\left(-\frac{i}{\sqrt{2}}(\delta\tilde{\mathcal{E}}_+ + \delta\tilde{\mathcal{E}}_-)\right) &= = gN\tilde{B} \qquad (7.28) \\
\frac{\partial}{\partial\bar{z}}\delta\tilde{\mathcal{E}}_y &= -\Gamma(\omega)\delta\tilde{\mathcal{E}}_y + \kappa(\omega)\left(\delta\tilde{\mathcal{E}}_y - \delta\tilde{\mathcal{E}}_y^\dagger\right) + \tilde{F}_y \qquad (7.29)
\end{aligned}$$

where $\bar{z} = z/l$ and

$$\begin{aligned}
\kappa(\omega) &= \kappa(0)\Lambda(\omega) \qquad (7.30) \\
\Gamma(\omega) &= -i\omega\frac{l}{c} + \kappa(\omega) + \kappa(0)^*\Lambda'(\omega) \\
\kappa(0) &= \frac{C\gamma}{2(\gamma + i\Delta)}\frac{1}{1+s} \\
\Lambda(\omega) &= \frac{I_x(\gamma - i\omega)(2\gamma - i\omega)}{2I_x(\gamma - i\omega)^2 - i\omega(2\gamma - i\omega)[(\gamma - i\omega)^2 + \Delta^2]} \\
\Lambda'(\omega) &= i\omega\frac{I_x(\gamma - i\omega) - (\gamma - i\Delta)(\gamma - i\Delta - i\omega)(2\gamma - i\omega)}{2I_x(\gamma - i\omega)^2 - i\omega(2\gamma - i\omega)[(\gamma - i\omega)^2 + \Delta^2]}
\end{aligned}$$

where $C = g^2Nl/\gamma c$ is the co-operativity parameter. The last term of Eq. (7.29) represents the atomic Langevin noise term and is responsible for a loss or degradation of squeezing. Its exact form and noise spectrum are given and discussed in Sec. 7.4.

Note that for $\omega = 0$, the imaginary part of $\kappa(0)$ from the second term on the right hand side of Eq. (7.29) equates to the first term on the right hand side of Eq. (7.1). This turns out to be the parameter $\mathcal{G}l$ given in Eq. (7.2). In the 4-level atom model, the PSR for one velocity class increases with the number of atoms and is maximum when $\Delta^2 = \gamma^2 + I_x$.

For a Doppler-broadened vapour, $\mathcal{G}l$ can be obtained by summing Eq. (7.30) over all the velocity classes. Note that $\kappa(\omega)$ also gives the amplitude of the cross-Kerr squeezing term in $\delta\tilde{\mathcal{E}}_y^\dagger$, as in Eq. (7.29). However, the associated atomic noise contribution must be evaluated in order to obtain the total noise spectrum for the output y-polarised field.

7.3 Experiment

In our experiment, a coherent beam at 795 nm (or 780 nm) was delivered from a Ti:Sapphire laser (Coherent MBR-110), as shown[2] in Fig. 7.2. The laser beam was measured to be quantum noise limited at sideband frequencies ≥ 1 MHz. A small fraction of the beam was sent through another Rubidium (Rb) vapour cell for saturated absorption spectroscopy. This provided us with a fine frequency reference for the laser and also allowed the possibility of laser frequency stabilisation. The majority of the beam was sent through a polariser which transmitted the x-polarised field.

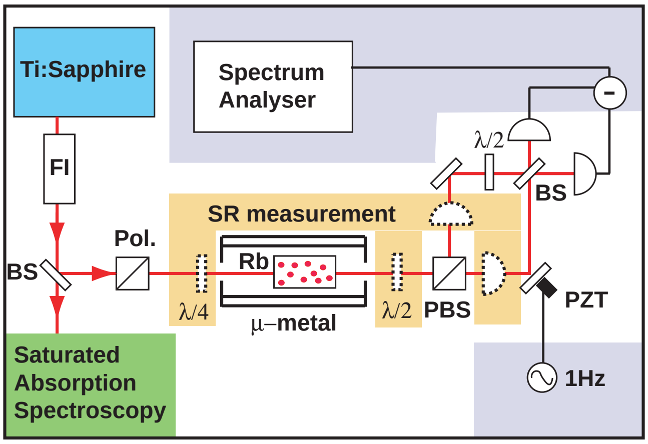

Figure 7.2: Schematic of experimental setup. All polarising optics are of the Glan-Thompson type. FI: Faraday isolator, BS: beam-splitter. Pol.: Polariser, PBS: polarising beam-splitter, $\lambda/4$: quarter wave-plate, $\lambda/2$: half wave-plate, PZT: piezo-electric actuator.

In order to measure the PSR and absorption of an input elliptically polarised beam through the vapour cell, the orange-shaded configuration of Fig. 7.2 was used. The x-linearly polarised beam was converted into an elliptically polarised beam using a $\lambda/4$ wave-plate. The beam (collimated to a waist size of ~ 425 μm) then passed through an isotopically enhanced ^{87}Rb vapour cell (75 mm length), which was temperature stabilised at 72°C (which corresponded to an atomic density of 10^{11} atoms/cm^3). The vapour cell was enclosed in a two-layer μ-metal alloy cylinder, with end caps. The stray magnetic fields within the shielding region were measured to be < 2 mG in all three spatial axes. The output beam from the cell was then analysed using a balanced polarimeter setup, which consisted of a $\lambda/2$ wave-plate, a polarising beam-splitter and two balanced photodetectors. The $\lambda/2$ wave-plate was adjusted to balance the powers in the x- and y-linearly polarised beams from the outputs of the polarising beam-splitter, when the frequency of the laser was tuned far off-resonance. Thus any rotation of the axis of the input elliptically

---

[2] A detailed schematic of the experimental layout is shown in Fig. 7.12

polarised beam could be measured using the relationship [180]

$$\phi = \frac{V_1 - V_2}{2(V_1 + V_2)} \tag{7.31}$$

where V_1 and V_2 are the DC signals from the photo-detectors.

To measure the quadrature noise properties of the y-linearly polarised vacuum beam, we then performed homodyne detection, as shown in Fig. 7.2, using the x-linearly polarised output of the polarising beam-splitter as a local oscillator.

7.3.1 Classical results

The PSR and transmission of an input elliptically polarised beam through the Rb vapour cell were measured by scanning the laser frequency across the energy levels of interest, for a fixed input beam intensity. For the D_2 line, the relevant levels were $|5^2S_{1/2}, F_g = 2\rangle$ to $|5^2P_{3/2}, F_e = 1, 2, 3\rangle$ and for the D_1 line, $|5^2S_{1/2}, F_g = 2\rangle$ to $|5^2P_{1/2}, F_e = 1, 2\rangle$. We repeated the measurements for varying input beam powers and obtained a contour map of PSR and transmission as a function of laser frequency detuning and input beam intensity, shown in Figs. 7.3, 7.4, 7.6 and 7.7.

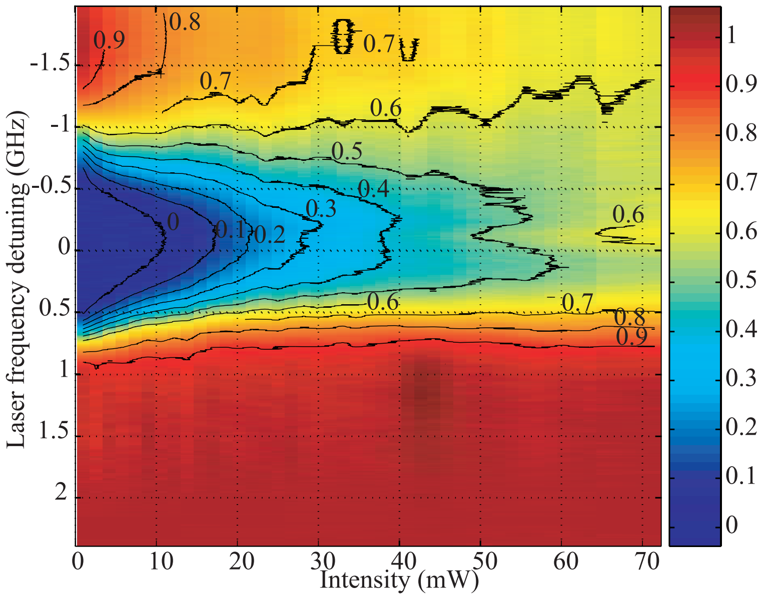

Figure 7.3: False colour contour plot of the normalised transmission results for the D_2 line, as a function of input beam intensity and laser frequency detuning. Zero frequency corresponds to the $|5^2S_{1/2}, F_g = 2\rangle$ to $|5^2P_{3/2}, F_e = 3\rangle$ energy levels.

The transmission results for the D_2 line are shown in Fig. 7.3. The region of lowest transmission < 10 % occurred at input beam intensities ≤ 15 mW, around laser frequencies close to zero detuning. For input beam powers ≥ 30 mW greater transmission (≥ 30 %) was observed. However, power broadening effects were also observed for higher input beam powers, with reduced transmission at frequencies ≤ -1 GHz. The transmission was non-symmetric with high transmission (> 90 %) for frequencies ≥ 1 GHz, whilst reduced transmission (> 60 %) for frequencies ≤ -1 GHz. This was due to the level structure of the excited states of the D_2 line, where the separations between the hyperfine levels are small (within a frequency band of ~ 0.5 GHz). Power broadening effects were also observed for input beam intensities ≥ 30 mW.

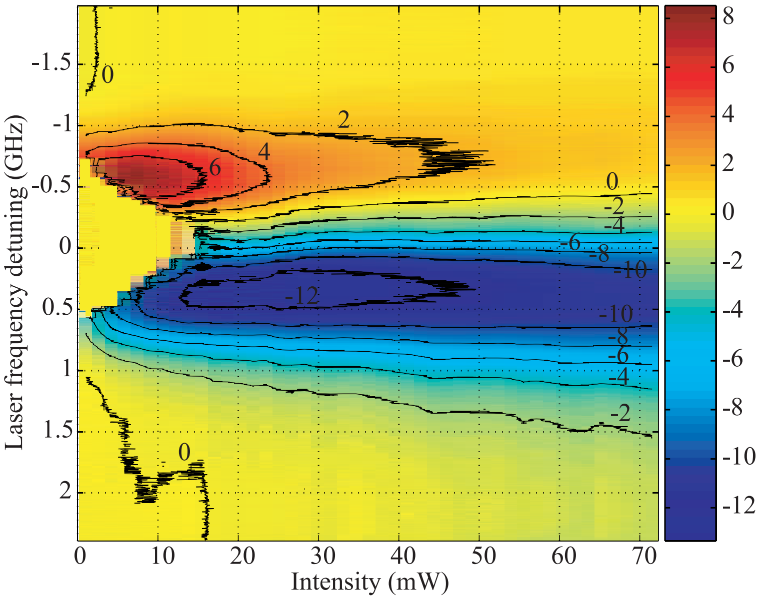

Figure 7.4: False colour contour plot of $\mathcal{G}l$ for the D_2 line, normalised to the input beam ellipticity of 2°, as a function of input beam intensity and laser frequency detuning. Zero frequency corresponds to the $|5^2S_{1/2}, F_g = 2\rangle$ to $|5^2P_{3/2}, F_e = 3\rangle$ energy levels.

The PSR results for the D_2 line are shown in Fig. 7.4. The regions of largest PSR were 0.3 GHz and -0.6 GHz. The input beam powers which gave the largest $\mathcal{G}l$ magnitudes of 8 and 13 were ~ 8 mW and ~ 30 mW, respectively. Zero $\mathcal{G}l$ around zero detuning for input beam powers ≤ 15 mW was due to the low transmission of the input beam for the optically thick ^{87}Rb vapour cloud. However, at frequency detuning ≥ 0.5 and ≤ -0.5 GHz, significant PSR was observed even though the transmission was reduced. For input beam intensities ≥ 20 mW, the PSR was preferentially larger with positive frequency detuning as opposed to negative frequency detuning.

In order to explain the asymmetry present in the PSR results, we modelled the hyperfine energy levels of the D_2 line and took into account Doppler broadening. The theoretical fits to the experimental data are shown in Fig. 7.5.

The reduction in PSR in the negative frequency detuning region was due to reduced transmission, as observed in Fig. 7.3. Broadening of the PSR profile was observed for higher input beam powers.

The transmission results for the D_1 line are shown in Fig. 7.6. The region of lowest transmission (< 50 %) occurred for input beam intensities ≤ 3 mW. These regions were confined around two frequency detuning bands, the -0.2 to 0.25 GHz band and the 0.4 to 0.8 GHz band. The two frequency bands corresponded to the absorption lines centred at the $|5^2S_{1/2}, F_g = 2\rangle$ to $|5^2P_{1/2}, F_e = 1\rangle$ and $|5^2S_{1/2}, F_g = 2\rangle$ to $|5^2P_{1/2}, F_e = 2\rangle$ energy levels, respectively. For input beam powers ≥ 5 mW, significant transmission was observed (> 70 %). For most input beam powers, the transmission of the D_1 line was significantly higher than that of the D_2 line. This was due to the weaker atom-field coupling in the D_1

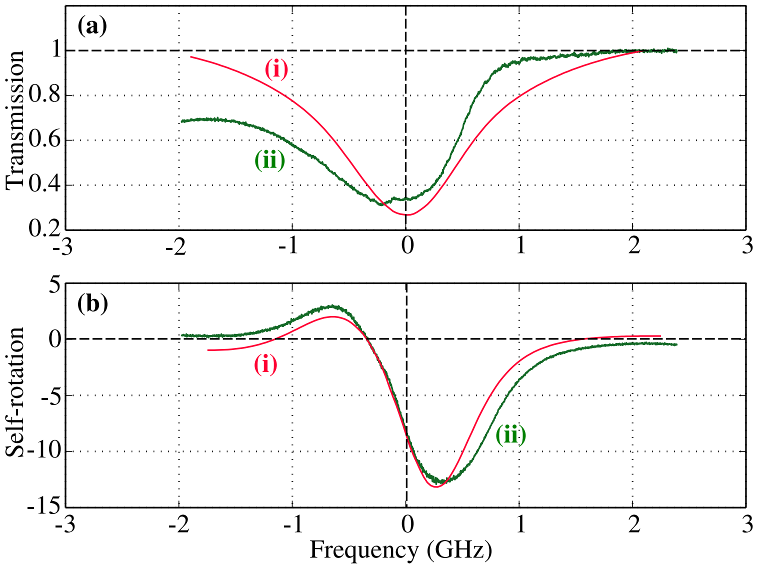

Figure 7.5: The normalised transmission and $\mathcal{G}l$ results for the D$_2$ line are shown in Figures (a) and (b), respectively. The (i) red curves are the theoretical fits to the experimental results ((ii) green curve). Input beam intensity= 31.5 mW, and zero frequency corresponds to the $|5^2S_{1/2}, F_g = 2\rangle$ to $|5^2P_{3/2}, F_e = 3\rangle$ energy levels.

line compared to the D$_2$ line.

The PSR results for the D$_1$ line are shown in Fig. 7.7. The regions of largest PSR occurred at frequency detuning -0.15 GHz and 0.6 GHz. The input beam powers that gave the largest $\mathcal{G}l$ magnitudes of 10 and 11 were $\sim$ 35 mW and $\sim$ 22 mW, respectively. Significant PSR was observed for input beam powers $>$ 3 mW since the transmission was always $>$ 50 %. The $\mathcal{G}l$ magnitude was almost equal in both frequency bands corresponding to the two absorption lines centred at the $|5^2S_{1/2}, F_g = 2\rangle$ to $|5^2P_{1/2}, F_e = 1\rangle$ and $|5^2S_{1/2}, F_g = 2\rangle$ to $|5^2P_{1/2}, F_e = 2\rangle$ energy levels, for most input beam powers. This was due to the excited state level structure of the D$_1$ line, where the two excited state levels have a large separation of $\sim$ 0.8 GHz. This is illustrated by modelling the hyperfine excited state level structure of the D$_1$ line. The theoretical fits to the experimental data are shown in Fig. 7.8.

The two transmission dips are of approximately the same magnitude, resulting in the two PSR peaks to be of equal magnitudes.

7.3.2 Quantum results

The input field was linearly polarised in the x-axis and we measured the quadrature noise of the outgoing y-polarised vacuum field, using the homodyne detection setup shown in Fig. 7.2. The bright x-polarised output field was used as a local oscillator. The fringe visibility of the interferometer was 99 %. The two outputs of the interferometer were then detected using two balanced Silicon photo-detectors (which consisted of Hamamatsu S3883 photo-diodes with measured quantum efficiency values of 94.6 %) with bandwidths of $\sim$ 20 MHz. Blocking the weak field provided a measurement of the QNL. The QNL was checked for linearity with beam power and the common mode rejection was optimised to $\sim$ 30-40 dB from 100 kHz to 10 MHz. We also checked that the polarising beam-

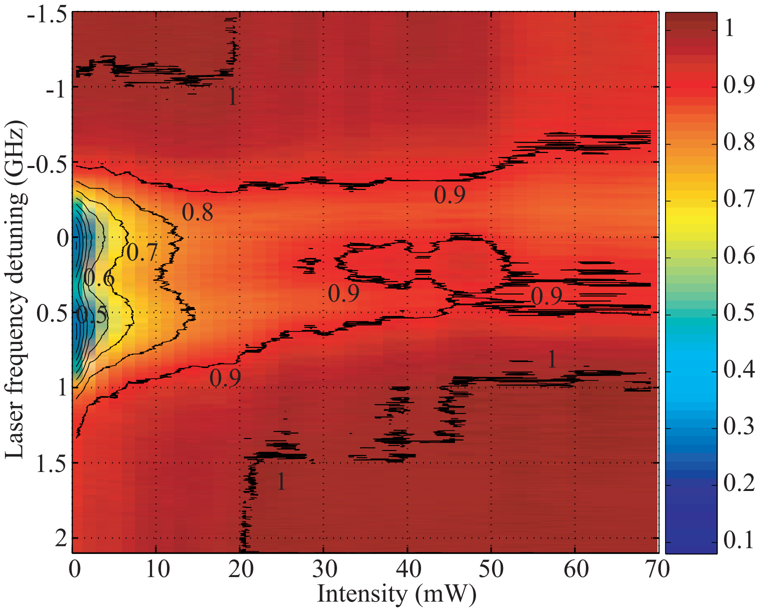

Figure 7.6: False colour contour plot of the normalised transmission results for the D$_1$ line, as a function of input beam intensity and laser frequency detuning. Zero frequency corresponds to the $|5^2S_{1/2}, F_g = 2\rangle$ to $|5^2P_{1/2}, F_e = 1\rangle$ energy levels.

splitter was well aligned such that negligible amounts of the x-polarised field emerged at the y-polarised output port. The result of the noise measurement for various sideband frequencies at various laser frequency detuning and input beam powers, are shown in Figs. 7.9 (D$_2$ line) and 7.11 (D$_1$ line).

The largest quadrature noise observed for the D$_2$ line was 10 dB at a detuning of -70 MHz as shown in Fig. 7.9 (c). A time scanned quadrature noise measurement is shown in Fig. 7.10.

In the noise plots of Figs. 7.9 (a), (c) and (d), we observed large levels of excess noise of typically 5 dB above the QNL. In Fig. 7.9 (b) the excess noise level was 0.8 dB above the QNL. This was the lowest noise level observed around zero detuning. The largest values of the phase quadrature noise level corresponded to the regions of maximum PSR as shown in Fig. 7.4. At large frequency detuning from resonance, both quadrature noise levels were reduced to the QNL.

The noise measurements of the output vacuum field, for the D$_1$ line, are shown in Fig. 7.11. The largest noise modulation observed was 7 dB which occurred at a frequency detuning of 150 MHz as shown in Fig. 7.11 (c). In Figs. 7.11 (a)-(d), the phase quadrature noise level around zero detuning was always above the QNL due to the presence of large excess noise (3-4 dB). The largest values of the amplitude noise level corresponded to the regions of maximum PSR as shown in Fig. 7.7. At large frequency detuning from resonance, both quadrature noise levels were reduced to the QNL.

The noise measurement results presented do not vary qualitatively with varying beam focussing geometry, incident power or temperature. A large amount of excess noise was systematically observed close to resonance. Although the PSR and transmission results measured were in a very similar regime to that of Ref. [177], the quantum noise results are not in agreement with either the predictions of Ref. [179] or the observations of Ref. [177].

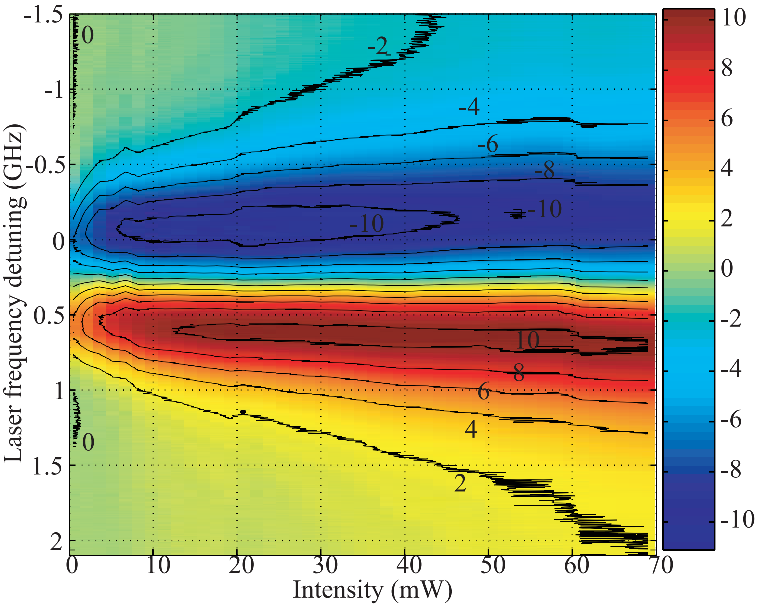

Figure 7.7: False colour contour plot of $\mathcal{G}l$ for the D$_1$ line, normalised to the input beam ellipticity of 2°, as a function of input beam intensity and laser frequency detuning. Zero frequency corresponds to the $|5^2S_{1/2}, F_g = 2\rangle$ to $|5^2P_{1/2}, F_e = 1\rangle$ energy levels.

We use the model presented in Sec. 7.2.2 to discuss our experimental observations.

7.4 Discussion

7.4.1 Langevin noise analysis

In order to contrast the effect of the atomic noise terms with the squeezing term in Eq. (7.29), we consider the Langevin term given by

$$\tilde{F}_y = \frac{gNl}{c}\left[(A+B)\tilde{f}_y + B\tilde{f}_y^\dagger + i\sqrt{I_x}A\left(\frac{\tilde{f}_z}{-i\omega} + \frac{\tilde{f}_z'}{2\gamma - i\omega}\right)\right] \tag{7.32}$$

where

$$\begin{aligned} A &= \frac{(\gamma - i\Delta - i\omega)(-i\omega)(2\gamma - i\omega)}{D} \\ B &= \frac{I_x(\gamma - i\omega)}{D} \\ D &= 2I_x(\gamma - i\omega)^2 - i\omega(2\gamma - i\omega)[(\gamma - i\omega)^2 + \Delta^2] \end{aligned}$$

with $I_x = |g\langle\tilde{\mathcal{E}}_x\rangle|^2$, $\tilde{f}_y = (\tilde{F}_{14} + \tilde{F}_{23})/\sqrt{2}$, $\tilde{f}_z = (\tilde{F}_{22} - \tilde{F}_{11})/\sqrt{2}$ and $\tilde{f}_z' = (\tilde{F}_{44} - \tilde{F}_{33})/\sqrt{2}$. The contribution of this noise term, which depends on the sideband frequency, is to be compared with the cross-Kerr squeezing term $\kappa(\omega)$. As shown in Ref. [221], in the below saturation regime, large excess atomic noise associated with optical pumping on the y-polarised field dominates at sideband frequencies *lower* than the spontaneous emission

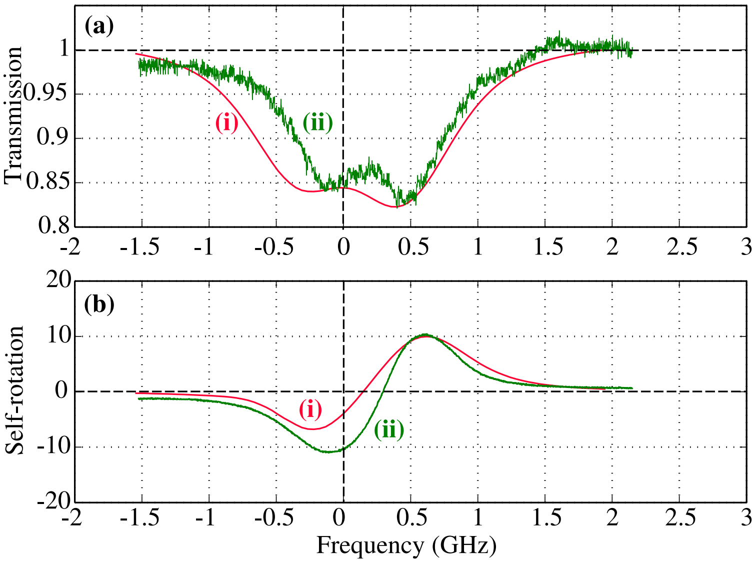

Figure 7.8: The normalised transmission and $\mathcal{G}l$ results for the D$_1$ line are shown in Figures (a) and (b), respectively. The (i) red curves are the theoretical fits to the experimental results ((ii) green curve). Input beam intensity= 22.3 mW, and zero frequency corresponds to the $|5^2S_{1/2}, F_g = 2\rangle$ to $|5^2P_{1/2}, F_e = 1\rangle$ energy levels.

rate ($\omega \ll \gamma$). In the low sideband frequency regime (assuming $\Delta \gg \gamma$), one obtains

$$\frac{\partial}{\partial \tilde{z}}\delta\tilde{\mathcal{E}}_y = i\frac{\delta_0}{1+s}\delta\tilde{\mathcal{E}}_y^\dagger + \frac{gNl}{2\gamma c}(\tilde{f}_y + \tilde{f}_y^\dagger + \frac{\Delta}{2\sqrt{I_x}}\tilde{f}_z) \tag{7.33}$$

where $\delta_0 = C\gamma/2\Delta$ denotes the linear dephasing. Ignoring depletion of the mean x-polarised field, the Langevin noise contribution is shown to be proportional to C/gl at least. For the experiment, this quantity is greater than the QNL, such that large excess noise is present in all quadratures for low sideband frequencies, even when absorption is ignored. One therefore cannot observe squeezing in this regime.

In the experiment, the quantum noise of the vacuum field was measured only for sideband frequencies *greater* than the excited state decay rate ($\omega \geq \gamma$). In this high sideband frequency regime (assuming $\Delta \gg \gamma$), we obtain succinct expressions for $\kappa(\omega)$, $\Gamma(\omega)$ and $\tilde{F}_y$ given by

$$\kappa(\omega) = \frac{-i\delta_0 s}{(1+s)(1+2s)}, \qquad \Gamma(\omega) = \frac{-i\delta_0}{1+s} \tag{7.34}$$

$$\begin{aligned}\tilde{F}_y &\simeq -i\frac{gNl}{\Delta c(1+2s)}\big[(1 + I_x/\omega\Delta)\tilde{f}_y + (I_x/\omega\Delta)\tilde{f}_y^\dagger \\ &\qquad -(\sqrt{I_x}/\omega)(\tilde{f}_z + \tilde{f}_z')\big].\end{aligned} \tag{7.35}$$

The above equations describe the atomic noise contribution that may degrade the squeezing of the output y-polarised vacuum field.

The optimisation of squeezing is dependent on finding a regime that has low absorption and strong non-linearity. We now proceed by dividing the discussion into low and high atomic transition saturation regimes.

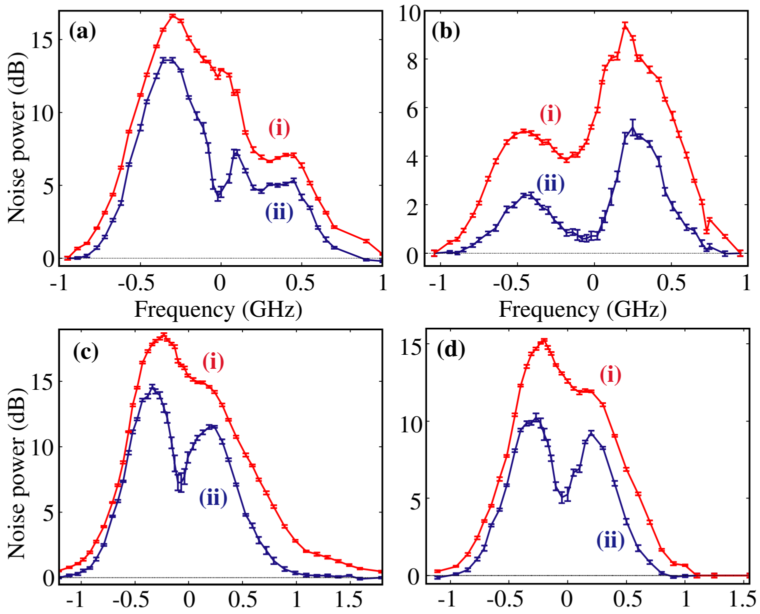

Figure 7.9: (i) Amplitude and (ii) phase quadrature noise results for the D_2 line, normalised to the QNL and dark noise-subtracted. Figures (a) and (b) correspond to an input beam power of 21 mW at sideband frequencies of 3 MHz and 6 MHz, respectively. Figures (c) and (d) are results for an input beam power of 35 mW, at sideband frequencies of 3 MHz and 6 MHz, respectively. Zero frequency corresponds to the $|5^2S_{1/2}, F_g = 2\rangle$ to $|5^2P_{3/2}, F_e = 3\rangle$ energy level. ResBW: 100 kHz and VBW: 30 Hz.

7.4.2 Below saturation regime with ultra-cold atoms

Since cold atoms have higher atomic density, one can operate in the below saturation regime ($s \ll 1$) and still obtain strong PSR with minimal atomic noise [91], when off-resonance. In the Kerr limit ($\Delta \gg \sqrt{I_x} \gg \gamma$), the equation of motion for the vacuum field fluctuations is given by

$$\frac{\partial}{\partial \tilde{z}} \delta\tilde{\mathcal{E}}_y = i\delta_0 \delta\tilde{\mathcal{E}}_y - i\delta_0 s(2\delta\tilde{\mathcal{E}}_y - \delta\tilde{\mathcal{E}}_y^\dagger) - i\frac{gNl}{c\Delta}\tilde{f}_y. \tag{7.36}$$

One recovers in the equation above the same terms as in the cavity model of Ref. [221] under the same approximations. The term in $\delta_0\delta\tilde{\mathcal{E}}_y$ corresponds to the linear dephasing, the second term gives the cross-Kerr squeezing term and the Langevin noise contribution corresponding to the last term can be shown to be proportional to $C\gamma^2/\Delta^2$, which can be small in the off-resonant situation ($\Delta \gg \gamma$). In accordance with the prediction of Ref. [221] and the experimental observations of Ref. [91] vacuum squeezing can be generated when $\delta_0 s \sim 1$ and $C\gamma^2/\Delta^2$.

7.4.3 Above saturation regime with thermal vapour cell

Contrary to the situation of cold atoms, the Doppler broadening in a thermal vapour makes it impossible to work in the below saturation regime while simultaneously having low absorption or high non-linearity. It is however possible to observe strong PSR in the above saturation regime. In this regime, the atomic noise term is significantly different to

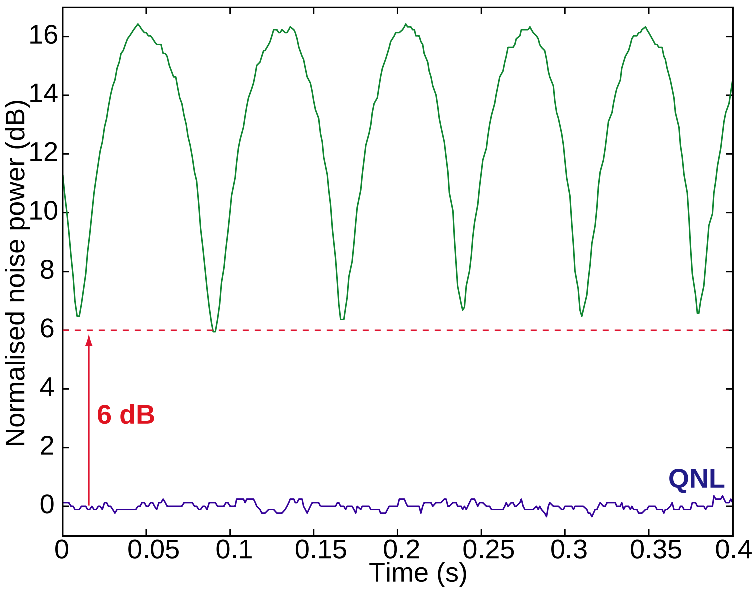

Figure 7.10: Scanned quadrature noise for the D_2 line measured in zero span at a sideband frequency of 3 MHz. The input beam power was 35 mW and the laser frequency was -70 MHz from the $|5^2S_{1/2}, F_g = 2\rangle$ to $|5^2P_{1/2}, F_e = 3\rangle$ energy level. All plots are dark noise subtracted. ResBW: 100 kHz and VBW: 30 Hz.

that given in Eq. (7.36). For $I_x \gg \Delta^2$, the equation of motion is given by

$$\frac{\partial}{\partial \tilde{z}} \delta\tilde{\mathcal{E}}_y = \frac{i\delta_0}{2s}(\delta\tilde{\mathcal{E}}_y + \delta\tilde{\mathcal{E}}_y^\dagger) - i\frac{gNl}{c\omega}(\tilde{f}_y + \tilde{f}_y^\dagger). \tag{7.37}$$

As we have seen experimentally with the PSR measurements, the non-linear term in $\delta_0/(2s) = \mathcal{G}l$ can still be significant when the number of atoms is increased. However, the optical pumping processes associated with PSR now produce a lot of excess noise even in the high sideband frequency regime. The contribution of the last term in Eq. (7.37) can be shown to be proportional to $C\gamma^2/\omega^2 \gg 1$. For our experimental parameters, the atomic noise prevents the observation of squeezing at all sideband frequencies.

7.4.4 Further considerations

We now discuss the possible discrepancies between the theoretical models and the experiment. Due to the complexity of the problem, many effects have not been taken into account in the various models discussed in this chapter.

Firstly, the presence of resonance fluorescence has not been considered in Ref. [179]. In Ref. [221], it was shown that PSR cannot generate squeezing in the below saturation regime because of optical pumping processes. We have shown in this chapter that this is also true in the above saturation regime where the resonance fluorescence noise dominates over the cross-Kerr squeezing term, *even* at high detection frequencies. This conclusion is in agreement with other observations [284, 285, 283].

Secondly, none of the models presented have included the Doppler effect. Since we are dealing with thermal atoms, the passage of light through the atoms will give rise to a range of observed atomic detuning. The integrated effect due to Doppler broadening will

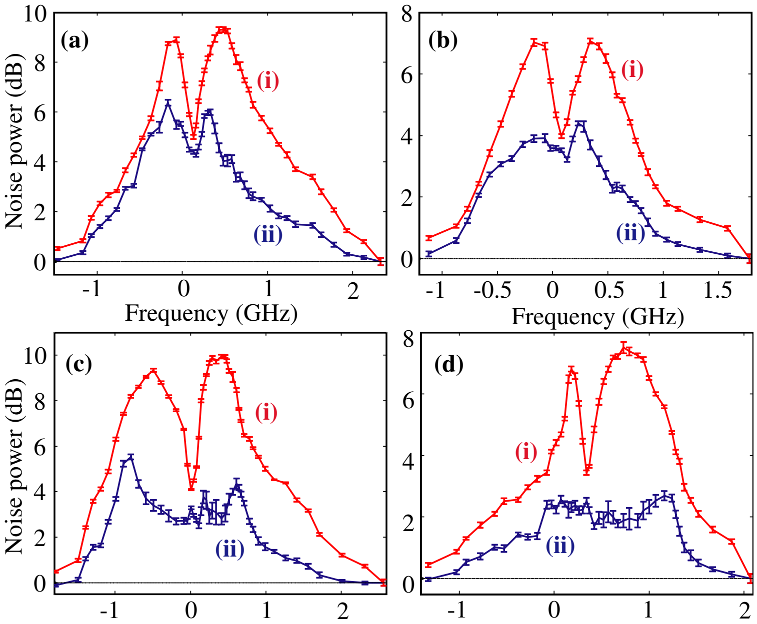

Figure 7.11: (i) Amplitude and (ii) phase quadrature noise results for the D_1 line, normalised to the QNL and subtracted by the dark noise. Figures (a) and (b) correspond to an input beam power of 21 mW at sideband frequencies of 3 MHz and 6 MHz, respectively. Figures (c) and (d) are results for an input beam power of 35 mW, at sideband frequencies of 3 MHz and 6 MHz, respectively. Zero frequency corresponds to the $|5^2S_{1/2}, F_g = 2\rangle$ to $|5^2P_{1/2}, F_e = 1\rangle$ energy level. ResBW: 100 kHz and VBW: 30 Hz.

be detrimental to the observation of squeezing.

Thirdly, the multi-level hyperfine structure of the excited states of ^{87}Rb have only been considered for the theoretical fits to the classical PSR results, but have not been included in any of the squeezing model. The experimental PSR data presented in this chapter clearly shows that the multi-level hyperfine structure causes observable asymmetry in the PSR spectrum. This feature cannot be explained by any of the theoretical models presented in Sec. 7.2. The multi-level theory can be expanded to include Langevin noise terms. However, a simple 4-level atom model is sufficient to demonstrate the lack of squeezing. The multi-level structure is also certainly less favourable to the generation of squeezing when compared with a simplified 4-level model. Different hyperfine levels will not contribute constructively towards a collective interaction that will generate squeezing. The added noise from these different levels will add up significantly. The inclusion of Doppler broadening and multi-level effects would only result in a dominance of the atomic noise term over the squeezing term.

Finally, the propagation of the transverse intensity profile of the input field has been totally ignored in all models. A full treatment of the process should include the multi-modal analysis of the evolution of the transverse field modes during propagation through the vapour cell. In the above saturation regime and for high atomic densities, self-focussing is readily observed. This is due to the atom induced Kerr lens-effect on the optical field. Thus the centre of the field intensity distribution will undergo greater PSR than the edges. The cross-Kerr non-linearity and the atomic absorption used in our calculations is a result of an “integrated” effect of the various transverse modes. It therefore does not model accurately the situation of the experiment. Similar to the previous argument, it is unlikely that the multi-modal consideration of the process will yield better squeezing.

7.5 Conclusion

We have presented experimental results of PSR and have observed no squeezing. Instead we have observed excess noise in the output field spectrum at all sideband frequencies. We have modelled semi-classically the multi-level hyperfine structure of ^{87}Rb and obtained theoretical fits to the experimental PSR data. Our multi-level modelling can predict the asymmetry in the PSR, that is due to the presence of other hyperfine excited states. We considered a quantum mechanical 4-level atomic model and showed that the squeezing term is overwhelmed by atomic noise terms in the situation of a thermal vapour. The effects of resonance fluorescence, the Doppler effect and the multi-level hyperfine structure of ^{87}Rb all contribute to overwhelm the squeezing term. Therefore, it is expected that a full quantum mechanical treatment of a multi-level ^{87}Rb atom will yield a result where squeezing is unlikely be generated. In spite of this, the results of Ries *et al.* [177] and recent experiments conducted in the group of A. I. Lvovsky[3] have demonstrated the observation of less than 1 dB of squeezing. The contradiction in experimental results [177, 181] should serve as a caveat that more comprehensive theoretical modelling and experimental studies are necessary to understand exactly the conditions in a thermal vapour cell under which PSR squeezing can be generated, or become overwhelmed by excess noise.

The 4-level atom model shows that squeezing can be generated in the situation of cold atoms where the Doppler effect is negligible. When the input field is off-resonance, the non-linearity is large but the absorption low, such that the atomic noise term does not overwhelm the squeezing term. Experimental demonstrations of squeezing generation from cold atoms in an optical cavity have been published in Refs. [90, 91].

---

[3] personal communication

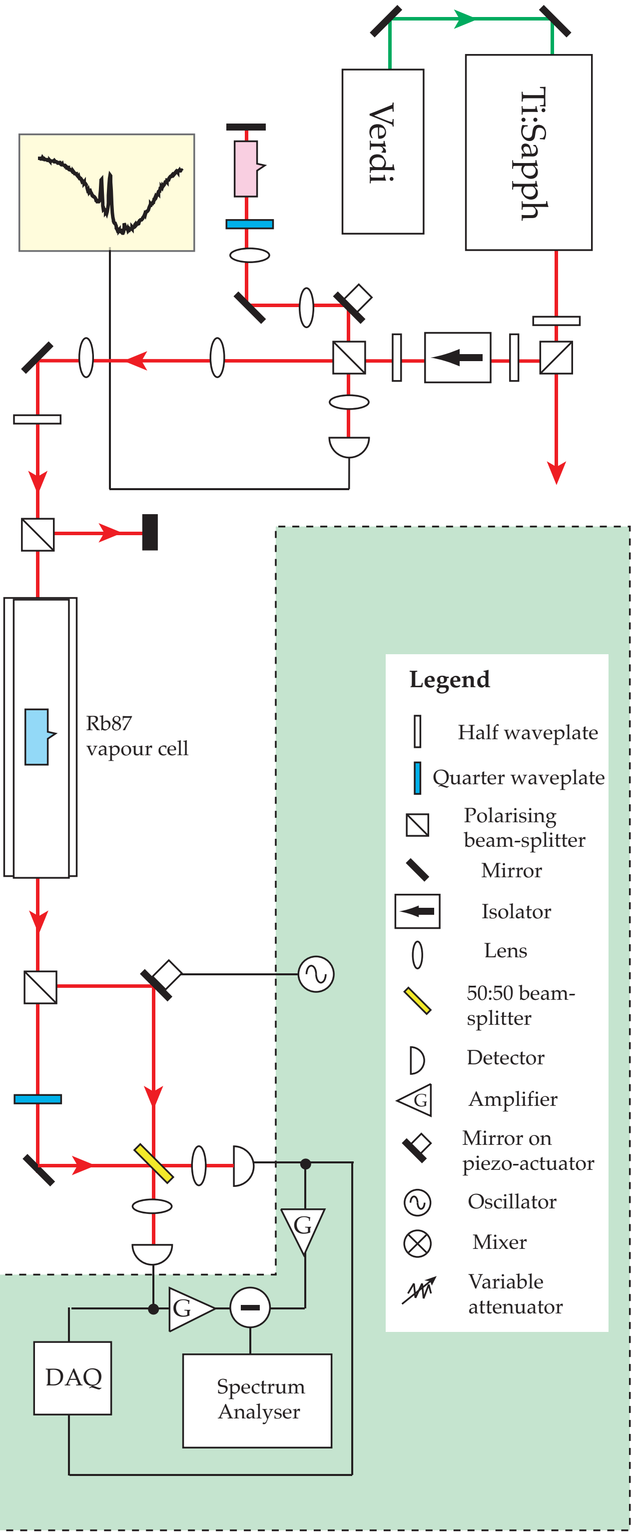

Figure 7.12: Detailed schematic of experimental setup.

Chapter 8

Electomagnetically induced transparency

Enlightenment is not imagining figures of light but making the darkness conscious.

- Carl Jung

Imagine if you could see through walls. Today, companies such as Camero Inc. and Cambridge Consultants are developing and selling products for 'seeing through walls'[1], based on X-ray or microwave technology. In 1991, *electromagnetically induced transparency* (EIT) was observed by the Harris group [162] in Stanford University. EIT was a clear demonstration that by shining a pump field into an atomic medium, transparency on the probe field can be obtained. This was due to a destructive interference process on the absorption pathways for the light fields and held promise for 'seeing through walls' technology.

However, EIT also has the potential for delaying and storing light in atomic ensembles. This was followed by impressive demonstrations of light delay to 17 m/s [163] and pulse storage [164]. Proposals have also been made to extend the classical pulse delay and storage in EIT to quantum information delay and storage [161]. However most EIT experiments analysed the shape of delayed and stored pulses. In our experiment, we measure continuous-wave signals encoded in the sidebands of a probe beam. We quantify the noise performance of an EIT system for the conjugate amplitude and phase quadratures of the probe beam. In analogy with other continuous-variable quantum information systems, the performance of our EIT system is characterised in terms of conditional variance and signal transfer. It is shown that our EIT system adds excess noise to the delayed light that has not hitherto been predicted by published theoretical modelling. A possible source of excess noise transfer from pump to probe is identified. We also speculate on other effects which may produce excess noise in EIT systems.

The work in this chapter has been published in

- M. T. L. Hsu, G. Hétet, O. Glöckl, J. J. Longdell, B. C. Buchler, H.-A. Bachor, and P. K. Lam, "Quantum study of information delay in electromagnetically induced transparency", Physical Review Letters **97**, 183601 (2006).
- G. Hétet, A. Peng, M. Johnsson, M. T. L. Hsu, O. Glöckl, P. K. Lam, H.-A. Bachor,

---

[1] http://www.camero-tech.com/ and http://www.cambridgeconsultants.com/

and J. J. Hope, “Erratum: Squeezing and entanglement delay using slow light”, Physical Review A **74**, 059902(E) (2006).

8.1 Introduction

Following theoretical proposals [161, 286], electromagnetically induced transparency (EIT) [162] has become the subject of much interest for controlled atomic storage of quantum states of light. Indeed, the delay and storage of optical qubits in an atomic medium via EIT has recently been shown allowing, in principle, the synchronisation of quantum information processing systems [287, 288]. Earlier works with classical signals in a vapour cell [289] and cold atoms [163] have shown large signal delay with group velocities as low as 17 ms^{-1}. Storage of classical pulses has also been shown for atomic vapour cells [164, 290], cold atomic clouds [291], and solid state systems [292, 293] (although it should be noted that alternative interpretations of such pulse storage experiments have also been published [294, 295, 296]). One experiment [297] has shown the transmission of a squeezed state through an EIT system in a vapour cell under the conditions of very small delay. A more recent experiment reported the ultraslow propagation of a squeezed pulse via EIT [298]. This experiment measured the delay as the shifting of the peak of the pulse, but in this instance, the pulse has undergone reshaping. Therefore, we would like to take a different approach to experimentally quantify the efficacy of EIT for continuous-variable quantum information systems.

Quantum-theoretical treatments of delay and storage via EIT, in the presence of decoherences, have suggested that no excess noise is added to the delayed light [223, 286, 299, 182]. These works show that the degradation of a quantum state in an EIT system results from - (i) the finite transparency window and (ii) a degradation in the transparency induced by ground state dephasing. The implication is that, within the EIT window and for small ground state dephasing, quantum states of light can be delayed and preserved in an EIT medium. In this chapter, we present experimental results that examine the quantum noise performance of an EIT system for conjugate amplitude and phase quadratures, that are measured at sideband frequencies (ω) around the optical carrier. Since much work on EIT is motivated by quantum information processing, we evaluate the performance of the EIT system using well established criteria for continuous variable (CV) quantum state measurements. In analogy with quantum teleportation and non-demolition experiments where states are transferred from an input to an output, we utilise the conditional variance and signal transfer coefficients to quantify the quantum noise properties of our EIT system.

This chapter describes our observations of excess noise in an EIT system [183]. It should be emphasised that some of the basic quantum theoretical treatments of EIT presented here have been reported elsewhere [182, 300], and have been included for completeness. In Section 8.2, we review the quantum treatment of a probe beam interacting with an EIT system, using a 3-level atomic system. We then describe the conditional variance measurement process and the noise penalties introduced from the use of coherent beams, instead of entanglement, to characterise the EIT system. The experimental scheme is described in detail in Section 8.3. In Section 8.4, we present experimental results of transmission and delay of sideband signals on the probe beam, through an EIT system. The results and discussion of conditional variance, signal transfer from pump-to-probe beams, signal transfer coefficient, as well as cross-quadrature signal transfer of the probe beam are described in this section. Finally, in the conclusion section, we speculate on the possible sources of excess noise and aspects of the experiment that theoretical studies should include for a comprehensive analysis of EIT.

8.2 Theory

8.2.1 Dark state

When resonant light is sent into a sample of 2-level atoms, the optical field will be absorbed by the atoms. It is possible to suppress the absorption by having a 3-level atomic system with the application of a second optical pump field. This effect is termed *electromagnetically induced transparency* (EIT). EIT is created by the interaction of probe (E_p) and pump (E_c) fields, in a 3-level Λ-atomic system, as shown in Fig. 8.1. The ground states are denoted by states $|1\rangle$ and $|2\rangle$, while the excited state is denoted by $|3\rangle$. When the probe and pump beams have zero two-photon detuning, a destructive quantum interference effect is induced which results in a dark state (i.e. a coherent superposition of the ground states $|1\rangle$ and $|2\rangle$ only), given by

$$|D\rangle = \frac{E_c}{\sqrt{|E_c|^2 + |E_p|^2}}|1\rangle + \frac{E_p}{\sqrt{|E_c|^2 + |E_p|^2}}|2\rangle \tag{8.1}$$

Thus the absorption pathways between states $|1\rangle \rightarrow |3\rangle$ and $|2\rangle \rightarrow |3\rangle$ are suppressed. The result is that transparency is obtained for the probe beam, which in the absence of the pump, would be fully absorbed.

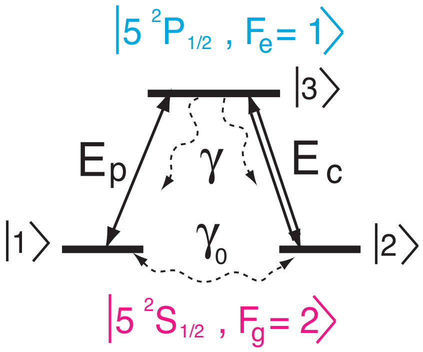

Figure 8.1: Atomic level scheme used in our experiment. E_p is the probe field, E_c is the pump field, γ is the spontaneous emission rate, γ_0 is the ground state dephasing rate, $|1\rangle$ and $|2\rangle$ are the ground states corresponding to different Zeeman sublevels in the experiment, $|3\rangle$ is the excited state.

8.2.2 Hamiltonian

To model the time evolution and propagation properties of the probe field through an EIT system, the Hamiltonian for a 3-level atomic system interacting with a probe and pump field is considered. Prior to this, we first formalise the relevant field and atomic dipole operators required for such a treatment.

The positive frequency part of the electric field operator is defined as

$$\hat{E}^{+}(z,t) = \hat{\mathcal{E}}^{+}(z,t) \exp\Big(i\omega_0(\frac{z}{c} - t)\Big) \tag{8.2}$$

where ω_0 is the central frequency of the field and z is the distance along the propagation direction of the field. $\hat{\mathcal{E}}^{+}(z,t)$ is the positive frequency part of the slowly varying field envelope operator. Following all previous theoretical treatments on EIT, the spatial dependence of the fields are not considered and thus the fields are assumed to be plane waves.

We now consider the locally averaged atomic dipole operator for a system of transverse slice with length Δz with $N_z \gg 1$ atoms. In this scenario, the slowly-varying field envelope operator $\hat{\mathcal{E}}(z,t)$ does not vary much and the spatial dependence is assumed to be planar. Therefore, the atomic dipole operator is given by

$$\hat{\sigma}_{\mu\nu}(z,t) = \frac{1}{N_z} \sum_{z_j \in N_z} \hat{\sigma}_{\mu\nu}^{(j)}(t) \exp\Big(i\omega_0(\frac{z}{c} - t)\Big) \tag{8.3}$$

where the j-th atom has dipole operator $\sigma_{\mu\nu}^{(j)}(t) = |\mu^{(j)}(t)\rangle\langle\nu^{(j)}(t)|$, and $\mu, \nu = 1, 2, 3$.

The interaction Hamiltonian for a 3-level atomic system interacting with a probe and pump field is given by

$$\begin{aligned} \hat{\mathcal{H}}_{\text{int}} &= \sum_{j=1}^{N} e\hat{\boldsymbol{r}}_j \cdot \hat{E}(\boldsymbol{r}_j, t) && (8.4) \\ &= -\sum_{j=1}^{N} \Big(d_{13}\hat{\sigma}_{13}^{(j)} + d_{13}^{*}\hat{\sigma}_{31}^{(j)} + d_{32}\hat{\sigma}_{32}^{(j)} + d_{32}^{*}\hat{\sigma}_{23}^{(j)}\Big) \cdot \Big(\hat{E}_p(\boldsymbol{r}_j, t) + \hat{E}_c(\boldsymbol{r}_j, t)\Big) && (8.5) \end{aligned}$$

where $d_{\mu\nu}$ is the dipole moment for the $|\mu\rangle \rightarrow |\nu\rangle$ transition. The atomic dipole operator for the j-th atom at location $\boldsymbol{r}_j$ is given by $\hat{\sigma}_{\mu\nu}^{(j)} = |\mu^{(j)}\rangle\langle\nu^{(j)}|$.

The interaction Hamiltonian can be written in terms of the electric field envelope operator given by

$$\begin{aligned} \hat{\mathcal{H}}_{\text{int}} &= -\sum_{j=1}^{N} \Big(g\hat{\sigma}_{13}^{(j)} + g\hat{\sigma}_{31}^{(j)} + g\hat{\sigma}_{32}^{(j)} + g\hat{\sigma}_{23}^{(j)}\Big) \\ &\quad \cdot \Big(\hat{\mathcal{E}}_p^{+}(\boldsymbol{r}_j, t)e^{-i\omega_p t} + \hat{\mathcal{E}}_p^{-}(\boldsymbol{r}_j, t)e^{i\omega_p t} + \hat{\mathcal{E}}_c^{+}(\boldsymbol{r}_j, t)e^{-i\omega_c t} + \hat{\mathcal{E}}_c^{-}(\boldsymbol{r}_j, t)e^{i\omega_c t}\Big) && (8.6) \end{aligned}$$

where we have assumed that the dipole moment for the transitions are all equal and real, given by $d_{13} = d_{13}^{*} = d_{23} = d_{23}^{*} = g$.

The interaction Hamiltonian, under the rotating wave approximation[2], for a 3-level atomic system (corresponding to Fig. 8.1) interacting with an intense, classical pump field, $\langle\hat{\mathcal{E}}_c\rangle$, and weak quantum probe field, $\hat{\mathcal{E}}_p$, for an optically thick medium (where we replace the sum by an integral over the atomic ensemble length L), is given by [182]

$$\hat{\mathcal{H}}_{\text{int}} = inA_{\text{eff}} \int_0^L dz\Big(- g\hat{\mathcal{E}}_p(z,t)\hat{\sigma}_{31}(z,t) - g\langle\hat{\mathcal{E}}_c(z,t)\rangle\hat{\sigma}_{32}(z,t) + \text{H.c.}\Big) \tag{8.7}$$

---

[2] The energy non-conserving terms have been removed as they have minimal probability of occurring.

where n is the atomic density and A_{eff} is the effective transverse area of the interaction region.

8.2.3 Equations of motion

The time and longitudinal propagation of the probe field through the EIT system is described by the equations of motion for the atomic dipole and field operators. The equation of motion for the atomic dipole operator is obtained from the Heisenberg equation of motion, given by

$$i\hbar\frac{\partial\hat{\sigma}_{\mu\nu}}{\partial t} = [\hat{\sigma}_{\mu\nu}, \hat{\mathcal{H}}_{\text{int}}] \tag{8.8}$$

and the equation of motion for the slowly varying field envelope operator is given by

$$i\hbar\left(\frac{\partial}{\partial t} + c\frac{\partial}{\partial z}\right)\hat{\mathcal{E}}(z,t) = [\hat{\mathcal{E}}(z,t), \hat{\mathcal{H}}_{\text{int}}] \tag{8.9}$$

By phenomenologically including spontaneous emission from the excited state to the ground states, γ, as well as a dephasing term for the ground state coherence, γ_0, the corresponding equations of motion for the atomic dipole operators are given by

$$\begin{aligned}
\frac{\partial}{\partial t}\hat{\sigma}_{13} &= -\gamma\hat{\sigma}_{13} + ig\hat{\mathcal{E}}_p(\hat{\sigma}_{11} - \hat{\sigma}_{33}) + ig\langle\hat{\mathcal{E}}_c\rangle\hat{\sigma}_{12} + \hat{F}_{13} && (8.10)\\
\frac{\partial}{\partial t}\hat{\sigma}_{23} &= -\gamma\hat{\sigma}_{23} + ig\langle\hat{\mathcal{E}}_c\rangle(\hat{\sigma}_{22} - \hat{\sigma}_{33}) + ig\hat{\mathcal{E}}_p\hat{\sigma}_{21} + \hat{F}_{23} && (8.11)\\
\frac{\partial}{\partial t}\hat{\sigma}_{12} &= -\gamma_0\hat{\sigma}_{12} + ig\langle\hat{\mathcal{E}}_c\rangle^*\hat{\sigma}_{12} - ig\hat{\mathcal{E}}_p\hat{\sigma}_{32} + \hat{F}_{12} && (8.12)\\
\frac{\partial}{\partial t}\hat{\sigma}_{11} &= \gamma\hat{\sigma}_{33} + ig\hat{\mathcal{E}}_p^\dagger\hat{\sigma}_{13} - ig\hat{\mathcal{E}}_p\hat{\sigma}_{31} + \hat{F}_{11} && (8.13)\\
\frac{\partial}{\partial t}\hat{\sigma}_{22} &= \gamma\hat{\sigma}_{33} + ig\langle\hat{\mathcal{E}}_c\rangle^*\hat{\sigma}_{23} - ig\langle\hat{\mathcal{E}}_c\rangle\hat{\sigma}_{32} + \hat{F}_{23} && (8.14)\\
\frac{\partial}{\partial t}\hat{\sigma}_{33} &= -2\gamma\hat{\sigma}_{33} - ig\hat{\mathcal{E}}_p^\dagger\hat{\sigma}_{13} + ig\hat{\mathcal{E}}_p\hat{\sigma}_{31} - ig\langle\hat{\mathcal{E}}_c\rangle^*\hat{\sigma}_{23} && (8.15)\\
&\quad +ig\langle\hat{\mathcal{E}}_c\rangle\hat{\sigma}_{32} + \hat{F}_{33} && (8.16)
\end{aligned}$$

where the corresponding Langevin noise operators corresponding to the atomic decoherences are denoted by $\hat{F}_{\mu\nu}$, where $\langle\hat{F}_{\mu\nu}\rangle = 0$. These terms are included in order to preserve the commutation relations of the observable operators for the system.

The corresponding Maxwell-Bloch equation for the probe field is given by

$$\left(\frac{\partial}{\partial t} + c\frac{\partial}{\partial z}\right)\hat{\mathcal{E}}_p = ig^*\hat{\sigma}_{13} \tag{8.17}$$

Note that the pump field does not undergo evolution due to the weak probe assumption. This assumption can be further verified by checking the mean-field steady state solution for $\langle\hat{\sigma}_{23}\rangle$, given in Eq. (8.18).

8.2.4 Mean-field steady state solutions

The steady state solutions of the equations of motion are obtained by setting the time-derivatives of Eqs. (8.10) - (8.16) to zero and solving for the mean-field components only,

given by

$$\begin{aligned}
\langle\hat{\sigma}_{13}\rangle &= \frac{i\gamma_0 g}{\gamma\gamma_0 + g^2|\langle\hat{\mathcal{E}}_c\rangle|^2}\langle\hat{\mathcal{E}}_p\rangle \\
\langle\hat{\sigma}_{23}\rangle &= \frac{-ig^3\langle\hat{\mathcal{E}}_c\rangle}{\gamma(\gamma\gamma_0 + g^2|\langle\hat{\mathcal{E}}_c\rangle|^2)}|\langle\hat{\mathcal{E}}_p\rangle|^2 \\
\langle\hat{\sigma}_{12}\rangle &= \frac{-g^2\langle\hat{\mathcal{E}}_c\rangle^*}{\gamma\gamma_0 + g^2|\langle\hat{\mathcal{E}}_c\rangle|^2}\langle\hat{\mathcal{E}}_p\rangle \\
\langle\hat{\sigma}_{11}\rangle &= 1 \\
\langle\hat{\sigma}_{22}\rangle &= \langle\hat{\sigma}_{33}\rangle = 0
\end{aligned} \tag{8.18}$$

where the population in the states $|2\rangle$ and $|3\rangle$ are zero due to population pumping into state $|1\rangle$ from the strong pump field. Note that the population in the states are conserved, given by $\langle\hat{\sigma}_{11}\rangle + \langle\hat{\sigma}_{22}\rangle + \langle\hat{\sigma}_{33}\rangle = 1$.

8.2.5 Probe field variance

Eqs. (8.10) - (8.12) are sufficient for obtaining a solution for the atomic operators. By expressing the atomic dipole operators in terms of $\hat{\sigma}_{\mu\nu} = \langle\hat{\sigma}_{\mu\nu}\rangle + \delta\hat{\sigma}_{\mu\nu}$, and the probe field operators as $\hat{\mathcal{E}}_p = \delta\hat{\mathcal{E}}_p$, the noise terms of Eqs. (8.10) - (8.12) are thus given by

$$\frac{\partial}{\partial t}\delta\hat{\sigma}_{13} = -\gamma\delta\hat{\sigma}_{13} + ig\delta\hat{\mathcal{E}}_p + ig\langle\hat{\mathcal{E}}_c\rangle\delta\hat{\sigma}_{12} + \hat{F}_{13} \tag{8.19}$$

$$\frac{\partial}{\partial t}\delta\hat{\sigma}_{23} = -\gamma\delta\hat{\sigma}_{23} + ig\delta\hat{\mathcal{E}}_p\langle\hat{\sigma}_{21}\rangle + \hat{F}_{23} \tag{8.20}$$

$$\frac{\partial}{\partial t}\delta\hat{\sigma}_{12} = -\gamma_0\delta\hat{\sigma}_{12} + ig\langle\hat{\mathcal{E}}_c\rangle^*\delta\hat{\sigma}_{13} + \hat{F}_{12} \tag{8.21}$$

Now take the Fourier transform of the equations,

$$-i\omega\delta\tilde{\sigma}_{13} = -\gamma\delta\tilde{\sigma}_{13} + ig\delta\tilde{\mathcal{E}}_p + ig\langle\tilde{\mathcal{E}}_c\rangle\delta\tilde{\sigma}_{12} + \tilde{F}_{13} \tag{8.22}$$

$$-i\omega\delta\tilde{\sigma}_{23} = -\gamma\delta\tilde{\sigma}_{23} + ig\delta\tilde{\mathcal{E}}_p\langle\tilde{\sigma}_{21}\rangle + \tilde{F}_{23} \tag{8.23}$$

$$-i\omega\delta\tilde{\sigma}_{12} = -\gamma_0\delta\tilde{\sigma}_{12} + ig\langle\tilde{\mathcal{E}}_c\rangle^*\delta\tilde{\sigma}_{13} + \tilde{F}_{12} \tag{8.24}$$

Solving these equations in terms of the probe field operator $\tilde{\mathcal{E}}_p$, gives

$$\delta\tilde{\sigma}_{13} = \frac{(\gamma_0 - i\omega)\left(ig\delta\tilde{\mathcal{E}}_p + \tilde{F}_{13}\right) + ig\langle\tilde{\mathcal{E}}_c\rangle\tilde{F}_{12}}{(\gamma_0 - i\omega)(\gamma - i\omega) + g^2|\langle\tilde{\mathcal{E}}_c\rangle|^2} \tag{8.25}$$

$$\begin{aligned}
\delta\tilde{\sigma}_{12} &= \frac{-g^2\langle\tilde{\mathcal{E}}_c\rangle^*}{(\gamma_0 - i\omega)(\gamma - i\omega) + g^2|\langle\tilde{\mathcal{E}}_c\rangle|^2}\delta\tilde{\mathcal{E}} \\
&\quad + \frac{(\gamma_0 - i\omega)ig\langle\tilde{\mathcal{E}}_c\rangle^*\tilde{F}_{13} - g^2|\langle\tilde{\mathcal{E}}_c\rangle|^2\tilde{F}_{12}}{(\gamma_0 - i\omega)\left((\gamma_0 - i\omega)(\gamma - i\omega) + g^2|\langle\tilde{\mathcal{E}}_c\rangle|^2\right)} + \frac{\tilde{F}_{12}}{\gamma_0 - i\omega}
\end{aligned} \tag{8.26}$$

Taking the Fourier transform of the probe field equation of motion gives

$$\left(-i\omega + c\frac{\partial}{\partial z}\right)\delta\tilde{\mathcal{E}}_p(\omega) = ig^*\delta\tilde{\sigma}_{13} \tag{8.27}$$

Since $(\delta\tilde{\mathcal{E}}_p(-\omega))^\dagger = \delta\tilde{\mathcal{E}}^\dagger(\omega)$, therefore, we get

$$\left(-i\omega + c\frac{\partial}{\partial z}\right)\delta\tilde{\mathcal{E}}_p^\dagger(\omega) = -ig\delta\tilde{\sigma}_{31} \tag{8.28}$$

We are interested in obtaining expressions for the amplitude and phase quadratures of the probe field, at the sidebands. The amplitude and phase quadratures are defined in terms of the Fourier transformed field envelope operators $(\tilde{\mathcal{E}}(\omega))$, as $\tilde{X}^+(\omega) = \tilde{\mathcal{E}}(\omega) + \tilde{\mathcal{E}}^\dagger(\omega)$, and $\tilde{X}^-(\omega) = i(\hat{\mathcal{E}}^\dagger(\omega) - \tilde{\mathcal{E}}(\omega))$, respectively. Writing the equation of motion in terms of the quadrature operator for the probe field, gives

$$\begin{aligned}\frac{\partial}{\partial z}\delta\tilde{X}_p^\theta(\omega) \quad = \quad & -\left(\frac{|g|^2(\gamma_0 - i\omega)}{c\left((\gamma_0 - i\omega)(\gamma - i\omega) + g^2|\langle\tilde{\mathcal{E}}_c\rangle|^2\right)} - \frac{i\omega}{c}\right)\delta\tilde{X}_p^\theta(\omega) \\ & -\frac{|g|^2\left(\langle\tilde{\mathcal{E}}_c\rangle\tilde{F}_{12}e^{-i\theta} + \langle\tilde{\mathcal{E}}_c\rangle^*\tilde{F}_{12}^\dagger e^{i\theta}\right)}{c\left((\gamma_0 - i\omega)(\gamma - i\omega) + g^2|\langle\tilde{\mathcal{E}}_c\rangle|^2\right)} \\ & +\frac{i(\gamma_0 - i\omega)\left(g^*\tilde{F}_{13}e^{-i\theta} - g\tilde{F}_{13}^\dagger e^{i\theta}\right)}{c\left((\gamma_0 - i\omega)(\gamma - i\omega) + g^2|\langle\tilde{\mathcal{E}}_c\rangle|^2\right)}\end{aligned} \tag{8.29}$$

The coefficient for $\delta\tilde{X}_p^\theta(\omega)$ is the complex transmission coefficient, given by

$$\Lambda(\omega) = \frac{N|g|^2(\gamma_0 - i\omega)}{c\left((\gamma_0 - i\omega)(\gamma - i\omega) + g^2|\langle\hat{\mathcal{E}}_c\rangle|^2\right)} - \frac{i\omega}{c} \tag{8.30}$$

where k is the wave number and N is the total number of atoms. The complex transmission parameter is related to the probe susceptibility [182, 105] by

$$\frac{ik\chi(\omega)}{2} = -\left(\Lambda(\omega) + \frac{i\omega}{c}\right) \tag{8.31}$$

The imaginary and real parts of $\chi(\omega)$ describe the respective transmission and dispersion, of the probe beam, shown in Figs. 8.2 (A) and (B), respectively. Full absorption of the probe beam occurs when the pump beam is not present. In the presence of the pump beam, a sharp transparency window is created. The transparency reduces with the presence of ground state dephasing γ_0, indicating that vapour cells with buffer gas or paraffin-coating would yield better transmissivity. In the situation that $\gamma_0 = 0$ and $\omega = 0$, the EIT system has perfect transmission. The corresponding dispersion curve shows a steep slope, leading to reduced group velocity of the probe field. For higher pump powers, broadening of the EIT transmission window occurs, as shown in Fig. 8.2 (C). The corresponding slope for the dispersion reduces significantly, leading to increased group velocities, as shown in Fig. 8.2 (D).

The solution to the equation of motion for the probe field operator in Eq. (8.29) is

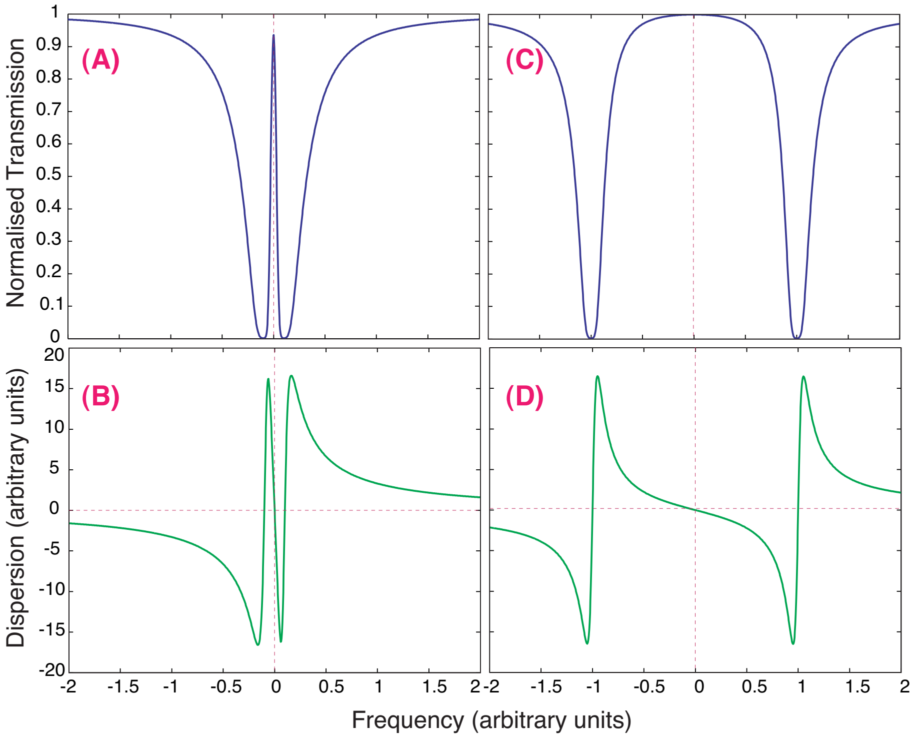

Figure 8.2: (A) Transmission and (B) dispersion plots for $\langle\hat{\mathcal{E}}_c\rangle = 10^6$ Hz. (C) Transmission and (D) dispersion plots for $\langle\hat{\mathcal{E}}_c\rangle = 10^7$ Hz. The common parameter values are $g = 10^7$, $N = 100$, $\gamma = 10^6$ Hz, $\gamma_0 = 10^4$ Hz, $L = 0.1$ m.

given by

$$\begin{aligned}\delta\tilde{X}^{\theta}_{p,\mathrm{out}}(\omega) &= e^{-\Lambda(\omega)L}\delta\tilde{X}^{\theta}_{p,\mathrm{in}}(\omega) - \frac{|g|^2}{c}\int_{-\frac{L}{2}}^{\frac{L}{2}} e^{-\Lambda(\omega)(\frac{L}{2}-s)}\frac{\langle\tilde{\mathcal{E}}_c\rangle\tilde{F}_{12}e^{-i\theta} + \langle\tilde{\mathcal{E}}_c\rangle^{*}\tilde{F}^{\dagger}_{12}e^{i\theta}}{(\gamma_0 - i\omega)(\gamma - i\omega) + g^2|\langle\tilde{\mathcal{E}}_c\rangle|^2}\mathrm{d}s \\ &\quad + \frac{g}{c}\int_{-\frac{L}{2}}^{\frac{L}{2}} e^{-\Lambda(\omega)(\frac{L}{2}-s)}\frac{(\omega + i\gamma_0)\left(\tilde{F}_{13}e^{-i\theta} - \tilde{F}^{\dagger}_{13}e^{i\theta}\right)}{(\gamma_0 - i\omega)(\gamma - i\omega) + g^2|\langle\tilde{\mathcal{E}}_c\rangle|^2}\mathrm{d}s \qquad (8.32)\end{aligned}$$

When computing the quadrature variance from this equation, one needs to compute the correlation between the Langevin terms. The Langevin correlation terms can be obtained using the Einstein relations, given by

$$\begin{aligned}
\langle\hat{F}_{12}\hat{F}_{12}^{\dagger}\rangle &= \langle\mathcal{D}(\hat{\sigma}_{12}\hat{\sigma}_{12}^{\dagger}) - \mathcal{D}(\hat{\sigma}_{12})\hat{\sigma}_{12}^{\dagger} - \hat{\sigma}_{12}\mathcal{D}(\hat{\sigma}_{12}^{\dagger})\rangle\frac{\delta(t-t')\delta(z-z')}{n\mathcal{A}} \\
&= \gamma\langle\hat{\sigma}_{33}\rangle + 2\gamma_0\langle\hat{\sigma}_{11}\rangle \\
\langle\hat{F}_{13}\hat{F}_{13}^{\dagger}\rangle &= \langle\mathcal{D}(\hat{\sigma}_{13}\hat{\sigma}_{13}^{\dagger}) - \mathcal{D}(\hat{\sigma}_{13})\hat{\sigma}_{13}^{\dagger} - \hat{\sigma}_{13}\mathcal{D}(\hat{\sigma}_{13}^{\dagger})\rangle\frac{\delta(t-t')\delta(z-z')}{n\mathcal{A}} \\
&= \gamma\langle\hat{\sigma}_{33}\rangle + 2\gamma\langle\hat{\sigma}_{11}\rangle \\
\langle\hat{F}_{12}\hat{F}_{13}^{\dagger}\rangle &= \langle\mathcal{D}(\hat{\sigma}_{12}\hat{\sigma}_{13}^{\dagger}) - \mathcal{D}(\hat{\sigma}_{12})\hat{\sigma}_{13}^{\dagger} - \hat{\sigma}_{12}\mathcal{D}(\hat{\sigma}_{13}^{\dagger})\rangle\frac{\delta(t-t')\delta(z-z')}{n\mathcal{A}} \\
&= 0 \\
\langle\hat{F}_{13}\hat{F}_{12}^{\dagger}\rangle &= \langle\mathcal{D}(\hat{\sigma}_{13}\hat{\sigma}_{12}^{\dagger}) - \mathcal{D}(\hat{\sigma}_{13})\hat{\sigma}_{12}^{\dagger} - \hat{\sigma}_{13}\mathcal{D}(\hat{\sigma}_{12}^{\dagger})\rangle\frac{\delta(t-t')\delta(z-z')}{n\mathcal{A}} \\
&= 0 \\
\langle\hat{F}_{12}^{\dagger}\hat{F}_{12}\rangle &= \langle\mathcal{D}(\hat{\sigma}_{12}^{\dagger}\hat{\sigma}_{12}) - \mathcal{D}(\hat{\sigma}_{12}^{\dagger})\hat{\sigma}_{12} - \hat{\sigma}_{12}^{\dagger}\mathcal{D}(\hat{\sigma}_{12})\rangle\frac{\delta(t-t')\delta(z-z')}{n\mathcal{A}} \\
&= 0 \\
\langle\hat{F}_{12}^{\dagger}\hat{F}_{13}\rangle &= \langle\mathcal{D}(\hat{\sigma}_{12}^{\dagger}\hat{\sigma}_{13}) - \mathcal{D}(\hat{\sigma}_{12}^{\dagger})\hat{\sigma}_{13} - \hat{\sigma}_{12}^{\dagger}\mathcal{D}(\hat{\sigma}_{13})\rangle\frac{\delta(t-t')\delta(z-z')}{n\mathcal{A}} \\
&= \gamma\langle\hat{\sigma}_{23}\rangle \\
\langle\hat{F}_{13}^{\dagger}\hat{F}_{12}\rangle &= \langle\mathcal{D}(\hat{\sigma}_{13}^{\dagger}\hat{\sigma}_{12}) - \mathcal{D}(\hat{\sigma}_{13}^{\dagger})\hat{\sigma}_{12} - \hat{\sigma}_{13}^{\dagger}\mathcal{D}(\hat{\sigma}_{12})\rangle\frac{\delta(t-t')\delta(z-z')}{n\mathcal{A}} \\
&= \gamma_0\langle\hat{\sigma}_{32}\rangle \\
\langle\hat{F}_{13}^{\dagger}\hat{F}_{13}\rangle &= \langle\mathcal{D}(\hat{\sigma}_{13}^{\dagger}\hat{\sigma}_{13}) - \mathcal{D}(\hat{\sigma}_{13}^{\dagger})\hat{\sigma}_{13} - \hat{\sigma}_{13}^{\dagger}\mathcal{D}(\hat{\sigma}_{13})\rangle\frac{\delta(t-t')\delta(z-z')}{n\mathcal{A}} \\
&= 0
\end{aligned} \tag{8.33}$$

The corresponding spectral variance for the field is then given by

$$V_{p,\mathrm{out}}^{\pm}(\omega) = \frac{c}{L}\langle\tilde{X}_{p,\mathrm{out}}^{\theta}(\omega)\tilde{X}_{p,\mathrm{out}}^{\theta}(\omega')\rangle\delta(\omega+\omega') \tag{8.34}$$

$$\begin{aligned}
&= \frac{c}{L}\Bigg[e^{(-2\Re\{\Lambda(\omega)\}L)}\langle\Big(\tilde{X}_{p,\mathrm{in}}^{\theta}(\omega)\Big)^2\rangle \\
&+\frac{\left(1-e^{(-\Re\{\Lambda(\omega)\}L)}\right)\Big(\langle\tilde{F}_{12}\tilde{F}_{12}^{\dagger}\rangle + \langle\tilde{F}_{12}^{\dagger}\tilde{F}_{12}\rangle\Big)|\langle\tilde{\mathcal{E}}_c\rangle|^2}{2\Re\{\Lambda(\omega)\}\Big|(\gamma_0-i\omega)(\gamma-i\omega)+|\langle\tilde{\mathcal{E}}_c\rangle|^2\Big|^2} \\
&-\frac{\left(1-e^{(-2\Re\{\Lambda(\omega)\}L)}\right)\Big((-\omega+i\gamma_0)\langle\tilde{\mathcal{E}}_c\rangle^*\langle\tilde{F}_{12}\tilde{F}_{13}^{\dagger}\rangle - (\omega+i\gamma_0)\langle\tilde{\mathcal{E}}_c\rangle\langle\tilde{F}_{13}^{\dagger}\tilde{F}_{12}\rangle\Big)}{2\Re\{\Lambda(\omega)\}\Big|(\gamma_0-i\omega)(\gamma-i\omega)+|\langle\tilde{\mathcal{E}}_c\rangle|^2\Big|^2} \\
&+\frac{\left(1-e^{(-2\Re\{\Lambda(\omega)\}L)}\right)\left(-\omega^2-\gamma_0^2\right)\Big(\langle\tilde{F}_{13}\tilde{F}_{13}^{\dagger}\rangle + \langle\tilde{F}_{13}^{\dagger}\tilde{F}_{13}\rangle\Big)}{2\Re\{\Lambda(\omega)\}\Big|(\gamma_0-i\omega)(\gamma-i\omega)+|\langle\tilde{\mathcal{E}}_c\rangle|^2\Big|^2}\Bigg]
\end{aligned} \tag{8.35}$$

Substituting Eqs. (8.18) and (8.33), into the variance expression, the variance of the output probe field reduces to [300]

$$V_{p,\mathrm{out}}(\omega) = \eta(\omega)V_{p,\mathrm{in}}(\omega) + (1-\eta(\omega)) \tag{8.36}$$

where the probe transmissivity is given by

$$\eta(\omega) = \exp[-2\Re\{\Lambda(\omega)\}L] \tag{8.37}$$

In particular, on propagation through an EIT medium of length L, Eq. (8.36) describes the transfer of classical probe sideband information at frequency ω through the EIT system, provided the modulation signal is much weaker than the coupling beam mean field amplitude. The conclusion from this theoretical model is that an EIT system only introduces passive loss to the output probe beam, and no excess noise is introduced.

8.2.6 Model inconsistencies

Peng *et al.* [182], formulated an EIT model where decoherence between the two ground states arises from ground state dephasing and population re-shuffling. Such decoherences may be due to effects such as elastic collisions that affects the phase between the ground states and inelastic collisions that modify the population in the two ground states. Experimentally, it has been shown that the dominant source of decoherence in atomic vapour cells is due to dephasing, with minimal effects due to population shuffling [301]. The equations of motion used in Peng *et al.* [182] are given by

$$\begin{aligned}
\frac{\partial}{\partial t}\hat{\sigma}_{13} &= -\gamma\hat{\sigma}_{13} + ig\hat{\mathcal{E}}_p(\hat{\sigma}_{11} - \hat{\sigma}_{33}) + ig\langle\hat{\mathcal{E}}_c\rangle\hat{\sigma}_{12} + \hat{F}_{13} && (8.38)\\
\frac{\partial}{\partial t}\hat{\sigma}_{23} &= -\gamma\hat{\sigma}_{23} + ig\langle\hat{\mathcal{E}}_c\rangle(\hat{\sigma}_{22} - \hat{\sigma}_{33}) + ig\hat{\mathcal{E}}_p\hat{\sigma}_{21} + \hat{F}_{23} && (8.39)\\
\frac{\partial}{\partial t}\hat{\sigma}_{12} &= -\gamma_0\hat{\sigma}_{12} + ig\langle\hat{\mathcal{E}}_c\rangle^*\hat{\sigma}_{12} - ig\hat{\mathcal{E}}_p\hat{\sigma}_{32} + \hat{F}_{12} && (8.40)\\
\frac{\partial}{\partial t}\hat{\sigma}_{11} &= \gamma\hat{\sigma}_{33} + \gamma_0'(\hat{\sigma}_{22} - \hat{\sigma}_{11}) + ig\hat{\mathcal{E}}_p^\dagger\hat{\sigma}_{13} - ig\hat{\mathcal{E}}_p\hat{\sigma}_{31} + \hat{F}_{11} && (8.41)\\
\frac{\partial}{\partial t}\hat{\sigma}_{22} &= \gamma\hat{\sigma}_{33} + \gamma_0'(\hat{\sigma}_{11} - \hat{\sigma}_{22}) + ig\langle\hat{\mathcal{E}}_c\rangle^*\hat{\sigma}_{23} - ig\langle\hat{\mathcal{E}}_c\rangle\hat{\sigma}_{32} + \hat{F}_{23} && (8.42)\\
\frac{\partial}{\partial t}\hat{\sigma}_{33} &= -2\gamma\hat{\sigma}_{33} - ig\hat{\mathcal{E}}_p^\dagger\hat{\sigma}_{13} + ig\hat{\mathcal{E}}_p\hat{\sigma}_{31} - ig\langle\hat{\mathcal{E}}_c\rangle^*\hat{\sigma}_{23} && (8.43)\\
&\quad +ig\langle\hat{\mathcal{E}}_c\rangle\hat{\sigma}_{32} + \hat{F}_{33} && (8.44)
\end{aligned}$$

In this subsection we show that an inclusion of population transfer terms leads to an inconsistency in the equations derived under the weak probe approximation [300].

Solving for $\langle\sigma_{13}\rangle$ under the weak probe assumption [182], and substituting the expression into the equations of motion for the populations, gives

$$\langle\sigma_{11}\rangle = \frac{-2g^2}{\gamma\gamma_0 + g^2|\langle\hat{\mathcal{E}}_c\rangle|^2}|\langle\hat{\mathcal{E}}_p\rangle|^2 = 0. \tag{8.45}$$

This relation is inconsistent with the weak probe approximation since the atomic population was assumed to optically pumped into state $|1\rangle$ (i.e. $\langle\sigma_{11}\rangle = 1$). The atomic population inconsistency does not affect the expression for absorption and dispersion of the probe field, since the susceptibility is only related to the off-diagonal elements of the atomic density matrix (i.e. the ground state dephasing term only). However, the atomic population inconsistency affects the Langevin noise terms since these terms are dependent on the equations for the populations of the states, given by the diagonal density matrix elements. Therefore the output probe variance expression of Eq. (19) in Peng *et al.* [182],

given by

$$V_{p,\mathrm{out}}(\omega) = V_{p,\mathrm{in}}(\omega)e^{-2\Re\{\Lambda(\omega)\}L} + (1 - e^{-2\Re\{\Lambda(\omega)\}L})\left(1 - \frac{\gamma_0(\omega^2+\gamma_0^2)}{\gamma(\omega^2+\gamma_0^2)+\gamma_0|\langle\hat{\mathcal{E}}_c\rangle|^2}\right), \tag{8.46}$$

violates the commutation relations for the output field. This violation is due to the use of the weak probe approximation in conjunction with the diagonal decoherence terms, arising from ground state population transfer.

Using the Heisenberg-Bloch equations of Eqs. (8.10) - (8.16) where only ground-state dephasing is included, a set of three closed equations is obtained, under the weak probe approximation (as given in Eqs. (8.19) - (8.21)). By solving for $\langle\sigma_{13}\rangle$ and substituting this into the steady-state equations of motion (Eqs. (8.18)), we find that the mean population expressions are all consistent with the weak probe approximation assumption.

The conclusion from our calculations is the same as that of Peng *et al.* [182], despite the inconsistency of the Peng *et al.* [182] analysis. A correct treatment of the propagation of a probe field through a 3-level atomic system shows that EIT does not introduce any additional noise to the probe field beyond that which is necessary to preserve the commutation relations of the probe field at the output, as shown in Eq. (8.36).

8.3 Experiment

We now describe the measurements performed to characterise the EIT system, in particular the conditional variance measure.

8.3.1 Measurement

Ideally, we would like to possess *a priori* information about the probe input state and then use this information to obtain the conditional variance ($V^{\pm}_{\mathrm{in|out}}$) between the probe input and output (see Fig. 8.3 (A)). The conditional variance is measured by minimising the subtraction of input and output signals with variable gain $G(\omega)$ and time delay $\tau(\omega)$, giving

$$V^{\pm}_{\mathrm{in|out}}(\omega) = \min|_{G,\tau}\langle|\tilde{X}^{\pm}_{\mathrm{out}}(\omega) - G(\omega)e^{i\omega\tau(\omega)}\tilde{X}^{\pm}_{\mathrm{in}}(\omega)|^2\rangle. \tag{8.47}$$

Without a pair of entangled beams at our disposal, such a direct measurement of $V^{\pm}_{\mathrm{in|out}}$ is not possible. In practice we measure the conditional variance between the probe reference and output beams, as shown in Fig. 8.3 (B), from which we can infer $V^{\pm}_{\mathrm{in|out}}$ between probe input and output, as if the beamsplitter that separates the probe and reference beams did not exist.

For an ideal delay line, the conditional variance limit is given by $V^{\pm}_{\mathrm{in|out}}(\omega) = 0$, since the input and output are exactly equal. A more practical benchmark is an ideal delay line with some inherent passive loss. Eq. (8.36) shows that EIT has frequency dependent transmissivity $\eta(\omega)$. The quantum limit of the conditional variance is therefore found for the situation where the loss is passive, in the sense that transmissivity $\eta(\omega)$ implies the addition of $1-\eta(\omega)$ unit of vacuum noise. In this case the quantum limit of the conditional variance is given by

$$V^{\pm}_{\mathrm{in|out}} = 1 - \eta(\omega). \tag{8.48}$$

Quantum models [182, 300] suggest that EIT systems should reach this passive loss limit, so that an experiment that compares the conditional variance to this quantum limit is a good test of theory.

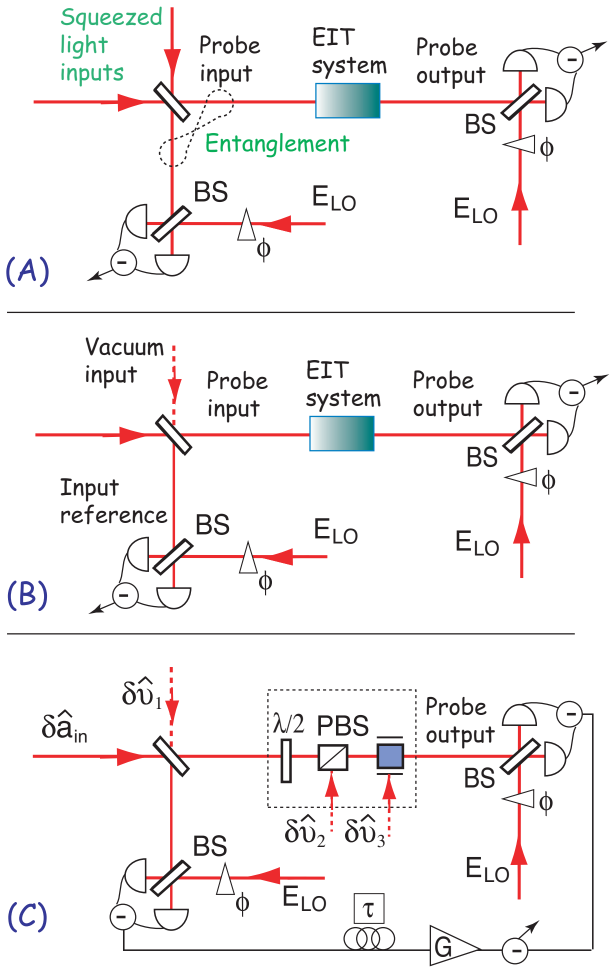

Figure 8.3: (A) Illustration showing the characterisation of the EIT system using a pair of entangled beams. In this instance, no vacuum penalty is incurred for the conditional variance measurement. (B) Illustration showing the characterisation of the EIT system using a coherent beam. A vacuum penalty is incurred for the conditional variance measurement, from the empty port of the first beamsplitter. (C) A linear optics analogue of the potential noise sources for the EIT system and the measurement scheme of (B).

Since we do not possess entanglement to characterise our system, we had to use a beamsplitter to split our input beam - one as a reference, the other as the probe beam for the EIT system (see Fig. 8.3 (B)). In Fig. 8.3 (C), we identify and model the possible noise sources for the measurement scheme corresponding to Fig. 8.3 (B). The splitting of the input beam into two introduces a vacuum loss corresponding to $\delta\hat{v}_1$. As the probe input propagates through the EIT system, two possible sources of noise are introduced - (i) passive loss and (ii) excess noise. For (i) passive loss, we use the analogy of a combination of a half-waveplate and a polarising beam splitter which attenuates the input beam by a variable amount, and in the process, introduces a second vacuum term $\delta\hat{v}_2$. For the introduction of (ii) excess noise, the analogy with an amplitude/phase modulator is used which introduces a noise term $\delta\hat{v}_3$.

The conditional variance for this setup is given by

$$\begin{aligned} V^{\pm}_{\mathrm{in|out}}(\omega) &= \frac{\left|G(\omega)e^{i\omega\tau(\omega)} - \sqrt{\eta(\omega)}e^{i\omega\tau'(\omega)}\right|^2}{2} V_{a_{\mathrm{in}}} \\ &+ \frac{\left|G(\omega)e^{i\omega\tau(\omega)} + \sqrt{\eta(\omega)}e^{i\omega\tau'(\omega)}\right|^2}{2} V_{v_1} \\ &+ (1-\eta(\omega))\, V_{v_2}(\omega) + V_{v_3}(\omega) \end{aligned} \tag{8.49}$$

In order to minimise the expression above, the first term of Eq. (8.49) has to be eliminated. This is best done experimentally by applying a large signal to the input beam ($V_{a_{\mathrm{in}}} \gg V_{v_1}, V_{v_2}, V_{v_3}$) and then optimising the electronic gain $G(\omega)$ and delay $\tau(\omega)$, such that $G(\omega)e^{i\omega\tau(\omega)} = \sqrt{\eta(\omega)}e^{i\omega\tau'(\omega)}$. The measurement of the $V^{\pm}_{\mathrm{in|out}}(\omega)$ thus yields

$$V_{\mathrm{in|out}}(\omega) = [1+\eta(\omega)] + V_{v_3}(\omega) \tag{8.50}$$

However in the event that the quantum system only introduces passive loss ($\delta\hat{v}_2$) and no excess noise ($\delta\hat{v}_3 = 0$), the $V^{\pm}_{\mathrm{in|out}}(\omega)$ then becomes

$$V^{\pm}_{\mathrm{in|out}}(\omega) = 1 + \eta(\omega) \tag{8.51}$$

where the vacuum penalty from the introduction of $\delta\hat{v}_1$ changes Eq. (8.51) with respect to Eq. (8.48), by two quanta of noise. Experimentally, we find the quantum limit by replacing the gas cell with a beamsplitter that has the same transmissivity as the EIT system. The transmission of the beamsplitter must be adjusted for each sideband frequency to account for the finite EIT transmission, since for probe modulations much larger than the noise added by the EIT medium, $G(\omega) \to \eta(\omega)$ in Eq. (8.49). This is how we determined $\eta(\omega)$ independent of the beamsplitter used to separate the reference and probe beams.

At this stage, we have enough information to reconstruct the quantum benchmark limit for a passive-loss EIT system and compare this with the $V^{\pm}_{\mathrm{in|out}}(\omega)$ for the EIT system, as if the first beamsplitter that separates the probe and reference beams did not exist. The quantum benchmark of Eq. (8.48) can be obtained from the $V^{\pm}_{\mathrm{in|out}}(\omega)$ minimisation process for large input signals, which gives $G(\omega)$. The presence of excess noise $V_{v_3}(\omega)$ is quantified by taking the difference between the measured $V^{\pm}_{\mathrm{in|out}}(\omega)$ of Eq. (8.50) with that of Eq. (8.51).

8.3.2 Experimental setup

A schematic of our experiment[3] is shown in Fig. 8.4. The experiment was driven using a Ti:Sapphire laser, tuned to the $|5^2S_{1/2}, F_g = 2\rangle$ to $|5^2P_{1/2}, F_e = 1\rangle$ transition of the D_1 line (795 nm) of Rubidium-87 (^{87}Rb). A small fraction of the beam was sent through another Rubidium (Rb) vapour cell for saturated absorption spectroscopy. This provided us with a fine frequency reference for the laser. The laser was then locked to a reference cavity, internal to the laser system.

The main fraction of the beam was then used for our experiment. This beam was then split into three parts for - (i) probe-reference beams, (ii) pump beam and (iii) local oscillator beams. One beam was encoded with sideband amplitude or phase modulation

---

[3] A detailed schematic of the experimental layout is shown in Fig. 8.13

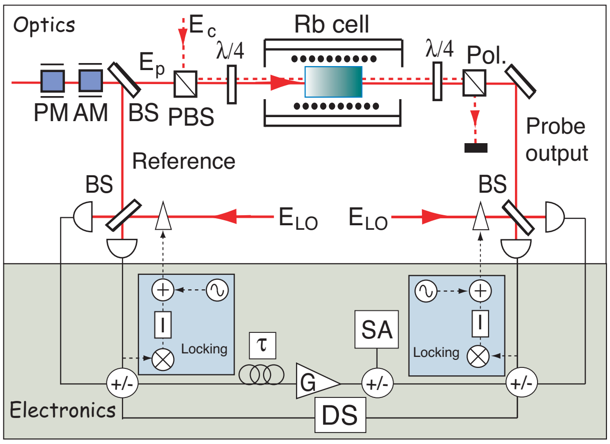

Figure 8.4: Schematic of experimental layout. BS: beamsplitter, PBS: polarising beamsplitter, SA: spectrum analyser, DS: digital storage oscilloscope, $\lambda/4$: quarter wave-plate, $\lambda/2$: half wave-plate and Pol.: polariser.

signals. The (i) probe-reference beam was polarised in the x-polarisation, and then split equally in power on a 50:50 beamsplitter. One part of this beam was sent to a homodyne detection system, as a reference beam for the input. The remainder of this beam was used as a probe, by combining with the (ii) y-polarised pump beam at a polarising beamsplitter. The overlapping pump and probe beams were converted to left and right circularly polarised modes by a quarter-wave plate before entering an uncoated, isotopically enhanced ^{87}Rb vapour cell (7 mm length, 25 mm diameter). The heated vapour cell was shielded in two layers of high permeability alloy, that reduced stray magnetic fields to ≤ 1 mG, in all three spatial axes. The probe beam was extracted from the output of the cell using a polariser and sent to a second homodyne detector. The homodyne detectors were locked either to detect the amplitude or phase quadratures, using Pound-Drever-Hall or DC-subtraction locking, respectively. The signals from the homodyne detectors were monitored either using a digital storage oscilloscope or a network analyser, to obtain data for delay measurements, and a spectrum analyser, which was used to measure the real-time conditional variance and signal transfer coefficients, in the frequency domain.

8.4 Results and Discussion

8.4.1 Transmission and delay results

The group velocity in an EIT system is typically quantified by measuring the delay of pulses. In our continuous wave system, we used a digital storage oscilloscope to measure the delay of a broadband noise modulation. A 60 kHz bandwidth broadband Gaussian noise modulation (i.e. using a function generator driving amplitude/phase modulators) was applied to either the amplitude or phase of the probe. By comparing the autocorrelation of the reference beam (Fig. 8.5 (i)) with the cross-correlation of the reference and probe output beams (Fig. 8.5 (ii)) we could accurately determine the delay of the amplitude or phase signal. The maximum correlation between the reference and probe output beams occurred at a time delay of 7.5 μs. This corresponded to a group velocity reduction of the input probe beam to $\sim c/30000$. The width of curve (ii) is broader than curve (i), indicating that the probe beam has been filtered by the EIT system. Mikhailov *et al.* [302] have reported the spectral narrowing of the modulation width through an EIT medium. This spectral narrowing effect leads to increased correlation times, as shown in Fig. 8.4 (C).

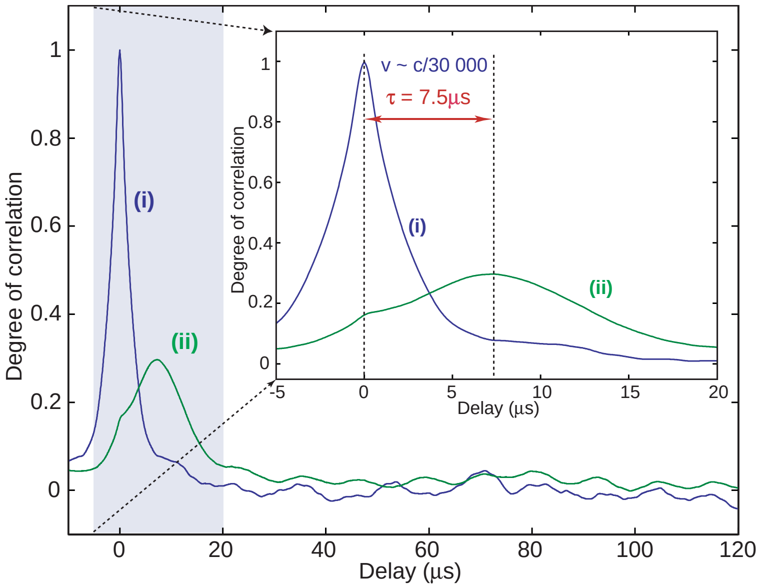

Figure 8.5: Amplitude quadrature correlation plots. Similar results were observed for the phase quadrature correlation. Cell temperature = 62°C, probe and pump power densities were 0.32 mW/cm^2 and 3.2 mW/cm^2, respectively.

8.4.2 Noise Results

We now analyse the noise performance of our EIT system as a quantum delay line for sidebands at a frequency ω, relative to the carrier frequency of the probe field. This measurement was performed using a spectrum analyser and broadband Gaussian noise modulation of the amplitude or phase of the probe input beam.

A sample set of $V^{\pm}_{\text{in}|\text{out}}$ data is shown in Fig. 8.6. The output (i) and reference (ii) signals, intersect at a sideband frequency of 305 kHz, corresponding to the frequency at which the $V^{\pm}_{\text{in}|\text{out}}$ for the EIT system (iii) is minimum. The $V^{\pm}_{\text{in}|\text{out}}$ for the beamsplitter benchmark (iv) is lower than the minimum point of curve (iii), indicating that the delayed probe beam has excess noise. Since the EIT system has frequency dependent absorption and delay, the gain and time delay for the $V^{\pm}_{\text{in}|\text{out}}$ measurement had to be optimised for each measurement frequency.

Conditional variance results for two different cell temperatures (corresponding to different atomic densities) of 42°C and 56°C are shown in Figs. 8.7 and 8.8, respectively. The $V^{\pm}_{\text{in}|\text{out}}$ found using a beamsplitter to simulate the passive loss of the EIT system are the datasets labelled (ii). Due to the limited bandwidth of EIT, the passive loss increases with sideband frequency so that in the limit of large frequency, the beamsplitter reference tends to a value of unity. Using Eq. (8.30), the EIT window has been fitted to this beamsplitter data and is represented by the upper limit of the shaded area. The shaded area therefore indicates the area in which a $V^{\pm}_{\text{in}|\text{out}}$ measurement would be exceeding the

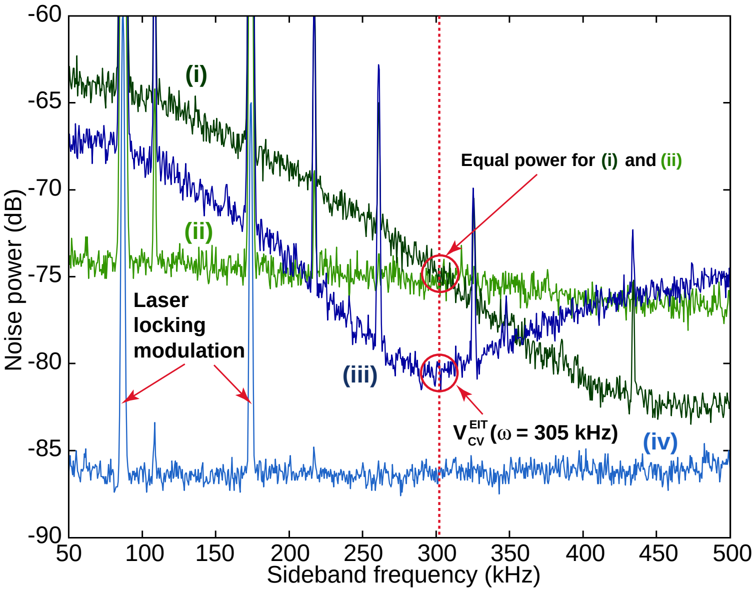

Figure 8.6: $V^{\pm}_{\mathrm{in|out}}$ for the amplitude quadrature, optimised for the sideband frequency of 305 kHz. The curves represent the (i) output probe signal, (ii) reference signal with gain G and delay τ, (iii) $V^{\pm}_{\mathrm{in|out}}$ between the reference and output signals and (iv) $V^{\pm}_{\mathrm{in|out}}$ for the beamsplitter benchmark. The modulation peaks at 87 kHz and 174 kHz are the laser locking signals. Cell temperature = 57°C, probe and pump power densities were 9.6 mW/cm^2 and 96 mW/cm^2, respectively . Measurements were made with a ResBW = 1 kHz, VBW = 30 Hz and 5 averages.

quantum measurement limit. EIT data (i) is well above the passive loss benchmark (ii), showing that excess noise is added to the delayed probe beam. Moreover, the excess noise is largest at low frequencies where the passive loss benchmark is at its best. For higher sideband frequencies the loss in the EIT system dominates the behaviour and $V^{\pm}_{\mathrm{in|out}} \rightarrow 1$.

The excess noise is larger at higher cell temperatures (higher densities). For the lower temperature data shown in Fig. 8.7, there exists a sideband frequency band ($\geq$ 350 kHz) where the EIT $V^{\pm}_{\mathrm{in|out}}$ is almost at the same level as the beamsplitter benchmark $V^{\pm}_{\mathrm{in|out}}$. However, in this region, the loss of the EIT system is large ($\geq$ 5 dB) whilst the delay is small ($\leq$ 0.12 μs).

One source of excess noise is coupling from the pump to the probe [303, 304] since our pump beam has amplitude and phase quadrature noise that lies about 7 dB above the QNL. By adding amplitude and phase modulation to the pump beam, we were able to measure the transfer functions of the pump-probe coupling, shown in Fig. 8.9.

The signal transfer from pump to probe beams has a quadrature-dependent frequency spectrum. There appears to be more signal transfer from phase-to-phase rather than from amplitude-to-amplitude. Cross-quadrature signal transfer is at least 10 dB less than that of same-quadrature signal transfer. A maximum coupling of 3 % for classical phase quadrature signals and 8 % for classical amplitude quadrature signals, with negligible levels of cross quadrature coupling, was observed. This is only enough to explain 0.5 dB of excess phase noise and 1.2 dB of excess amplitude noise.

We also measured cross-quadrature transfer of a signal on the input probe to the

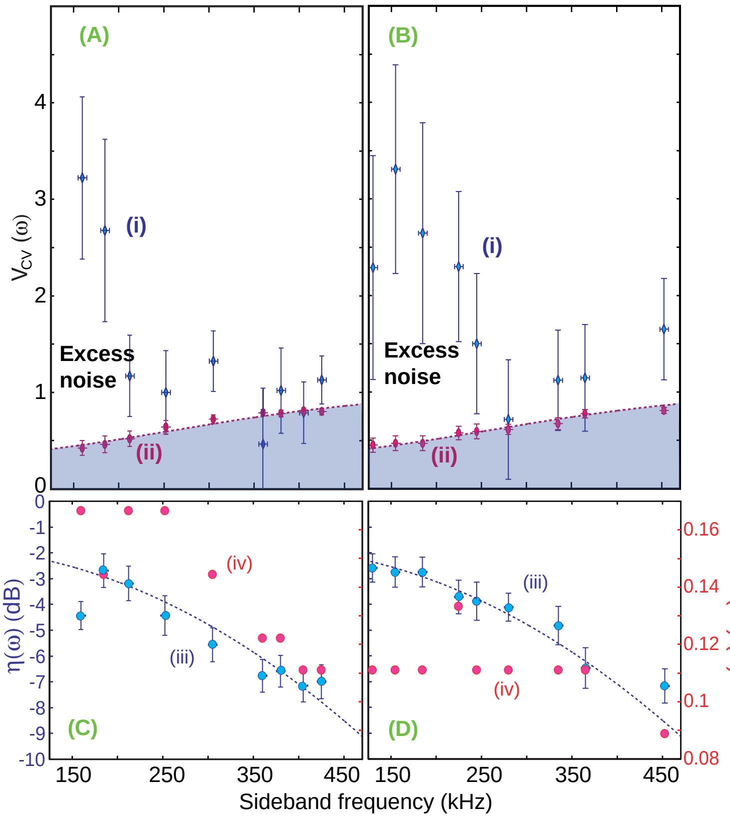

Figure 8.7: $V^{\pm}_{\mathrm{in|out}}$ measurements for the (A) phase and (B) amplitude quadratures, for cell temperature of 42°C. The data point groups represent the (i) EIT $V^{\pm}_{\mathrm{in|out}}$ and (ii) beamsplitter benchmark $V^{\pm}_{\mathrm{in|out}}$. The shape of the shaded area has been fitted using the passive loss described in Eq. (8.30). The corresponding (iii) gain and (iv) delay values measured for the (C) phase and (D) amplitude quadratures are also shown. ResBW = 1 kHz, VBW = 30 Hz and 10 averages. The beamsplitter benchmark and gain data points were fitted with $\gamma_0 = 3.5$ kHz. The probe and pump power densities were 9.6 mW/cm^2 and 96 mW/cm^2, respectively.

orthogonal quadrature of the output probe, given in Fig. 8.10. By adding amplitude or phase modulation to the probe beam, we were able to measure the transfer functions of the signal transfer to the phase and amplitude quadratures, respectively, of the output probe beam, shown in Fig. 8.9.

The signal transfer from amplitude-to-phase is greater than that from phase-to-amplitude. However, the amount of cross-quadrature coupling on the probe beam is less than -15 dB.

We also quantify the performance of our EIT system in terms of the signal transfer between probe input and output. The signal transfer coefficient is given by

$$T_s^{\pm}(\omega) = \frac{\mathrm{SNR}^{\pm}_{\mathrm{out}}(\omega)}{\mathrm{SNR}^{\pm}_{\mathrm{in}}(\omega)} \tag{8.52}$$

where $\mathrm{SNR}^{\pm}_{\mathrm{out}}(\omega)$ and $\mathrm{SNR}^{\pm}_{\mathrm{in}}(\omega)$ are the signal-to-noise ratios of the output and input probe fields, respectively. A signal transfer coefficient of unity indicates perfect transfer. This would be the result for a loss-less delay line. For a passive system with transmission

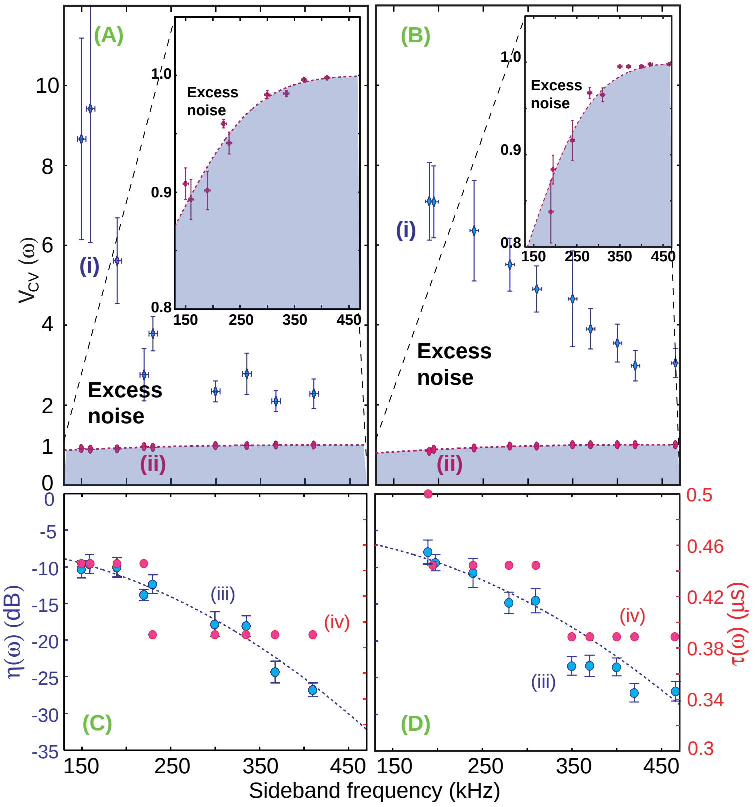

Figure 8.8: $V^{\pm}_{\mathrm{in|out}}$ measurements for the (A) phase and (B) amplitude quadratures, for cell temperature of 57°C. The data point groups represent the (i) EIT $V^{\pm}_{\mathrm{in|out}}$ and (ii) beamsplitter benchmark $V^{\pm}_{\mathrm{in|out}}$. The shape of the shaded area has been fitted using the passive loss described in Eq. (8.30). The insets show the zoom-in data points. The corresponding (iii) gain and (iv) delay values measured for the (C) phase and (D) amplitude quadratures are also shown. ResBW = 1 kHz, VBW = 30 Hz and 10 averages. The beamsplitter benchmark and gain data points were fitted with $\gamma_0 = 4$ kHz. The probe and pump power densities were 9.6 mW/cm^2 and 96 mW/cm^2, respectively.

$\eta(\omega)$, the vacuum noise coupled in by the loss gives a signal transfer of $\eta(\omega)$. Measurements of the signal transfer are shown in Fig. 8.11.

The signal transfer degrades as the frequency increases due to the limited bandwidth of EIT. The EIT system signal transfer is similar to that of the beamsplitter benchmark indicating that absorption in the EIT system is the dominant cause of reduced signal transfer. There is some deviation from this behaviour for the phase quadrature for both cell temperatures indicating that there is some extra degradation of the phase information.

8.4.3 Effects due to ground state population exchange

The model presented in the preceding sections showed that in the presence of ground state dephasing, γ_0, no excess noise is added to the output probe beam. The only effect due to the presence of dephasing is reduced delay and transmission. However, in a realistic atomic vapour cell, atom collision with the wall of the vapour cell could induce ground state population exchange. Hétet *et al.* [305] have explored the quantum effects of population

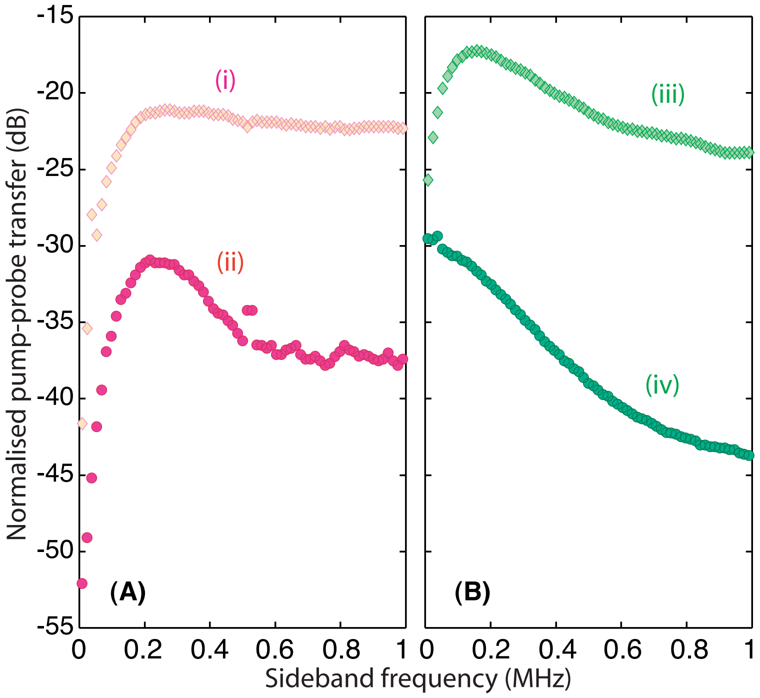

Figure 8.9: Pump-to-probe signal transfer measurements for cell temperature of 56°C. The data point groups in (A) represent amplitude modulation on the pump with an (i) amplitude measurement of the output probe, and a (ii) phase measurement of the output probe. The data point groups in (B) represent phase modulation on the pump with a (iii) phase measurement of the output probe, and an (iv) amplitude measurement of the output probe. The probe and pump power densities were 9.6 mW/cm^2 and 96 mW/cm^2, respectively. ResBW = 1 kHz, VBW = 300 Hz and 5 averages.

exchange on the output probe beam. In Ref. [305], a correct form of decoherence due to population exchange was derived and the equations of motion were solved without the weak probe assumption. Therefore, the equations were self-consistent, as opposed to the earlier work of Peng *et al.* [182].

The Heisenberg-Langevin equations, including both ground state dephasing and population shuffling, are given by [305]

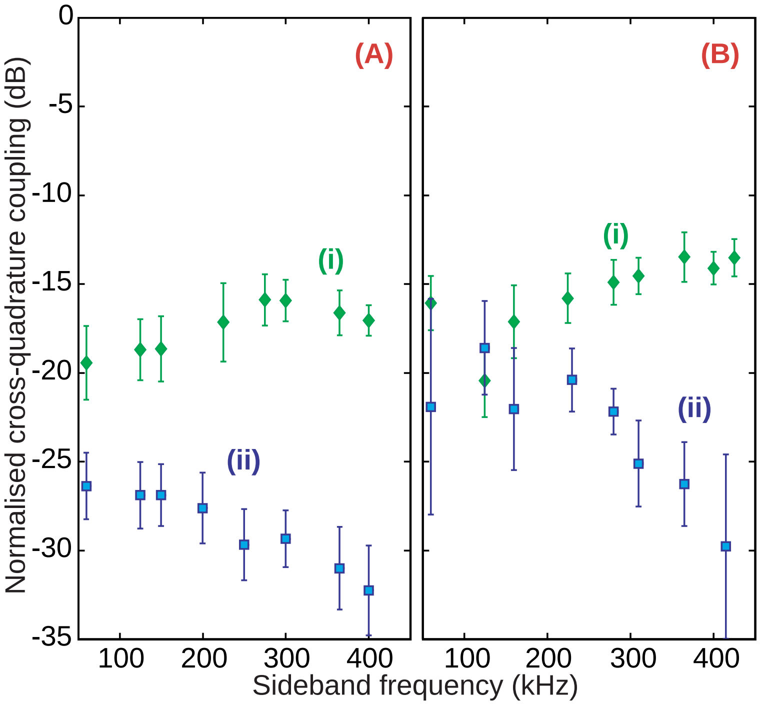

Figure 8.10: Cross-quadrature transfer measurements for two different cell temperatures of (A) 42°C and (B) 56°C. The data point groups represent (i) amplitude modulation of the input probe with a phase measurement of the output probe, and (ii) phase modulation of the input probe with an amplitude measurement of the output probe. The probe and pump power densities were 9.6 mW/cm^2 and 96 mW/cm^2, respectively.

$$\frac{\partial}{\partial t}\hat{\sigma}_{13} = -\left(\gamma+\frac{\gamma_0}{2}+\frac{\gamma_0'}{2}\right)\hat{\sigma}_{13}+ig\hat{\mathcal{E}}_p(\hat{\sigma}_{11}-\hat{\sigma}_{33})+ig\langle\hat{\mathcal{E}}_c\rangle\hat{\sigma}_{12}+\hat{F}_{13} \tag{8.53}$$

$$\frac{\partial}{\partial t}\hat{\sigma}_{23} = -\left(\gamma+\frac{\gamma_0}{2}+\frac{\gamma_0'}{2}\right)\hat{\sigma}_{23}+ig\langle\hat{\mathcal{E}}_c\rangle(\hat{\sigma}_{22}-\hat{\sigma}_{33})+ig\hat{\mathcal{E}}_p\hat{\sigma}_{21}+\hat{F}_{23} \tag{8.54}$$

$$\frac{\partial}{\partial t}\hat{\sigma}_{12} = -(\gamma_0+\gamma_0')\hat{\sigma}_{12}+ig\langle\hat{\mathcal{E}}_c\rangle^*\hat{\sigma}_{12}-ig\hat{\mathcal{E}}_p\hat{\sigma}_{32}+\hat{F}_{12} \tag{8.55}$$

$$\frac{\partial}{\partial t}\hat{\sigma}_{11} = \gamma\hat{\sigma}_{33}+\gamma_0'(\hat{\sigma}_{22}-\hat{\sigma}_{11})+ig\hat{\mathcal{E}}_p^\dagger\hat{\sigma}_{13}-ig\hat{\mathcal{E}}_p\hat{\sigma}_{31}+\hat{F}_{11} \tag{8.56}$$

$$\frac{\partial}{\partial t}\hat{\sigma}_{22} = \gamma\hat{\sigma}_{33}+\gamma_0'(\hat{\sigma}_{11}-\hat{\sigma}_{22})+ig\langle\hat{\mathcal{E}}_c\rangle^*\hat{\sigma}_{23}-ig\langle\hat{\mathcal{E}}_c\rangle\hat{\sigma}_{32}+\hat{F}_{23} \tag{8.57}$$

$$\frac{\partial}{\partial t}\hat{\sigma}_{33} = -2\gamma\hat{\sigma}_{33}-ig\hat{\mathcal{E}}_p^\dagger\hat{\sigma}_{13}+ig\hat{\mathcal{E}}_p\hat{\sigma}_{31}-ig\langle\hat{\mathcal{E}}_c\rangle^*\hat{\sigma}_{23} \tag{8.58}$$

$$+ig\langle\hat{\mathcal{E}}_c\rangle\hat{\sigma}_{32}+\hat{F}_{33} \tag{8.59}$$

where the ground state population exchange rate is given by γ_0'. The population of the atoms are no longer assumed to be fully pumped into state $|1\rangle$. However, it is assumed that $|g\langle\hat{\mathcal{E}}_c\rangle|^2 \gg \gamma\gamma_0, \gamma\gamma_0'$.

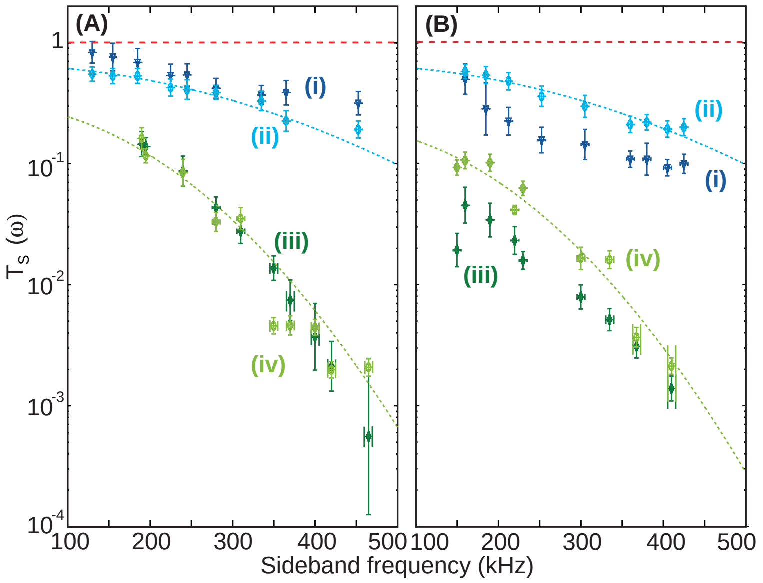

Figure 8.11: Signal transfer coefficient for the (A) amplitude and (B) phase quadratures. (i) $T = 42°$C and (ii) corresponding beamsplitter benchmark. (iii) $T = 57°$C and (iv) corresponding beamsplitter benchmark. ResBW = 1 kHz, VBW = 30 Hz and 10 averages. The probe and pump power densities were 9.6 mW/cm^2 and 96 mW/cm^2, respectively. The 57°C and 42°C beamsplitter benchmark data points were fitted with $\gamma_0 = 4$ kHz and $\gamma_0 = 3.5$ kHz, respectively. ResBW = 1 kHz, VBW = 30 Hz and 10 averages.

Solving the equations of motion yields the output probe field variance, given by

$$V_{p,\mathrm{out}}(\omega) = \eta(\omega)V_{p,\mathrm{in}}(\omega) + (1 - \eta(\omega))(1 + N_{\mathrm{excess}}(\omega)) \tag{8.60}$$

where the absorption loss is given by

$$\eta(\omega) = \exp\left(-2L\Re\left(\frac{g^2N}{c}\frac{(\gamma_0 + \gamma_0' - i\omega)(1 - \frac{3\gamma_0'}{\gamma}) - \frac{\gamma_0'\langle\hat{\mathcal{E}}_c\rangle}{\langle\hat{\mathcal{E}}_c\rangle^*}}{g^2\langle\hat{\mathcal{E}}_c\rangle^2 - i\omega(\gamma + \frac{\gamma_0}{2} + \frac{\gamma_0'}{2})}\right)\right) \tag{8.61}$$

and the frequency-dependent excess noise term is given by

$$N_{\mathrm{excess}}(\omega) = \frac{4\gamma_0' g^2\langle\hat{\mathcal{E}}_c\rangle^2}{2\gamma_0 g^2\langle\hat{\mathcal{E}}_c\rangle^2 + \omega^2(2\gamma + \gamma_0 - 3\gamma_0')} \tag{8.62}$$

The excess noise term $N_{\mathrm{excess}}(\omega)$ arises from the amplification of vacuum noise and is phase-insensitive. The energy required for the amplification process is provided by the coupling beam. $N_{\mathrm{excess}}(\omega)$ has the feature of large excess noise at low frequencies with reduced noise at higher frequencies.

8.4.4 Model incompleteness

One should be circumspect in attributing entirely the observed excess noise to the ground state population shuffling effect. This is because there are many other effects present in the atomic vapour cell system. The theoretical modelling [223, 286, 299, 182] of EIT does not include several effects. For example,

- In principle, the pump-probe configuration of EIT means that the experiment is performed on atoms of a particular longitudinal velocity class so that any effects of atomic motion can be ignored. Transverse velocities, however, could play a crucial role. The Gaussian intensity profiles of the pump and probe beams mean that atoms with motion in the transverse plane will experience varying optical field intensities, whereas the theory assumes uniform field intensities.

- Effects due to high atomic density have also been neglected. Various decoherence mechanisms mean that there is always some fluorescence in the cell. The probability that these photons are reabsorbed by the atoms grows exponentially with atomic density. The quantum noise properties of such “radiation trapping” [306] has not been considered in the context of EIT. Density dependent effects may be of particular interest since they should be more severe in cold atom systems where the density is higher.

- The coupling field was assumed to be classical. Whilst this is a reasonable theoretical assumption, many experiments have pump-probe beam power ratios of $(10 \rightarrow 100)$:1, where the pump noise could have a small effect on the output probe noise. Our experiments have measured the effect of pump-induced noise and found the pump noise transfer to be small but present.

The presence of excess noise could be due to a combination of the various effects aforementioned.

8.5 Conclusion and future directions

8.5.1 Conclusion

As discussed above, a deviation of EIT system performance from the passive loss benchmark indicates a discrepancy with published theoretical modelling [223, 286, 299, 182]. Both in terms of conditional variance and signal transfer we see that the EIT system performance measured in our experiment does not reach the passive loss limit.

In summary, our work shows that light delayed by EIT can have significant amounts of excess noise. The latest theoretical modelling of Hétet *et al.* [305] shows that the presence of ground state population shuffling terms do indeed give excess noise to the output probe field, via a phase-insensitive amplification of vacuum noise. Experimentally, the ground state population shuffling rate can be reduced via the introduction of a buffer gas in the EIT system, and recent experiments have shown that excess noise may indeed be reduced [297, 298]. In spite of this, one should be cautious in attributing the population shuffling decoherence as the sole cause of excess noise. Recently, two experiments have shown the storage of squeezed light via EIT. The experiments of Appel *et al.* [307] and Honda *et al.* [308] demonstrated the retrieval of up to 0.28 ± 0.05 dB and 0.07 ± 0.005 dB of squeezing, respectively. In their experiments, the input probe beam had 3 dB and 2 dB of squeezing, respectively. In Ref. [307], excess noise in the form of Raman scattering from pump to probe and small EIT transmissions (~ 20 %) was attributed to the observation of significantly reduced squeezing on the output probe beam. The experimental results of Refs. [183, 297, 298, 307, 308] and the theoretical model of Hétet *et al.* [305] should serve as a motivation for more complete theoretical models to identify the origins of the noise and also as a caveat to claims that EIT in thermal vapour cells is a good method for storing and delaying quantum states.

8.5.2 Future directions

Measurements of EIT in cold atoms in a MOT were performed, the results shown in Fig. 8.12. For a detailed description of the MOT setup, please refer to Chapter 10. The results were measured by applying the coupling and probe beams after the MOT was turned off.

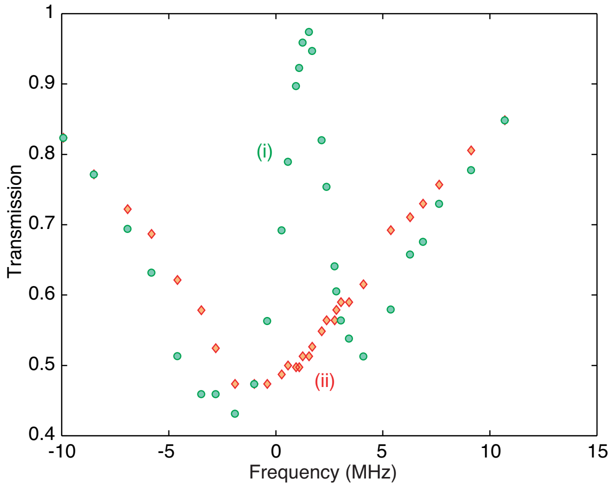

Figure 8.12: Transmission of a probe beam through a cold Rb^{87} atom cloud in a MOT, (i) with and (ii) without the application of a coupling beam. The asymmetry of the EIT feature is possibly due to the presence of stray magnetic fields and inefficient optical pumping in the ground state levels.

The results indicate that close to 100 % transmission is achievable with EIT in a MOT. This result is a significant improvement over the results observed in a vapour cell, with approximately the same densities. Future experiments of EIT could therefore be performed on cold atoms, as the following advantages are offered over a vapour cell:

- The confinement of atoms. Significantly reduced motion of atoms out of the interaction region reduces the ground state dephasing rate γ_0. Therefore, more efficient EIT can be generated, as evident in the results of Fig. 8.12. However, a MOT system restricts the measurement time since the MOT is turned off during the EIT process. Typical measurement times for cold atoms in a MOT are less than 10 ms and therefore EIT storage experiments have to be performed within this time window.

- In a vapour cell, atoms are constantly moving and may be lost from the interaction region. Therefore the assumption that the population of atoms are conserved is not valid for a vapour cell. During short measurement times of cold atoms released from a MOT, the expansion of the atom cloud is minimal. Therefore the population of atoms during the measurement time are conserved. Based on this, the population shuffling term γ_0' is expected to be small.

In conclusion, EIT measurements of cold atoms in a MOT hold promise for greater transmission and reduced excess noise, since decoherences are reduced. This is possibly one avenue for EIT experiments in the future.

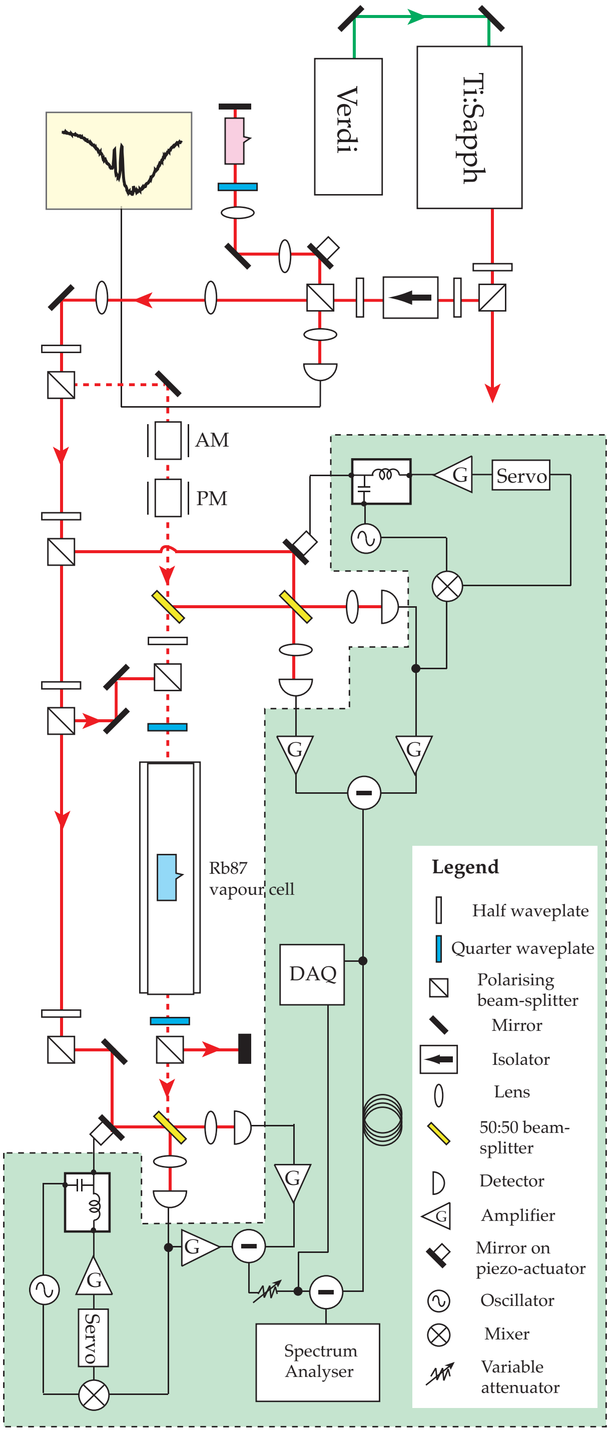

Figure 8.13: Detailed schematic of experimental layout.

Chapter 9

Spin squeezing theory

Man needs difficulties; they are necessary for health.

- Carl Jung

9.1 Introduction

In the last decade, there has been an augmentation of optical experiments demonstrating EPR entanglement [17, 218], violation of Bell's inequality [14, 15, 16, 309], quantum gates [310, 28], quantum teleportation [41, 42], quantum cryptography [311, 312, 51, 313, 314, 315] and quantum non-demolition (QND) [316, 47, 46]; performed in the discrete-variable and continuous-variable regimes. For atomic media, there has been a corresponding suite of single atom and single ion experiments demonstrating atomic state entanglement [160, 317, 318, 319, 320, 321], atomic state teleportation [322, 323], atomic gates [36, 324, 325, 326] and quantum networking [327, 328]. The Polzik group has pursued atomic ensemble measurements and demonstrated atomic spin squeezing [129, 130, 131], spin entanglement [132, 133], atomic memory [134, 135, 136, 107, 137] and atomic state teleportation [222, 106].

Many of the aforementioned experiments have been motivated by quantum information and quantum computing goals. However, there is a corresponding suite of experiments with applications in improving the sensitivity of practical measurements. For example, the enhancement of the measurement of the Cs clock transition pseudo-spin [115, 116, 117] and performing sub-shot noise atomic magnetometry [111, 112, 113, 114]. In such applications, squeezing of the collective atomic spin state is important. We are motivated by such goals as well and dedicate the remainder of this thesis to studying atomic spin squeezing[1].

In the experiment of Hald *et al.* [129], a squeezed light source was propagated through a cold atom cloud. The state of the polarisation squeezed probe light was mapped onto the atomic spin state. In order to verify the existence of spin squeezing, off-resonant light was then propagated through the cold atoms. Faraday rotation measurements were performed on the probe light to infer the atomic spin state via a QND interaction [128, 184, 107, 131]. A quantum spin noise reduction by -3 % was observed but the actual degree of spin squeezing could not be inferred due to uncertainties in the atomic state read-out efficiency.

---

[1] For comprehensive treatments of this subject matter, please refer to B. Julsgaard's [329] and J. K. Stockton's [330] PhD theses. This chapter is by no means a comprehensive treatment of this subject matter but is aimed to provide the absolute necessary formalism to understand the work, which is currently in progress.

In the experiment of Kuzmich *et al.* [331], continuous QND measurements were performed on a collective atomic spin state in a vapour cell. Spin noise reduction of up to 5 dB below the quantum noise level for a coherent spin state was reported. A subsequent QND-spin squeezing experiment by Geremia *et al.* [332] reported up to 10 dB of spin squeezing. In their experiment, unconditional and conditional spin squeezing were shown, using an applied magnetic field as the feedback to re-orient the collective spin direction. However, there exists controversy with the results of Ref. [332]. The optical depth of the experiment in Ref. [332] was at least an order of magnitude larger than that in typical cold atom experiments and tensor effects were also not considered and characterised. Classical polarisation noise in the probe laser beam (due to birefringence of cell windows) was also present. All these issues are described in detail in the PhD thesis of J. K. Stockton [330].

In this chapter, we present the necessary formalism to explain the interaction between optical Stokes polarisation and atomic spin state operators. We identify the different components in the interaction Hamiltonian, in particular the tensor term. Important experimental parameters that influence the degree of spin squeezing are also identified and discussed.

9.2 Atomic spin states

In the previous chapters on atom-light interactions, we worked in the bases of amplitude and phase quadrature operators for the optical field; and atomic dipole operators for the atomic system. We now introduce alternate bases for the atomic and optical states. The variables are transformed into bases which observe the SU(2) group properties, such as the spin observables of an atom and the polarisation Stokes operators for the optical field (introduced in Chapter 4).

The atomic spin operators are defined in terms of the total angular momentum operator. The total angular momentum operator, $\hat{f}$, for a single atom is given by

$$\hat{f} = \hat{\jmath} + \hat{\imath} \tag{9.1}$$

where $\hat{\imath}$ is the nuclear spin operator and $\hat{\jmath} = \hat{l} + \hat{s}$ is the total electronic angular momentum operator. $\hat{l}$ and $\hat{s}$ are the electronic orbital angular momentum and spin operators, respectively.

For Rubidium, the ground state is given by the outermost electron in the $5S_{1/2}$ state. In this case, the electronic angular momentum is zero. Since an electron has spin-1/2, the total electronic angular momentum is thus $j = 1/2$. The nuclear spin of Rubidium-87 is $i = 3/2$. Therefore the total angular momentum for the ground state of Rubidium-87 is given by $f = 1, 2$. For Cesium-133, the nuclear spin is given by $i = 7/2$. Therefore the total angular momentum for the ground state of Cesium-133 is given by $f = 3, 4$.

We denote the ground and excited states of an atom respectively by

$$|f, m_f\rangle \qquad |f', m_{f'}\rangle \tag{9.2}$$

where f denotes the relevant hyperfine state and m_f is the corresponding quantum number for the state. $|f, m_f\rangle$ are the eigenstates of the $\hat{f}^2$ and $\hat{f}_z$ operators, given by

$$\begin{aligned} \hat{f}^2|f, m_f\rangle &= \hbar^2 f(f+1)|f, m_f\rangle && (9.3) \\ \hat{f}_z|f, m_f\rangle &= \hbar m_f|f, m_f\rangle && (9.4) \end{aligned}$$

Here we are only interested in the atomic ground state. The excited state population is assumed to be negligible since in the experiment, the probe beam which interacts with the atom is far-detuned from the atomic transition. As will be shown in the following section, any excitation into the excited state will spontaneously emit into the ground state and thus it is reasonable to only consider the ground state.

The angular momentum operator can be written in the x, y and z components, given by $\hat{f}_x$, $\hat{f}_y$ and $\hat{f}_z$, respectively. These operators satisfy the cyclic commutation relations given by

$$\left[\hat{f}_x, \hat{f}_y\right] = i\hbar \hat{f}_z \tag{9.5}$$

$$\left[\hat{f}_y, \hat{f}_z\right] = i\hbar \hat{f}_x \tag{9.6}$$

$$\left[\hat{f}_z, \hat{f}_x\right] = i\hbar \hat{f}_y \tag{9.7}$$

Thus far, we have only considered the spin states for a single atom. In reality, we are dealing with an ensemble of atoms and therefore, we introduce collective angular momentum operators, given by

$$\hat{F} = \sum_{i=1}^{N} \hat{f}^{(i)} \qquad \hat{F}_z = \sum_{i=1}^{N} \hat{f}_z^{(i)} \tag{9.8}$$

where N is the total number of atoms in the ensemble and $\hat{f}^{(i)}$ is the angular momentum operator corresponding to the i-th atom.

9.2.1 Dicke state

We now introduce the state corresponding to an ensemble of atoms. The eigenstate of the $\hat{F}_z$ operator is given by the Dicke state[2], $|F, m_F\rangle$, where

$$\hat{F}_z|F, m_F\rangle = \hbar m_F|F, m_F\rangle \tag{9.9}$$

where F is the hyperfine ground state corresponding to an ensemble of atoms and m_F is the quantum number.

9.2.2 Coherent spin state

For a coherent spin state, all the atoms are prepared in the same state (e.g. the $m_f = f$ or $m_f = -f$ state). We can write the spin state for the atomic ensemble prepared in the $m_F = F$ state as a product of individual atomic states, given by

$$|F, F\rangle = |f, f\rangle^{(1)}|f, f\rangle^{(2)} \cdots |f, f\rangle^{(N)} \tag{9.10}$$

where the superscript $^{(i)}$ denotes each atom in the N-atom ensemble.

For an atomic system prepared with all the spins aligned in the z-direction, the total spin of the system therefore has a mean spin value given by $\langle \hat{F}_z \rangle$. The expectation values

---

[2] The Dicke state is strictly speaking applicable to both a single atom and an ensemble of atoms. In this instance, we are interested in the Dicke state for the collective atomic system.

for the $\hat{F}_z$, $\hat{F}_x^2$ and $\hat{F}_y^2$ are given by

$$\begin{aligned}
\langle F,F|\hat{F}_z|F,F\rangle &= \hbar F \qquad (9.11)\\
\langle F,F|\hat{F}_x^2|F,F\rangle &= \langle F,F|\hat{F}_y^2|F,F\rangle\\
&= \frac{\hbar^2}{2}(F(F+1)-F^2)\\
&= \frac{\hbar^2}{2}F \qquad (9.12)
\end{aligned}$$

In this instance, the commutation relation between the $\hat{F}_x$ and $\hat{F}_y$ operators is given by

$$[\hat{F}_x,\hat{F}_y] = i\langle\hat{F}_z\rangle \qquad (9.13)$$

where the corresponding variances are related by

$$\begin{aligned}
V(\hat{F}_x)V(\hat{F}_y) &\geq \frac{\langle\hat{F}_z\rangle^2}{4}\\
&\geq \frac{\hbar^2}{4}F^2 \qquad (9.14)
\end{aligned}$$

These expressions show that the collective atomic system has a product of x and y-spin variances proportional to the mean $\langle\hat{F}_z\rangle^2$. We define the *coherent spin state* (CSS) as the state where the spin variances in the x and y-directions are equal (i.e. $V(\hat{F}_x) = V(\hat{F}_y)$) and satisfy Eq. (9.14) in the equality.

9.2.3 Mixed state

In the situation where the ensemble of N number of atoms are not coherently populated in their ground states, a mixed state is obtained. The density matrix corresponding to a mixed state is given by

$$\hat{\rho} = \sum_{m=0}^{Nf}|Nf,m\rangle\langle Nf,m| \qquad (9.15)$$

where the variances of the spin operators, in a mixed state, are greater than that of the coherent spin state.

9.2.4 Spin squeezed state

A spin squeezed state [333] is obtained when the spins of the atoms are quantum correlated. The variance of a spin squeezed state in one observable is reduced below that of the CSS, whilst the variance of the orthogonal observable is increased. For example, for a spin squeezed state in the x-direction, the variances are given by

$$V(\hat{F}_x) < \frac{\langle\hat{F}_z\rangle}{2} \qquad (9.16)$$

whilst the variance in the y-direction is given by

$$V(\hat{F}_y) > \frac{\langle\hat{F}_z\rangle}{2} \qquad (9.17)$$

Likewise, it is possible to squeeze in the y-direction with a corresponding anti-squeezing in the x-direction. For a pure squeezed state, the product of the variances always satisfy Eq. (9.14) in the equality.

9.3 Atom-light interaction

We have introduced all the observables corresponding to the spin state of an atomic system, as well as the polarisation Stokes operators of an optical field (in Chapter 4). Now we would like to derive the Hamiltonian for the interaction of an optical field with an atomic ensemble in terms of the spin and polarisation bases.

The Hamiltonian describing the interaction between an atomic dipole with an electromagnetic field $\hat{\boldsymbol{E}}$ is given by

$$\hat{H}_{\text{int}} = -\hat{\boldsymbol{d}}.\hat{\boldsymbol{E}}(\boldsymbol{r}) \tag{9.18}$$

where the atomic dipole operator is given by $\hat{\boldsymbol{d}}$, located at position $\boldsymbol{r}$.

For an atom in the presence of a magnetic field $\hat{\boldsymbol{B}}$, the Hamiltonian describing the interaction between the magnetic field and the magnetic dipole of the atom is given by

$$\hat{H}_B = -\sum_{f,m_f} \mu_B g_f^B \hat{\boldsymbol{f}}_j^B.\hat{\boldsymbol{B}}(\boldsymbol{r}_j) \tag{9.19}$$

where $\hat{\boldsymbol{f}}_j^B$ is the magnetic dipole operator, μ_B is the magnetic permeability of the atomic medium and g_f^B is the magnetic coupling constant.

The total Hamiltonian for an atom interacting with optical and magnetic fields is given by

$$\hat{H}_{\text{tot}} = \hat{H}_{\text{int}} + \hat{H}_B + \hat{H}_e + \hat{H}_g \tag{9.20}$$

where the atomic excited state and ground state Hamiltonians are given by $\hat{H}_e$ and $\hat{H}_g$, respectively. The explicit form for $\hat{H}_e$ and $\hat{H}_g$ are given by

$$\hat{H}_e = \sum_{f,m_f} \hbar\omega_f |f, m_f\rangle\langle f, m_f| = \sum_{f,m_f} \hbar\omega_f \hat{\sigma}^{ff}_{m_f m_f} \tag{9.21}$$

$$\hat{H}_g = \sum_{f',m_{f'}} \hbar\omega_{f'} |f', m_{f'}\rangle\langle f', m_{f'}| = \sum_{f',m_{f'}} \hbar\omega_{f'} \hat{\sigma}^{f'f'}_{m_{f'} m_{f'}} \tag{9.22}$$

where ω_f and $\omega_{f'}$ are the optical frequencies corresponding to the ground state f and excited state f' transitions.

9.3.1 Far detuned limit

Now we would like to show that in the far detuned limit, the excited state dependence is adiabatically eliminated. The derivation presented henceforth follows that of Ref. [329] but we re-derive it here for completeness and introduce some additional details.

Let us consider the electric dipole interaction only and write the Hamiltonian in terms of the atomic dipole operators corresponding to the ground state f and excited state f' with the respective quantum numbers given by m_f and $m_{f'}$. The sum over all possible values of f and f' is also taken, to model all the hyperfine states in a real atom. The integral across the atomic ensemble of cross-section area A and length L is taken. Therefore the total Hamiltonian for the interaction of an atomic ensemble with and optical field is

given by

$$\begin{aligned}\hat{H}'_{\text{tot}} &= \hat{H}_{\text{atom}} + \hat{H}_{\text{int}} &(9.23)\\ &= \hbar n A \sum_{f', m_{f'}} \int_0^L (\omega_0 + \Delta_{f'}) \hat{\sigma}^{f'f'}_{m_{f'}m_{f'}} dz \\ &+ \hbar n A \sum_{f, f', m_f, m_{f'}} \int_0^L \left(\left(g^{(+)f'f}_{m_{f'}m_f} \hat{a}_+ + g^{(-)f'f}_{m_{f'}m_f} \hat{a}_- \right) \hat{\sigma}^{f'f}_{m_{f'}m_f} + \text{H.C.} \right) dz &(9.24)\end{aligned}$$

where $g^{(+)f'f}_{m_{f'}m_f}$ and $g^{(-)f'f}_{m_{f'}m_f}$ are the atom-field coupling constants corresponding to the m_f-$m_{f'}$ transitions, with the superscript $^{(+)}$ and $^{(-)}$ denoting relevant coupling with the circularly polarised light, $\hat{a}_+$ and $\hat{a}_-$, respectively. n and A are the respective atomic density and interaction cross-section, and $\Delta_{f'}$ is the detuning from resonance.

In the far-detuned limit, the optical field has to be sufficiently far detuned from the atomic transition such that there is no population in the excited state. Therefore the coherences between the excited and ground states, $\hat{\sigma}^{ff'}_{m_f m_{f'}}$ becomes dependent on the ground states and optical fields only. The equation of motion for the coherence term $\hat{\sigma}^{ff'}_{m_f m_{f'}}$ is obtained from the Heisenberg equations. Since we only consider dipole allowed transitions, the equation of motion for the $|m_f = m-1\rangle$ to $|m_{f'} = m\rangle$ state is given by

$$\begin{aligned} i\hbar \frac{\partial}{\partial t} \hat{\sigma}^{ff'}_{m-1,m}(z,t) &= [\hat{\sigma}^{ff'}_{m-1,m}(z,t), \hat{H}_{tot}(z,t)] &(9.25)\\ &= \hbar(\omega_0 + \Delta_{f'}) \hat{\sigma}^{ff'}_{m-1,m}(z,t) \hat{\sigma}^{f'f'}_{m,m}(z,t) \\ &+ \hat{\sigma}^{ff'}_{m-1,m}(z,t) \left(\hbar g^{(+)f'f}_{m,m-1} \hat{a}_+(z,t) \right) \hat{\sigma}^{f'f}_{m,m-1}(z,t) \\ &+ \hat{\sigma}^{ff'}_{m-1,m}(z,t) \left(\hbar g^{(-)f'f}_{m,m+1} \hat{a}_-(z,t) \right) \hat{\sigma}^{f'f}_{m,m+1}(z,t) \\ &- \left(\hbar g^{(+)f'f}_{m,m-1} \hat{a}_+(z,t) \right) \hat{\sigma}^{f'f}_{m,m-1}(z,t) \hat{\sigma}^{ff'}_{m-1,m}(z,t) \\ &- \left(\hbar g^{(-)f'f}_{m-2,m-1} \hat{a}_-(z,t) \right) \hat{\sigma}^{f'f}_{m-2,m-1}(z,t) \hat{\sigma}^{ff'}_{m-1,m-2}(z,t) &(9.26)\end{aligned}$$

where all the other terms have zero state overlap. We can simplify the expression to obtain

$$\begin{aligned} i\hbar \frac{\partial}{\partial t} \hat{\sigma}^{ff'}_{m-1,m}(z,t) &= \hbar(\omega_0 + \Delta_{f'}) \hat{\sigma}^{ff'}_{m-1,m}(z,t) \\ &+ \left(\hbar g^{(+)f'f}_{m,m-1} \hat{a}_+(z,t) \right) \hat{\sigma}^{ff}_{m-1,m-1}(z,t) \\ &+ \left(\hbar g^{(-)f'f}_{m,m+1} \hat{a}_-(z,t) \right) \hat{\sigma}^{ff}_{m-1,m+1}(z,t) \\ &- \underbrace{\hbar \left(g^{(+)f'f}_{m,m-1} \hat{a}_+(z,t) \right) \hat{\sigma}^{f'f'}_{m,m}(z,t)}_{\simeq 0} \\ &- \underbrace{\hbar \left(g^{(-)f'f}_{m-2,m-1} \hat{a}_-(z,t) \right) \hat{\sigma}^{f'f'}_{m-2,m}(z,t)}_{\simeq 0} &(9.27)\end{aligned}$$

We now neglect the last two terms on the right hand side of the Eq. (9.27) as they are dependent on the population in the excited states. To solve Eq. (9.27), we move into the rotating frame of the optical field. The atomic dipole operators and photon annihilation operators are written in terms of the slowly varying envelope operators, given respectively by

$$\begin{aligned} \hat{\sigma}^{ff'}_{m-1,m}(z,t) &= \hat{\sigma'}^{ff'}_{m-1,m}(z,t)e^{-i\omega_0 t} \qquad (9.28) \\ \hat{a}_{\pm}(z,t) &= \hat{a'}_{\pm}(z,t)e^{-i\omega_0 t} \qquad (9.29) \end{aligned}$$

where $\hat{\sigma'}^{ff'}_{m-1,m}(z,t)$ and $\hat{a'}_{\pm}(z,t)$ are the slowly varying envelope operators for the atoms and photons, respectively. We substitute these equations into Eq. (9.27) and relabel the envelope operators whereby $\hat{\sigma'}^{ff'}_{m-1,m}(z,t) \rightarrow \hat{\sigma}^{ff'}_{m-1,m}(z,t)$, and $\hat{a'}_{\pm}(z,t) \rightarrow \hat{a}_{\pm}(z,t)$, for notational convenience, giving

$$\begin{aligned} i\hbar\frac{\partial}{\partial t}\hat{\sigma}^{ff'}_{m-1,m}(z,t) &= \hbar\Delta_{f'}\hat{\sigma}^{ff'}_{m-1,m}(z,t) + \left(\hbar g^{(+)f'f}_{m,m-1}\hat{a}_{+}(z,t)\right)\hat{\sigma}^{ff}_{m-1,m-1}(z,t) \\ &\quad + \left(\hbar g^{(-)f'f}_{m,m+1}\hat{a}_{-}(z,t)\right)\hat{\sigma}^{ff}_{m-1,m+1}(z,t) \qquad (9.30) \end{aligned}$$

Since the rate at which atomic dynamics varies is less than that of the laser detuning, therefore we can set the time derivative of the atomic coherence term to zero, giving

$$\hat{\sigma}^{ff'}_{m-1,m}(z,t) = -\frac{1}{\Delta_{f'}}\left(g^{(+)f'f}_{m,m-1}\hat{a}_{+}(z,t)\hat{\sigma}^{ff}_{m-1,m-1}(z,t) + g^{(-)f'f}_{m,m+1}\hat{a}_{-}(z,t)\hat{\sigma}^{ff}_{m-1,m+1}(z,t)\right) \tag{9.31}$$

The coherence between the excited and ground state now adiabatically follows the ground state and the optical fields. Similarly, the dipole operator describing the coherence between the $|m_f = m+1\rangle$ to $|m_{f'} = m\rangle$ transition is given by

$$\hat{\sigma}^{ff'}_{m+1,m}(z,t) = -\frac{1}{\Delta_{f'}}\left(g^{(+)f'f}_{m,m-1}\hat{a}_{+}(z,t)\hat{\sigma}^{ff}_{m+1,m-1}(z,t) + g^{(-)f'f}_{m,m+1}\hat{a}_{-}(z,t)\hat{\sigma}^{ff}_{m+1,m+1}(z,t)\right) \tag{9.32}$$

We now substitute these two expressions into the interaction Hamiltonian, given by

$$\begin{aligned} \hat{H}_{\text{int}} &= \hbar nA\sum_{f,m,f',m_{f'}}\int_0^L\Big[-\frac{2g^{(+)f'f}_{m,m-1}\hat{a}^{\dagger}_{+}}{\Delta_{f'}}\left(g^{(+)f'f}_{m,m-1}\hat{a}_{+}\hat{\sigma}^{ff}_{m-1,m-1} + g^{(-)f'f}_{m,m+1}\hat{a}_{-}\hat{\sigma}^{ff}_{m-1,m+1}\right) \\ &\quad -\frac{2g^{(-)f'f}_{m,m+1}\hat{a}^{\dagger}_{-}}{\Delta_{f'}}\left(g^{(+)f'f}_{m,m-1}\hat{a}_{+}\hat{\sigma}^{ff}_{m+1,m-1} + g^{(-)f'f}_{m,m+1}\hat{a}_{-}\hat{\sigma}^{ff}_{m+1,m+1}\right)\Big]dz \qquad (9.33) \end{aligned}$$

We can simplify the product of the atom-field coupling constants by calculating the Clebsch-Gordon coefficients for the relevant atom with ground state f and excited state f'. The product of the coupling constants are given by

$$\begin{aligned} \left(g^{(\pm)f'f}_{m,m-1}\right)^2 &= \frac{c\gamma\lambda^2}{8\pi A}\left(\alpha^{(0)} \pm m\alpha^{(1)} + m^2\alpha^{(2)}\right) \qquad (9.34) \\ g^{(+)f'f}_{m,m-1}g^{(-)f'f}_{m,m+1} &= \frac{c\gamma\lambda^2}{8\pi A}\sqrt{(f+m)(f+1+m)(f-m)(f+1-m)}\alpha^{(2)} \qquad (9.35) \end{aligned}$$

where the atomic polarisability are given by $\alpha^{(0)}$, $\alpha^{(1)}$ and $\alpha^{(2)}$

Now substitute these into the interaction Hamiltonian to obtain

$$\begin{aligned}\hat{H}_{\mathrm{int}} &= \frac{\hbar n c\gamma\lambda^2}{8\pi\Delta_{f'}}\sum_{f,m}\int_0^L -2\Big[\left(\alpha^{(0)}+m\alpha^{(1)}+m^2\alpha^{(2)}\right)\hat{a}_+^\dagger\hat{a}_+\hat{\sigma}^{ff}_{m-1,m-1} \\ &+\left(\alpha^{(0)}-m\alpha^{(1)}+m^2\alpha^{(2)}\right)\hat{a}_-^\dagger\hat{a}_-\hat{\sigma}^{ff}_{m+1,m+1} \\ &+\sqrt{(f+m)(f+1+m)(f-m)(f+1-m)}\alpha^{(2)}\left(\hat{a}_+^\dagger\hat{a}_-\hat{\sigma}^{ff}_{m-1,m+1}+\hat{a}_-^\dagger\hat{a}_+\hat{\sigma}^{ff}_{m+1,m-1}\right)\Big]dz \end{aligned} \tag{9.36}$$

We further simplify the expression above using the identities for the spin and polarisation Stokes operators to obtain

$$\hat{H}_{\mathrm{int}} = -\frac{\hbar n c\gamma\lambda^2}{4\pi\Delta_{f'}}\int_0^L \underbrace{\alpha^{(0)}\hat{S}_0}_{\text{Scalar}}+\underbrace{\alpha^{(1)}\hat{S}_z\hat{f}_z}_{\text{Vector}}+\underbrace{\alpha^{(2)}\left(\hat{S}_0\hat{f}_z^2-2\hat{S}_x(\hat{f}_x^2-\hat{f}_y^2)-2\hat{S}_y(\hat{f}_x\hat{f}_y+\hat{f}_y\hat{f}_x)\right)}_{\text{Tensor}} \tag{9.37}$$

The Hamiltonian above is highly illustrative, with the different components given by the following:

- **Scalar term** - This is a phase shift imposed on the optical field, independent of the atomic state. The shift is the same on both polarisation components and therefore does not affect the state-dependent result.

- **Vector term** - This is the term which gives rise to Faraday rotation signals. It couples the polarisation state with the atomic state. A phase shift is introduced between the two polarisation modes which is proportional to the spin polarisation operator, $\hat{f}_z$.

- **Tensor term** - This is a second order term which couples the polarisation Stokes operators to the atomic spin operators in a non-linear manner. In the case that $f = 1/2$, this term is always zero as can be seen in Eq. (9.36). This term is non-zero for higher values of f. In general, this term is undesirable as it affects the Faraday rotation signal in a non-linear manner.

9.3.2 Equations of motion

In order to model the dynamics of the spin and polarisation variables, the equations of motion are derived from the Hamiltonian given in Eq. (9.37). The optical Bloch equations for the atomic spin operators are given by

$$\begin{align}
i\hbar\frac{\partial}{\partial t}\hat{f}_x &= [\hat{f}_x, \hat{H}_{\text{int}}] \tag{9.38}\\
\frac{\partial}{\partial t}\hat{f}_x &= \frac{nc\gamma\lambda^2}{4\pi\Delta_{f'}}\left[\alpha^{(1)}\hat{S}_z\hat{f}_y + \alpha^{(2)}\left((\hat{S}_0 - 2\hat{S}_x)(\hat{f}_y\hat{f}_z + \hat{f}_z\hat{f}_y) + 2\hat{S}_y(\hat{f}_x\hat{f}_z + \hat{f}_z\hat{f}_x)\right)\right] \notag\\
i\hbar\frac{\partial}{\partial t}\hat{f}_y &= [\hat{f}_y, \hat{H}_{\text{int}}] \tag{9.39}\\
\frac{\partial}{\partial t}\hat{f}_y &= \frac{nc\gamma\lambda^2}{4\pi\Delta_{f'}}\left[-\alpha^{(1)}\hat{S}_z\hat{f}_x - \alpha^{(2)}\left((\hat{S}_0 + 2\hat{S}_x)(\hat{f}_x\hat{f}_z + \hat{f}_z\hat{f}_x) + 2\hat{S}_y(\hat{f}_y\hat{f}_z + \hat{f}_z\hat{f}_y)\right)\right] \notag\\
i\hbar\frac{\partial}{\partial t}\hat{f}_z &= [\hat{f}_z, \hat{H}_{\text{int}}] \tag{9.40}\\
\frac{\partial}{\partial t}\hat{f}_z &= \frac{nc\gamma\lambda^2}{4\pi\Delta_{f'}}4\alpha^{(2)}\left(\hat{S}_x(\hat{f}_y\hat{f}_x + \hat{f}_x\hat{f}_y) + \hat{S}_y(\hat{f}_y^2 - \hat{f}_x^2)\right) \notag
\end{align}$$

Correspondingly the Maxwell wave equation for the polarisation Stokes operators for the fields are given by

$$\begin{align}
i\hbar\left(c\frac{\partial}{\partial z} + \frac{\partial}{\partial t}\right)\hat{S}_x &= [\hat{S}_x, \hat{H}_{\text{int}}] \tag{9.41}\\
\left(c\frac{\partial}{\partial z} + \frac{\partial}{\partial t}\right)\hat{S}_x &= \frac{nc\gamma\lambda^2}{4\pi\Delta_{f'}}\left[\alpha^{(1)}\hat{S}_y\hat{f}_z + 2\alpha^{(2)}\hat{S}_z(\hat{f}_x\hat{f}_y + \hat{f}_y\hat{f}_x)\right] \notag\\
i\hbar\left(c\frac{\partial}{\partial z} + \frac{\partial}{\partial t}\right)\hat{S}_y &= [\hat{S}_y, \hat{H}_{\text{int}}] \tag{9.42}\\
\left(c\frac{\partial}{\partial z} + \frac{\partial}{\partial t}\right)\hat{S}_y &= \frac{nc\gamma\lambda^2}{4\pi\Delta_{f'}}\left[-\alpha^{(1)}\hat{S}_x\hat{f}_z - 2\alpha^{(2)}\hat{S}_z(\hat{f}_x^2 - \hat{f}_y^2)\right] \notag\\
i\hbar\left(c\frac{\partial}{\partial z} + \frac{\partial}{\partial t}\right)\hat{S}_z &= [\hat{S}_z, \hat{H}_{\text{int}}] \tag{9.43}\\
\left(c\frac{\partial}{\partial z} + \frac{\partial}{\partial t}\right)\hat{S}_z &= \frac{nc\gamma\lambda^2}{4\pi\Delta_{f'}}2\alpha^{(2)}\left[\hat{S}_y(\hat{f}_x^2 - \hat{f}_y^2) - \hat{S}_x(\hat{f}_x\hat{f}_y + \hat{f}_y\hat{f}_x)\right] \notag
\end{align}$$

where the first order terms (i.e. scaling with $\alpha^{(1)}$) are the QND terms. The tensor terms which scale with $\alpha^{(2)}$ affects the QND measurement as non-linear phase shifts are induced between the polarisation modes of the output probe beam.

9.4 Spin squeezing schemes

9.4.1 Squeezing via squeezed probe transfer

From the equations of motion given in Eqs. (9.38)-(9.43), we can observe that state transfer from light to atoms and vice versa is possible, when the optical field is sufficiently far detuned from the atomic transitions and therefore the second order tensor terms are negligible (since $\alpha^{(2)} \propto 1/\Delta_{f'}^2$ for detuning greater than the excited state separation [330]). The equations of motion for atoms that are spin polarised in the x-direction and the probe field with x linear polarisation, propagating in the z-direction through the atomic ensemble, are given by

$$\begin{aligned}
\frac{\partial}{\partial t}\hat{f}_x &= 0 && (9.44)\\
\frac{\partial}{\partial t}\hat{f}_y &= \frac{nc\gamma\lambda^2}{4\pi\Delta_{f'}}\left[-\alpha^{(1)}\hat{S}_z\langle\hat{f}_x\rangle\right] && (9.45)\\
\frac{\partial}{\partial t}\hat{f}_z &= 0 && (9.46)\\
\left(c\frac{\partial}{\partial z}+\frac{\partial}{\partial t}\right)\hat{S}_x &= 0 && (9.47)\\
\left(c\frac{\partial}{\partial z}+\frac{\partial}{\partial t}\right)\hat{S}_y &= \frac{nc\gamma\lambda^2}{4\pi\Delta_{f'}}\left[-\alpha^{(1)}\langle\hat{S}_x\rangle\hat{f}_z\right] && (9.48)\\
\left(c\frac{\partial}{\partial z}+\frac{\partial}{\partial t}\right)\hat{S}_z &= 0 && (9.49)
\end{aligned}$$

where the macroscopic spin and polarisation are given by $\langle\hat{f}_x\rangle$ and $\langle\hat{S}_x\rangle$, respectively.

The dynamics of the system are assumed to occur on a long time scale such that the time evolution of the optical field is negligible. The resulting equations of motion for the spin and polarisation operators can therefore be reduced to the following four equations

$$\begin{aligned}
\frac{\partial}{\partial t}\hat{F}_z &= 0 && (9.50)\\
\frac{\partial}{\partial t}\hat{F}_y &= -\frac{nc\gamma\lambda^2}{4\pi\Delta_{f'}}\alpha^{(1)}\hat{S}_z^{\text{in}}\langle\hat{F}_x\rangle && (9.51)\\
\hat{S}_y^{\text{out}} &= \hat{S}_y^{\text{in}} - \frac{nc\gamma\lambda^2}{4\pi\Delta_{f'}}\alpha^{(1)}\langle\hat{S}_x\rangle\hat{F}_z && (9.52)\\
\hat{S}_z^{\text{out}} &= \hat{S}_z^{\text{in}} && (9.53)
\end{aligned}$$

where $\hat{S}_y^{\text{in}}$ and $\hat{S}_z^{\text{in}}$ are the y and z Stokes operators of the input probe field. Following the interaction of the probe field with the atomic ensemble, the output Stokes operators are given by $\hat{S}_y^{\text{out}}$ and $\hat{S}_z^{\text{out}}$.

We can observe in the equations above that information on the atomic spin state $\hat{F}_z$ can be obtained from the Stokes operator $\hat{S}_y^{\text{out}}$. However, the noise contribution from the input probe field $\hat{S}_y^{\text{in}}$ is always present. In order to maximise the information on $\hat{F}_z$, the polarisability constant $\alpha^{(1)}$ has to be large. A back-action term is also introduced on the atomic state as the evolution[3] of $\hat{F}_y$ is dependent on $\hat{S}_z^{\text{in}}$.

9.4.2 Squeezing by averaging

Thomsen *et al.* [334] proposed a scheme to perform quantum non-demolition (QND) measurements on a cloud of atoms enclosed in an optical cavity. The cavity field interacts with the atoms and the polarisation rotation of the optical field provides information on the atomic spin state. The atomic spin state information can then be used to apply a feedback control signal to alter the atomic spin state to a desired value, giving unconditional spin squeezing.

---

[3] An experimental demonstration of the interaction of a polarisation squeezed field with a cold atomic sample was shown in Refs. [129, 134, 130].

In the experimental demonstration of spin squeezing, reported by Geremia *et al.* [332, 111], the free-space propagation of an optical probe field through a cold atom cloud scheme was used. The probe field was far detuned from resonance such that the excited-ground state coherences adiabatically follow the ground state coherences. The atom cloud was first prepared to have a macroscopic spin vector in the x-direction. The probe field was linearly polarised and sent through the atom cloud. Upon interaction with the atoms, the polarisation state was rotated slightly and the rotation $y^{(1)}$ corresponded to $\hat{F}_z^{(1)}$ only[4]. Following the initial measurement, there was a dark time window where the atomic state was not measured or perturbed. Subsequently, a measurement of the atomic state was performed and the polarisation rotation $y^{(2)}$ gave $\hat{F}_z^{(2)}$. Conditional spin squeezing is obtained when

$$\langle (y^{(2)} - y^{(1)})^2 \rangle < \langle (y^{(1)})^2 \rangle \tag{9.54}$$

In order to perform unconditional spin squeezing, a feedback signal has to be applied to reorient the atomic state. This was performed during the dark time window, where an external magnetic field was applied to the atomic ensemble, to rotate the atomic spin polarisation such that $\hat{F}_z^{(2)} = 0$. This was verified by performing a subsequent measurement of the atomic state to confirm that $y^{(2)} = 0$.

The important component in the QND spin squeezing experiment is the estimation of the atomic spin state by averaging away noise in the polarisation rotation signal. Technical noise and quantum noise of the probe field are the main noise sources which contribute to the variance in the polarisation rotation signal.

Optimal filters can be derived and used to obtain the best estimate of the polarisation rotation signal. However, in the experiment of Geremia *et al.* [332], the signal was obtained by averaging within a limited time window. The fundamental limitation to the amount of observed squeezing was due to shot noise. In principle, one could average for a longer period of time to obtain better estimates of the signal, however, decays such as atom cloud diffusion and atomic spin state decoherence, limit the measurement time. We would like to work in the regime where these decays are slow and whereby the primary limitation is due to that of the spontaneous emission-limited decay time of the atomic spin state.

Stockton *et al.* [113, 335] modelled the measured photo-current by an Ornstein-Uhlenbeck damped diffusion process, given by

$$y_t dt = \sqrt{M} F_z dt + dW_t \tag{9.55}$$

where M is the measurement strength (i.e. the rate at which information on the stochastic value F_z is obtained) and dW_t is a delta-correlated Gaussian white noise term with zero mean (i.e. a Wiener increment). A filter equation can be derived to obtain an optimal estimate for F_z in Eq. (9.55). The resulting variance of the F_z estimate at time $t = \tau$ is given by [113, 335]

$$(\Delta^2 F_z)|_{t=\tau} = \frac{(\Delta^2 F_z)|_{t=0}}{1 + 4M\tau(\Delta^2 F_z)|_{t=0}} \tag{9.56}$$

where $(\Delta^2 F_z)|_{t=0}$ is the variance of F_z at time $t = 0$. Experimentally this is obtained from the initial measurement of $y^{(1)}$.

The degree of squeezing is defined as the ratio of the variance of $F_z|_{t=\tau}$ to the variance

---

[4] This is assuming that the tensor terms are negligible, with a sufficiently far detuned probe beam. As will be discussed in the following section, this is not the case.

of $F_z|_{t=0}$, given by

$$W = \frac{(\Delta^2 \hat{F}_z)|_{t=\tau}}{(\Delta^2 \hat{F}_z)|_{t=0}} \tag{9.57}$$

$$= \frac{1}{1 + 4M\tau(\Delta^2 F_z)|_{t=0}} \tag{9.58}$$

Ref. [335] defines the square of the signal-to-noise ratio (SNR^2) as

$$\mathrm{SNR}^2 = 4M\tau(\Delta^2 \hat{F}_z)|_{t=0} \tag{9.59}$$

$$= \mathrm{OD}\frac{f}{4}\frac{\tau}{\tau_{ss}} \tag{9.60}$$

where the spin squeezing time τ_{ss} has been introduced. OD is the optical depth, f refers to the hyperfine ground state level and SNR is the signal-to-noise ratio of the measurement of F_z. A formal definition of the spin squeezing rate is the rate at which photons are scattered by the atomic medium, given by

$$\frac{1}{\tau_{ss}} = \frac{2I\sigma_0}{\hbar\omega}\left(\frac{\gamma}{4}\sum_{f'}\frac{\alpha^{(1)}_{ff'}}{\alpha_0 \Delta_{ff'}}\right)^2 \tag{9.61}$$

where I is the intensity of the probe beam, σ_0 is the scattering cross section and α_0 is the polarizability constant given by

$$\alpha_0 = \frac{3\epsilon_0 \hbar\gamma\lambda_0^3}{8\pi^2} \tag{9.62}$$

In order for the squeezing to be large, we would like the value of W to be as small as possible. This is only possible by maximising the SNR and this involves either one or both of the following:

- Attaining large optical depths. Experimentally, this involves attaining a compressed atomic cloud with high atomic densities.

- Minimising the spin squeezing time τ_{ss}. This can be achieved either by increasing the intensity and/or decrease the detuning of the probe beam. However, to minimise the tensor term, the probe beam has to be far detuned. In such an instance, a corresponding quadratic increase in the intensity of the probe beam is required to maintain the same τ_{ss}.

Decay times

We have thus far identified the important parameters to achieve spin squeezing - the optical depth (OD) and the spin squeezing time (τ_{ss}). Experimentally, many decay mechanisms are present in a cold atom cloud. These include decays due to atomic cloud diffusion and spontaneous emission decay. The atomic cloud diffusion can be minimised by cooling the atom cloud using schemes such as polarisation gradient cooling and by optimising the diameter of the probe beam with respect to the cloud size.

We now consider the decoherence of the spin state [336] due to the spontaneous emission. The decoherence model of the spin state $\hat{F}_z$ assumes an exponential decay [330],

given by

$$\frac{d}{dt}\langle \hat{F}_z \rangle \Big|_{t=0} = -\frac{\langle \hat{F}_z \rangle}{\tau_{sc}}\Big|_{t=0} \tag{9.63}$$

where here we consider the decay of a macroscopic atom spin vector in the z direction. The decay time τ_{sc} for Cs-133 is given by [330]

$$\begin{aligned} \tau_{sc} &= \frac{I\sigma_0}{2\hbar\omega}\Big(\frac{\gamma^2}{\gamma^2+4\Delta_{45}^2}(0.16|\epsilon_0|^2+0.04|\epsilon_-|^2)+\frac{\gamma^2}{\gamma^2+4\Delta_{44}^2}(0.83|\epsilon_0|^2+0.41|\epsilon_-|^2) \\ &\quad +\frac{\gamma^2}{\gamma^2+4\Delta_{43}^2}(0.6|\epsilon_-|^2)\Big) \end{aligned} \tag{9.64}$$

where $|\epsilon_+|^2 = |\epsilon_-|^2 = 0$ and $|\epsilon_+|^2 = 1$ for parallel spin and polarisation. $|\epsilon_+|^2 = |\epsilon_-|^2 = 0.5$ and $|\epsilon_+|^2 = 0$ for orthognal spin and polarisation.

The decay time can be measured by preparing the atomic state to have a macroscopic spin in the x-direction and then adiabatically rotating the spin vector to the z or y-directions. The decay times corresponding to parallel or orthogonally oriented polarisation and spin vectors can then be measured.

9.5 Tensor influence

The PhD thesis of J. K. Stockton [330] discusses in great detail the effects of technical noise sources and tensor terms on the QND measurement. Ref. [330] claims that earlier published spin squeezing results [332, 111] were erroneous. The results of Refs. [332, 111] will not be discussed in this thesis. However we will focus this section to discussing the effects of the tensor terms. Discussions of technical noise sources as well as measurements of the tensor effect are presented in Chapter 10.

The tensor terms scaling with $\alpha^{(2)}$ in the interaction Hamiltonian (given in Eq. (9.37)), couples the various spin polarisation components with the polarisation Stokes operators, in a non-linear manner. The tensor effects are present in a multi-level alkali atomic system such as ^{87}Rb and ^{133}Cs (see Eq. 9.36), the only exception being atomic systems with $f = 1/2$. The tensor terms scale according to $\propto 1/\Delta_{ff'}^2$. Therefore, for small detuning from resonance, the tensor terms are significant [330]. Consequently in this regime, the evolution of the probe beam polarisation is non-linear as it is not solely dependent on the vector term $\alpha^{(1)}$.

The tensor terms could be reduced in a multi-level atomic system by increasing the detuning of the probe beam. However, in order to maintain the same measurement time (Eq. 9.61), a quadratic increase in the intensity of the probe beam is required. Due to technical considerations, a quadratic increase in the intensity is often not possible (e.g. limited laser power, saturation of detectors). As a result, a compromise between minimising the tensor effect whilst ensuring a short measurement time (less than the decay time of the cold atom cloud and the coherent spin state τ_{sc}) is required.

9.6 Conclusion and future directions

9.6.1 Conclusion

We have presented the basic formalism to describe spin squeezing. The QND-type spin squeezing via averaging scheme was described. Second order tensor terms in the interaction

Hamiltonian, which could affect the QND measurement, was discussed. The relevant measurement times, and associated decays are also described.

9.6.2 Future directions

The models presented have assumed homogeneous atomic samples interacting with plane wave optical fields. In an experiment, the cold atom cloud typically has a Gaussian atomic density profile. The optical fields have Gaussian modes. Therefore, the decay time of the collective atomic spin state τ_{sc} varies across the transverse plane of the atomic sample. Modifications to theory, taking into account the spatial profile of both the atom cloud and optical fields, are currently being conducted by O. Crisafulli[5].

---

[5] personal communication

Chapter 10

Towards spin squeezing

Remember that not getting what you want is sometimes a wonderful stroke of luck.

- Dalai Lama

10.1 Introduction

In the previous chapter, the theoretical formalism for spin squeezing was established. The important experimental parameters to optimise for spin squeezing are the optical depth, and the probe beam detuning and intensity. High optical depths are required to achieve maximum spin squeezing. Large detuning and high probe beam intensities are necessary for minimising tensor effects whilst maintaining short measurement times τ_{ss}. In this chapter, we present the details of the experimental scheme towards generating spin squeezing[1].

In order to minimise decoherence and achieve high optical depths, confined and dense atomic samples are a requisite. There are many means to produce confinement of atoms. The most basic technique involves the confinement of atoms in a vapour cell, with the introduction of a buffer gas to increase the transit time of atoms within an interaction region. However, the atomic sample in a vapour cell is limited by its optical depth. Therefore more sophisticated techniques have to be used to cool and trap atoms [67, 68, 69, 70, 71, 72, 73, 74, 75, 76, 77, 78, 79, 80, 81]. In a magneto-optical trap (MOT), cold atom clouds are produced with typical atom numbers of 10^7 at μK temperatures. Cold atoms produced in a MOT offer high optical depths and reduced ground state dephasing, due to the significantly reduced mean free path of atoms. After MOTs were invented, the production of Bose-Einstein condensates (BECs) [92, 93, 337, 338, 339] was accomplished. A BEC is essentially a cloud of ultra-cold atoms all prepared in the same ground state. BECs have high phase space density and and have minimal decoherence due to their ultra-cold temperatures. With all these atomic samples on offer, the question remains, "What is the ideal atomic source for spin squeezing?".

---

[1] Some of the work in this chapter was performed at the California Institute of Technology (Caltech), under the supervision of Prof. H. Mabuchi. The Caltech experiment was built by J. K. Stockton during the course of his PhD research. Details of the experimental setup can be obtained from the thesis of J. K. Stockton [330]. Whilst spin squeezing was not observed during the research of this thesis, the experimental setup towards this goal was further developed, together with A. E. Miller. My specific role in the Caltech experiment involved improving the optical depth of the cold atom cloud and reducing the classical noise for the polarimeter measurement. The experiment at the ANU was developed by the author and N. Robins and D. Oblak.

For atoms in a vapour cell, atoms are constantly moving in and out of the probe beam interaction region. The resulting change of atomic state population and loss of atomic coherence affects the QND measurement. A BEC is an ideal source of trapped atoms as the BEC has the largest optical depth. However, BECs are complicated to produce and therefore a 'middle ground' was adopted. We decided to use cold atoms produced in a MOT. Cold atoms in a MOT have long lived coherent spin states and high optical depths. MOTs are also relatively inexpensive and less time-consuming to produce.

Typical optical depths attainable for cold atoms in a MOT are between 20-30 [69, 73]. However, this is insufficient for observing spin squeezing, as simulations have shown that the atomic spin projection noise is below that of shot noise, under a large range of experimental parameters [330]. A fiducial value for observing spin squeezing under reasonable experimental conditions is an optical depth of at least 100 [330]. Therefore, more sophisticated laser cooling and trapping techniques have to be employed to increase the atomic density of cold atoms. The various schemes explored during the course of this thesis included transient compression schemes [340] where the transient tightening of the trapping potential increases the atomic density of cold atoms. This yielded an increase in optical depths by up to 50% but was insufficient for the observation of spin squeezing. A spatial dark spontaneous force trap (dark-SPOT) [341] was implemented and this yielded optical depths close to the fiducial value of 100. The experimental setup for yielding high optical depths is described in detail in this chapter. We conclude this chapter by presenting results on tensor effects and suggesting future directions towards observing spin squeezing.

10.2 Magneto-optical trap theory

The main force involved in the cooling of atoms is due to radiation pressure. When a photon scatters off an atom, a recoil force is applied on the atom, in the opposing direction to that of the scattered photon, via the conservation of momentum. Although the atom recoil force is quite small (since typical atom velocity changes are 1 cm/s), by tuning the laser to be on-resonance, the atom scatters strongly (typically 10^7 photons).

In order to cool and trap a thermal cloud of atoms, velocity dependent photon scattering was used. Let us detune the laser frequency, ν_L, to the red of the atomic transition (for example, by one atomic linewidth). An atom counter-propagating with the laser beam will experience the laser at a frequency of $(1+\frac{v}{c})\nu_L$. A co-propagating atom with the laser beam will experience a laser frequency of $(1-\frac{v}{c})\nu_L$. Therefore the scattering rate for an atom counter-propagating with the laser beam is higher than that of a co-propagating atom. In order to perform velocity-dependent damping of atomic motion in all spatial axes, counter-propagating laser beams were applied along 3 orthogonal axes. Experimentally, the atoms will be pumped into an alternate ground state (since alkali atoms have multiple hyperfine levels). Therefore in order to maintain the population of atoms in the relevant ground state hyperfine level, for cooling, a repump beam is applied on the alternate ground state level. The resulting cooled atoms are termed "optical molasses".

However, in this scheme, the atoms are cooled and trapped at various locations, without any form of spatial confinement. The atoms could also diffuse since there is no position-dependent force. In order to introduce position dependence into the cooling and trapping process, an inhomogeneous magnetic field is introduced, as shown in Fig. 10.1. The idea is to introduce Zeeman shifts to the energy levels of the atoms, which varies with spatial direction (see Fig. 10.1 (A)). The laser beams are appropriately circularly polarised in order to interact with the relevant shifted Zeeman sublevels (see Fig. 10.1 (B)). This results

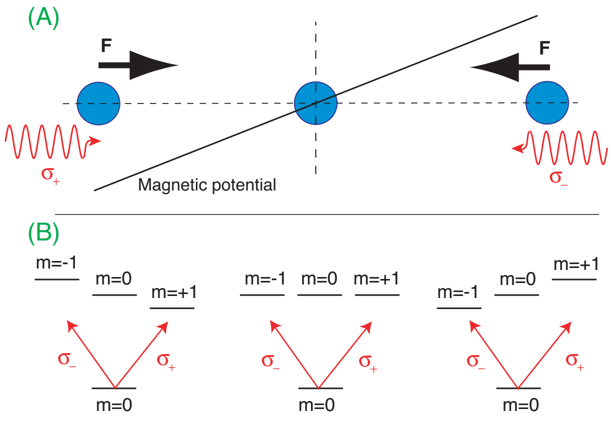

Figure 10.1: (A) Illustration showing the inhomogeneous magnetic potential applied across the central trapping region of the MOT. The atom on the left will scatter strongly from the σ_+ light, whilst the atom on the right will scatter strongly from the σ_- light. The result is a force pushing the atoms to the centre of the trap. At the centre of the trap, there is zero effective force acting on the atom, thus confining the atom. (B) Atomic energy levels as a function of magnetic potential, which varies spatially.

in position-dependent scattering which 'pushes' atoms towards the zero of the magnetic potential. The combined use of inhomogeneous magnetic fields with optical fields to trap and cool atoms is termed a *magneto-optical trap* (MOT).

10.3 Magneto-optical trap experiment

This section details the magneto-optical trap (MOT) experiments. The MOTs at the Australian National University (ANU) and the California Institute of Technology (Caltech) have similar layouts. The main difference lies in the atomic source, where

- Rubidium-87 (^{87}Rb) is used in the ANU experiment, and
- Cesium-133 (^{133}Cs) is used in the Caltech experiment.

10.3.1 Lasers

ANU experiment

The trapping and cooling lasers used in the ANU experiment were derived from two separate extended-cavity diode lasers (ECDLs). In our early experiments, we used home-built ECDLs. However, these lasers tended to be insufficient in power and mechanical stability was constantly an issue. Thereafter we replaced our home-built ECDLs with commercial ECDLs from Toptica Systems.

Our two diode lasers were at 780 nm and each had a maximum output power of 90 mW. The lasers were frequency stabilised via Pound-Drever-Hall (PDH) locking, whose error signal was derived via frequency modulation (FM) on saturated absorption spectroscopy signals (see Chapter 6). The trapping laser was locked and frequency shifted using acousto-optic modulators (AOMs) to the red of the $2 \rightarrow 3'$ transition of ^{87}Rb, by 14 MHz. The repump beam was also locked and frequency shifted to the $1 \rightarrow 2'$ transition of ^{87}Rb. The trapping beam had a total power of 80 mW and the repump beam had a total power of 5 mW.

The trapping and repump beams were combined and overlapped using a polarising beam splitter. The beams were then expanded and collimated to a diameter of 25 mm. Subsequently, the beams were split equally in power, into three orthogonal directions - two in the horizontal plane and one in the vertical axis. The beams were circularly polarised using quarter wave-plates and intersected orthogonally in the central MOT region. The MOT beams were then retro-reflected and a second set of quarter wave-plates ensured the reflected beam polarisation had the correct circular polarisation.

The probe laser used was derived from a Ti:Sapphire laser, described in Chapter 6.

Caltech experiment

The Caltech experiment used home-made ECDLs. The trapping and repump lasers were locked to the $4 \rightarrow 5'$ and $3 \rightarrow 4'$ transitions of ^{133}Cs, respectively. The locking was performed via FM modulation on saturated absorption spectroscopy signals. The trapping ECDL served as a seed to an amplified system which gave approximately 100 mW of optical power at 852 nm.

The trapping beam was then passed through AOMs to detune the laser frequency to the red of the $4 \rightarrow 5'$ transition of ^{133}Cs. The AOMs also provided intensity control on the laser. The repump laser was passed through a mechanical shutter which served to turn the beam on or off. The power of the repump beam was adjusted manually via a waveplate and polarising beam-splitter configuration. Both repump and trapping beams were combined and expanded to a diameter of approximately 25 mm. Subsequently, the beams were split equally in power and sent into the MOT region along three orthogonal directions - two in the vertical plane and one along the horizontal axis.

The probe laser used was derived from a commercial ECDL (Vortex from New Focus). The probe laser was left unlocked and was seeded into an amplified system to provide up to 30 mW of optical power at 852 nm. A beat-note measurement of the probe laser frequency with respect to the locked trapping laser was also set up to provide a frequency reference for the probe laser. The probe laser was sent through an AOM for intensity control and was subsequently coupled into a polarisation-maintaining fibre. The fibre output was situated close to the glass cell of the MOT to minimise the free-space propagation of the probe beam.

10.3.2 Quadrupole magnetic coils

The quadrupole magnetic coils consisted of a pair of anti-Helmholtz coils. The coils were driven by a DC current power supply with typically 3 A, giving a magnetic field gradient of 10 G/cm. The zero of the magnetic field potential was aligned to be at the centre of the crossing of all MOT laser beams. Upon turning off the current supply to the coils, the magnetic field decay was measured to be up to 100 μs for the ANU experiment[2]. The Caltech experiment had a measured magnetic field decay of up to 500 μs.

---

[2] The magnetic field decay was measured using a single-loop coil, placed next to the quadrupole coils.

10.3.3 Coils for the cancellation of background fields

Three pairs of Helmholtz coils were used to cancel out background magnetic fields. The Helmholtz coil pairs were arranged in all three orthogonal axes and were driven independently by three separate DC current supplies. Each coil had approximately 20 windings of wire and could provide up to 0.5 G magnetic fields. We used the cold atom cloud in the MOT to perform coarse tuning of background magnetic field cancellation. When the quadrupole fields of the MOT were turned off, the cold atom cloud expanded. In the presence of a stray magnetic field, the expansion of the MOT is non-isotropic and follows the directionality of the field. By continuously switching the MOT coils on and off, and tuning the current to the three pairs of Helmholtz coils, the cold atom cloud expansion can be made isotropic. When such a state is achieved, the background DC fields in the central MOT region are reasonably-well cancelled.

10.3.4 Vacuum chamber

The vacuum chamber is a setup consisting of a glass cell and an ion pump. In the ANU experiment, a Rubidium dispenser was attached inside the vacuum chamber, as a supply of Rubidium atoms. The glass cell was pointing in the horizontal axis with significant optical beam access from all directions. A schematic diagram of the ANU MOT apparatus is shown in Fig. 10.2.

10.4 Optical depth

Now that the experimental details of the MOT setup have been described, we proceed to discuss the optimisation of the cold atom cloud optical depth. We also describe the various techniques used to measure optical depth (or atomic density).

10.4.1 Definition

A measure of the absorption of a light beam in a medium is the optical depth (OD), given by

$$\mathrm{OD} = \sigma_0 n L \tag{10.1}$$

where σ_0 is the on-resonance scattering cross-section, n is the atomic density and L is the length of the sample. The optical depth can also be obtained by taking the logarithm of the ratio of the output to input intensities of a probe beam propagating through the absorbing medium, given by

$$\frac{I}{I_0} = \exp(-\mathrm{OD}) \tag{10.2}$$

where I is the output beam intensity and I_0 is the input beam intensity. There are various means to measure the optical depth of a system. The various techniques are described in the following subsections.

10.4.2 Fluorescence measurement

When near-resonant light is illuminating an atomic sample, photons are absorbed and scattered. By performing a fluorescence measurement (i.e. measuring the intensity of the scattered light), the total number of atoms can be inferred. The total power of scattered

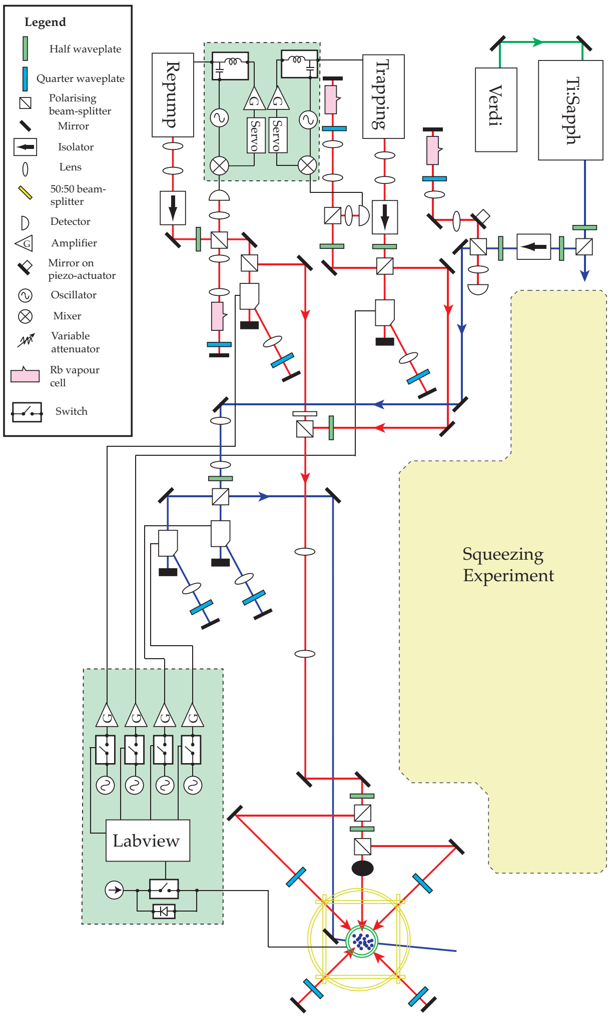

Figure 10.2: Schematic diagram of the MOT apparatus. The Ti:Sapphire laser beam was split into two parts, one which was used as a probe beam in the MOT experiment, whilst the other was used in the optical squeezing experiment [8]. The legend on the top left corner of the diagram describes the various optical and electronic components.

photons is given by

$$P = N\hbar\omega_0\gamma \frac{\frac{I}{2I_{\mathrm{sat}}}}{1 + 4\left(\frac{\Delta}{\gamma}\right)^2 + \frac{I}{I_{\mathrm{sat}}}} \tag{10.3}$$

where I is the total intensity of the beams illuminating the atomic sample, I_{sat} is the saturation intensity for the atomic transition, Δ is the detuning of the laser beams from resonance[3], γ is the spontaneous emission rate and N is the total number of atoms interacting with the light.

The atom is treated as a dipole which scatters isotropically in all directions. Therefore, all the scattered photons have to be collected in order to measure the total scattered power. However, this is typically not feasible in an experiment, and thus often a certain solid angle

---

[3] We assume here that the detuning is on the order of the atomic linewidth of the transition.

of the scattered light is collected. Experimentally this is achieved by using a high numerical aperture optic to collect and image the light onto a photo-detector. The measured light power is given by

$$P_c = \frac{A_{\text{lens}} P}{4\pi r^2} \tag{10.4}$$

where A_{lens} is the area of the collecting lens, r is the distance from the scattering medium to the lens and P is the total power of the scattered light.

We can now infer the total power of the scattered light and therefore further infer the total number of interacting atoms. The spatial extent of the scattered light can be measured using a CCD camera. Therefore an estimate of the atomic density can be obtained and consequently the optical depth. The fluorescence technique is usually used to obtain an order estimate of the atomic density. More direct and precise measurements of atomic density can be obtained using absorption spectroscopy measurements which is described in the following subsection.

Fig. 10.3 shows a typical atomic density distribution of a ^{87}Rb cloud in a MOT (i.e. the column density), obtained from fluorescence imaging. The transverse plane is the spatial extent of the cold atom cloud whilst the vertical axis gives the number of atoms.

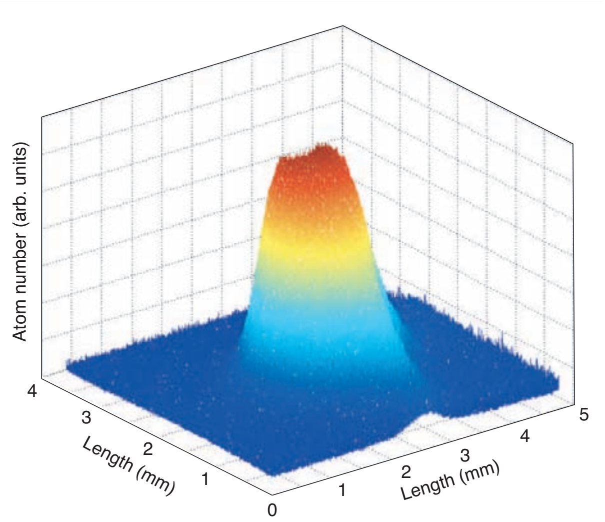

Figure 10.3: Fluorescence image of a cold ^{87}Rb cloud in a MOT. The total number of atoms is $\sim 10^7$.

We can also characterise the loading time of the cloud in a MOT by measuring the total number of atoms collected in the MOT, as a function of time. The increase in the fluorescence signal during the loading period is shown in Fig. 10.4. The experimental curve was fit using the expression, given by

$$N = N_0 \left(1 - \exp\left(-\frac{t}{\tau}\right)\right) \tag{10.5}$$

where τ is the time taken to load the MOT until it reaches a steady state atom number N_0. τ is also a measure of the mean time an atom will remain in the MOT before it gets ejected from the MOT region via collisions with another atom. The atom cloud in the MOT reaches a steady state in its atom number when the number of atoms leaving and entering the MOT are equal.

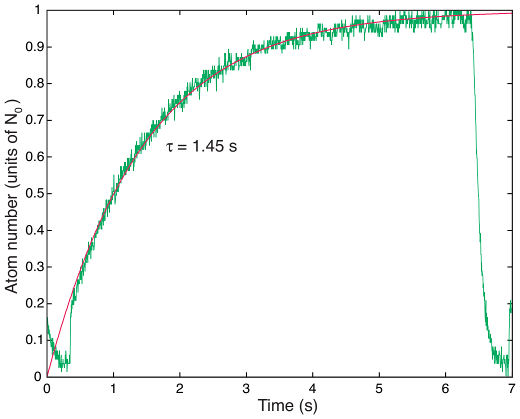

Figure 10.4: Fluorescence signal measured during the loading of ^{87}Rb atoms in a MOT. The theoretical fit yielded a loading time of $\tau = 1.45$ s.

10.4.3 Absorption measurement

We now describe a more accurate means of measuring the optical depth (or atomic density) of an atomic medium. This technique involves measuring the absorption profile of a non-saturating probe beam, which is scanned in its frequency. A standard model for absorption in an atomic medium was then used to fit with the experimental data. As will be shown, the theoretical fits agree very well with the experimental data and this technique yields accurate values for the optical depth[4].

We need to determine the scattering cross-section for an atom illuminated by a laser beam of intensity I with detuning $\Delta_{ff'}$ from the resonance line $f \rightarrow f'$. We assume that the atoms are populated in the ground state f and the total scattered power is the sum of the scattered powers from all the atomic transitions, given by

$$\begin{aligned} P_{\text{tot}} &= \sum_{f'} P_{ff'} \qquad (10.6)\\ &= \sum_{f'} \hbar\omega_0\gamma \frac{\frac{I}{2I_{ff'}}}{1 + 4\left(\frac{\Delta_{ff'}}{\gamma}\right)^2 + \frac{I}{I_{ff'}}} \qquad (10.7)\end{aligned}$$

where f, f' are the ground and excited state hyperfine levels, respectively. $I_{ff'} = I_{\text{sat,lin}}/S_{ff'}$ is the saturation intensity for the $f \rightarrow f'$ transition. $I_{\text{sat,lin}}$ is the saturation intensity assuming linearly polarised light and the transition strength for the $f \rightarrow f'$ transition is given by $S_{ff'}$, which can be computed from the Clebsch-Gordon coefficients[5].

The scattered power is related to the scattering cross-section via $P_{\text{tot}} = \sigma_0 I$. For probe

---

[4] This technique gives many data points as a function of detuning from atomic resonance. Note that the signal-to-noise ratio of measurements around the edges of the absorption profile are higher than that on-resonance. One can therefore be confident that a fit which replicates exactly both the shape and widths of the absorption profile gives a reliable estimate of the optical depth of the medium.

[5] The numbers for the alkali atoms were obtained from D. A. Steck (http://steck.us/alkalidata/).

beam intensities below saturation, $I \ll I_{ff'}$, the scattering cross-section is given by

$$\sigma_0 = \sum_{f'} \frac{\hbar\omega_0\gamma}{2I_{ff'}\left(1 + 4\left(\frac{\Delta_{ff'}}{\gamma}\right)^2\right)} \tag{10.8}$$

This equation gives the scattering cross-section for stationary atoms. However, atoms are often non-stationary. In the absorption measurement of an atom cloud in a MOT, the background gas contribution has to be considered. Therefore, the line broadening due to the Doppler effect of the background gas, has to be included into the absorption model. The background gas scattering cross-section is obtained by the convolution of the scattering cross-section of stationary atoms, with a Voight lineshape, given by

$$\sigma_{0,\mathrm{bg}} = \sum_{f'} \frac{\hbar\omega_0\gamma}{2I_{ff'}} \int_{-\infty}^{\infty} dt \frac{\exp(-t^2)}{\sqrt{\pi}\left(1 + 4\left(\frac{\Delta_{ff'} - \alpha_D t}{\gamma}\right)^2\right)} \tag{10.9}$$

where $\alpha_D = 2\pi v/\lambda$ is the parameter which takes into account the mean velocity v of the atoms in the background gas. In the limit where the temperature is sufficiently high such that the Doppler broadening is much greater than that of the atomic linewidth, Eq. (10.9) simplifies to that of a gaussian function given by

$$\sigma_{0,\mathrm{bg}} = \sum_{f'} \frac{\hbar\omega_0\gamma}{2I_{ff'}} \frac{\gamma\sqrt{\pi}}{2\alpha_D} \exp\left(\frac{-\Delta_{ff'}^2}{\alpha_D^2}\right)^2 \tag{10.10}$$

Therefore the total optical depth for a measurement of atoms in a MOT, including the background gas contribution, is given by

$$\mathrm{OD} = \sigma_0 n L + \sigma_{0,\mathrm{bg}} n_{\mathrm{bg}} L_{\mathrm{bg}} \tag{10.11}$$

where n and L are the atomic densities and length of the cold atom cloud in the MOT. n_{bg} and L_{bg} are the atomic densities and 'effective length' of the background gas surrounding the cold atom cloud. The typical experimental errors for the OD measurement via absorption are ±15 %.

10.5 Optimisation of the MOT OD

As discussed in Chapter 9, maximising the optical depth maximises the spin squeezing. Therefore, this section describes in detail the procedures in optimising the optical depth of a cold atom cloud in a MOT.

In order to align the laser beams for the MOT, we first apertured the trapping and repump beams. The apertured repump and trapping beams were then aligned such that they overlapped each other. The beams were then sent in three orthogonal directions into the central MOT region, with the frequencies of the lasers scanning across the atomic transitions. The power in the beams was adjusted to be distributed equally across all three beams. At this stage, the vacuum chamber was filled with Rb (or Cs) atoms and the fluorescence due to the laser beams was observed. The laser beams were then aligned such that they were orthogonal and intersected at the centre of the MOT. Once the alignment was satisfactory, the beams were then expanded and the lasers were locked to the appropriate transitions and the magnetic coils were turned on. A small cold atom cloud should appear at the centre of the MOT. The waveplates were then adjusted slightly and the alignment of the beams were optimised qualitatively by observing the fluorescence of the MOT using a CCD camera. Once the cold atom cloud was significant in size (a couple of mm in size and had a strong fluorescence signal), we proceeded to be more systematic and quantitative in optimising the MOT beam alignment.

A probe beam scanning in frequency across the $4 \rightarrow 3', 4', 5'$ transitions of ^{133}Cs was applied to the centre of the cold atom cloud. Detection of the absorption signal of the probe beam gave a quantitative measure for optimising the optical depth of the cold atom cloud. At this stage, the alignment of the MOT beams and the strength of the magnetic field gradient were all optimised to minimise the $4 \rightarrow 3'$ transmission. The transmission attainable for the $4 \rightarrow 3'$ transition for a cold atom cloud is typically $\sim 15 - 20$ %, as shown in Fig. 10.5. The $4 \rightarrow 4', 5'$ transitions should at this stage be at the dark level of the detector, indicating full absorption at those transitions.

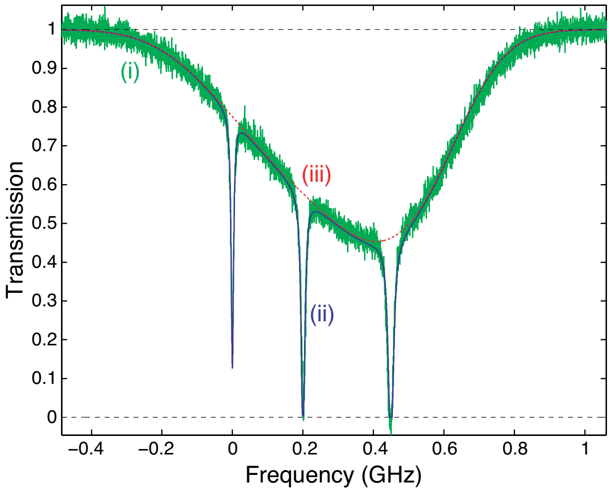

Figure 10.5: (i) Experimental absorption profile of a probe beam propagating through the central region of a cold atom cloud in a MOT. The theoretical fit to the absorption profile is shown as curve (ii) whilst the background gas absorption fit is shown as curve (iii). The theoretical fit yielded an optical depth of 19.6 with a background gas optical depth of 0.79. The probe beam had a power of 0.3 μW, beam diameter of 1 mm and was measured 1 ms after turning off MOT. The probe beam was swept in frequency across the $4 \rightarrow 3', 4', 5'$ transitions of ^{133}Cs. The scan rate was 100 Hz.

The probe beam causes scattering of atoms in the cloud and therefore it is important that the probe beam has a low intensity yet can provide a significant signal-to-noise ratio for the absorption measurement. The model for optical depth also assumes intensities below saturation and thus for reliable estimates of the optical depth, the probe beam has to be less than the saturation intensity of the atoms. Fig. 10.6 shows the effect of the probe beam on the optical depth measurements for the (A) cold atom cloud and (B) the background gas.

Fig. 10.6 shows that to minimise scattering loss, the probe beam power power should be less than 1 μW, for a 1 mm diameter beam (which is less than the saturation intensity for ^{133}Cs, given by 1.6 mW/cm^2). We typically performed the optical depth measurements with probe powers of 0.3 μW and obtained sufficient signal-to-noise ratio for the absorption

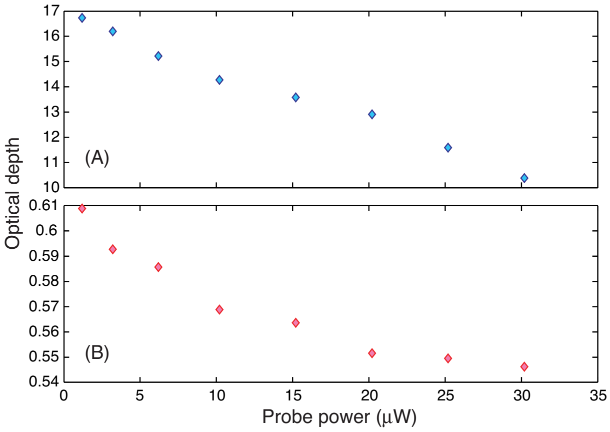

Figure 10.6: Optical depth as a function of probe beam power for the (A) cold atom cloud and (B) background gas. The ^{133}Cs cloud was measured 1 ms after turning off the MOT. The probe beam had a beam diameter of 1 mm and was scanned in frequency across the ^{133}Cs, $4 \rightarrow 3', 4', 5'$ transitions, with a scan rate of 100 Hz.

signal.

An important requirement of the MOT is its reliability in producing stable shot-to-shot cold atom clouds with minimal variations in its optical depth. This is particularly important in the spin squeezing experiment as the statistics of the spin squeezing have to be obtained over many shot-to-shot measurements of the cold atom cloud. We measured the variability of the optical depth of the ^{133}Cs cloud by performing shot-to-shot optical depth measurements, shown in Fig. 10.7.

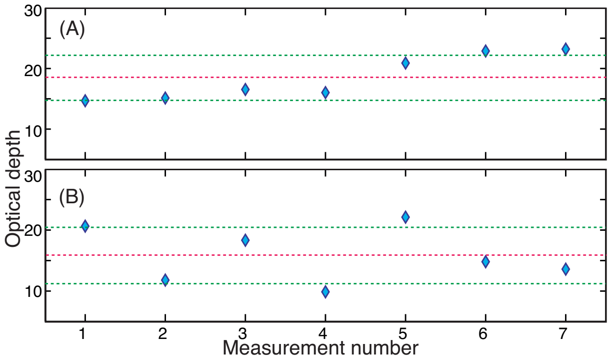

Figure 10.7: Shot-to-shot measurements of the optical depth of a ^{133}Cs cold atom cloud in a MOT. The measurement was performed 1 ms after turning off the MOT, with probe power of 0.3 μW, probe beam diameter 1 mm. The probe beam was scanned in frequency across the ^{133}Cs, $4 \rightarrow 3', 4', 5'$ transitions, with a scan rate of (A) 100 Hz and (B) 200 Hz. The red dashed line shows the average optical depth, with the green dashed curve showing the standard deviation of the measurement.

The standard deviation in optical depth is between 10-15 % from a shot-to-shot measurement. This is an important factor to take into account when performing measurements for spin squeezing. Improvements in the shot-to-shot reliability for the MOT is therefore crucial. The reliability could potentially be accomplished by improving the alignment of the MOT beams and cancelling ambient magnetic fields.

10.6 Transient compression

In order to further increase the optical depth of cold atoms in a MOT, more sophisticated compression schemes were utilised. Various groups [342, 340] have reported an increase in atomic density via transient compression of cold atoms in a MOT. Transient compression essentially involves tightening the confining potential of the atoms in a MOT.

We implemented a transient compression scheme which involved increasing the magnetic field gradient from 10 G/cm to 20 G/cm, in four time steps of 5 ms. The trapping laser was frequency detuned from -15 MHz to -25 MHz to reduce scattering loss. The resulting probe beam absorption profile following transient compression is shown in Fig. 10.8.

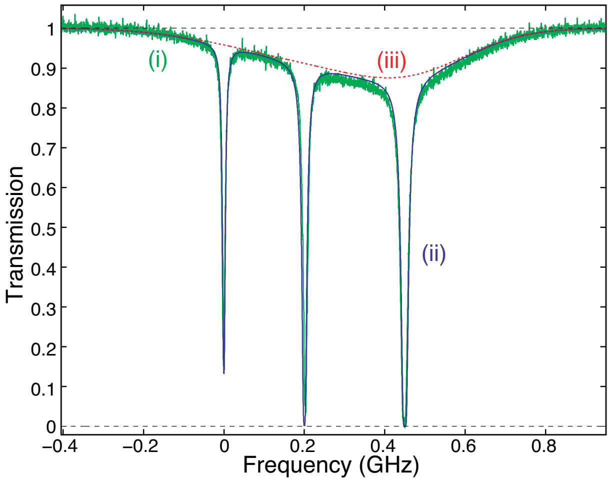

Figure 10.8: (i) Experimental probe beam absorption profile for a compressed MOT. The optical depth was measured 1 ms after turning off the MOT, with probe power of 0.3 μW and beam diameter of 1 mm. The probe beam was scanned in frequency across the ^{133}Cs, $4 \rightarrow 3', 4', 5'$ transitions, with a scan rate of 100 Hz. (ii) The theoretical fit gives a cold atom cloud optical depth of 30.7 and the (iii) background optical depth is 0.133.

The increase in the OD of cold atoms in a transient compressed MOT is approximately 50 % relative to that of a normal MOT. However, the OD increase is insufficient and we decided instead to adopt an alternate compression scheme.

10.7 Dark-SPOT

In the Caltech MOT experiment, atoms were cooled on the red-detuned frequency of the ^{133}Cs $4 \rightarrow 5'$ transition, whilst a repump beam was applied on the $3 \rightarrow 4'$ transition to repopulate atoms into the $F = 4$ ground state. The number of atoms being scattered out of and cooled into the MOT region will reach an equilibrium and this limits the density achievable in a standard MOT. In order to increase the density of the atoms further, we implemented a *dark-spontaneous force trap* (dark-SPOT) [341, 343].

The dark-SPOT involved applying a repump beam with a dark central region (i.e. a doughnut-shaped beam). A depump beam was also applied to this central dark region, tuned to the $4 \rightarrow 4'$ transition. The result of this was a central region in the cold atom cloud which was optically pumped into the $F = 3$ ground state. Since the cooling beams were tuned to the red of the $4 \rightarrow 5'$ transition, atoms in the central region were unaffected by the cooling beams. Therefore, scattering in the central region of the atom cloud was reduced significantly, but the temperature of the atoms was increased. The atoms in this region were continuously loaded with atoms from the surrounding trapped and cooled 'ring' MOT region, resulting in an increase in the density of atoms in the dark region.

We now describe the OD optimisation procedure for atoms in the dark-SPOT. First, the optical depth of the atoms in a standard MOT was optimised. The MOT beams were then reduced in size via aperturing. The depump beam, tuned on the $4 \rightarrow 4'$ transition, was aligned such that it "blew away" the atoms in the reduced MOT[6]. Once this was accomplished, the MOT beams were expanded to the original sizes and a dark spot was inserted into the central region of the repump beam. The probe laser was applied in the central region of the dark-SPOT and scanned in frequency across the ^{133}Cs $3 \rightarrow 2', 3', 4'$ transitions (since the atoms were now populated in the $F = 3$ ground state). The optical depth of the atom cloud in the dark-SPOT was optimised by aligning the location of the dark-spot in the repump beam, as well as varying the power and alignment of the depump beam[7]. The resulting probe beam absorption profile for atoms in a dark-SPOT is shown in Fig. 10.9.

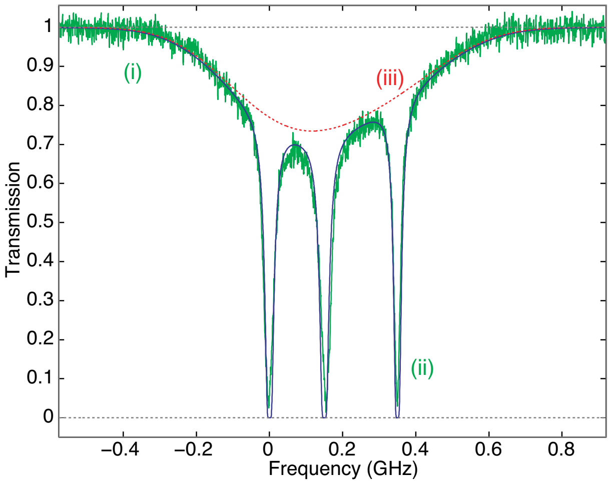

Figure 10.9: (i) Experimental probe beam absorption profile. The optical depth was measured 0.5 ms after turning off the dark-SPOT. The probe beam had a power of 0.3 μW, beam diameter of 1 mm and was scanned in frequency across the ^{133}Cs, $3 \rightarrow 2', 3', 4'$ transitions with a 150 Hz scan rate. The (ii) theoretical fit yielded a cold atom cloud optical depth of 93 and a (iii) background optical depth of 0.31.

---

[6] The depump beam may have to increased in power to observe this effect.

[7] A simulation of the absorption profile for high optical depths was performed and the fine tuning of the depump beam power and alignment was performed to attain this. The 'key' feature to observe was the width and depth of the absorption dips. The wider and deeper the absorption dips, the higher the optical depth.

We observed that cold atoms in the dark-SPOT gave a factor of 4.5 improvement in the optical depth of the cold atoms, relative to the standard MOT. However, the population of the atoms were in the $F = 3$ ground state and needed to be repopulated into the $F = 4$ ground state, for spin squeezing experiments. Following the preparation of cold atoms in a dark-SPOT (for 5 s), the dark-SPOT was then turned off and a repump beam was applied for 2.5 ms. The repump beam served to repump the atoms back into the $F = 4$ ground state. The measured probe absorption profile is shown in Fig. 10.10.

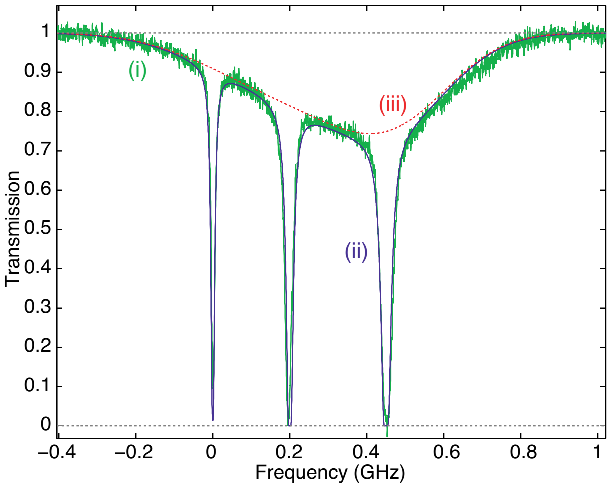

Figure 10.10: (i) Experimental probe beam absorption profile. The optical depth was measured 0.5 ms after turning off the dark-SPOT. The probe beam had a power of 0.3 μW, beam diameter of 1 mm and was scanned in frequency across the ^{133}Cs, $4 \rightarrow 3', 4', 5'$ transitions with a 150 Hz scan rate. The (ii) theoretical fit yielded a cold atom cloud optical depth of 65 and a (iii) background optical depth of 0.30.

The optical depth after pumping into the $F = 4$ ground state was 65. This was an improvement of about a factor of 3 over cold atoms produced in a MOT. However, the lifetime of the cold atom cloud was significantly reduced from 15 ms (for the MOT) to 5 ms (for the dark-SPOT). This was measured by applying the probe beam at different times following the turning off of the trapping and cooling beams and observing the decay of the absorption signal.

10.8 Larmor precession measurements

Larmor precession measurements were performed on the cold atoms. For Cesium-133, the Larmor precession frequency to magnetic field ratio is given by 350 kHz/G.

In order to measure the Larmor signal, the cold atom cloud was spin polarised in the x-direction[8]. The spin polarisation was then adiabatically rotated to the z-direction, by smoothly varying the strengths of the magnetic fields in the appropriate directions. The rotation rate had to be less than the Larmor precession rate in order to maintain adiabaticity. Following this, a magnetic field was applied in the x-axis, causing the spin vector

---

[8] The spin polarisation was prepared by applying a circularly polarised optical pumping beam on the $4 \rightarrow 5'$ transition, propagating in the x-direction. A magnetic field was also applied in the x-direction.

to precess around the magnetic field. Due to the vector-Hamiltonian interaction between the spin vector and an x-linearly polarised probe field (propagating in the z-direction), a Faraday rotation was induced on the probe beam polarisation. The Faraday rotation signal (due to the Larmor precession) corresponding to a field strength of 29.68 mG is shown in Fig. 10.11.

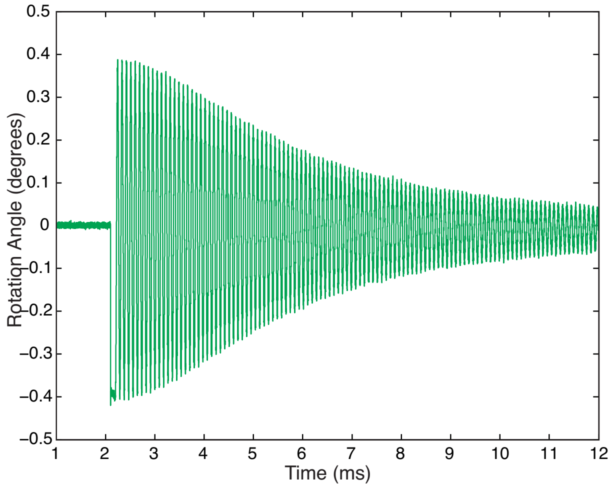

Figure 10.11: Polarisation rotation signal due to the Larmor precession in a cold ^{133}Cs atom cloud, prepared in a MOT. The Larmor precession frequency was 10 kHz with an applied magnetic field strength of 29.68 mG. The probe power was 1 mW, probe beam diameter 1 mm and detuned by 2 GHz to the blue of the ^{133}Cs, $4 \rightarrow 5'$ transition. The optical depth was 30.

The amplitude of the Larmor precession signal was also used to optimise the preparation of the spin polarisation. By re-cycling the Larmor precession measurement, the intensity and alignment of the optical pumping beam relative to the applied magnetic field can be optimised. Also, the optical depth can be optimised by maximisation of the Larmor precession signal.

The Larmor precession signal decays due to a few factors, which we describe as follows

- Atomic diffusion decay. The atom cloud begins to diffuse when the MOT (or dark-SPOT) is turned off. Therefore, the atomic density decreases over time. It is important that the decay due to atomic diffusion is small over the measurement time for spin squeezing. This can be accomplished by reducing the temperature of the cold atom cloud and minimising all ambient magnetic fields.

- The tensor term. Since the tensor term couples the spin and polarisation vectors in a non-linear manner, misalignment between the spin and polarisation vectors affects the decay rate of the Larmor signal. The decay rate can thus be used as a measure of the alignment between the polarisation of the probe beam and the spin polarisation vector.

- Spontaneous emission. Ideally, the decay of the Larmor signal should be limited by spontaneous emission, given in Eq. (9.64).

10.9 Tensor measurements

The tensor terms discussed in Chapter 9 were undesirable for our experiment. We therefore performed near-resonant probe measurements on the collective spin vector, to characterise the effects due to the tensor term. The measurement involved initially preparing a collective spin vector in the x-direction and then adiabatically rotating the vector in the x-z plane or the x-y plane, to induce a misalignment between the spin vector and the x-polarised probe beam (propagating in the z-direction). A holding field was applied in the direction of the spin vector. The polarisation oscillations on the probe beam, due to the holding field, were measured and the results are shown in Fig. 10.12

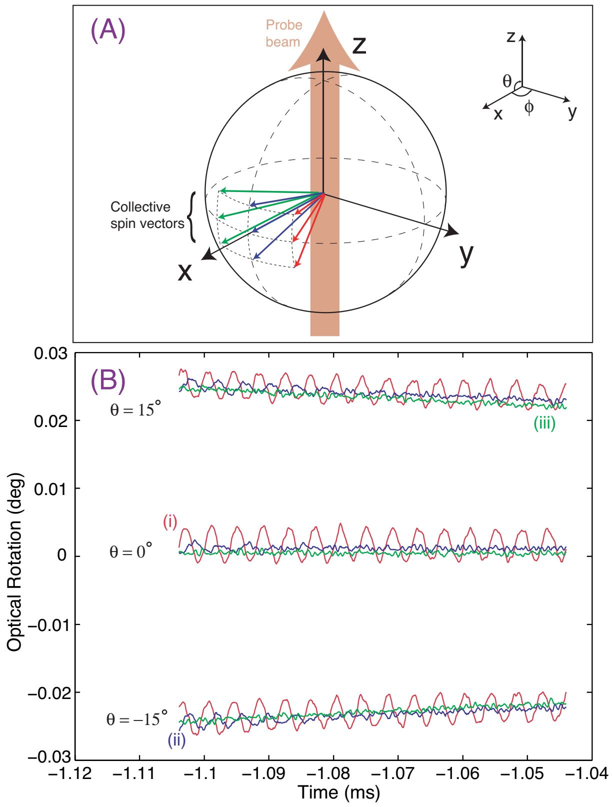

Figure 10.12: (A) Illustration showing the various orientation of collective spin vectors. The probe beam was propagating in the z-direction, with linear polarisation in the x-axis. A cold atom cloud was prepared in a MOT, for 5 s. Following this, the MOT was turned off and a collective spin direction was induced in the atoms via the application of a magnetic field and an optical pumping beam, both in the x-direction. The optical pumping beam was locked on the $3 \rightarrow 4'$ transition. The spin vector was then adiabatically rotated by polar θ and azimuthal ϕ angles. The magnetic holding field was applied throughout the measurement time. (B) The measured trajectories corresponding to various spin vector orientation. The various coloured curves correspond to a ϕ angle of (i) 15°, (ii) 0° and (iii) −15°. The probe power was 11 mW, beam diameter of 1 mm and had a frequency detuning of 1.1 GHz. The optical pumping beam had a power of 17 μW and was applied for 4 ms. The holding field corresponded to a Larmor frequency of 250 kHz. The optical depth of the cold atom cloud was 35.

The effect on the oscillations due to the tensor terms have been reproduced by solving the single-atom master equation, in Ref. [330]. In particular, a few effects due to the tensor term should be present - (i) the oscillation phase is fixed irrespective of when the probe beam is applied, (ii) the oscillation decay rate is faster than the spin vector decay and (iii) the oscillation amplitude increases relative to the spin vector offset for decreasing detuning.

The results in Fig. 10.12 show that for various angles of ϕ (assuming the same θ angle), the oscillations have different phases and amplitudes. However, the oscillation phase does not vary with the time that the probe beam is applied. The oscillations for the different ϕ values decay at different rates (e.g. the oscillation in curve (ii) decays faster than that in curve (i)) and decay faster than the atomic spin state decay rate (which is due to spontaneous emission).

The phases and amplitudes for different values of θ (assuming the same ϕ angle) do not vary. This suggests that the effects from the misalignment about the azimuthal angle ϕ is more significant than that about the polar angle θ. Since the tensor effect is critically dependent on the alignment between the spin and polarisation vectors, the misalignment result of Fig. 10.12 shows that tensor effects are present at a probe detuning of 1.1 GHz. Also, it was observed that the oscillation amplitude increases relative to the spin vector offset for decreasing detuning, further verifying the presence of tensor effects.

As a consequence, the probe detuning has to be made larger. Simulations in Ref. [330] have shown that a detuning of approximately 2 GHz would reduce the tensor effects significantly. However, ODs of at least 100 is required in order to observe spin squeezing [330].

10.10 Conclusion and future directions

10.10.1 Conclusion

We have described the magneto-optical trap developed towards the production of cold atoms with high ODs. Cold atoms with high optical depth (OD $\sim$ 65) have been produced. It is expected that improvements on the OD (possibly up to 100 on the $4 \rightarrow F'$) can be achieved with slight modification and further optimisation of the system. In spite of the achievement of high ODs, the lifetime of the cold atoms were short ($\sim$ 5 ms). The cold atom cloud (produced in a dark-SPOT) lifetime can be further extended via the implementation of polarisation gradient cooling. We also examined the decay times and the effects due to the tensor term.

10.10.2 Future directions

In order to observe spin squeezing, the following ameliorations to the experiment have to be implemented.

- Extension of the lifetime of the cold atom cloud. The dark-SPOT scheme yields significant improvement in optical depth. However, the lifetime of the cold atoms produced via the dark-SPOT are short (less than 5 ms). Therefore, the temperature of the atoms produced by the dark-SPOT have to be reduced further in order to extend the decay time due to atomic diffusion. A reduction in temperature can be achieved via the implementation of the polarisation gradient cooling (PGC) scheme [344, 345, 346].

- Optimisation of probe beam intensity and detuning. The motivation is to minimise the tensor effect whilst ensuring a short measurement time τ_{ss}.

- If the probe polarisation and atomic spin vectors are not aligned (i.e. $\langle \hat{F}_y \rangle$ and $\langle \hat{F}_z \rangle$ are non-zero), then oscillations on the $\langle \hat{S}_x \rangle$ will occur, due to the holding field. The alignment between the probe polarisation and atomic spin vector can be optimised by minimising the oscillation signal. However, despite this improved alignment, the noise properties of the spin and polarisation operators will still be affected by the tensor terms, if the probe detuning is not large enough.

- Background magnetic field and field-gradient cancellation. Larmor signals due to background magnetic fields can be observed using the cold atom cloud and therefore minimised.

- Reliable shot-to-shot optical depth for the cold atom cloud. The stability of the atom cloud for a shot-to-shot measurement is crucial as deviations in optical depth affects each QND trajectory measurement. The dark-SPOT and MOT alignment have to be optimised such that the cold atom cloud produced is stable and does not "jitter" from shot-to-shot.

Chapter 11

Conclusions

The future directions for the research of this thesis are discussed at the conclusion of each chapter. This chapter summarises the results of the work in this thesis.

11.1 Quantum multi-mode optical imaging

We have shown that split detection is non-optimal for the detection of optical beam displacement and tilt. For a TEM_{00} beam, the split detector is at best 80 % efficient. We proposed an optimum displacement measurement scheme based on homodyne detection. By using an optimally-tailored local oscillator beam, small displacement signals can be extracted with 100 % efficiency. We have also shown that by mixing the input beam with a squeezed beam in the appropriate mode, we can significantly improve the sensitivity of the spatial homodyne detection.

We identified the conjugate observables - position, x, and momentum, p, of an optical beam. Correspondingly, an x-p entanglement scheme was proposed, which generates macroscopic entanglement between optical beams. A form of spatial entanglement which has applications in split-detection quantum imaging was also explored. We then studied the generation of spatial Stokes entanglement, analogous to that of polarisation Stokes entanglement.

An application of quantum multi-mode optical imaging to increasing the storage capacities of optical memories was proposed. The optical memory scheme involved performing longitudinal and transverse spatial phase coding of continuous-wave optical beams. The total number of encodable phase values scales with the power of the read-out optical beam. Squeezed light could be used as the read-out beam to enhance the resolution of the different phase values and as a result, further increase the storage capacity of optical disks compared to a coherent state read-out beam.

11.2 Light-atom ensemble quantum interactions

We present a quantum mechanical 4-level atomic model to describe PSR quantum effects and show that the squeezing term is overwhelmed by atomic noise terms in the situation of a thermal vapour. Our experimental results show the non-observation of squeezing, and the observation of excess noise in the output field spectrum at all sideband frequencies. In spite of this, the results of Ries *et al.* [177] and recent experiments conducted in the group of A. I. Lvovsky[1] have demonstrated the observation of squeezing via PSR. Therefore, more

---

[1] personal communication

comprehensive theoretical modelling and experimental studies are necessary to understand the exact conditions under which PSR squeezing can be generated or become overwhelmed by excess noise.

Our measurements of delayed light via EIT, in vapour cells, show significant amounts of excess noise, hitherto unpredicted by published theoretical modelling [223, 286, 299, 182]. The latest theoretical modelling of Hétet *et al.* [305] showed that the presence of ground state population shuffling terms do indeed give excess noise to the output probe field, via a phase-insensitive amplification of vacuum noise. Recent experiments have shown that excess noise may indeed be reduced [297, 298, 307, 308] by the use of buffer gas and cold atom systems. The differing experimental and theoretical results should serve as a motivation for more complete theoretical models to identify the origins of the noise.

We studied the light-atom ensemble coupling via the Faraday interaction. A QND measurement of the atomic spin state, with the application of feedback, can generate spin squeezed atoms. However, second order tensor terms in the interaction Hamiltonian, which could affect the QND measurement were discussed. We then described the spin squeezing experiment developed towards the production of cold atoms with high optical depths, as well as examined the decay times and the effects due to the tensor term.

Appendix A

Circuit diagrams

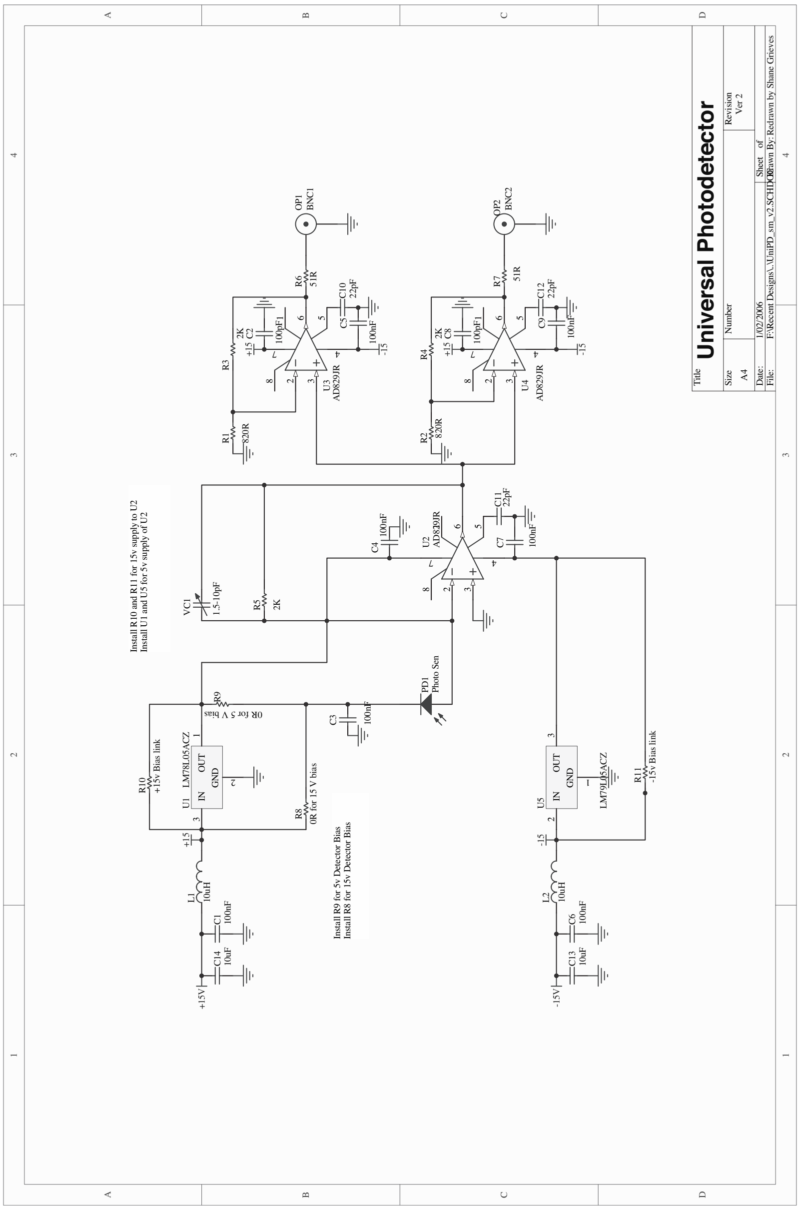

Figure A.1: Electronic circuit diagram for the optical detector.

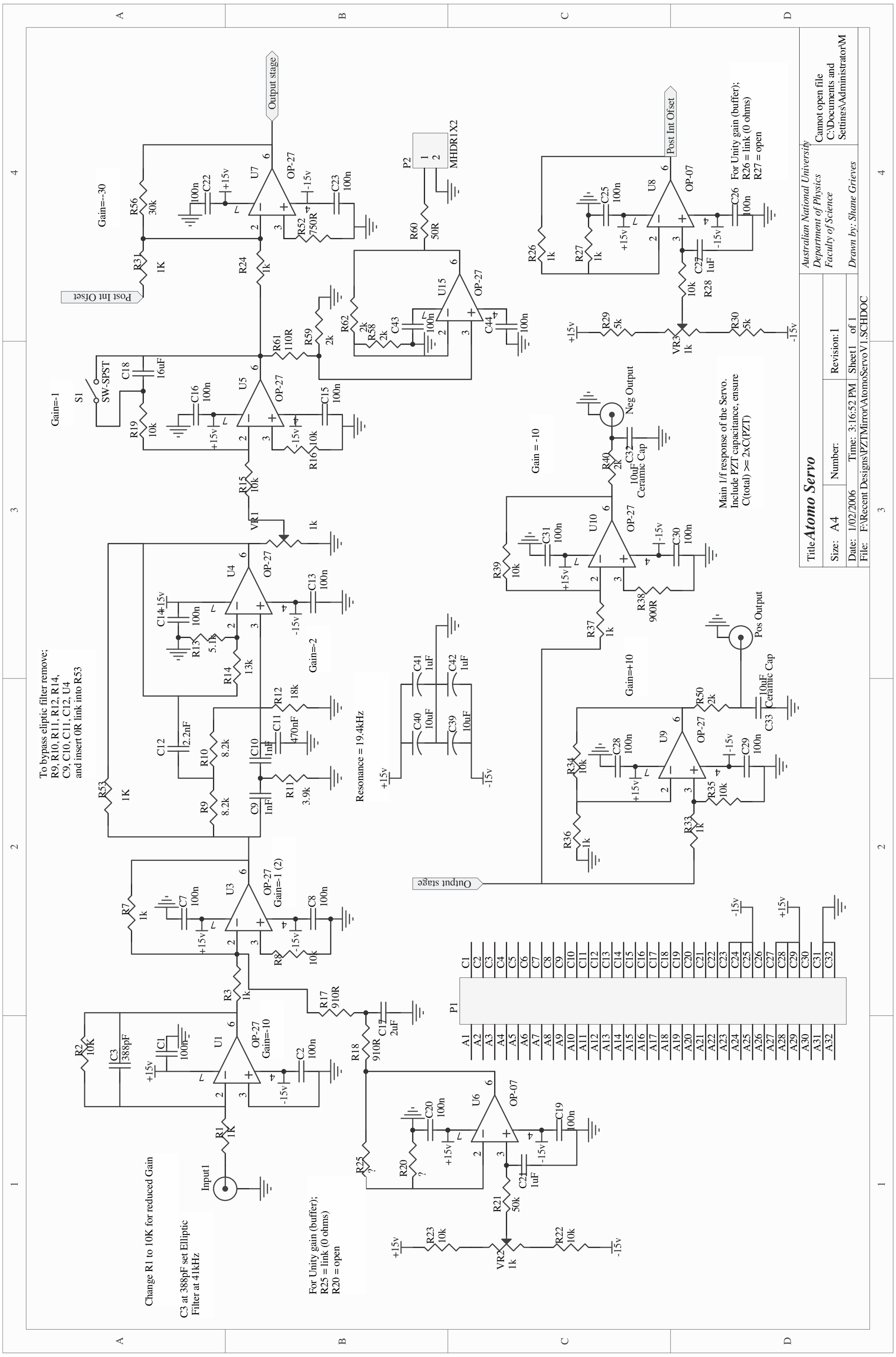

Figure A.2: Electronic circuit diagram for the locking servo.

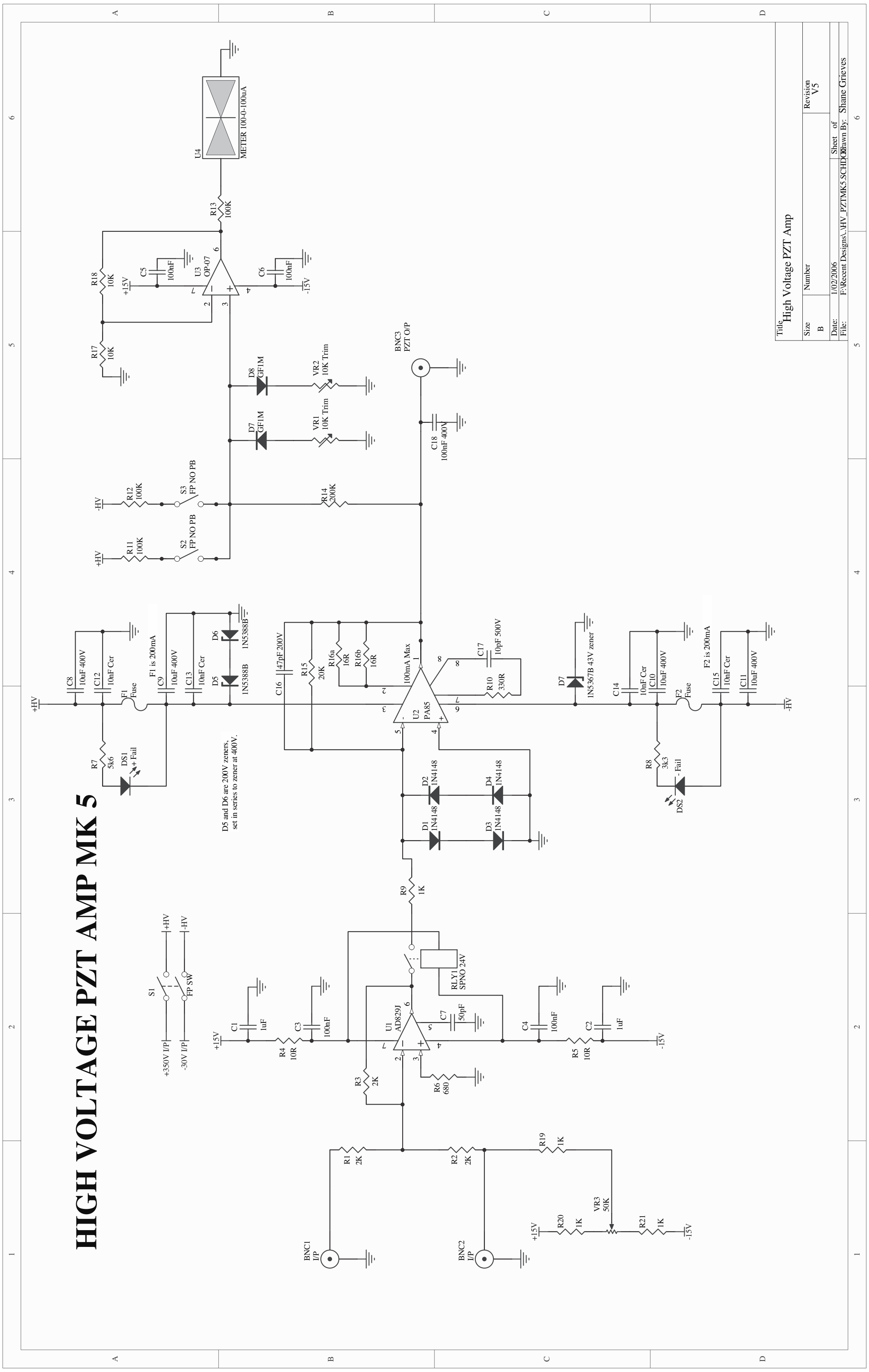

Figure A.3: Electronic circuit diagram for the high voltage amplifier.

Appendix B

Mechanical diagrams

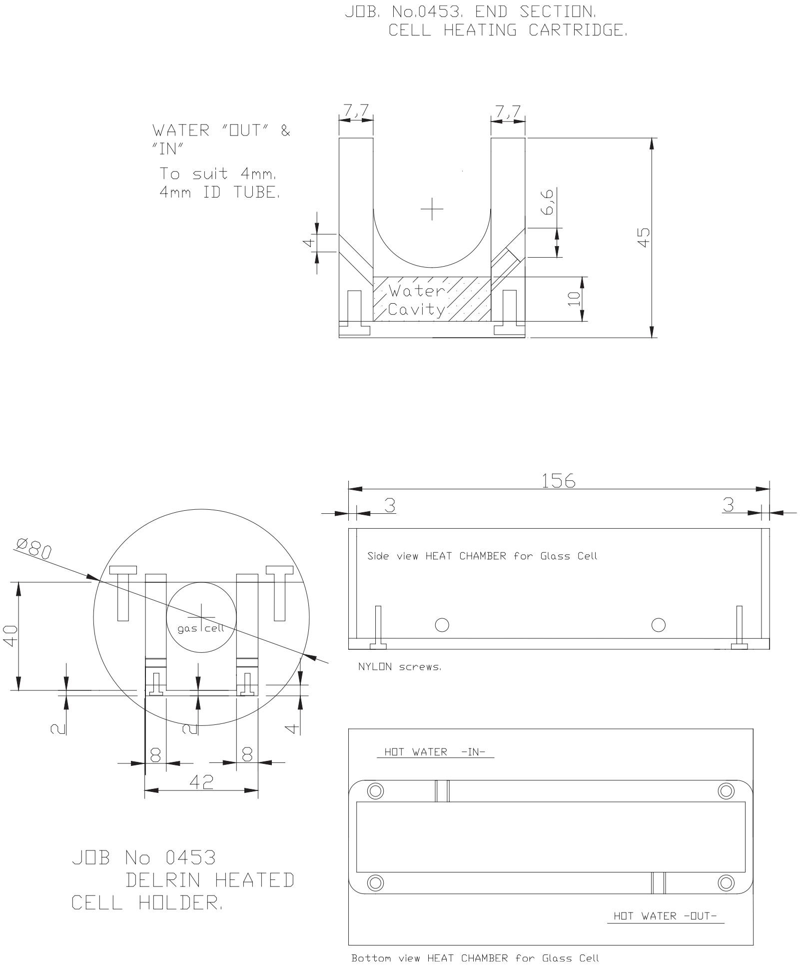

Figure B.1: Mechanical diagram for the inner cell holder unit.

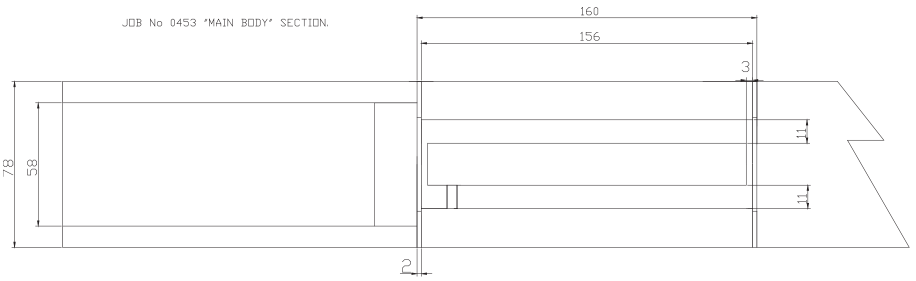

Figure B.2: Mechanical diagram for the main body of the cell holder.

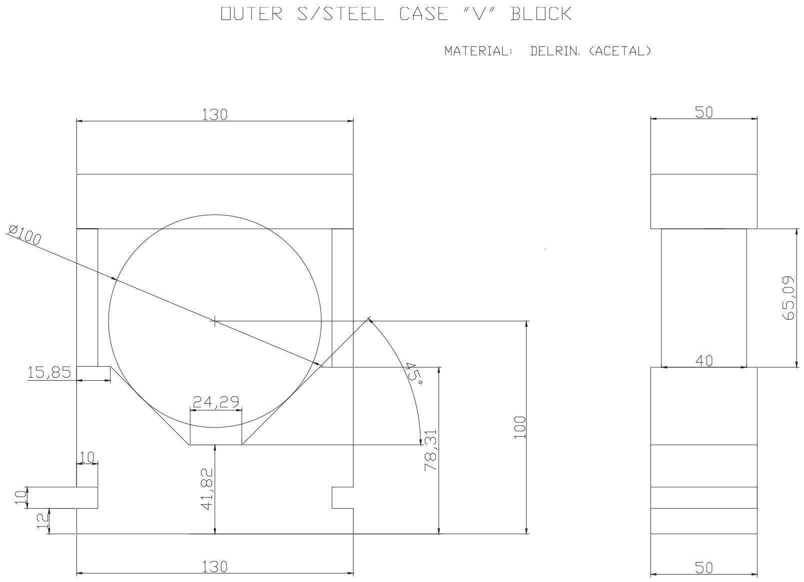

Figure B.3: Mechanical diagram for the V-blocks for mounting the main body of cell holder.

Bibliography

[1] N. Treps, N. Grosse, W. P. Bowen, C. Fabre, H.-A. Bachor, and P. K. Lam, *A Quantum Laser Pointer*, Science **301**, 940 (2003).

[2] V. Delaubert, N. Treps, M. Lassen, C. C. Harb, C. Fabre, P. K. Lam, and H.-A. Bachor, *TEM_{10} homodyne detection as an optimal small-displacement and tilt-measurement scheme*, Physical Review A **74**, 053823 (2006).

[3] V. Delaubert, N. Treps, C. C. Harb, P. K. Lam, and H.-A. Bachor, *Quantum measurements of spatial conjugate variables: displacement and tilt of a Gaussian beam*, Optics Letters **31**, 1537 (2006).

[4] M. W. Beijersbergen, L. Allen, H. E. L. O. van der Veen, and J. P. Woerdman, *Astigmatic laser mode converters and transfer of orbital angular momentum*, Optics Communications **96**, 123 (1993).

[5] J. Ye, S. Swartz, P. Jungner, and J. L. Hall, *Hyperfine structure and absolute frequency of the 87Rb 5P3/2 state*, Optics Letters **21**, 1280 (1996).

[6] G. P. Barwood, P. Gill, and W. R. C. Rowley, *Frequency measurements on optically narrowed Rb-stabilised laser diodes at 780 nm and 795 nm*, Applied Physics B: Lasers and Optics **53**, 142 (1991).

[7] S. Bize, Y. Sortais, M. S. Santos, C. Mandache, A. Clairon, and C. Salomon, *High-accuracy measurement of the ^{87}Rb ground-state hyperfine splitting in an atomic fountain*, Europhysics Letters **45**, 558 (1999).

[8] G. Hétet, O. Glöckl, K. Pilypas, C. C. Harb, B. C. Buchler, H.-A. Bachor, and P. K. Lam, *Squeezed light for bandwidth limited atom optics experiments at the Rubidium D1 line*, Journal of Physics B: Atomic, Molecular and Optical Physics **40**, 221 (2007).

[9] A. L. Schawlow and C. H. Townes, *Infrared and Optical Masers*, Physical Review **112**, 1940 (1958).

[10] A. Einstein, B. Podolsky, and N. Rosen, *Can Quantum-Mechanical Description of Physical Reality Be Considered Complete?*, Physical Review **47**, 777 (1935).

[11] C. S. Wu and I. Shaknov, *The Angular Correlation of Scattered Annihilation Radiation*, Physical Review **77**, 136 (1950).

[12] R. Hanbury Brown and R. Q. Twiss, *Correlation between Photons in two Coherent Beams of Light*, Nature **177**, 27 (1956).

[13] H. J. Kimble, M. Dagenais, and L. Mandel, *Photon Antibunching in Resonance Fluorescence*, Physical Review Letters **39**, 691 (1977).

[14] A. Aspect, P. Grangier, and G. Roger, *'Experimental Realization of Einstein-Podolsky-Rosen-Bohm Gedankenexperiment: A New Violation of Bell's Inequalities'*, Phys. Rev. Lett. **49**, 91 (1982).

[15] A. Aspect, J. Dalibard, and G. Roger, *Experimental Test of Bell's Inequalities Using Time- Varying Analyzers*, Physical Review Letters **49**, 1804 (1982).

[16] A. Aspect, P. Grangier, and G. Roger, *Experimental Tests of Realistic Local Theories via Bell's Theorem*, Physical Review Letters **47**, 460 (1981).

[17] Z. Y. Ou, S. F. Pereira, H. J. Kimble, and K. C. Peng, *Realization of the Einstein-Podolsky-Rosen paradox for continuous variables*, Physical Review Letters **68**, 3663 (1992).

[18] C. Silberhorn, P. K. Lam, O. Weiß, F. König, N. Korolkova, and G. Leuchs, *Generation of Continuous Variable Einstein-Podolsky-Rosen Entanglement via the Kerr Nonlinearity in an Optical Fiber*, Physical Review Letters **86**, 4267 (2001).

[19] V. Jacques, E. Wu, F. Grosshans, F. Treussart, P. Grangier, A. Aspect, and J.-F. Roch, *Experimental Realization of Wheeler's Delayed-Choice Gedanken Experiment*, Science **315**, 966 (2007).

[20] A. I. Lvovsky, H. Hansen, T. Aichele, O. Benson, J. Mlynek, and S. Schiller, *Quantum State Reconstruction of the Single-Photon Fock State*, Physical Review Letters **87**, 050402 (2001).

[21] A. Ourjoumtsev, R. Tualle-Brouri, J. Laurat, and P. Grangier, *Generating Optical Schrödinger Kittens for Quantum Information Processing*, Science **312**, 83 (2006).

[22] J. S. Neergaard-Nielsen, B. M. Nielsen, C. Hettich, K. Mølmer, and E. S. Polzik, *Generation of a Superposition of Odd Photon Number States for Quantum Information Networks*, Physical Review Letters **97**, 083604 (2006).

[23] A. Ourjoumtsev, H. Jeong, R. Tualle-Brouri, and P. Grangier, *Generation of optical 'Schrödinger cats' from photon number states*, Nature **448**, 784 (2007).

[24] K. McKenzie, D. A. Shaddock, D. E. McClelland, B. C. Buchler, and P. K. Lam, *Experimental Demonstration of a Squeezing-Enhanced Power-Recycled Michelson Interferometer for Gravitational Wave Detection*, Physical Review Letters **88**, 231102 (2002).

[25] K. McKenzie, N. Grosse, W. P. Bowen, S. E. Whitcomb, M. B. Gray, D. E. McClelland, and P. K. Lam, *Squeezing in the Audio Gravitational-Wave Detection Band*, Physical Review Letters **93**, 161105 (2004).

[26] M. A. Nielsen and I. L. Chuang, *Quantum Computation and Quantum Information*, Cambridge University Press, 2000.

[27] J. L. O'Brien, G. J. Pryde, A. Gilchrist, D. F. James, N. K. Langford, T. C. Ralph, and A. G. White, *Quantum Process Tomography of a Controlled-NOT Gate*, Physical Review Letters **93**, 080502 (2004).

[28] J. L. O'Brien, G. J. Pryde, A. G. White, T. C. Ralph, and D. Branning, *Demonstration of an all-optical quantum controlled-NOT gate*, Nature **426**, 264 (2003).

[29] N. K. Langford, T. J. Weinhold, R. Prevedel, K. J. Resch, A. Gilchrist, J. L. O'Brien, G. J. Pryde, and A. G. White, *Demonstration of a Simple Entangling Optical Gate and Its Use in Bell-State Analysis*, Physical Review Letters **95**, 210504 (2005).

[30] P. Kok, W. J. Munro, K. Nemoto, T. C. Ralph, J. P. Dowling, and G. J. Milburn, *Linear optical quantum computing with photonic qubits*, Reviews of Modern Physics **79**, 135 (2007).

[31] J. J. Longdell, M. J. Sellars, and N. B. Manson, *Demonstration of Conditional Quantum Phase Shift Between Ions in a Solid*, Physical Review Letters **93**, 130503 (2004).

[32] J. J. Longdell and M. J. Sellars, *Experimental demonstration of quantum-state tomography and qubit-qubit interactions for rare-earth-metal-ion-based solid-state qubits*, Physical Review A **69**, 032307 (2004).

[33] M. D. Barrett, B. Demarco, T. Schaetz, D. Leibfried, J. Britton, J. Chiaverini, W. M. Itano, B. Jelenković, J. D. Jost, C. Langer, T. Rosenband, and D. J. Wineland, *Sympathetic cooling of* $^9Be^+$ *and* $^{24}Mg^+$ *for quantum logic*, Physical Review A **68**, 042302 (2003).

[34] J. Chiaverini, D. Leibfried, T. Schaetz, M. D. Barrett, R. B. Blakestad, J. Britton, W. M. Itano, J. D. Jost, E. Knill, C. Langer, R. Ozeri, and D. J. Wineland, *Realization of quantum error correction*, Nature **432**, 602 (2004).

[35] S. Gulde, M. Riebe, G. P. T. Lancaster, C. Becher, J. Eschner, H. Häffner, F. Schmidt-Kaler, I. L. Chuang, and R. Blatt, *Implementation of the Deutsch-Jozsa algorithm on an ion-trap quantum computer*, Nature **421**, 48 (2003).

[36] F. Schmidt-Kaler, H. Häffner, M. Riebe, S. Gulde, G. P. T. Lancaster, T. Deuschle, C. Becher, C. F. Roos, J. Eschner, and R. Blatt, *Realization of the Cirac-Zoller controlled-NOT quantum gate*, Nature **422**, 408 (2003).

[37] C. Monroe, D. M. Meekhof, B. E. King, W. M. Itano, and D. J. Wineland, *Demonstration of a fundamental quantum logic gate*, Physical Review Letters **75**, 4714 (1995).

[38] L. M. K. Vandersypen, M. Steffen, G. Breyta, C. S. Yannoni, R. Cleve, and I. L. Chuang, *Experimental Realization of an Order-Finding Algorithm with an NMR Quantum Computer*, Physical Review Letters **85**, 5452 (2000).

[39] D. G. Cory, A. F. Fahmy, and T. F. Havel, *Ensemble Quantum Computing by NMR Spectroscopy*, Proceedings of the National Academy of Science **94**, 1634 (1997).

[40] B. E. Kane, *A silicon-based nuclear spin quantum computer*, Nature **393**, 133 (1998).

[41] A. Furusawa, J. L. Sorensen, S. L. Braunstein, C. A. Fuchs, H. J. Kimble, and E. S. Polzik, *'Unconditional Quantum Teleportation'*, Science **282**, 706 (1998).

[42] W. P. Bowen, N. Treps, B. C. Buchler, R. Schnabel, T. C. Ralph, H.-A. Bachor, T. Symul, and P. K. Lam, *Experimental investigation of continuous-variable quantum teleportation*, Physical Review A **67**, 032302 (2003).

[43] T. Schaetz, M. D. Barrett, D. Leibfried, J. Chiaverini, J. Britton, W. M. Itano, J. D. Jost, C. Langer, and D. J. Wineland, *Quantum Dense Coding with Atomic Qubits*, Physical Review Letters **93**, 040505 (2004).

[44] K. Mattle, H. Weinfurter, P. G. Kwiat, and A. Zeilinger, *Dense Coding in Experimental Quantum Communication*, Physical Review Letters **76**, 4656 (1996).

[45] S. L. Braunstein and H. J. Kimble, *Dense coding for continuous variables*, Physical Review A **61**, 042302 (2000).

[46] P. Grangier, J. A. Levenson, and J.-P. Poizat, *Quantum non-demolition measurements in optics*, Nature **396**, 537 (1998).

[47] U. L. Andersen, B. C. Buchler, H.-A. Bachor, and P. K. Lam, *Quantum nondemolition measurement with a nonclassical meter input and an electro-optic enhancement*, Journal of Optics B: Quantum and Semiclassical Optics **4**, 229 (2002).

[48] G. J. Pryde, J. L. O'Brien, A. G. White, S. D. Bartlett, and T. C. Ralph, *Measuring a Photonic Qubit without Destroying It*, Physical Review Letters **92**, 190402 (2004).

[49] T. C. Ralph, S. D. Bartlett, J. L. O'Brien, G. J. Pryde, and H. M. Wiseman, *Quantum nondemolition measurements for quantum information*, Physical Review A **73**, 012113 (2006).

[50] C. H. Bennett and G. Brassard, *Quantum Cryptography: Public Key Distribution and Coin Tossing*, Proceedings of IEEE International Conference on Computers Systems and Signal Processing , 175 (1984).

[51] N. Gisin, G. Ribordy, W. Tittel, and H. Zbinden, *Quantum cryptography*, Reviews of Modern Physics **74**, 145 (2002).

[52] Magnus T. L. Hsu, Warwick P. Bowen, Nicolas Treps, and Ping Koy Lam, *Continuous-variable spatial entanglement for bright optical beams*, Phys. Rev. A **72**, 013802 (2005).

[53] A. Gatti, E. Brambilla, L. A. Lugiato, and M. I. Kolobov, *Quantum Entangled Images*, Physical Review Letters **83**, 1763 (1999).

[54] A. Gatti, L. A. Lugiato, K. I. Petsas, and I. Marzoli, *Spatial Einstein-Podolsky-Rosen aspects in the optical parametric oscillator below threshold*, Europhysics Letters **46**, 461 (1999).

[55] A. Gatti, E. Brambilla, and L. A. Lugiato, *Entangled Imaging and Wave-Particle Duality: From the Microscopic to the Macroscopic Realm*, Physical Review Letters **90**, 133603 (2003).

[56] M. I. Kolobov, *The spatial behavior of nonclassical light*, Reviews of Modern Physics **71**, 1539 (1999).

[57] M. I. Kolobov and P. Kumar, *Sub-shot-noise microscopy - Imaging of faint phase objects with squeezed light*, Optics Letters **18**, 849 (1993).

[58] M. I. Kolobov and C. Fabre, *Quantum Limits on Optical Resolution*, Physical Review Letters **85**, 3789 (2000).

[59] M.T.L. Hsu, V. Delaubert, W.P. Bowen, C. Fabre, H.-A. Bachor, and P.K. Lam, *A Quantum Study of Multibit Phase Coding for Optical Storage*, IEEE Journal of Quantum Electronics **42**, 1001 (2006).

[60] V. Delaubert, N. Treps, G. Bo, and C. Fabre, *Optical storage of high-density information beyond the diffraction limit: A quantum study*, Physical Review A **73**, 013820 (2006).

[61] S. Knappe, V. Shah, P. D. D. Schwindt, L. Hollberg, J. Kitching, L.-A. Liew, and J. Moreland, *A microfabricated atomic clock*, Applied Physics Letters **85**, 1460 (2004).

[62] C. Affolderbach, M. Stähler, S. Knappe, and R. Wynands, *An all-optical, high-sensitivity magnetic gradiometer*, Applied Physics B: Lasers and Optics **75**, 605 (2002).

[63] D. Budker, V. Yashchuk, and M. Zolotorev, *Nonlinear Magneto-optic Effects with Ultranarrow Widths*, Physical Review Letters **81**, 5788 (1998).

[64] D. Budker, D. F. Kimball, S. M. Rochester, V. V. Yashchuk, and M. Zolotorev, *Sensitive magnetometry based on nonlinear magneto-optical rotation*, Physical Review A **62**, 043403 (2000).

[65] D. Budker, D. F. Kimball, V. V. Yashchuk, and M. Zolotorev, *Nonlinear magneto-optical rotation with frequency-modulated light*, Physical Review A **65**, 055403 (2002).

[66] T. L. Gustavson, A. Landragin, and M. A. Kasevich, *Rotation sensing with a dual atom-interferometer Sagnac gyroscope* , Classical and Quantum Gravity **17**, 2385 (2000).

[67] E. L. Raab, M. Prentiss, A. Cable, S. Chu, and D. E. Pritchard, *Trapping of neutral sodium atoms with radiation pressure*, Physical Review Letters **59**, 2631 (1987).

[68] S. Chu, J. E. Bjorkholm, A. Ashkin, and A. Cable, *Experimental observation of optically trapped atoms*, Physical Review Letters **57**, 314 (1986).

[69] S. Chu, *Nobel Lecture: The manipulation of neutral particles*, Reviews of Modern Physics **70**, 685 (1998).

[70] S. Chu, L. Hollberg, J. E. Bjorkholm, A. Cable, and A. Ashkin, *Three-dimensional viscous confinement and cooling of atoms by resonance radiation pressure*, Physical Review Letters **55**, 48 (1985).

[71] P. D. Lett, R. N. Watts, C. I. Westbrook, W. D. Phillips, and P. L. Gould, *Observation of atoms laser cooled below the Doppler limit*, Physical Review Letters **61**, 169 (1988).

[72] W. D. Phillips, H. Metcalf, and H. Metcalf, *Laser Deceleration of an Atomic Beam*, Physical Review Letters **48**, 596 (1982).

[73] William D. Phillips, *Nobel Lecture: Laser cooling and trapping of neutral atoms*, Rev. Mod. Phys. **70**, 721 (1998).

[74] A. L. Migdall, W. D. Phillips, J. V. Prodan, T. H. Bergeman, and H. J. Metcalf, *First observation of magnetically trapped neutral atoms*, Physical Review Letters **54**, 2596 (1985).

[75] P. D. Lett, W. D. Phillips, S. L. Rolston, C. E. Tanner, R. N. Watts, and C. I. Westbrook, *Optical molasses*, Journal of the Optical Society of America B Optical Physics **6**, 2084 (1989).

[76] J. Prodan, A. Migdall, W. D. Phillips, I. So, H. Metcalf, and J. Dalibard, *Stopping atoms with laser light*, Physical Review Letters **54**, 992 (1985).

[77] C. Cohen-Tannoudji, J. Dupont-Roc, G. Grynberg, and T. A. B. Kennedy, *Atom-Photon Interactions: Basic Processes and Applications*, American Journal of Physics **61**, 572 (1993).

[78] C. Cohen-Tannoudji, *Manipulating Atoms with Photons*, Physica Scripta Volume T **76**, 33 (1998).

[79] J. Dalibard and C. Cohen-Tannoudji, *Dressed-atom approach to atomic motion in laser light - The dipole force revisited*, Journal of the Optical Society of America B Optical Physics **2**, 1707 (1985).

[80] A. Aspect, J. Dalibard, A. Heidmann, C. Salomon, and C. Cohen-Tannoudji, *Cooling atoms with stimulated emission*, Physical Review Letters **57**, 1688 (1986).

[81] J. Dalibard and C. Cohen-Tannoudji, *Atomic motion in laser light: connection between semiclassical and quantum descriptions* , Journal of Physics B Atomic Molecular Physics **18**, 1661 (1985).

[82] J. M. McGuirk, G. T. Foster, J. B. Fixler, M. J. Snadden, and M. A. Kasevich, *Sensitive absolute-gravity gradiometry using atom interferometry*, Physical Review A **65**, 033608 (2002).

[83] M. A. Kasevich, E. Riis, S. Chu, and R. G. Devoe, *RF spectroscopy in an atomic fountain*, Physical Review Letters **63**, 612 (1989).

[84] T. Udem, R. Holzwarth, and T. W. Hänsch, *Optical frequency metrology*, Nature **416**, 233 (2002).

[85] S. Bize, P. Laurent, M. Abgrall, H. Marion, I. Maksimovic, L. Cacciapuoti, J. Grünert, C. Vian, F. Pereira dos Santos, P. Rosenbusch, P. Lemonde, G. Santarelli, P. Wolf, A. Clairon, A. Luiten, M. Tobar, and C. Salomon, *Cold atom clocks and applications*, Journal of Physics B Atomic Molecular Physics **38**, 449 (2005).

[86] S. Wildermuth, S. Hofferberth, I. Lesanovsky, S. Groth, P. Krüger, J. Schmiedmayer, and I. Bar-Joseph, *Sensing electric and magnetic fields with Bose-Einstein condensates*, Applied Physics Letters **88**, 4103 (2006).

[87] M. Kasevich and S. Chu, *Atomic interferometry using stimulated Raman transitions*, Physical Review Letters **67**, 181 (1991).

[88] T. L. Gustavson, P. Bouyer, and M. A. Kasevich, *Precision Rotation Measurements with an Atom Interferometer Gyroscope*, Physical Review Letters **78**, 2046 (1997).

[89] D. S. Weiss, B. C. Young, and S. Chu, *Precision measurement of the photon recoil of an atom using atomic interferometry*, Physical Review Letters **70**, 2706 (1993).

[90] A. Lambrecht, T. Coudreau, A. M. Steinberg, and E. Giacobino, *Squeezing with cold atoms*, Europhysics Letters **36**, 93 (1996).

[91] V. Josse, A. Dantan, L. Vernac, A. Bramati, M. Pinard, and E. Giacobino, *Polarization Squeezing with Cold Atoms*, Physical Review Letters **91**, 103601 (2003).

[92] M. H. Anderson, J. R. Ensher, M. R. Matthews, C. E. Wieman, and E. A. Cornell, *Observation of Bose-Einstein Condensation in a Dilute Atomic Vapor*, Science **269**, 198 (1995).

[93] K. B. Davis, M.-O. Mewes, M. R. Andrews, N. J. van Druten, D. S. Durfee, D. M. Kurn, and W. Ketterle, *Bose-Einstein condensation in a gas of sodium atoms*, Physical Review Letters **75**, 3969 (1995).

[94] Wolfgang Ketterle, *Nobel lecture: When atoms behave as waves: Bose-Einstein condensation and the atom laser*, Rev. Mod. Phys. **74**, 1131 (2002).

[95] I. Bloch, T. W. Hänsch, and T. Esslinger, *Atom Laser with a cw Output Coupler*, Physical Review Letters **82**, 3008 (1999).

[96] N. P. Robins, C. Figl, S. A. Haine, A. K. Morrison, M. Jeppesen, J. J. Hope, and J. D. Close, *Achieving Peak Brightness in an Atom Laser*, Physical Review Letters **96**, 140403 (2006).

[97] E. W. Hagley, L. Deng, M. Kozuma, J. Wen, K. Helmerson, S. L. Rolston, and W. D. Phillips, *A Well-Collimated Quasi-Continuous Atom Laser*, Science **283**, 1706 (1999).

[98] B. Demarco, S. B. Papp, and D. S. Jin, *Pauli Blocking of Collisions in a Quantum Degenerate Atomic Fermi Gas*, Physical Review Letters **86**, 5409 (2001).

[99] C. Chin, M. Bartenstein, A. Altmeyer, S. Riedl, S. Jochim, J. H. Denschlag, and R. Grimm, *Observation of the Pairing Gap in a Strongly Interacting Fermi Gas*, Science **305**, 1128 (2004).

[100] M. W. Zwierlein, J. R. Abo-Shaeer, A. Schirotzek, C. H. Schunck, and W. Ketterle, *Vortices and superfluidity in a strongly interacting Fermi gas*, Nature **435**, 1047 (2005).

[101] M. Bartenstein, A. Altmeyer, S. Riedl, S. Jochim, C. Chin, J. H. Denschlag, and R. Grimm, *Crossover from a Molecular Bose-Einstein Condensate to a Degenerate Fermi Gas*, Physical Review Letters **92**, 120401 (2004).

[102] M. Greiner, C. A. Regal, and D. S. Jin, *Emergence of a molecular Bose-Einstein condensate from a Fermi gas*, Nature **426**, 537 (2003).

[103] C. Barceló, S. Liberati, and M. Visser, *Analogue gravity from Bose-Einstein condensates* , Classical and Quantum Gravity **18**, 1137 (2001).

[104] S. Weinfurtner, *Analogue model for an expanding universe*, General Relativity and Gravitation **37**, 1549 (2005).

[105] M. O. Scully and M. S. Zubairy, *'Quantum Optics'*, Cambridge University Press, 1997.

[106] J. F. Sherson, H. Krauter, R. K. Olsson, B. Julsgaard, K. Hammerer, I. Cirac, and E. S. Polzik, *Quantum teleportation between light and matter*, Nature **443**, 557 (2006).

[107] J. Hald and E. S. Polzik, *Mapping a quantum state of light onto atoms* , Journal of Optics B: Quantum and Semiclassical Optics **3**, 83 (2001).

[108] K. Hammerer, K. Mølmer, E. S. Polzik, and J. I. Cirac, *'Light-matter quantum interface'*, Phys. Rev. A **70**, 044304 (2004).

[109] S. A. Haine, M. K. Olsen, and J. J. Hope, *Generating Controllable Atom-Light Entanglement with a Raman Atom Laser System*, Physical Review Letters **96**, 133601 (2006).

[110] S. A. Haine and J. J. Hope, *Outcoupling from a Bose-Einstein condensate with squeezed light to produce entangled-atom laser beams*, Physical Review A **72**, 033601 (2005).

[111] J. Geremia, J. K. Stockton, and H. Mabuchi, *Suppression of Spin Projection Noise in Broadband Atomic Magnetometry*, Physical Review Letters **94**, 203002 (2005).

[112] J. Geremia, J. K. Stockton, A. C. Doherty, and H. Mabuchi, *Quantum Kalman Filtering and the Heisenberg Limit in Atomic Magnetometry*, Physical Review Letters **91**, 250801 (2003).

[113] J. K. Stockton, J. M. Geremia, A. C. Doherty, and H. Mabuchi, *Robust quantum parameter estimation: Coherent magnetometry with feedback*, Physical Review A **69**, 032109 (2004).

[114] S. Wildermuth, S. Hofferberth, I. Lesanovsky, S. Groth, P. Krüger, J. Schmiedmayer, and I. Bar-Joseph, *Sensing electric and magnetic fields with Bose-Einstein condensates*, Applied Physics Letters **88**, 4103 (2006).

[115] S. Chaudhury, G. A. Smith, K. Schulz, and P. S. Jessen, *Continuous Nondemolition Measurement of the Cs Clock Transition Pseudospin*, Physical Review Letters **96**, 043001 (2006).

[116] D. Oblak, J. K. Mikkelsen, W. Tittel, A. K. Vershovski, J. L. Sorensen, P. G. Petrov, C. L. Garrido Alzar, and E. S. Polzik, *Quantum noise limited interferometric measurement of atomic noise: towards spin squeezing on the Cs clock transition*, ArXiv Quantum Physics e-prints (2003).

[117] E. S. Polzik, J. Carri, and H. J. Kimble, *Atomic spectroscopy with squeezed light for sensitivity beyond the vacuum-state limit*, Applied Physics B Photophysics Laser Chemistry **55**, 279 (1992).

[118] L.-M. Duan, M. D. Lukin, J. I. Cirac, and P. Zoller, *Long-distance quantum communication with atomic ensembles and linear optics*, Nature **414**, 413 (2001).

[119] S. F. Pereira, M. Xiao, H. J. Kimble, and J. L. Hall, *Generation of squeezed light by intracavity frequency doubling*, Physical Review A **38**, 4931 (1988).

[120] L.-A. Wu, H. J. Kimble, J. L. Hall, and H. Wu, *Generation of squeezed states by parametric down conversion*, Physical Review Letters **57**, 2520 (1986).

[121] L.-A. Wu, M. Xiao, and H. J. Kimble, *Squeezed states of light from an optical parametric oscillator*, Journal of the Optical Society of America B Optical Physics **4**, 1465 (1987).

[122] M. D. Levenson, R. M. Shelby, A. Aspect, M. Reid, and D. F. Walls, *Generation and detection of squeezed states of light by nondegenerate four-wave mixing in an optical fiber*, Physical Review A **32**, 1550 (1985).

[123] M. D. Levenson, R. M. Shelby, and S. H. Perlmutter, *Squeezing of classical noise by nondegenerate four-wave mixing in an optical fiber*, Optics Letters **10**, 514 (1985).

[124] W. P. Bowen, N. Treps, R. Schnabel, and P. K. Lam, *Experimental Demonstration of Continuous Variable Polarization Entanglement*, Physical Review Letters **89**, 253601 (2002).

[125] W. P. Bowen, R. Schnabel, H.-A. Bachor, and P. K. Lam, *Polarization Squeezing of Continuous Variable Stokes Parameters*, Physical Review Letters **88**, 093601 (2002).

[126] Natalia Korolkova, Gerd Leuchs, Rodney Loudon, Timothy C. Ralph, and Christine Silberhorn, *Polarization squeezing and continuous-variable polarization entanglement*, Phys. Rev. A **65**, 052306 (2002).

[127] W. Happer, *Optical pumping.*, Reviews of Modern Physics **44**, 169 (1972).

[128] Y. Takahashi, K. Honda, N. Tanaka, K. Toyoda, K. Ishikawa, and T. Yabuzaki, *Quantum nondemolition measurement of spin via the paramagnetic Faraday rotation*, Physical Review A **60**, 4974 (1999).

[129] J. Hald, J. L. Sørensen, C. Schori, and E. S. Polzik, *Spin Squeezed Atoms: A Macroscopic Entangled Ensemble Created by Light*, Physical Review Letters **83**, 1319 (1999).

[130] A. Kuzmich, K. Mølmer, and E. S. Polzik, *Spin Squeezing in an Ensemble of Atoms Illuminated with Squeezed Light*, Physical Review Letters **79**, 4782 (1997).

[131] J. Hald, J. Lykke Sorensen, L. Leich, and E. S. Polzik, *Quantum noise of cold atomic spins illuminated with non-classical light*, Optics Express **2**, 93 (1998).

[132] E. S. Polzik, *Einstein-Podolsky-Rosen-correlated atomic ensembles*, Physical Review A **59**, 4202 (1999).

[133] B. Julsgaard, A. Kozhekin, and E. S. Polzik, *Experimental long-lived entanglement of two macroscopic objects*, Nature **413**, 400 (2001).

[134] C. Schori, B. Julsgaard, J. L. Sørensen, and E. S. Polzik, *Recording Quantum Properties of Light in a Long-Lived Atomic Spin State: Towards Quantum Memory*, Physical Review Letters **89**, 057903 (2002).

[135] B. Julsgaard, J. Sherson, J. I. Cirac, J. Fiurásek, and E. S. Polzik, *Experimental demonstration of quantum memory for light*, Nature **432**, 482 (2004).

[136] J. Sherson, A. S. Sørensen, J. Fiurásek, K. Mølmer, and E. S. Polzik, *Light qubit storage and retrieval using macroscopic atomic ensembles*, Physical Review A **74**, 011802 (2006).

[137] A. E. Kozhekin, K. Mølmer, and E. Polzik, *'Quantum memory for light'*, Phys. Rev. A **62**, 033809 (2000).

[138] A. Gatti, E. Brambilla, L. A. Lugiato, and M. Kolobov, *Quantum aspects of imaging*, Journal of Optics B: Quantum and Semiclassical Optics **2**, 196 (2000).

[139] A. Gatti and L. Lugiato, *Quantum images and critical fluctuations in the optical parametric oscillator below threshold*, Physical Review A **52**, 1675 (1995).

[140] L. A. Lugiato, A. Gatti, and E. Brambilla, *Quantum imaging*, Journal of Optics B: Quantum and Semiclassical Optics **4**, 176 (2002).

[141] A. Gatti, E. Brambilla, M. Bache, and L. A. Lugiato, *Correlated imaging, quantum and classical*, Physical Review A **70**, 013802 (2004).

[142] R. S. Bennink, S. J. Bentley, R. W. Boyd, and J. C. Howell, *Quantum and Classical Coincidence Imaging*, Physical Review Letters **92**, 033601 (2004).

[143] M. I. Kolobov and I. V. Sokolov, *Multimode squeezing, antibunching in space and noise-free optical images*, Europhysics Letters **15**, 271 (1991).

[144] I. V. Sokolov, M. I. Kolobov, A. Gatti, and L. A. Lugiato, *Quantum holographic teleportation*, Optics Communications **193**, 175 (2001).

[145] A. Gatti, E. Brambilla, M. Bache, and L. A. Lugiato, *Ghost Imaging with Thermal Light: Comparing Entanglement and Classical Correlation*, Physical Review Letters **93**, 093602 (2004).

[146] R. S. Bennink, S. J. Bentley, and R. W. Boyd, *"Two-Photon" Coincidence Imaging with a Classical Source*, Physical Review Letters **89**, 113601 (2002).

[147] J. C. Howell, R. S. Bennink, S. J. Bentley, and R. W. Boyd, *Realization of the Einstein-Podolsky-Rosen Paradox Using Momentum- and Position-Entangled Photons from Spontaneous Parametric Down Conversion*, Physical Review Letters **92**, 210403 (2004).

[148] N. K. Langford, R. B. Dalton, M. D. Harvey, J. L. O'Brien, G. J. Pryde, A. Gilchrist, S. D. Bartlett, and A. G. White, *Measuring Entangled Qutrits and Their Use for Quantum Bit Commitment*, Physical Review Letters **93**, 053601 (2004).

[149] M. T. L. Hsu, V. Delaubert, P. K. Lam, and W. P. Bowen, *Optimal optical measurement of small displacements*, Journal of Optics B: Quantum and Semiclassical Optics **6**, 495 (2004).

[150] M. J. Padgett and J. Courtial, *Poincare-sphere equivalent for light beams containing orbital angular momentum*, Optics Letters **24**, 430 (1999).

[151] H.-L. Guo, C.-X. Liu, Z.-L. Li, J.-F. Duan, X.-H. Han, B.-Y. Cheng, and D.-Z. Zhang, *Displacement and Force Measurements with Quadrant Photodetector in Optical Tweezers*, Chinese Physics Letter **20**, 950 (2003).

[152] R. M. Simmons, J. T. Finer, S. Chu, and J. A. Spudich, *Quantitative measurements of force and displacement using an optical trap*, Biophysical Journal **70**, 1813 (1996).

[153] F. Gittes and C. F. Schmidt, *Interference model for back-focal-plane displacement detection in optical tweezers*, Optics Letters **23**, 7 (1998).

[154] W. Denk and W. W. Webb, *Optical measurement of picometer displacements of transparent microscopic objects*, Applied Optics **29**, 2382 (1990).

[155] T. Santhanakrishnan, N. Krishna Mohan, M. D. Kothiyal, and R. S. Siroshi, *A Non-Contact Simultaneous Measurement of Out-Of-Plane Displacement and Tilt of a Cantilever using a Quadrant Detector*, Journal of Optics **24**, 109 (1995).

[156] C. A. J. Putman, B. G. de Grooth, N. F. van Hulst, and J. Greve, *A detailed analysis of the optical beam deflection technique for use in atomic force microscopy*, Journal of Applied Physics **72**, 6 (1992).

[157] D. A. Shaddock, M. B. Gray, and D. E. McClelland, *Frequency locking alaser to an optical cavity by use of spatial mode interference*, Optics Letters **24**, 1499 (1999).

[158] P. Török and F.-J. Kao, *'Optical imaging and microscopy'*, Springer-Verlag, 2003.

[159] J. Ye, D. W. Vernooy, and H. J. Kimble, *Trapping of Single Atoms in Cavity QED*, Physical Review Letters **83**, 4987 (1999).

[160] J. M. Raimond, M. Brune, and S. Haroche, *Manipulating quantum entanglement with atoms and photons in a cavity*, Reviews of Modern Physics **73**, 565 (2001).

[161] M. Fleischhauer and M. D. Lukin, *Dark-State Polaritons in Electromagnetically Induced Transparency*, Phys. Rev. Lett. **84**, 5094 (2000).

[162] K.-J. Boller, A. Imamolu, and S. E. Harris, *Observation of electromagnetically induced transparency*, Phys. Rev. Lett. **66**, 2593 (1991).

[163] L. Vestergaard Hau, S. E. Harris, Z. Dutton, and C. H. Behroozi, *Light speed reduction to 17 metres per second in an ultracold atomic gas*, Nature **397**, 594 (1999).

[164] D. F. Phillips, A. Fleischhauer, A. Mair, R. L. Walsworth, and M. D. Lukin, *Storage of Light in Atomic Vapor*, Phys. Rev. Lett. **86**, 783 (2001).

[165] R. E. Slusher, B. Yurke, J. C. Mertz, J. F. Valley, and L. W. Hollberg, *Observation of squeezed states generated by four-wave mixing in an optical cavity*, Physical Review Letters **55**, 2409 (1985).

[166] R. E. Slusher, B. Yurke, P. Grangier, A. Laporta, and D. F. Walls, *Squeezed-light generation by four-wave mixing near an atomic resonance*, Journal of the Optical Society of America B Optical Physics **4**, 1453 (1987).

[167] L. A. Orozco, M. G. Raizen, M. Xiao, R. J. Brecha, and H. J. Kimble, *Squeezed-state generation in optical bistability*, Journal of the Optical Society of America B Optical Physics **4**, 1490 (1987).

[168] M. G. Raizen, L. A. Orozco, M. Xiao, T. L. Boyd, and H. J. Kimble, *Squeezed-state generation by the normal modes of a coupled system*, Physical Review Letters **59**, 198 (1987).

[169] D. M. Hope, H.-A. Bachor, P. J. Manson, D. E. McClelland, and P. T. H. Fisk, *Observation of quadrature squeezing in a cavity-atom system*, Physical Review A **46**, 1181 (1992).

[170] G. Breitenbach, T. Müller, S. F. Pereira, J.-P. Poizat, S. Schiller, and J. Mlynek, *Squeezed vacuum from a monolithic optical parametric oscillator*, Journal of the Optical Society of America B Optical Physics **12**, 2304 (1995).

[171] M. J. Collett and C. W. Gardiner, *Squeezing of intracavity and traveling-wave light fields produced in parametric amplification*, Physical Review A **30**, 1386 (1984).

[172] M. J. Collett and R. Loudon, *Output properties of parametric amplifiers in cavities*, Journal of the Optical Society of America B Optical Physics **4**, 1525 (1987).

[173] A. Heidmann, R. J. Horowicz, S. Reynaud, E. Giacobino, C. Fabre, and G. Camy, *Observation of quantum noise reduction on twin laser beams*, Physical Review Letters **59**, 2555 (1987).

[174] P. K. Lam, T. C. Ralph, B. C. Buchler, D. E. McClelland, H.-A. Bachor, and J. Gao, *Optimization and transfer of vacuum squeezing from an optical parametric oscillator* , Journal of Optics B: Quantum and Semiclassical Optics **1**, 469 (1999).

[175] S. Suzuki, H. Yonezawa, F. Kannari, M. Sasaki, and A. Furusawa, *7 dB quadrature squeezing at 860 nm with periodically poled* $KTiOPO_4$, Applied Physics Letters **89**, 1116 (2006).

[176] H. Vahlbruch, M. Mehmet, N. Lastzka, B. Hage, S. Chelkowski, A. Franzen, S. Gossler, K. Danzmann, and R. Schnabel, *Observation of squeezed light with 10dB quantum noise reduction*, ArXiv Quantum Physics e-prints (2007).

[177] J. Ries, B. Brezger, and A. I. Lvovsky, *Experimental vacuum squeezing in rubidium vapor via self-rotation*, Physical Review A **68**, 025801 (2003).

[178] C. F. McCormick, V. Boyer, E. Arimondo, and P. D. Lett, *Strong relative intensity squeezing by four-wave mixing in Rb vapor*, Optics Letters **32**, 178 (2007).

[179] A. B. Matsko, I. Novikova, G. R. Welch, D. Budker, D. F. Kimball, and S. M. Rochester, *Vacuum squeezing in atomic media via self-rotation*, Physical Review A **66**, 043815 (2002).

[180] S. M. Rochester, D. S. Hsiung, D. Budker, R. Y. Chiao, D. F. Kimball, and V. V. Yashchuk, *Self-rotation of resonant elliptically polarized light in collision-free rubidium vapor*, Physical Review A **63**, 043814 (2001).

[181] M. T. L. Hsu, G. Hétet, A. Peng, C. C. Harb, H.-A. Bachor, M. T. Johnsson, J. J. Hope, P. K. Lam, A. Dantan, J. Cviklinski, A. Bramati, and M. Pinard, *Effect of atomic noise on optical squeezing via polarization self-rotation in a thermal vapor cell*, Phys. Rev. A **73**, 023806 (2006).

[182] Amy Peng, Mattias Johnsson, W. P. Bowen, P. K. Lam, H.-A. Bachor, and J. J. Hope, *Squeezing and entanglement delay using slow light*, Phys. Rev. A **71**, 033809 (2005).

[183] M. T. L. Hsu, G. Hétet, O. Glöckl, J. J. Longdell, B. C. Buchler, H.-A. Bachor, and P. K. Lam, *Quantum Study of Information Delay in Electromagnetically Induced Transparency*, Phys. Rev. Lett. **97**, 183601 (2006).

[184] J. L. Sørensen, J. Hald, and E. S. Polzik, *Quantum Noise of an Atomic Spin Polarization Measurement*, Physical Review Letters **80**, 3487 (1998).

[185] G. Santarelli, P. Laurent, P. Lemonde, A. Clairon, A. G. Mann, S. Chang, A. N. Luiten, and C. Salomon, *Quantum Projection Noise in an Atomic Fountain: A High Stability Cesium Frequency Standard*, Physical Review Letters **82**, 4619 (1999).

[186] D. Leibfried, M. D. Barrett, T. Schaetz, J. Britton, J. Chiaverini, W. M. Itano, J. D. Jost, C. Langer, and D. J. Wineland, *Toward Heisenberg-Limited Spectroscopy with Multiparticle Entangled States*, Science **304**, 1476 (2004).

[187] J. C. Maxwell, *A dynamical theory of the electromagnetic field*, Philosophical Transactions of the Royal Society of London **155**, 459 (1864).

[188] R. Loudon, *'The quantum theory of light'*, Oxford University Press, 2000.

[189] K. Nemoto and S. L. Braunstein, *Quantum coherence: myth or fact?*, Physics Letters A **333**, 378 (2004).

[190] D. F. Walls and G. J. Milburn, *'Quantum Optics'*, Springer-Verlag, 1994.

[191] D. T. Smithey, M. Beck, M. G. Raymer, and A. Faridani, *Measurement of the Wigner distribution and the density matrix of a light mode using optical homodyne tomography - Application to squeezed states and the vacuum*, Physical Review Letters **70**, 1244 (1993).

[192] W. P. Bowen, *'Experiments towards a quantum information network with squeezed light and entanglement'*, PhD thesis, Australian National University, Canberra, ACT, Australia, 2003.

[193] P. K. Lam, *'Application of quantum electro-optic control and squeezed light'*, PhD thesis, Australian National University, Canberra, ACT, Australia, 1998.

[194] A. E. Siegman, *'Lasers'*, University Science Books, 1986.

[195] B. C. Buchler, *'Electro-optic control of quantum measurements'*, PhD thesis, Australian National University, Canberra, ACT, Australia, 2001.

[196] J. Schwarzenbach, *'Essentials of Control'*, Addison Wesley Longman, 1996.

[197] R. W. P. Drever, J. L. Hall, F. V. Kowalski, J. Hough, G. M. Ford, A. J. Munley, and H. Ward, *Laser phase and frequency stabilization using an optical resonator*, Applied Physics B: Lasers and Optics **31**, 97 (1983).

[198] S. Arnon, *Use of Satellite Natural Vibrations to Improve Performance of Free-Space Satellite Laser Communication*, Applied Optics **37**, 5031 (1998).

[199] V. V. Nikulin, M. Bouzoubaa, V. A. Skormin, and T. E. Busch, *Modeling of an acousto-optic laser veam steering system intended for satellite communication*, Optical Engineering **40**, 2208 (2001).

[200] K. Svoboda, C. F. Schmidt, B. J. Schnapp, and S. M. Block, *Direct observation of kinesin stepping by optical trapping interferometry*, Nature **365**, 721 (1993).

[201] A. Mair, A. Vaziri, G. Weihs, and A. Zeilinger, *Entanglement of the orbital angular momentum states of photons*, Nature **412**, 313 (2001).

[202] J. Leach, M. J. Padgett, S. M. Barnett, S. Franke-Arnold, and J. Courtial, *Measuring the Orbital Angular Momentum of a Single Photon*, Physical Review Letters **88**, 257901 (2002).

[203] C. Fabre, J. B. Fouet, and A. Maître, *Quantum limits in the measurement of very small displacements in optical images*, Optics Letters **25**, 76 (2000).

[204] N. Treps, U. Andersen, B. Buchler, P. K. Lam, A. Maître, H.-A. Bachor, and C. Fabre, *Surpassing the Standard Quantum Limit for Optical Imaging Using Nonclassical Multimode Light*, Phys. Rev. Lett. **88**, 203601 (2002).

[205] N. Treps, N. Grosse, W. P. Bowen, M. T. L. Hsu, A. Maître, C. Fabre, H.-A. Bachor, and P. K. Lam, *Nano-displacement measurements using spatially multimode squeezed light*, Journal of Optics B: Quantum and Semiclassical Optics **6**, 664 (2004).

[206] N. Treps, V. Delaubert, A. Maître, J. M. Courty, and C. Fabre, *Quantum noise in multipixel image processing*, Physical Review A **71**, 013820 (2005).

[207] V. Delaubert, D. A. Shaddock, P. K. Lam, B. C. Buchler, H.-A. Bachor, and D. E. McClelland, *Generation of a phase-flipped Gaussian mode for optical measurements*, Journal of Optics A: Pure and Applied Optics **4**, 393 (2002).

[208] D. Z. Anderson, *Alignment of resonant optical cavities*, Applied Optics **23**, 2944 (1984).

[209] N. B. Simpson, K. Dholakia, L. Allen, and M. J. Padgett, *Mechanical equivalenceof spin and orbital angular momentum of light : an optical spanner*, Optics Letters **22**, 52 (1997).

[210] A. Peres and L. E. Ballentine, *Quantum Theory: Concepts and Methods*, American Journal of Physics **63**, 285 (1995).

[211] N. Bohr, *Can Quantum-Mechanical Description of Physical Reality be Considered Complete?*, Physical Review **48**, 696 (1935).

[212] R. W. Clark, *Einstein: The Life and Times*, American Journal of Physics **41**, 1029 (1973).

[213] A. Calaprice, *The expanded quotable Einstein*, The expanded quotable Einstein. Princeton, NJ: Princeton University Press, 2000. xliii, 407 p. With a foreword by Freeman Dyson. ISBN 0691070210, 2000.

[214] J. Bell, *'On the Einstein Podolsky Rosen Paradox'*, Physics **1**, 195 (1964).

[215] S. J. Freedman and J. F. Clauser, *Experimental Test of Local Hidden-Variable Theories*, Physical Review Letters **28**, 938 (1972).

[216] David Bohm, *A Suggested Interpretation of the Quantum Theory in Terms of "Hidden" Variables. I*, Phys. Rev. **85**, 166 (1952).

[217] H. M. Wiseman, *'From Einstein's theorem to Bell's theorem: a history of quantum non-locality'*, Contemporary Physics **47**, 79 (2006).

[218] W. P. Bowen, R. Schnabel, P. K. Lam, and T. C. Ralph, *Experimental Investigation of Criteria for Continuous Variable Entanglement*, Physical Review Letters **90**, 043601 (2003).

[219] W. P. Bowen, R. Schnabel, P. K. Lam, and T. C. Ralph, *Experimental characterization of continuous-variable entanglement*, Physical Review A **69**, 012304 (2004).

[220] O. Glöckl, J. Heersink, N. Korolkova, G. Leuchs, and S. Lorenz, *A pulsed source of continuous variable polarization entanglement*, Journal of Optics B: Quantum and Semiclassical Optics **5**, 492 (2003).

[221] V. Josse, A. Dantan, A. Bramati, M. Pinard, and E. Giacobino, *Continuous Variable Entanglement using Cold Atoms*, Physical Review Letters **92**, 123601 (2004).

[222] A. Kuzmich and E. S. Polzik, *Atomic Quantum State Teleportation and Swapping*, Physical Review Letters **85**, 5639 (2000).

[223] A. Dantan and M. Pinard, *Quantum-state transfer between fields and atoms in electromagnetically induced transparency*, Physical Review A **69**, 043810 (2004).

[224] A. F. Abouraddy, B. E. Saleh, A. V. Sergienko, and M. C. Teich, *Role of Entanglement in Two-Photon Imaging*, Physical Review Letters **87**, 123602 (2001).

[225] T. B. Pittman, Y. H. Shih, D. V. Strekalov, and A. V. Sergienko, *Optical imaging by means of two-photon quantum entanglement*, Physical Review A **52**, 3429 (1995).

[226] A. F. Abouraddy, B. A. Saleh, A. V. Sergienko, and M. C. Teich, *Quantum holography*, Optics Express **9**, 498 (2001).

[227] I. V. Sokolov, *Imaging of faint phase objects at the Heisenberg limit with quadrature-squeezed light*, Journal of Optics B: Quantum and Semiclassical Optics **2**, 179 (2000).

[228] D. J. Griffiths, *'Introduction to Quantum Mechanics'*, Prentice Hall, New Jersey, 1995.

[229] L.-M. Duan, G. Giedke, J. I. Cirac, and P. Zoller, *Inseparability Criterion for Continuous Variable Systems*, Physical Review Letters **84**, 2722 (2000).

[230] M. D. Reid and P. D. Drummond, *'Quantum Correlations of Phase in Nondegenerate Parametric Oscillaton'*, Phys. Rev. Lett. **60**, 2731 (1988).

[231] S. M. Tan, *Confirming entanglement in continuous variable quantum teleportation*, Physical Review A **60**, 2752 (1999).

[232] S. Mancini, V. Giovannetti, D. Vitali, and P. Tombesi, *Entangling Macroscopic Oscillators Exploiting Radiation Pressure*, Physical Review Letters **88**, 120401 (2002).

[233] H. H. Arnaut and G. A. Barbosa, *Orbital and Intrinsic Angular Momentum of Single Photons and Entangled Pairs of Photons Generated by Parametric Down-Conversion*, Physical Review Letters **85**, 286 (2000).

[234] S. Franke-Arnold, S. M. Barnett, M. J. Padgett, and L. Allen, *Two-photon entanglement of orbital angular momentum states*, Physical Review A **65**, 033823 (2002).

[235] L. Allen, M. W. Beijersbergen, R. J. C. Spreeuw, and J. P. Woerdman, *Orbital angular momentum of light and the transformation of Laguerre-Gaussian laser modes*, Physical Review A **45**, 8185 (1992).

[236] J. Arlt, K. Dholakia, L. Allen, and M. J. Padgett, *Parametric down-conversion for light beams possessing orbital angular momentum*, Physical Review A **59**, 3950 (1999).

[237] S. M. Barnett and R. Zambrini, *Resolution in rotation measurements*, Journal of Modern Optics **53**, 613 (2006).

[238] J. Leach, J. Courtial, K. Skeldon, S. M. Barnett, S. Franke-Arnold, and M. J. Padgett, *Interferometric Methods to Measure Orbital and Spin, or the Total Angular Momentum of a Single Photon*, Physical Review Letters **92**, 013601 (2004).

[239] J. Leach, M. R. Dennis, J. Courtial, and M. J. Padgett, *Laser beams: Knotted threads of darkness*, Nature **432**, 165 (2004).

[240] A. A. Malyutin, *Properties of an astigmatic $\pi/2$-mode converter*, Quantum Electronics **33**, 235 (2003).

[241] K. T. Kapale and J. P. Dowling, *Vortex Phase Qubit: Generating Arbitrary, Counterrotating, Coherent Superpositions in Bose-Einstein Condensates via Optical Angular Momentum Beams*, Physical Review Letters **95**, 173601 (2005).

[242] T. Isoshima, M. Nakahara, T. Ohmi, and K. Machida, *Creation of a persistent current and vortex in a Bose-Einstein condensate of alkali-metal atoms*, Physical Review A **61**, 063610 (2000).

[243] D. Akamatsu and M. Kozuma, *Coherent transfer of orbital angular momentum from an atomic system to a light field*, Physical Review A **67**, 023803 (2003).

[244] M. E. J. Friese, J. Enger, H. Rubinsztein-Dunlop, and N. R. Heckenberg, *Optical angular-momentum transfer to trapped absorbing particles*, Physical Review A **54**, 1593 (1996).

[245] H. He, M. E. J. Friese, N. R. Heckenberg, and H. Rubinsztein-Dunlop, *Direct Observation of Transfer of Angular Momentum to Absorptive Particles from a Laser Beam with a Phase Singularity*, Physical Review Letters **75**, 826 (1995).

[246] L. Paterson, M. P. MacDonald, J. Arlt, W. Sibbett, P. E. Bryant, and K. Dholakia, *Controlled Rotation of Optically Trapped Microscopic Particles*, Science **292**, 912 (2001).

[247] U. Fano, *A Stokes-Parameter Technique for the Treatment of Polarization in Quantum Mechanics*, Physical Review **93**, 121 (1954).

[248] E. W. Williams, *'The CD-ROM and optical disc recording systems'*, Oxford University Press, 1996.

[249] L. W. Couch, *'Digital and analog communication systems'*, Macmillan, 1993.

[250] J. Laurat, T. Coudreau, G. Keller, N. Treps, and C. Fabre, *Compact source of Einstein-Podolsky-Rosen entanglement and squeezing at very low noise frequencies*, Physical Review A **70**, 042315 (2004).

[251] L. Lopez, S. Gigan, N. Treps, A. Maître, C. Fabre, and A. Gatti, *Multimode squeezing properties of a confocal optical parametric oscillator: Beyond the thin-crystal approximation*, Physical Review A **72**, 013806 (2005).

[252] C. J. Foot, *'Atomic Physics'*, Oxford University Press, 2005.

[253] S. R. Amin, C. D. Caldwell, and W. Lichten, *Crossed-Beam Spectroscopy of Hydrogen: A New Value for the Rydberg Constant*, Physical Review Letters **47**, 1234 (1981).

[254] C. L. Cesar, D. G. Fried, T. C. Killian, A. D. Polcyn, J. C. Sandberg, I. A. Yu, T. J. Greytak, D. Kleppner, and J. M. Doyle, *Two-Photon Spectroscopy of Trapped Atomic Hydrogen*, Physical Review Letters **77**, 255 (1996).

[255] M. Aymar, P. Camus, M. Dieulin, and C. Morillon, *Two-photon spectroscopy of neutral barium: Observations of the highly excited even levels and theoretical analysis of the J=0 spectrum*, Physical Review A **18**, 2173 (1978).

[256] C. Wieman and T. W. Hänsch, *Doppler-Free Laser Polarization Spectroscopy*, Physical Review Letters **36**, 1170 (1976).

[257] J. L. Hall, C. J. Bordé, and K. Uehara, *Direct Optical Resolution of the Recoil Effect Using Saturated Absorption Spectroscopy*, Physical Review Letters **37**, 1339 (1976).

[258] D. S. Gough and P. Hannaford, *High quality saturated absorption spectroscopy in a sputtered vapour: Application to hyperfine structure in Zr I*, Optics Communications **67**, 209 (1988).

[259] R. W. Boyd, *Nonlinear Optics*, Nonlinear Optics, 2nd ed.. by R.W. Boyd. London: Academic Press, 2003 ISBN 9780121216825, 2003.

[260] J. L. Hall, L. Hollberg, T. Baer, and H. G. Robinson, *Optical heterodyne saturation spectroscopy*, Applied Physics Letters **39**, 680 (1981).

[261] A. Schenzle, R. G. Devoe, and R. G. Brewer, *Phase-modulation laser spectroscopy*, Physical Review A **25**, 2606 (1982).

[262] G. C. Bjorklund, *Frequency-modulation spectroscopy: a new method for measuring weak absorptions and dispersions*, Optics Letters **5**, 15 (1980).

[263] R. J. Glauber, *Coherent and Incoherent States of the Radiation Field*, Physical Review **131**, 2766 (1963).

[264] D. F. Walls, *Squeezed states of light*, Nature **306**, 141 (1983).

[265] P. Kürz, R. Paschotta, K. Fiedler, and J. Mlynek, *Bright squeezed light by second-harmonic generation in a monolithic resonator*, Europhysics Letters **24**, 449 (1993).

[266] A. Sizmann, R. J.. Horowicz, E. Wagner, and G. Leuchs, *Observation of amplitude squeezing of the up-converted mode in second harmonic generation*, Optics Communications **80**, 138 (1990).

[267] R. Paschotta, M. Collett, P. Kürz, K. Fiedler, H. A. Bachor, and J. Mlynek, *Bright squeezed light from a singly resonant frequency doubler*, Physical Review Letters **72**, 3807 (1994).

[268] T. C. Ralph, M. S. Taubman, A. G. White, D. E. McClelland, and H.-A. Bachor, *Squeezed light from second-harmonic generation: experiment versus theory*, Optics Letters **20**, 1316 (1995).

[269] H. Tsuchida, *Generation of amplitude-squeezed light at 431 nm from a singly resonant frequency doubler*, Optics Letters **20**, 2240 (1995).

[270] A. G. White, T. C. Ralph, and H.-A. Bachor, *Active versus passive squeezing by second-harmonic generation*, Journal of the Optical Society of America B Optical Physics **13**, 1337 (1996).

[271] M. J. Lawrence, R. L. Byer, M. M. Fejer, W. Bowen, P. K. Lam, and H.-A. Bachor, *Squeezed singly resonant second-harmonic generation in periodically poled lithium niobate*, Journal of the Optical Society of America B Optical Physics **19**, 1592 (2002).

[272] H. P. Yuen and J. H. Shapiro, *Generation and detection of two-photon coherent states in degenerate four-wave mixing*, Optics Letters **4**, 334 (1979).

[273] L. Boivin and H. A. Haus, *$\chi(3)$ squeezed vacuum generation without a Sagnac interferometer*, Optics Letters **21**, 146 (1996).

[274] M. Margalit, C. X. Yu, E. P. Ippen, and H. A. Haus, *Cross phase modulation squeezing in optical fibers*, Optics Express **2**, 72 (1998).

[275] K. Bergman and H. A. Haus, *Squeezing in fibers with optical pulses*, Optics Letters **16**, 663 (1991).

[276] K. Bergman, C. R. Doerr, H. A. Haus, and M. Shirasaki, *Sub-shot-noise measurement with fiber-squeezed optical pulses*, Optics Letters **18**, 643 (1993).

[277] M. Rosenbluh and R. M. , *Squeezed optical solitons*, Physical Review Letters **66**, 153 (1991).

[278] S. Machida, Y. Yamamoto, and Y. Itaya, *Observation of amplitude squeezing in a constant-current-driven semiconductor laser*, Physical Review Letters **58**, 1000 (1987).

[279] S. Machida and Y. Yamamatu, *Ultrabroadband amplitude squeezing in a semiconductor laser*, Physical Review Letters **60**, 792 (1988).

[280] Y. Yamamoto, N. Imoto, and S. Machida, *Amplitude squeezing in a semiconductor laser using quantum nondemolition measurement and negative feedback*, Physical Review A **33**, 3243 (1986).

[281] C. Schori, J. L. Sørensen, and E. S. Polzik, *Narrow-band frequency tunable light source of continuous quadrature entanglement*, Physical Review A **66**, 033802 (2002).

[282] I. Novikova, A. B. Matsko, and G. R. Welch, *Large polarization self-rotation in rubidium vapour: application for squeezing of electromagnetic vacuum*, Journal of Modern Optics **49**, 2565 (2002).

[283] A. S. Zibrov and I. Novikova, *Observation of quantum noise in the polarization of laser light in a Rubidium-vapor cell*, JETP Letters **82**, 110 (2005).

[284] M. Kauranen, A. L. Gaeta, R. W. Boyd, and G. S. Agarwal, *Amplification of vacuum fluctuations by two-beam coupling in atomic vapors*, Physical Review A **50**, 929 (1994).

[285] G. S. Agarwal and R. W. Boyd, *Quantum theory of Rabi sideband generation by forward four-wave mixing*, Physical Review A **38**, 4019 (1988).

[286] M. Fleischhauer and M. D. Lukin, *Quantum memory for photons: Dark-state polaritons*, Physical Review A **65**, 022314 (2002).

[287] M. D. Eisaman, A. André, F. Massou, M. Fleischhauer, A. S. Zibrov, and M. D. Lukin, *Electromagnetically induced transparency with tunable single-photon pulses*, Nature **438**, 837 (2005).

[288] T. Chanelière, D. N. Matsukevich, S. D. Jenkins, S.-Y. Lan, T. A. B. Kennedy, and A. Kuzmich, *Storage and retrieval of single photons transmitted between remote quantum memories*, Nature **438**, 833 (2005).

[289] Michael M. Kash, Vladimir A. Sautenkov, Alexander S. Zibrov, L. Hollberg, George R. Welch, Mikhail D. Lukin, Yuri Rostovtsev, Edward S. Fry, and Marlan O. Scully, *Ultraslow Group Velocity and Enhanced Nonlinear Optical Effects in a Coherently Driven Hot Atomic Gas*, Phys. Rev. Lett. **82**, 5229 (1999).

[290] M. Bajcsy, A. S. Zibrov, and M. D. Lukin, *Stationary pulses of light in an atomic medium*, Nature **426**, 638 (2003).

[291] C. Liu, Z. Dutton, C. H. Behroozi, and L. V. Hau, *Observation of coherent optical information storage in an atomic medium using halted light pulses*, Nature **409**, 490 (2001).

[292] J. J. Longdell, E. Fraval, M. J. Sellars, and N. B. Manson, *Stopped Light with Storage Times Greater than One Second Using Electromagnetically Induced Transparency in a Solid*, Phys. Rev. Lett. **95**, 063601 (2005).

[293] A. V. Turukhin, V. S. Sudarshanam, M. S. Shahriar, J. A. Musser, B. S. Ham, and P. R. Hemmer, *Observation of Ultraslow and Stored Light Pulses in a Solid*, Phys. Rev. Lett. **88**, 023602 (2001).

[294] E. B. Aleksandrov and V. S. Zapasskii, *A fairy tale of stopped light*, Physics-Uspekhi **47**, 1033 (2004).

[295] A. Lezama, A. M. Akulshin, A. I. Sidorov, and P. Hannaford, *Storage and retrieval of light pulses in atomic media with "slow" and "fast" light*, Physical Review A **73**, 033806 (2006).

[296] A M Akulshin, A Lezama, A I Sidorov, R J McLean, and P Hannaford, *‘Storage of light’ in an atomic medium using electromagnetically induced absorption*, Journal of Physics B: Atomic, Molecular and Optical Physics **38**, L365 (2005).

[297] D. Akamatsu, K. Akiba, and M. Kozuma, *Electromagnetically Induced Transparency with Squeezed Vacuum*, Physical Review Letters **92**, 203602 (2004).

[298] D. Akamatsu, Y. Yokoi, T. Tanimura, A. Furusawa, and M. Kozuma, *Ultraslow Propagation of a Squeezed Vacuum with Electromagnetically Induced Transparency*, ArXiv Quantum Physics e-prints (2006).

[299] A. B. Matsko, Y. V. Rostovtsev, O. Kocharovskaya, A. S. Zibrov, and M. O. Scully, *Nonadiabatic approach to quantum optical information storage*, Phys. Rev. A **64**, 043809 (2001).

[300] G. Hétet, A. Peng, M. T. Johnsson, M. T. L. Hsu, O. Glöckl, P. K. Lam, H. A. Bachor, and J. J. Hope, *Erratum: Squeezing and entanglement delay using slow light [Phys. Rev. A 71, 033809 (2005)]*, Physical Review A **74**, 059902 (2006).

[301] E. Figueroa, F. Vewinger, J. Appel, and A. I. Lvovsky, *Decoherence of electromagnetically induced transparency in atomic vapor*, Optics Letters **31**, 2625 (2006).

[302] E. E. Mikhailov, V. A. Sautenkov, Y. V. Rostovtsev, A. Zhang, M. S. Zubairy, M. O. Scully, and G. R. Welch, *Spectral narrowing via quantum coherence*, Physical Review A **74**, 013807 (2006).

[303] C. L. Garrido Alzar, L. S. Cruz, J. G. Aguirre Gómez, M. França Santos, and P. Nussenzveig, *Super-Poissonian intensity fluctuations and correlations between pump and probe fields in Electromagnetically Induced Transparency*, Europhysics Letters **61**, 485 (2003).

[304] C. L. Garrido Alzar, L. S. da Cruz, J. G. Aguirre Gómez, M. Martinelli, M. França Santos, D. Felinto, P. Valente, H. Failache, A. Lezama, and P. Nussenzveig, *Statistical properties of macroscopic laser fields after coherent interaction with an atomic vapour*, Journal of Optics B: Quantum and Semiclassical Optics **6**, 518 (2004).

[305] G. Hétet, A. Peng, M. T. Johnsson, J. J. Hope, and P. K. Lam, *Characterization of EIT-based continuous variable quantum memories*, ArXiv e-prints **707** (2007).

[306] A. B. Matsko, I. Novikova, M. O. Scully, and G. R. Welch, *Radiation Trapping in Coherent Media*, Phys. Rev. Lett. **87**, 133601 (2001).

[307] J. Appel, E. Figueroa, D. Korystov, and A. I. Lvovsky, *Quantum memory for squeezed light*, ArXiv e-prints **709** (2007).

[308] K. Honda, D. Akamatsu, M. Arikawa, Y. Yokoi, K. Akiba, S. Nagatsuka, T. Tanimura, A. Furusawa, and M. Kozuma, *Storage and retrieval of a squeezed vacuum*, ArXiv e-prints **709** (2007).

[309] Z. Y. Ou and L. Mandel, *'Violation of Bell's Inequality and Classical Probability in a Two-Photon Correlation Experiment'*, Phys. Rev. Lett. **61**, 50 (1988).

[310] P. Kok, W. J. Munro, K. Nemoto, T. C. Ralph, J. P. Dowling, and G. J. Milburn, *Linear optical quantum computing with photonic qubits*, Reviews of Modern Physics **79**, 135 (2007).

[311] A. M. Lance, T. Symul, W. P. Bowen, B. C. Sanders, and P. K. Lam, *Tripartite Quantum State Sharing*, Physical Review Letters **92**, 177903 (2004).

[312] A. M. Lance, T. Symul, V. Sharma, C. Weedbrook, T. C. Ralph, and P. K. Lam, *No-Switching Quantum Key Distribution Using Broadband Modulated Coherent Light*, Physical Review Letters **95**, 180503 (2005).

[313] C. H. Bennett, G. Brassard, and N. D. Mermin, *Quantum cryptography without Bell's theorem*, Physical Review Letters **68**, 557 (1992).

[314] A. K. Ekert, *Quantum cryptography based on Bell's theorem*, Physical Review Letters **67**, 661 (1991).

[315] F. Grosshans and P. Grangier, *Continuous Variable Quantum Cryptography Using Coherent States*, Physical Review Letters **88**, 057902 (2002).

[316] B. C. Buchler, P. K. Lam, H.-A. Bachor, U. L. Andersen, and T. C. Ralph, *Squeezing more from a quantum nondemolition measurement*, Physical Review A **65**, 011803 (2002).

[317] E. Hagley, X. Maître, G. Nogues, C. Wunderlich, M. Brune, J. M. Raimond, and S. Haroche, *Generation of Einstein-Podolsky-Rosen Pairs of Atoms*, Physical Review Letters **79**, 1 (1997).

[318] D. N. Matsukevich, T. Chanelière, S. D. Jenkins, S.-Y. Lan, T. A. Kennedy, and A. Kuzmich, *Entanglement of Remote Atomic Qubits*, Physical Review Letters **96**, 030405 (2006).

[319] C. A. Sackett, D. Kielpinski, B. E. King, C. Langer, V. Meyer, C. J. Myatt, M. Rowe, Q. A. Turchette, W. M. Itano, D. J. Wineland, and C. Monroe, *Experimental entanglement of four particles*, Nature **404**, 256 (2000).

[320] Q. A. Turchette, C. S. Wood, B. E. King, C. J. Myatt, D. Leibfried, W. M. Itano, C. Monroe, and D. J. Wineland, *Deterministic Entanglement of Two Trapped Ions*, Physical Review Letters **81**, 3631 (1998).

[321] H. Häffner, W. Hänsel, C. F. Roos, J. Benhelm, D. Chek-Al-Kar, M. Chwalla, T. Körber, U. D. Rapol, M. Riebe, P. O. Schmidt, C. Becher, O. Gühne, W. Dür, and R. Blatt, *Scalable multiparticle entanglement of trapped ions*, Nature **438**, 643 (2005).

[322] M. D. Barrett, J. Chiaverini, T. Schaetz, J. Britton, W. M. Itano, J. D. Jost, E. Knill, C. Langer, D. Leibfried, R. Ozeri, and D. J. Wineland, *Deterministic quantum teleportation of atomic qubits*, Nature **429**, 737 (2004).

[323] M. Riebe, H. Häffner, C. F. Roos, W. Hänsel, J. Benhelm, G. P. T. Lancaster, T. W. Körber, C. Becher, F. Schmidt-Kaler, D. F. V. James, and R. Blatt, *Deterministic quantum teleportation with atoms*, Nature **429**, 734 (2004).

[324] S. Gulde, M. Riebe, G. P. T. Lancaster, C. Becher, J. Eschner, H. Häffner, F. Schmidt-Kaler, I. L. Chuang, and R. Blatt, *Implementation of the Deutsch-Jozsa algorithm on an ion-trap quantum computer*, Nature **421**, 48 (2003).

[325] L. M. K. Vandersypen, M. Steffen, G. Breyta, C. S. Yannoni, M. H. Sherwood, and I. L. Chuang, *Experimental realization of Shor's quantum factoring algorithm using nuclear magnetic resonance*, Nature **414**, 883 (2001).

[326] C. Monroe, D. M. Meekhof, B. E. King, W. M. Itano, and D. J. Wineland, *Demonstration of a fundamental quantum logic gate*, Physical Review Letters **75**, 4714 (1995).

[327] A. Kuzmich, W. P. Bowen, A. D. Boozer, A. Boca, C. W. Chou, L.-M. Duan, and H. J. Kimble, *Generation of nonclassical photon pairs for scalable quantum communication with atomic ensembles*, Nature **423**, 731 (2003).

[328] D. Felinto, C. W. Chou, J. Laurat, E. W. Schomburg, H. de Riedmatten, and H. J. Kimble, *Conditional control of the quantum states of remote atomic memories for quantum networking*, Nature Physics **2**, 844 (2006).

[329] B. Julsgaard, *'Entanglement and quantum interactions with macroscopic gas samples'*, PhD thesis, University of Aarhus, Aarhus, Denmark, 2003.

[330] J. K. Stockton, *'Continuous quantum measurement of cold alkali-atom spins'*, PhD thesis, California Institute of Technology, Pasadena, California, U.S.A., 2007.

[331] A. Kuzmich, L. Mandel, and N. P. Bigelow, *Generation of Spin Squeezing via Continuous Quantum Nondemolition Measurement*, Physical Review Letters **85**, 1594 (2000).

[332] J. Geremia, J. K. Stockton, and H. Mabuchi, *Real-Time Quantum Feedback Control of Atomic Spin-Squeezing*, Science **304**, 270 (2004).

[333] M. Kitagawa and M. Ueda, *Squeezed spin states*, Phys. Rev. A **47**, 5138 (1993).

[334] L. K. Thomsen, S. Mancini, and H. M. Wiseman, *Spin squeezing via quantum feedback*, Physical Review A **65**, 061801 (2002).

[335] J. K. Stockton, R. van Handel, and H. Mabuchi, *Deterministic Dicke-state preparation with continuous measurement and control*, Physical Review A **70**, 022106 (2004).

[336] B. Julsgaard, J. Sherson, J. L. Sørensen, and E. S. Polzik, *Characterizing the spin state of an atomic ensemble using the magneto-optical resonance method*, Journal of Optics B: Quantum and Semiclassical Optics **6**, 5 (2004).

[337] M. D. Barrett, J. A. Sauer, and M. S. Chapman, *All-Optical Formation of an Atomic Bose-Einstein Condensate*, Physical Review Letters **87**, 010404 (2001).

[338] C. C. Bradley, C. A. Sackett, J. J. Tollett, and R. G. Hulet, *Evidence of Bose-Einstein Condensation in an Atomic Gas with Attractive Interactions*, Physical Review Letters **75**, 1687 (1995).

[339] Dale G. Fried, Thomas C. Killian, Lorenz Willmann, David Landhuis, Stephen C. Moss, Daniel Kleppner, and Thomas J. Greytak, *Bose-Einstein Condensation of Atomic Hydrogen*, Phys. Rev. Lett. **81**, 3811 (1998).

[340] W. Petrich, M. H. Anderson, J. R. Ensher, and E. A. Cornell, *Behavior of atoms in a compressed magneto-optical trap*, Journal of the Optical Society of America B Optical Physics **11**, 1332 (1994).

[341] W. Ketterle, K. B. Davis, M. A. Joffe, A. Martin, and D. E. Pritchard, *High densities of cold atoms in a dark spontaneous-force optical trap*, Physical Review Letters **70**, 2253 (1993).

[342] M. T. DePue, S. Lukman Winoto, D. J. Han, and D. S. Weiss, *Transient compression of a MOT and high intensity fluorescent imaging of optically thick clouds of atoms*, Optics Communications **180**, 73 (2000).

[343] C. G. Townsend, N. H. Edwards, K. P. Zetie, C. J. Cooper, J. Rink, and C. J. Foot, *High-density trapping of cesium atoms in a dark magneto-optical trap*, Physical Review A **53**, 1702 (1996).

[344] C. Salomon, J. Dalibard, W. D. Phillips, A. Clairon, and S. Guellati, *Laser cooling of cesium atoms below* $3\mu K$, Europhysics Letters **12**, 683 (1990).

[345] J. Dalibard and C. Cohen-Tannoudji, *Laser cooling below the Doppler limit by polarization gradients: Simple theoretical models*, Journal of the Optical Society of America B Optical Physics **6**, 2023 (1989).

[346] P. J. Ungar, D. S. Weiss, E. Riis, and S. Chu, *Optical molasses and multilevel atoms: theory*, Journal of the Optical Society of America B Optical Physics **6**, 2058 (1989).